

Compositional Characterization of Organo-Lead tri-Halide Perovskite Solar Cells

THÈSE N° 8410 (2018)

PRÉSENTÉE LE 9 MARS 2018

À LA FACULTÉ DES SCIENCES DE BASE

LABORATOIRE DE PHOTONIQUE ET INTERFACES

PROGRAMME DOCTORAL EN CHIMIE ET GÉNIE CHIMIQUE

ÉCOLE POLYTECHNIQUE FÉDÉRALE DE LAUSANNE

POUR L'OBTENTION DU GRADE DE DOCTEUR ÈS SCIENCES

PAR

Paul GRATIA

acceptée sur proposition du jury:

Prof. A. Züttel, président du jury
Prof. M. K. Nazeeruddin, Prof. M. Graetzel, directeurs de thèse
Prof. A. Di Carlo, rapporteur
Prof. G. Boschloo, rapporteur
Prof. A. Hagfeldt, rapporteur



ÉCOLE POLYTECHNIQUE
FÉDÉRALE DE LAUSANNE

Suisse
2018

Abstract

Perovskite photovoltaics is one of the fastest growing research fields in materials science. Apart from photovoltaics, a wide range of energy-related research fields have gained substantial new momentum owing to the fantastic optoelectronic properties of hybrid lead halide perovskites. Starting with solar cells showing a mere 3% power conversion efficiency in 2009, researchers have been able to increase this value to over 22% in 2017, comparable to the best monocrystalline silicon solar cells. These improvements are chiefly due to the compositional tuning and mixing of the ABX_3 perovskite structure. However, this strategy increases not only the efficiency but also in the same time the complexity of the perovskite formulation. Different phases, from the nano- to macroscale, can potentially form. In order to rationalize the efficiency progress, one needs to understand and characterize the complex perovskite composition and crystal structure in great detail. The main focus of this thesis lies in the in-depth compositional and phase analysis of perovskite thin films as well as full perovskite solar cells, trying to rationalize the consequences of A cation and X anion tuning and mixing.

In the first part, it is shown that fabricating solar cells from a non-stoichiometric perovskite precursor composition, namely one with PbI_2 excess, leads to increased grain size, enhanced crystallinity, reduced recombination as well as an improved TiO_2 /perovskite interface. As opposed to lead iodide phases resulting from film degradation, which is hampering device performance, unreacted excess PbI_2 phases originating from an excess of PbI_2 in the precursor solution are very beneficial for the final solar cell efficiency, reproducibility and stability.

The next scientific challenge addressed in this thesis is related to the nano- and microscale composition of the record-breaking mixed cation/mixed anion perovskite composition. Macroscale investigations have previously suggested that this formulation results in a single homogenous phase. However, using nanoscale elemental and charge carrier distribution mapping as well as microscale structural and optical film analysis, it is here found that in high efficient solar cells partial phase segregation does take place at the micro- and nanoscale.

Moreover, it is shown that mixed cation/anion formulations allow the formation of never reported 3D hexagonal lead halide perovskite polytypes, namely 4H and 6H. These polytypes are shown to play a key role during the crystallization process, which is also revealed for the first time here. Indeed, mixed cation/mixed anion perovskite films are fabricated via the crystallization sequence $2H \rightarrow 4H \rightarrow 6H \rightarrow 3R(3C)$. It is demonstrated that the complex crystallization via these defect-prone hexagonal intermediates can be by-passed by the incorporation of low amounts of Cs^+ cations into the structure. This can explain the improved stability as well as the increased power conversion efficiency and device reproducibility. It gives for the first time a rational explanation as to why the halide perovskite community rapidly adopted the incorporation of Cs^+ in mixed perovskites.

The last results presented in this thesis are related to the hole-transporting materials (HTM) used in perovskite solar cells. It is shown that carbazole-based small molecule HTMs are a cheap and efficient alternative to the much costlier commercial spiro-OMeTAD.

Considering the motivating research results presented in this work as well as the many breakthrough applications reported within the halide perovskite community, optoelectronic applications based on halide perovskites will have a bright future.

Keywords

halide perovskites; solar cell; hexagonal perovskite; phase segregation; lead iodide excess; stoichiometry; nanoscale composition; perovskite polytype; 2H; 4H; 6H; electrical conductivity; hole transporting materials; carbazole; power conversion efficiency.

Résumé

La photovoltaïque à base de perovskite constitue un domaine de recherche de sciences des matériaux dont l'intérêt a explosé ces dernières années. À côté des applications photovoltaïques, une multitude de domaines de recherche liés à l'énergie ont su profiter des excellentes propriétés optoélectroniques des perovskites hybrides à base de plomb. Rapportant seulement 3% de rendement en 2009, les chercheurs ont réussi à augmenter le rendement de ces cellules solaires à des valeurs proches de 23% en 2017, comparable à ce qu'on observe pour les meilleures cellules solaires à base de Silicium monocristallin. Ces progrès sont dans un premier temps dus à l'ajustement des propriétés optoélectroniques en échangeant A et/ou X dans la formule perovskite ABX_3 et en formant des mélanges de composition à partir de compositions simples. Mais cette stratégie ne permet pas uniquement d'obtenir de meilleurs rendements, elle augmente aussi la complexité de la formulation de la perovskite. Il faut désormais étudier la possibilité d'obtenir plusieurs phases de perovskite différentes, que ce soit à l'échelle nanométrique ou macroscopique. Dans un but mieux comprendre les rapides progrès qui ont été faits, il faut s'intéresser à la composition et la structure cristalline de ces perovskites complexes. L'objectif principal de cette thèse est l'analyse fondamentale, c.-à-d. la composition et les phases présentes, des films de perovskite utilisés pour fabriquer des cellules solaires, tout en essayant de découvrir les conséquences de l'échange et du mélange des cations A ou anions X.

Dans la première partie de cette thèse, le rendement des cellules solaires est amélioré en utilisant des solutions précurseurs non-stoichiométriques, notamment contenant un excès d'iodure de plomb. Cet excès de PbI_2 engendre à la fois des tailles de grains plus grands, une meilleure cristallinité, une diminution de la recombinaison des charges et une meilleure interface TiO_2 /perovskite. Contrairement aux phases de PbI_2 résultant de la dégradation des films de perovskite qui entravent le rendement, le PbI_2 en excès originaire des solutions de précurseurs est très bénéfique à la stabilité, à la reproductibilité et au rendement.

Le prochain défi scientifique lancé durant cette thèse est en relation avec la composition à l'échelle nanométrique et micrométrique des perovskites à anions et cations mixtes records. Les investigations à l'échelle macroscopique d'autres scientifiques ont suggéré que les perovskites réalisées à partir de cette formulation mixte mènent à la formation d'une seule phase de perovskite homogène. En réalité, des techniques à l'échelle nanométrique et micrométrique révèlent que le film de perovskite mixte est partiellement ségrégué à cette échelle-là.

Par la suite, il est montré ici que ces perovskites à anions et cations mixtes permettent la formation de polytypes hexagonales trois-dimensionnels à base d'halogénure de plomb qui n'ont jamais été rapportés auparavant, notamment désignés 4H et 6H. A ces polytypes incombe un rôle clé pendant le processus de cristallisation. La séquence de cristallisation s'est révélée être du type $2H \rightarrow 4H \rightarrow 6H \rightarrow 3R(3C)$. Il est montré que ce chemin de cristallisation passant par des polytypes hexagonales ayant une densité de défauts potentiellement élevée est évité en incorporant de petites quantités du cation césium dans la structure cristalline des perovskites mixtes. Ceci peut expliquer la stabilité accrue, les meilleurs rendements et surtout la meilleure reproductibilité obtenus pour les perovskites contenant du césium. De plus, c'est la première explication rationnelle permettant de comprendre pourquoi la communauté travaillant sur les perovskites a aussi rapidement adopté cette nouvelle composition à base de césium.

La dernière partie de cette thèse porte sur les matériaux transporteurs de trous appliqués aux cellules solaires à base de perovskite. Ces résultats montrent que des transporteurs de trous à base de carbazole peuvent être utilisés comme alternative bon marché et efficace comparée à la molécule de référence chère qu'est le spiro-OMeTAD.

En tenant compte des résultats motivants présentés dans ce travail de thèse et des découvertes capitales obtenues par la communauté scientifique grandissante travaillant sur les perovskites à base d'halogénure de plomb, on peut dire que les applications optoélectroniques de ces perovskites sont promis à un bel avenir.

Mots-clés

Perovskites halogénées; cellule solaire; perovskites hexagonales; ségrégation de phase; excès d'iode de plomb; stoechiométrie; composition à l'échelle nanométrique; conductivité électronique; polytype de perovskite; 2H; 4H; 6H; matériau conducteur de trous; carbazole; rendement solaire

Contents

Abstract	1
Keywords	2
Résumé	3
Mots-clés	4
Contents	5
Chapter 1 Introduction	9
1.1 Lead halide perovskites: origins, state-of-the-art and trends	14
1.1.1 Methylammonium lead triiodide (MAPbI ₃) perovskite	14
1.1.2 Optimization of the optoelectronic properties by cation and anion tuning	15
1.2 Perovskite solar cells: device components and architecture, device fabrication and device physics	18
1.2.1 Perovskite solar cell components and architectures.....	18
1.2.2 Fabrication of a perovskite solar cell: Procedure and reproducibility	20
1.2.3 Device physics: from the pn-junction to perovskite photovoltaics.....	22
1.3 Perovskite Single Crystal Growth: Liquid-Liquid Diffusion.....	32
1.4 Perovskite crystal structure: from oxide perovskites to hybrid lead halide perovskites	34
1.4.1 Goldschmidt tolerance factor.....	36
1.4.2 Hexagonal perovskites	37
1.4.3 Octahedral connectivity and octahedral tilting	41
1.5 Characterization techniques	42
1.5.1 Current-Voltage (J-V) and External Quantum Efficiency (EQE) measurements.....	42
1.5.2 Conductivity and hole mobility using Organic-Field-Effect-Transistors (OFET).....	44
1.5.3 Secondary Electron Microscopy (SEM) – Energy Dispersive X-ray analysis (EDX).....	46
1.5.4 Secondary Ion Mass Spectrometry (SIMS): correlative imaging and depth profiling	47
1.5.5 Atomic Force Microscopy (AFM)/Kelvin Probe Force Microscopy (KPFM)	49
1.5.6 Raman and Photoluminescence spectroscopy of thin films	50
1.5.7 X-ray diffraction of single crystals and polycrystalline thin films.....	51
1.6 Motivation and Strategies.....	54
Chapter 2 Relevance of the stoichiometry of precursors in MAPbI₃ perovskite solar cells	57
2.1 Introduction.....	57
2.2 Results and Discussion	59

2.3	Conclusion and Perspective	71
Chapter 3	Nano- and microscale properties of high-efficiency mixed cation/mixed anion perovskite thin films	73
3.1	Introduction.....	74
3.2	Results and Discussion	75
3.3	Conclusion and Perspective	88
Chapter 4	The crystallization process of mixed cation-mixed anion perovskite: discovery and role of 3D hexagonal lead halide perovskites	89
4.1	Introduction.....	92
4.2	Results and Discussion	93
4.3	Conclusion and Perspective	116
Chapter 5	The relevance of lead-halide hexagonal perovskites	119
5.1	Introduction.....	120
5.2	Results and Discussion	120
5.3	Conclusion and Perspective	125
Chapter 6	Carbazole-based Small Molecule Hole-transporting Materials for Perovskite Solar Cells..	127
6.1	Introduction.....	130
6.2	Results and Discussion	131
6.3	Conclusion and Perspective	140
Chapter 7	General Conclusion.....	143
7.1	Achieved results	143
7.2	Future development	145
Chapter 8	Appendix	147
8.1	Appendix to Chapter 2	147
8.1.1	Sample preparation	147
8.1.2	Grain size analysis.....	147
8.1.3	Transient PL measurements	147
8.2	Appendix to Chapter 3	148
8.2.1	Sample preparation	148
8.2.2	HIM-SIMS.....	149
8.2.3	Micro-PL and Micro-Raman measurements	149
8.2.4	Computational Details	149
8.2.5	AFM/KPFM measurements	150
8.2.6	Dynamic SIMS.....	150
8.3	Appendix to Chapter 4	150
8.3.1	XRD measurements	150
8.3.2	Single Crystal Growth.....	151

Contents

8.3.3	UV-Visible measurements	151
8.3.4	SEM-EDX measurements.....	151
8.3.5	Rietveld refinements.....	152
8.3.6	Preparation of perovskite precursor solutions.....	153
8.3.7	Tolerance factor calculations.....	154
8.3.8	Thin film preparation	154
8.3.9	HIM-SIMS measurements	154
8.3.10	KPFM measurements.....	154
8.4	Appendix to Chapter 6	154
8.4.1	Structures of the various carbazole derivatives	154
8.4.2	Solar cell performance of carbazole derivatives.....	155
	References.....	157
	Acknowledgements.....	163
	Curriculum Vitae	165

Chapter 1 Introduction

Switching to an energy production strategy relying on renewable rather than fossil sources is unavoidable in order to avoid exacerbating global warming. Although a majority of researchers agree that a combination of wind, water, geothermal and solar energy can potentially supply the global energy needs, scientific studies need to provide clear roadmaps and cost-benefit analysis before far-fetching political decisions will be taken. In a recent Stanford study, much more visionary than the 2016 Paris agreement¹, Jacobson et al. unveil a strategy² for 139 countries allowing for a transition to 100% renewable energy by 2050 (80% by 2030). Such a scenario requires electrification of all the energy sectors by covering only 1% of total rooftops and land. Additionally, it is shown that reducing carbon emissions does not only help the climate but also dramatically increases air quality- responsible for many casualties every year- and job opportunities.

Today, the mean power consumption of the world is about 15 TW³, which corresponds to ~2000 W per person, only a fraction of which is actually needed to power the human body (about 100 W), thus the survival of our species. The fact that power consumption is not homogenously distributed even further increases the number to well above 2000 W per person in industrialized countries. In order to meet these high energy demands in a sustainable way, several renewable energy sources should be considered. Out of the mean power that can be generated by the main sustainable energy sources, solar energy has by far the biggest potential (~86 TW) to largely contribute to the near future carbon-free energy landscape³.

It can either be harvested as heat and converted into electricity using steam turbines in solar thermal power plants or directly converted to electricity using photovoltaic solar panels. A combination of both technologies is interesting because at present heat storage is generally easier than storing electricity. Consequently, solar thermal power plants could cover night-time electricity consumption by storing the heat generated during the day, whereas solar cells would produce most electricity during peak day-time electricity consumption.

Currently, the photovoltaic market is largely dominated by polycrystalline silicon solar cells. Whereas Si-based solar cells could potentially supply the required energy in a sustainable way,

several drawbacks required the development of new generation solar cells. High performance Si solar cells have a relatively high production cost (monocrystallinity without many defects), they are bulky, heavy, esthetically not very appealing and the solar cell efficiencies can reach at best the Shockley-Queisser limit ($\sim 30\%$).

For new solar cell technologies to be competitive with or even outperform the well-established Silicon solar cells (first generation solar cells), the requirements are clear: lower material consumption (thin film technology), lightweight (flexible), lower production cost and high efficiencies. Currently, second generation solar cells based on CIGS (copper indium gallium selenide) and CdTe reach performances approaching 20% ⁴. Third generation solar cells include organic solar cells (OPV)⁵, dye sensitized solar cells (DSC)⁶, which have reached efficiencies between $11-14\%$ ^{7,8,9} respectively. As third generation solar cells are solution-processable, they have the potential to fulfill all the above-mentioned requirements.

However, dreams of rapid large-scale commercialization of OPV and DSSC shattered due to various encountered problems related to the optimization in the fabrication process and projected reproducibility/efficiency. Fortunately, a 4th generation solar cell based on the DSSC concept, namely the perovskite solar cell (PSC), arose in 2009¹⁰. Immensely promising research results within only a few years were achieved such that perovskite photovoltaics appeared in the list of the “Top 10 Emerging Technologies of 2016”¹¹, thus promising to be a major player in the near future carbon-free energy landscape. The perovskite solar cell technology has been already proven to be remarkably efficient (approx. 23% for small devices¹²) and has scope to compete with the very best crystalline semiconductor and thin film photovoltaic systems while offering the very lowest potential cost for materials and solution processed manufacturing.

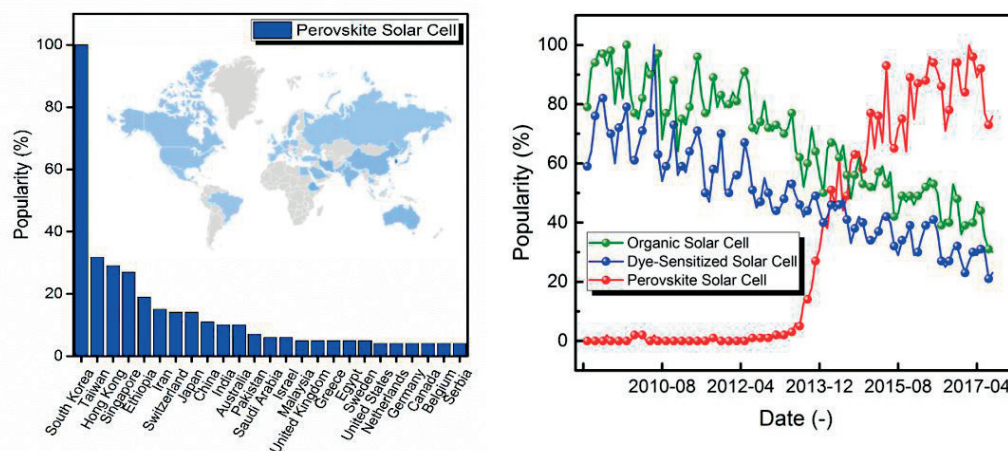


Figure 1.1 right: Comparison of the popularity of Organic Solar Cells, Dye-Sensitized Solar Cells and Perovskite photovoltaics according to the relative number of worldwide google searches¹. **left:** Comparison of the *relative* worldwide distribution of the popularity of the search term “Perovskite Solar Cell” (amount of google searches related to “Perovskite Solar Cell” compared to the total number of google searches in that country)

Figure 1.1 compares the popularity trend of the three most promising new-generation solar cell technologies over the last 10 years. One can observe a constant decrease in interest in OPV and DSSC, which can be correlated to the general decrease in popularity of renewable energy (cf. **Figure 1.2**) over the last years. The perovskite solar cell popularity however increased rapidly in 2012 after the breakthrough papers by Grätzel et al.¹³ and Snaith et al.¹⁴. They appear as a game changer potentially able to reverse the almost ten-year long decrease of interest in renewable energy.

The interest by world region (% of search queries / total queries) reveals that South Korea is by far the country in which people are the most interested in perovskite solar cells. This probably means that this is the country where the awareness of new and promising technologies is the highest among the population. In general, the four most interested countries are Asian countries. Note that these google search results from “google trends” represent the popularity (searches divided by total searches), not the absolute number of searches, thus representing trends rather than actual impact on society.

Although the price of Si panels has plummeted over the course of the last decade, making the development of new generation solar cells less attractive, one has to consider that the price is

¹ Data retrieved from google trends

largely low due to overproduction in China, thus not representing true production costs. Moreover, more important than simple cost considerations are the additional benefits of second, third and fourth generation solar cells. These advantages include flexible substrates (DSSC¹⁵, perovskite¹⁶), higher efficiencies than Si under low light intensity¹⁷ (DSSC), esthetic considerations as well as higher open-circuit voltage, V_{oc} (perovskite¹⁸, DSSC¹⁹). The higher V_{oc} allows operation of the solar cell at higher voltages than the standard Si solar cell, which is of particular interest in applications such as water splitting, CO₂ reduction and solar fuel production in general. Especially flexible and lightweight substrates are increasingly important because it allows for roll-to-roll processing of solar cells (similar to news paper production). Furthermore, installation costs of solar panels would dramatically decrease. One could even think of installing the lightweight, flexible and thus mobile solar cells without the help of a professional company which generates costs that are generally not included when comparing the different photovoltaic technologies. In this scenario, one could imagine to buy a roll of plastic solar cells in the supermarket. Even if these would show a shorter lifespan than Si solar panels, it would be very easy to exchange them for example every 2 years, of course provided that recycling is possible.

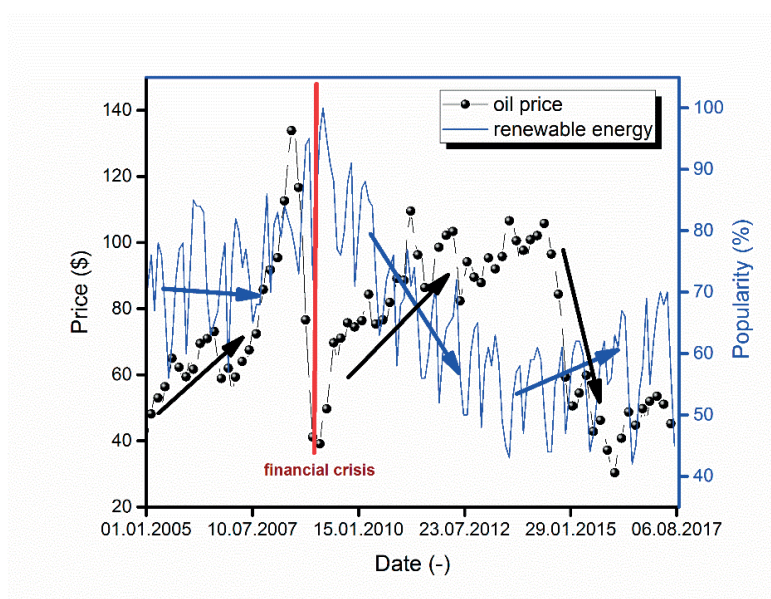


Figure 1.2 Comparison of oil price² evolution and google search interest of the keyword “renewable energy” between 2005 and 2017. The start date of the financial crisis of 2008 marks a short period of highest interest in renewable energy and a minimum in the oil price curve at the same time. Oil price trends and interest in renewable energy mostly follow inverse trends.

² Cushing OK WTI Spot Price FOB (in \$ per barrel)

Figure 1.2 compares the oil price as well as the popularity of the google search term “renewable energy³”. There are several interesting observations to be made: First, the start of the financial crisis in 2008, when the oil price plummeted, corresponds exactly to a maximum interest in renewable energy. Second, if there is a trend of increasing oil price, the interest in renewable energy decreases. This seems counterintuitive at the first glance since an increasing oil price should make the search for alternative energy sources more attractive. However, the observed trends are merely a result of a general investment trend. During periods of low oil price, investments generally increase. In 2012-2013, the interest in renewable energy seems to have reached a low. However, if the oil price stays low, the interest is expected to increase again.

Especially the projected electrification of car industry and increasing demand of electrical energy storage in batteries will in turn boost the demand for clean electrical energy sources. As electrical cars can be charged at home, it makes sense to install solar cells on top of individual roofs. Excess energy could then be not only fed into the public electrical grid but also stored in the electric car’s battery or in an additional battery such as the Tesla wall battery²⁰. In the upcoming years, the electrification, low oil prices as well as the tremendously fast progress of perovskite photovoltaics will boost the interest in renewable energy in general and new generation solar cells in particular.

While this thesis includes only work on organic-inorganic perovskites, good knowledge about the original oxide perovskites and solid-state p-n junction device physics is of crucial importance. Many concepts developed within the oxide perovskite community have been shown to have analogues for inorganic-organic perovskites. In this work I show that one additional important concept can be adopted to hybrid perovskites. Indeed, the most important result of this thesis, namely the discovery of the existence of 3D lead halide hexagonal perovskites, needs good understanding of concepts originally elaborated for oxide perovskites. In the upcoming theoretical part, I will start with the different lead halide perovskite material compositions and properties (**Section 1.1**). Then I write about device physics (**Section 1.2**) and briefly introduce perovskite single crystal growth (**Section 1.3**), before focusing on the oxide perovskites, including only concepts that have also been useful for hybrid halide perovskites (**Section 1.4**). I will finish with a brief introduction into the characterization techniques (**Section 1.5**) as well as the motivation and strategies for this thesis (**Section 1.6**).

³ Data retrieved from google trends.

1.1 Lead halide perovskites: origins, state-of-the-art and trends

1.1.1 Methylammonium lead triiodide (MAPbI₃) perovskite

Originally a mineral, perovskite corresponds to the nominal formula ABX₃, where A is a monovalent cation, B is a bi-valent cation and X is a monovalent anion. Gustav Rose, a German mineralogist, discovered the mineral CaTiO₃ in 1839 and named it after the Russian count Lev Aleksevich von Perovski. But perovskites gained widespread attention only after the discovery of the dielectric and ferroelectric properties of the perovskite material BaTiO₃ in the 1940s. Perovskite makes up 38% of the volume of the Earth. Component of the Earth mantle, Bridgmanite i.e. (Fe,Mg)SiO₃, occurs in depth of around 700km-3000km because it is only stable under high pressure and temperature. Throughout the years, more and more minerals were found to adopt the perovskite structure and “perovskites” now describe a large class of materials that adopt a crystal structure similar to the original CaTiO₃. It is one of the most important class of materials in solid-state materials science, although named after a relatively unimportant Russian dignitary.

Laboratory synthesis of halide perovskites started in the 1860s, when alkali-metal lead and tin halides were synthesized for the first time. The discovery that the compound CsPbI₃ actually adopts a perovskite structure was only found out much later by Danish scientist Moller in 1958²¹. He also made the first observation of photoconductivity of this material, a first indication that it is a semiconductor. Then, German scientist Dieter Weber went on to replace Cs⁺ by CH₃NH₃⁺ cations, in this way reporting the first ever hybrid organic-inorganic 3D perovskite structure^{22,23}. It was found that the 800nm absorption onset would be perfect for solar energy harvesting. First charge carrier mobility results were also favorable in using halide perovskites in light-to-energy converting devices. However, research on hybrid perovskites slowed down until American scientist David Mitzi made important progress in organic-inorganic perovskites²⁴⁻²⁶. He studied the use of these materials in thin-film transistors and light-emitting diodes (LED) and although he anticipated the photovoltaic behavior of these materials, he failed to provide any experimental proof of perovskite photovoltaics.

The potential of this material to be used for photovoltaic applications only appeared in 2009, from researchers (Miyasaka et al.) working on liquid DSSC²⁷. Undoubtedly, perovskite solar cells emerged from the mesoporous DSSC concept, as the first perovskite solar cell started as a quantum dot solar cell in which the dye was replaced by the quantum dot sensitizer perovskite²⁷. The use of MAPbI₃ as the sensitizing pigment was immediately considered as a replacement for the standard ruthenium dye N3 because it was noticed that MAPbI₃ has superior light harvesting properties. In the DSSC, the light-harvesting limitations of sensitizers were partially overcome by

the breakthrough concept of O'Regan and Grätzel in 1991, who used a mesoporous TiO₂ scaffold to allow for micrometer thick sensitized films²⁸. This concept greatly facilitated the introduction of perovskite into a solar cell configuration and is now still an important component of most of the high-efficiency perovskite device architectures.

After 2009, intensive research on MAPbI₃ began²⁷ and, very quickly, the many astonishing optical and electrical properties of MAPbI₃ were discovered, rivaling with the best single crystal semiconducting materials, such as GaAs. Some of the properties explaining the excellent photovoltaic behavior of metal halide perovskites include the strong light absorption in the visible, the tunable band gap, the low defect concentration and the small exciton dissociation energy less than 30meV²⁹. Comparing this value to the thermal energy kT at 25°C, which is 26 meV, it becomes evident that the exciton binding energy is so low that light absorption mostly results in free carriers under device operation temperatures. Apart from the role as a light absorber, the metal halide perovskites are also ambivalent charge carriers, showing high mobility values for both electrons and holes³⁰. This is a consequence of the low effective mass.

1.1.2 Optimization of the optoelectronic properties by cation and anion tuning

Structural modifications by cation and/or anion tuning have been identified as simple, yet effective for changing the optoelectronic properties of the hybrid perovskite materials. In this section, I will briefly introduce the milestone discoveries in A cation, B cation, X anion as well as combined anion/cation tuning.

- **A cation tuning**

After methylammonium, the next organic cation that was shown to form a photovoltaic hybrid perovskite structure was formamidinium³¹ (**Figure 1.4** and **Figure 1.4**). FAbI₃ exhibits higher photocurrents, but it is not stable at room temperature, quickly yielding a yellow non-perovskite “delta” (or 2H) phase. Just as MAPbI₃, the stability towards moisture is poor. Pellet et al. showed that FA/MA mixing is possible and that this is the right strategy to yield a black photoactive 3D perovskite phase, namely FA_xMA_{1-x}PbI₃, where $x \leq 0.8$ ³¹. The FA/MA mixed formulations perform better than the single cation counter-part because the absorption spectrum onset is red-shifted by about 20 nm, which explains the higher photocurrents typically observed in these devices.

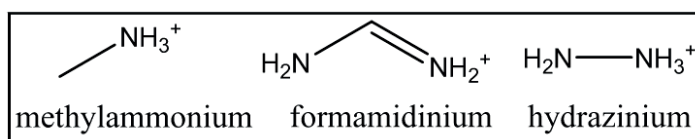


Figure 1.3 Cation structures.

Like FAPbI₃, CsPbI₃ also forms a yellow 2H phase at room temperature. Choi et al. have shown that Cs_xMA_{1-x}PbI₃ mixing also results in a stable black 3D perovskite phase at room temperature³². However, efficiency as well as stability of the Cs_xMA_{1-x}PbI₃ solar cells are less good than in the case of FA_xMA_{1-x}PbI₃.

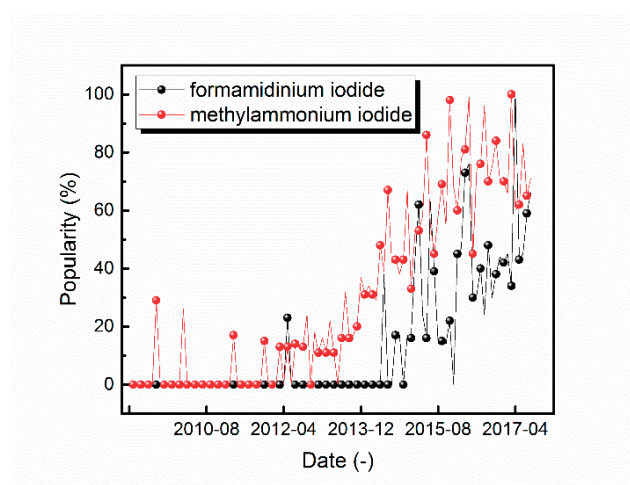


Figure 1.4 Comparison of the popularity of the google search terms “formamidinium iodide” and “methylammonium iodide”. The onset date corresponds exactly to the publication date of the respective milestone publications.

Cs/FA mixing, namely Cs_xFA_{1-x}PbI₃ has been shown to yield a stable black perovskite phase and high efficient perovskite solar cells³³. Using first principle calculations, the authors show that the stabilization of the perovskite phase by mixing the Cs and FA cations originates from a higher entropy.

Other cations of interest are for example trimethylsulfonium³⁴, hydrazinium³⁵ and guanidinium³⁶. These cations however do not yield a 3D perovskite structure. Only, Cs, MA⁺ and FA⁺ have been shown to be a suitable A cation for obtaining a 3D perovskite structure.

- **B cation tuning**

Tremendous research efforts aiming to find alternatives for the toxic Pb^{2+} cation have been undertaken. However, so far, only Sn-halide perovskites have been shown to have potentially interesting photovoltaic properties. Pure Sn perovskites have reached efficiencies up to about 9% PCE³⁷. However, they are extremely sensitive to oxygen exposure, which results in the oxidation of Sn^{2+} to Sn^{4+} , yielding a perovskite with unsuitable metallic properties. Recently, mixed PbSn have gained increased attention due to the possibility of obtaining an ideal bandgap for single junction as well as for tandem applications³⁸.

- **X anion tuning**

Simple halide substitution such as bromide as well as chloride substitution has been investigated in combination with either pure FA^+ cation or the original MA^+ cation. The larger the amount of Br, the larger the increase of the bandgap. The $\text{MAPbI}_x\text{Br}_{1-x}$ is a perovskite formulation that has been shown to be not photostable³⁹. Upon illumination this perovskite segregates into two macroscopic phases, one bromide phase and one iodide phase. Concerning Cl substitution, debates are ongoing whether Cl can actually form a 3D perovskite structure. In Chapter 5, I partially solve some of the misunderstandings related to Cl⁻ substitution.

- **Combined A cation/X anion tuning**

Owing to their high stability and efficiency, the most promising perovskite formulations are mixed A cation/mixed X anion perovskites. As previously explained, the simple cation mixing of two room temperature unstable phases, namely FAPbI_3 and CsPbI_3 , allows the formation of a room-temperature stable perovskite phase. By tuning both the A cation and the X anion in the same time, perovskite formulations such as $\text{FA}_x\text{MA}_{1-x}\text{PbI}_y\text{Br}_{1-y}$ can be easily obtained⁴⁰. The possibility of varying both x and y leads to a vast number of perovskite phases having different optoelectronic properties.

Remarkably these mixed cation/mixed anion perovskites are stable under photoillumination and do not show the undesirable light induced segregation into the pure phases that has been observed for the $\text{MAPbI}_x\text{Br}_{1-x}$ based mixed anion formulation. However, I show in Chapter 3 that these $\text{FA}_x\text{MA}_{1-x}\text{PbI}_y\text{Br}_{1-y}$ formulations lead to the formation of a variety of nanoscale phases, at least at the surface, which seems to be beneficial for device performance. Mixed cation/mixed anion

perovskites required the development of an antisolvent engineering approach for solution processing of perovskite solar cells⁴¹. Recently, anti-solvent-free approaches have also been developed for mixed perovskites⁴².

Increasing the complexity of the perovskite formulation even further, Saliba et al.⁴³ introduced a triple cation formation containing Cs^+ , namely $[\text{CsPbI}_3]_x[(\text{FAPbI}_3)_{0.85}(\text{MAPbBr}_3)_{0.15}]_{1-x}$. They showed improved efficiencies and reproducibility as well as higher stability compared to the $(\text{FAPbI}_3)_{0.85}(\text{MAPbBr}_3)_{0.15}$ formulation. Later, it was also shown that the Cs^+ formulation allows the fabrication of perovskite solar cells at room-temperature, by leaving out the standard 100°C crystallization step⁴⁴. However, the reason behind all these improvements remained unclear. In this thesis, by studying the crystallization process of mixed perovskites, I elucidate some of the main roles and benefits of Cs^+ incorporation (Chapter 4).

Continuing the trend of increasing complexity by cation mixing, Saliba et al. additionally introduced small amounts of Rb cations in order to further improve electroluminescence and photovoltaic properties⁴⁵. It is however unclear whether the small rubidium cation can go into the perovskite structure. Solid-state NMR data by Emsley et al. suggest that Rb cannot form a quadruple cation perovskite structure⁴⁶.

1.2 Perovskite solar cells: device components and architecture, device fabrication and device physics

1.2.1 Perovskite solar cell components and architectures

The main component of a solar cell containing molecular materials is a light absorbing material (semiconductor or a dye) that allows for efficient charge carrier separation. The photo-generated electrons and holes are then transported to the external circuit using an electron transporting material (ETM), respectively a hole-transporting material (HTM). The substrate is usually made from Indium Tin oxide (ITO) or Fluorine doped tin oxide (FTO) deposited on glass. Flexible substrates made from PET are also used.

In third-generation solar cells such as DSSCs, on which perovskite solar cells are based, both the hole-transporting material and the electron-transporting material are required and unavoidable. Indeed, the dye is a monolayer and takes the role of the light absorber and sensitizer, by injecting the photo-generated electron and hole into the adjacent HTM and ETM.

In perovskite solar cells, both the HTM and ETM layers are generally required in order to achieve the highest solar cell efficiencies, but they are not absolutely crucial because it has been shown that photovoltaic perovskites are not only good light absorbing materials but also very efficient in transporting charges, both electrons and holes. Details about perovskite device operation physics can be found in **Section 1.2.3**. Two single junction architectures, namely p-i-n and n-i-p (**Figure 1.5**), are considered for perovskite solar cell fabrication. The perovskite material is usually referred to as an intrinsic material (i), the HTM is p-doped and the ETM n-doped. Other research efforts include tandem configurations, such as hybrid tandems composed of a perovskite (high band gap)/silicon (low bandgap) stack or pure perovskite tandems of the form perovskite (high band gap)/perovskite (low band gap).

In this thesis, I exclusively worked on the n-i-p architecture. Due to solution-processing, the requirements on the HTM and ETM materials usually depend whether they are to be used in a p-i-n, an n-i-p or a tandem configuration. In the n-i-p configuration, the typical hole transporting material is spiro-OMeTAD. Although it has been used as the work-horse for many years, tremendous efforts have been undertaken to replace mainly due to the high cost and limited stability. More details about the challenges to replace Spiro-OMeTAD are presented in Chapter 6. Small molecular HTMs, polymers and inorganic HTMs are all investigated as potential cheap, stable and high-efficiency candidates in perovskite solar cells. The ETM material is TiO₂ and it is used in a bilayer approach, as a hole-blocking layer and a mesoporous scaffold. As soon as the perovskite solar cells are fabricated using a typical solution-processing approach, it is not possible to use spiro-OMeTAD in a p-i-n configuration because it would be washed away during perovskite deposition from solution. At the same time, due to the high-temperature sintering steps that are necessary for TiO₂ anode fabrication, it would not be possible to use TiO₂ in a p-i-n configuration. A large number of different materials are investigated in order to fabricate the ideal solar cell, which would be efficient, cheap, lightweight and stable in the same time.

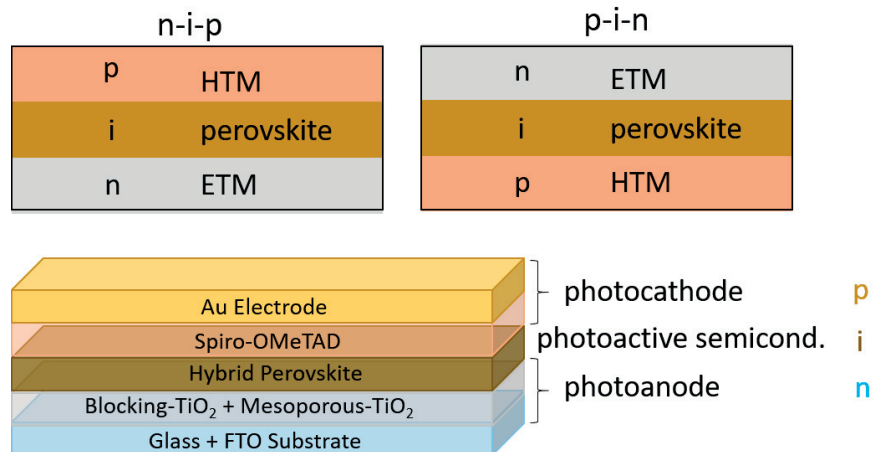


Figure 1.5 Typical perovskite solar cell architectures: p-i-n or n-i-p. The highest power conversion efficiencies are generally achieved using the n-i-p architecture in which the ETM is TiO₂ and the HTM is spiro-OMeTAD.

1.2.2 Fabrication of a perovskite solar cell: Procedure and reproducibility

Many perovskite solar architectures have been shown to yield efficient solar cells. Here I briefly describe the typical perovskite solar fabrication process used during this thesis. The process involves several steps and takes about 2 days (**Figure 1.6**). The precise deposition process of each layer is absolutely crucial for the final device efficiency and therefore experience is a great asset in order to achieve high solar cell efficiencies.

- 1) Anode preparation: processing of TiO₂ electron extracting layer from solution (FTO glass substrate)
- 2) Perovskite photoactive material processing from solution
- 3) Cathode preparation: processing of hole transporting layer from solution
- 4) Cathode metal (Au) contact evaporation using physical vapor deposition

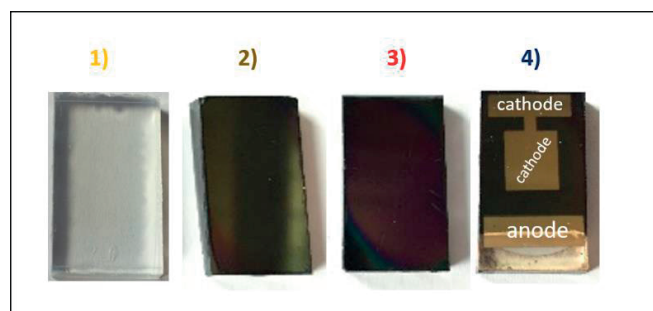


Figure 1.6 The different main steps of the solution-processed n-i-p perovskite solar cell fabrication (substrate=glass). 1) FTO/**TiO₂**; 2) FTO/TiO₂/**perovskite**; 3) FTO/TiO₂/perovskite/**HTM**; 4) FTO/TiO₂/perovskite/HTM/**Au**.

Reproducibility is a general challenge for device fabrication that includes several layers. The more interfaces there are, the more difficult it will be to reproduce the devices. Solution-processing, although cheap and relatively easy, lacks from precise crystallization control as compared to vacuum deposition techniques. Laboratory humidity and the choice and age of chemicals is of crucial importance.

- 1) The anode preparation generally involves two steps: first, a TiO₂ hole-blocking layer is sprayed from an ethanol solution at 450°C. The mesoporous particles are applied from a TiO₂ paste (Dyesol NRD 30nm) via spincoating. Subsequently, several sintering steps guarantee the good crystallinity and connectivity between the particles. This step is followed by an optional LiTFSI treatment, which is recommended because it has been shown to result in solar cells showing higher photovoltages⁴⁷. As LiTFSI is a very hygroscopic material, the reproducibility of this LiTFSI treatment is not very good. Although the highest reported efficiencies are obtained using TiO₂ nanoparticles, recent reports using SnO₂⁴⁸ or organic ETMs are very promising⁴⁹.
- 2) The perovskite precursor materials are dissolved in high concentrations (~1.35M) in DMF, DMSO or DMF/DMSO mixtures. Given the large size of the Pb²⁺ ions and the organic cations, concentrations are generally wrongly reported due to extensive volume change upon dissolution of high quantities of these ions.
- 3) The HTM layer plays the role of the electron blocking layer and is generally deposited via spin-coating from a chlorobenzene solution
- 4) Cleaning of the anode is carried out with cotton swaps previously dipped into an Acetonitrile/DMSO mixture before the thermally evaporating gold pellets under high vacuum.

1.2.3 Device physics: from the pn-junction to perovskite photovoltaics

The rational derivation of the ideal diode equation is freely adapted and interpreted from reference [50]

When p- and n-doped semiconductors are brought in contact, a so-called pn-junction with important optoelectronic properties forms. Diffusion of excess electrons from the n-side to the p-side as well as diffusion of excess holes from p-side to n-side takes place. In the same time, this charge flow results in the emergence of an electric field E made up of the “left-behind” immobile acceptor ions (N_A) and donor ions (N_D), *opposing* the diffusion along the carrier concentration gradient. At equilibrium, the Fermi level across the junction is thus equilibrated (see **Figure 1.7**), leading to the appearance of a contact potential qV_0 . As no net current is allowed flow at equilibrium (definition of equilibrium), the sum of drift (due to E) and diffusion (due to concentration gradient) needs to exactly cancel for the electrons as well as for the holes. Thus:

$$J_p(\text{drift}) + J_p(\text{diffusion}) = 0 \quad (1)$$

$$J_n(\text{drift}) + J_n(\text{diffusion}) = 0 \quad (2)$$

In the one-dimensional case, the expression for the hole current (1) yields:

$$J_p(x) = q \left[\overbrace{\mu_p p(x) E(x)}^{\text{drift}} - \overbrace{D_p \frac{dp(x)}{dx}}^{\text{diffusion}} \right] = 0$$

where μ_p refers to hole mobility and $p(x)$ to the concentration of the holes. Rearranging yields:

$$\frac{\mu_p}{D_p} E(x) = \frac{1}{p(x)} \frac{dp(x)}{dx}$$

Using Einstein’s relation ($\mu/D = -kt/q$) and re-writing the Electric field as a potential gradient ($E = dV/dx$):

$$\frac{-q}{kT} \cdot \frac{dV(x)}{dx} = \frac{1}{p(x)} \cdot \frac{dp(x)}{dx}$$

Thus, by integrating:

$$\frac{-q}{kT} \int_{V_p}^{V_n} dV = \int_{p_p}^{p_n} \frac{1}{p} dp$$

$$\frac{-q}{kT} \left(\frac{V_0}{V_n - V_p} \right) = \ln \frac{p_n}{p_p}$$

$$V_0 = \frac{kT}{q} \ln \frac{p_p}{p_n}$$

$$\frac{p_p}{p_n} = e^{qV_0/kT} \quad (3)$$

The equilibrium condition being $pn=n_i^2$ (n_i being the intrinsic carrier concentration), one can easily extend equation (3) to the electron concentrations n on either side of the junction. Moreover, inserting $p_0 = N_v e^{-(E_F - E_v)/kT}$, where p_0 corresponds to the concentration of holes in the valence band and N_v is the effective density of states in the valence band, into equation (3) yields ($E_{F,n} - E_{F,p} = 0$ at equilibrium):

$$e^{qV_0/kT} = \frac{N_v e^{-(E_{F,p} - E_{v,p})/kT}}{N_v e^{-(E_{F,n} - E_{v,n})/kT}} \rightarrow qV_0 = E_{v,p} - E_{v,n}$$

This shows that, if one applies bias to the junction, the potential barrier deviates from the contact potential by shifting the Fermi levels on each side with respect to each other by exactly the applied bias value.

The non-mobile ionized donor and acceptor ions create a space charge on each side of the junction that needs to be equal at equilibrium (charge balance equation):

$$qN_A A x_{p,1} = qN_D A x_{n,1}$$

where $x_{p,1}$ and $x_{n,1}$ correspond to the penetration of the depletion region (space charge region) into the p-side, resp. n-side. A represents the area of the cross-section of the junction. The sum $W = x_{p,1} + x_{n,1}$ is called the depletion layer width.

In order to relate the charge at any position x to an electric field gradient, the 1D Poisson equation is utilized:

$$\frac{dE}{dx} = \frac{q}{\epsilon} \left(\overbrace{p - n}^{\text{neglected}} + N_A^- + N_D^+ \right)$$

The approximation that only the ionized donors contribute to the space charge (neglecting the carrier contribution) yields a constant derivative and therefore a linear relation between the electric field E and the position x after integration (x_n and x_p are positive numbers).

$$\begin{aligned} \frac{dE}{dx} &= -\frac{q}{\epsilon} N_A \Rightarrow E = -\frac{q}{\epsilon} N_A x & x_{p,1} < x < 0 \\ \frac{dE}{dx} &= \frac{q}{\epsilon} N_D \Rightarrow E = \frac{q}{\epsilon} N_D x & 0 < x < x_{n,1} \end{aligned}$$

Integration with the above boundaries yields the maximum value of the electric field E_{max} .

$$E_{max} = -\frac{q}{\epsilon} N_A x_{p,1} = -\frac{q}{\epsilon} N_D x_{n,1}$$

One can see that the value of E_{max} is negative, which is expected because the field points from + (n side) to - (p-side), thus in the negative x direction. Since $E(x) = -dV(x)/dx$, the electrostatic

potential expression is found by integration of the linear electric field, yielding a quadratic expression for the p-side as well as the n-side. The contact potential V_0 corresponds to the area of the triangle delimited by $E(x)$:

$$V_0 = -\frac{1}{2}E_{max}W = \frac{1}{2}\frac{q}{\epsilon}N_D x_{n,1}W$$

Introducing the charge balance requirement $x_{n,1} \cdot N_D = x_{p,1} \cdot N_A \rightarrow x_{n,1} = W \cdot N_D / (N_A + N_D)$ yields

$$V_0 = \frac{1}{2}\frac{q}{\epsilon}\frac{N_D N_A}{N_D + N_A}W^2$$

The expression for the depletion layer width (space charge region) W as a function of contact potential and doping concentration becomes:

$$W = \sqrt{\frac{2\epsilon_0 V_0}{q} \left(\frac{1}{N_A} + \frac{1}{N_D} \right)}$$

This formula shows that the depletion width depends on doping, which is very relevant for device engineering and will be discussed later in the section. It also predicts that the depletion layer width can be varied by applying a potential.

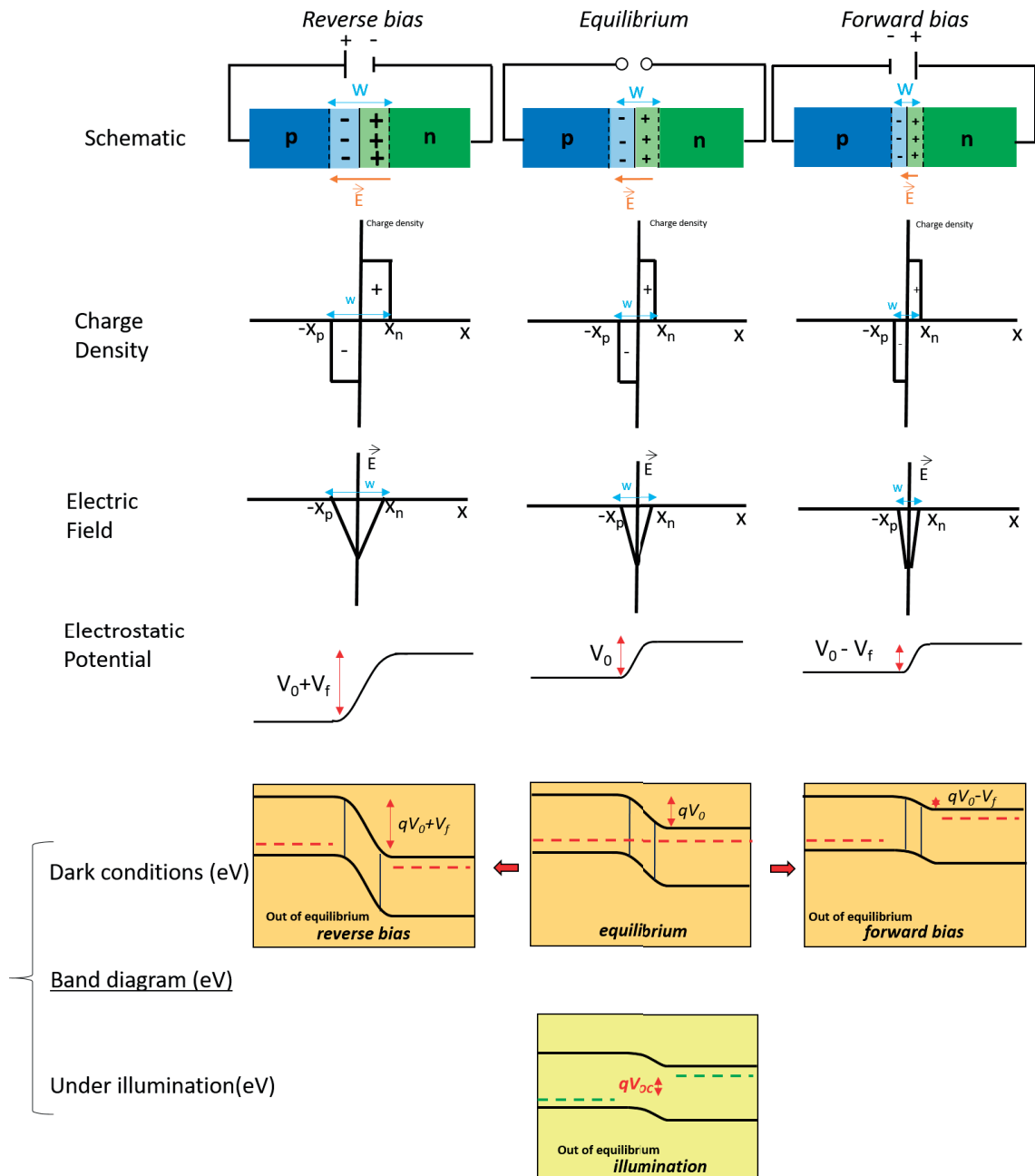


Figure 1.7 Illustration of the derivation of the ideal diode equation starting from a typical p-n junction (here, the concentration of p and n dopants as well as the material is the same.) The effect of bringing the junction out of equilibrium by applying a reverse bias, a forward bias or by illuminating the junction is depicted.

What happens upon applying a bias potential? Considering now $x_{n,1}$ and $-x_{p,1}$ as the edge of the space charge region in the n side respectively p side ($x=0$ being the contact), one can introduce

the concept of carrier injection. The system is said to be out of equilibrium and the equilibrium condition from equation (3), i.e. $p_p/p_n=e^{qV/kt}$ is now presented in the following form:

$$\frac{\overbrace{p(-x_{p,1})}^{\approx p_p}}{p(x_{n,1})} = e^{\frac{q(V_0-V)}{kT}} \quad (4) \quad \overset{\frac{3}{4}}{\rightsquigarrow} \frac{p(x_{n,1})}{p_n} = e^{\frac{qV}{kT}} \quad (5)$$

Provided that injection is low so that one can neglect change in majority carrier concentration. Equation (5) shows what happens to the minority carrier hole concentration at the edge of the space charge region. For example, under forward bias ($V > 0$), the minority carrier hole concentration at the edge $p(x_{n,1})$ is much higher than the concentration at equilibrium p_n . This is called minority carrier injection. Under reverse bias ($V < 0$), the opposite takes place.

Now one can calculate the excess hole and electron concentration Δp_n and Δn_p at the edge of the depletion region.

$$\Delta p_n = p(x_{n,1}) - p_n = p_n(e^{\frac{qV}{kT}} - 1)$$

$$\Delta n_p = n(-x_{p,1}) - n_p = n_p(e^{\frac{qV}{kT}} - 1)$$

Introducing new coordinates x_p and x_n , and by using the diffusion equation $\delta p(x) = \Delta p e^{-x/L_p}$:

$$\delta n(x_p) = \Delta n_p e^{-x_p/L_n} = n_p \left(e^{\frac{qV}{kT}} - 1 \right) e^{-x_p/L_n}$$

$$\delta p(x_n) = \Delta p_n e^{-x_n/L_p} = p_n \left(e^{\frac{qV}{kT}} - 1 \right) e^{-\frac{x_n}{L_p}} \quad (6)$$

Steady-state excess holes result in a hole diffusion current in the direction of decreasing concentration. Starting from the general hole diffusion current expression $J_p(x) = q \frac{D_p}{L_p} \delta p(x)$, one can replace $\delta p(x)$ by (6) and calculate the derivative with respect to x . L corresponds to the diffusion length and D is the diffusion coefficient.

$$I_p = qAD_p \frac{d\delta p}{dx} = \frac{qAD_p}{L_p} \Delta p e^{-x_n/L_p} = \frac{qAD_p}{L_p} \delta p(x_n)$$

The injected junction hole current at $x_n=0$ and $x_p=0$:

$$I_p(x_n = 0) = \frac{qAD_p}{L_p} \Delta p_n = \frac{qAD_p}{L_p} p_n \left(e^{\frac{qV}{kT}} - 1 \right)$$

$$I_n(x_p = 0) = \frac{qAD_n}{L_n} \Delta n_p = \frac{qAD_p}{L_p} p_n \left(e^{\frac{qV}{kT}} - 1 \right)$$

Thus, the total dark current, known as the **diode equation** yields:

$$I = I_p(x_n = 0) - I_n(x_p = 0) = \overbrace{qA\left(\frac{D_p}{L_p}p_n + \frac{D_p}{L_p}n_p\right)}^{I_0} \left(e^{\frac{qV}{kT}} - 1\right)$$

$$I = I_0 \left(e^{\frac{qV}{kT}} - 1\right)$$

Where I_0 is called reverse saturation current.

In this equation the voltage can be negative (reverse bias) or positive (forward bias). In the reverse bias situation $V = -V_r$, the total current I equals I_0 if V_r is bigger than a few kT/q :

$$I = I_0 \left(e^{\frac{-qV_r}{kT}} - 1\right) = -I_0$$

As is also illustrated in **Figure 1.7**, forward bias reduces the barrier for diffusion while reverse bias increases it.

A diode in the dark is a minority carrier device, because operation is based only on minority carrier injection (within the approximations made). Upon illumination, electrons and holes are generated in the conduction and valence band, resulting in a photocurrent in the opposite direction (from n to p, hence the negative sign in front of I_{photo}) than the dark diode current:

$$I_{photo} = qAg_{opt}(L_p + L_n + W)$$

$$I_{total} = \overbrace{I_0 \left(e^{\frac{qV}{kT}} - 1\right)}^{\text{"dark current"}} - \overbrace{I_{photo}}^{\text{"photocurrent"}}$$

The I-V curve of a diode is thus “vertically lowered” proportional to the photocurrent, enabling power extraction if operated anywhere between open-circuit and short-circuit conditions. A solar cell is operated in the “4th quadrant” by applying positive voltage (forward bias), resulting in negative current output. A diode operated in the 3rd quadrant does not produce power; however, it allows for very important applications as a photodiode.

Even without external bias, a forward bias voltage arises upon illumination of a pn junction. This is called “the photovoltaic effect”.

Under short-circuit conditions, $I_{total} = I_{photo}$. In this case, the I-axis is crossed at negative values proportional to I_{photo} (**Figure 1.8a**)

Under open-circuit conditions, $I_{\text{total}}=0$ (x-axis crossing point, **Figure 1.8b**). Thus, the voltage expression V_{OC} becomes:

$$\frac{I_{\text{photo}} + I_0}{I_0} = e^{qV_{\text{oc}}/kT}$$

$$V_{\text{oc}} = \frac{kT}{q} \ln\left(\frac{I_{\text{photo}}}{I_0} + 1\right)$$

The V_{oc} is raising when increasing the optical generation rate, i.e. increasing illumination intensity. However, the V_{OC} can not raise indefinitely because the contact potential of a pn junction sets the limit for V_{OC} .

Open-circuit conditions result in highest possible voltage and short-circuit conditions yield the highest possible current that can be extracted. However, in order to extract power, which is the product of current and voltage, one needs to operate the solar cell by applying a voltage between these two conditions. The maximum power-point thus corresponds to the ideal operating conditions (**Figure 1.8b**). The “squareness” of the I-V curve plays an important role in order to achieve optimal maximum power point conditions. The more quadratic the I-V curve, the better. This concept is denoted as the fill factor, which corresponds to the ratio of the areas V_{MPP} times J_{MPP} and V_{OC} times J_{SC} . The fill factor values are thermodynamically limited about 86% (Carnot-limited). Please note that most of the researchers in the perovskite solar cell community, including me, use a convention of axes where the upward direction corresponds to negative current (**Figure 1.8c**). This still corresponds to the “4th quadrant”. The Fill factor (FF) is immediately affected by series resistance losses within the device as well as shunting pathways. Ideally, a solar cell should show low series resistance as well as high shunt resistance since both conditions increase the fill factor as can be seen from **Figure 1.8d**. The equivalent circuit of a solar cell model based on exactly one diode is depicted in **Figure 1.8e**.

The power conversion efficiency is thus calculated as follows:

$$\eta = \frac{P_{\text{output}}}{P_{\text{input}}} = \frac{FF \cdot V_{\text{OC}} \cdot J_{\text{SC}}}{\underbrace{P_{\text{input}}}_{(1\text{sun}=1000\frac{\text{W}}{\text{m}^2)}}$$

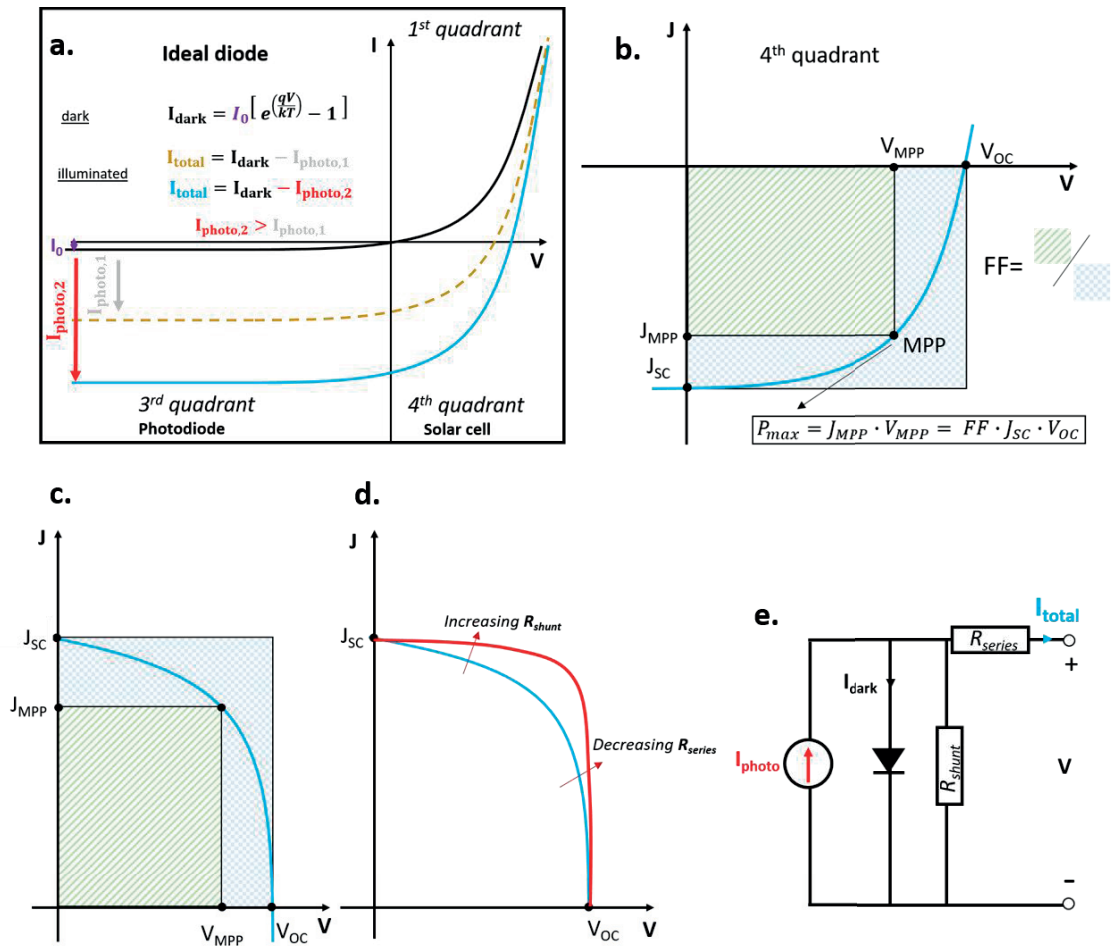


Figure 1.8 a. Ideal diode equation under dark conditions and under illumination. Operation in the 4th quadrant delivers power from the device to the load. b. Illustration of the maximum power point and the concept of fill factor (FF) as “squareness” of the diode J-V curve. c. Common alternative J-V representation used throughout this thesis. d. Schematic illustration of the effect of series and shunt resistance. e. Equivalent circuit for a solar cell based only on one ideal diode, a source of additional photocurrent, one resistor in series (R_{series}) and one resistor in parallel (R_{shunt}).

Perovskite solar cells operate somewhat differently from the classical pn-junction. Indeed, the perovskite solar cell is rather considered a p-i-n junction, where the perovskite is an intrinsic (undoped) semiconductor. The advantage of a p-i-n solar cell over a pn solar cell is related to the fact that the depletion layer width W (thus the electric field) actually extends deep in the device, almost entirely defined by the intrinsic region. In this way, long wavelength photons, which are penetrating deeper in the film, can be efficiently extracted and contribute to the current. In practice, in a pin device, the intrinsic semiconductor does not need to be perfectly intrinsic (can be lightly n or

p doped), just highly resistive. Contrary to the pn-junction solar cell, the depletion layer width does not significantly vary according to the applied bias voltage, rather it is fixed by the thickness of the the intrinsic region.

As opposed to the role of the dye within the DSSC, which acts purely as a sensitizer, the perovskite semiconductor ensures charge generation as well as transport in thin films over several hundreds of nanometer. The perovskite is sandwiched between the p and n contacts, which act as selective contacts only. After photoexcitation (**Figure 1.9**), the photogenerated charges are immediately free carriers at room temperature. Indeed, the exciton binding energy has been determined to lie in the range of 30-50meV⁵¹ when using a dielectric constant of 6.5. With a larger dielectric constant, this value decreases to 1-10 meV⁵², to be compared with the thermal energy at 25°C, which equals 26 meV. It has been found that exciton dissociation takes place in the timescale of ~2ps⁵³. Electron as well as hole mobilities (μ_n and μ_p) of halide perovskites range from 10-30 cm² V⁻¹ s⁻¹⁵⁴ and the decay in this films is slow, reaching tens of microseconds⁵⁵. The electron-hole lifetime τ is typically determined to range from 300ns to μ seconds⁵⁵ and thus the diffusion length L is correspondingly long, more than 1 μ m for MAPbI_xCl_{1-x} perovskite. The diffusion length, the charge carrier mobility and the lifetime of the holes, respectively electrons are linked by the following formulas:

$$L = \sqrt{D\tau}, \quad D = \frac{kT}{q} \mu \rightarrow L = \sqrt{\frac{kT}{q} \mu \tau} \quad (1)$$

Both the electron and hole diffusion length are absolutely critical for optimal device performance. Indeed, the hole (electron) diffusion length L_p (L_n) is defined as the distance at which the excess-hole (electron) distribution is reduced to 1/e of the initial value. It can be shown that this corresponds to the average distance a hole diffuses before recombining. In order to absorb most of the incoming light, thicker perovskite layers (300-500 nm) are preferred and thus the diffusion length needs to be accordingly large.

Electron-hole recombination has been shown to be bimolecular and mostly radiative, the room temperature photoluminescence quantum yield (PLQE) being 70%⁵⁶ and the low temperature PLQE 100%⁵⁷. The possibility of reaching the ideal PLQE of 100% is important and promising for reaching efficiencies close to the Shockley-Queisser limit (~33%) because this assumption is based on the recombination being 100% radiative. At this point, I would like to quote Prof. Yablouovitch (Berkeley University): “A good solar cell needs to be a good LED”. Under device

operation, other recombination mechanisms such as a monomolecular trap-assisted recombination have been shown to take place. Taking into account all of the properties described above, the most probable operating principle of a perovskite solar cell (**Figure 1.9**) is that free charge carriers are photogenerated at room temperature in the bulk of the film, before they diffuse through the film and selectively transfer to the anode resp. cathode, resulting in an external current. Whether the band gap of the halide perovskite is direct or indirect is actively debated, the most recent publication even reports a mixed direct-indirect character⁵⁸.

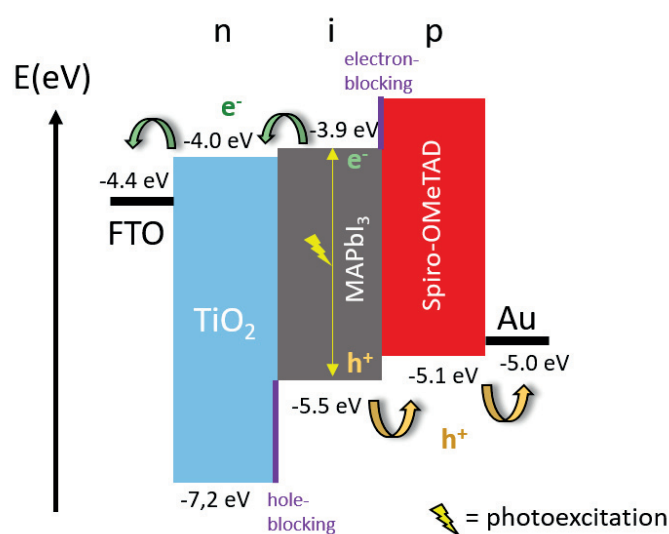


Figure 1.9 Perovskite device operation schematic. After photoexcitation, the photogenerated electron-hole pair dissociates into free charge carriers within ~ 2 ps. The charge carriers now have hundreds of nanoseconds (before they recombine) to travel to the extraction layers (HTM and ETM), which are respectively selective for electrons (TiO₂) and holes (Spiro-OMeTAD). The anode material (FTO) and the cathode material (Au) are selected in such a way that their work function matches the ETM conduction band (LUMO) and the HTM valence band (HOMO), respectively.

I would like to finish the device physics introduction with a very brief discussion about the concept of doping in perovskite solar cells and semiconductors in general. In general, doping is required for good semiconductor-semiconductor or metal-semiconductor junctions in order to optimize the contact potential or to produce Ohmic contacts. These are contacts that are not rectifying (such as Schottky contacts). However, higher doping levels, for example within the photoactive perovskite layer, although potentially decreasing interface resistance, also increase electron-hole recombination due to the presence of additional free carriers. This can result in serious open-circuit voltage loss. A typical example of device degradation due to excessive doping is the MASnI₃ perovskite, which adopts almost a metallic character (degenerate doping) due to oxidation from

Sn^{2+} to Sn^{4+} . Thus, in the case of photo-active materials, there is generally a trade-off between doping and interface optimization. In the case of the HTM/Au interface for example, higher doping would be welcome to decrease interfacial resistance which results in a lower fill factor. Ohmic contact between the HTM and the metal electrode is absolutely crucial. For organic semiconductors, this theory is however not entirely applicable, leaving room for molecular engineering strategies to optimize organic semiconductor/metal or organic semiconductor/inorganic semiconductor junctions.

1.3 Perovskite Single Crystal Growth: Liquid-Liquid Diffusion

Many different single crystal growth methods have been adopted to lead halide perovskite single crystal growth. Of particular interest is the “inverse temperature crystallization (ITC)” method, which has been shown to produce lead halide perovskite single crystals of very high quality within a relatively short growth time⁵⁹.

Although ITC provides high-quality single crystals, it is based on the use of gammabutyrolactone (GBL) rather than the exact precursor solution used to fabricate perovskite solar cells. As a result, the comparison between thin film crystal symmetry and single crystal symmetry is potentially skewed. During this thesis, I essentially rely on the “liquid-liquid diffusion” growth method because it can be based on the exact precursor solution used for solar cell fabrication.

The liquid-liquid diffusion growth method is here adopted for the first time to lead halide perovskite single crystal growth. Although it is one of the simplest single crystal growth methods, it has not yet been adopted to lead halide perovskites, most likely due to the difficulty of finding the right solvent mixture. It is based on two layers of different but miscible solvents that slowly interdiffuse (*solvent 1* and *solvent 2*) and the main requirement is that the solubility of the crystallizing materials in *solvent 1* is different from the one in *solvent 2*. The crystals should not be soluble in the final solvent mixture (see **Figure 1.10**).

To grow crystals, one first solubilizes the crystallizing material in the high-solubility solvent (*solvent 1*), ideally forming a saturated solution. Then, depending on the density of the used solvents, the low-solubility phase (*solvent 2*) is either deposited on top of the first phase or below. Subsequently, *solvent 2* diffuses into the high-solubility solvent, creating an ideal interface for crystal growth. Typical solvent mixtures for purely organic crystal growth include dichloromethane/toluene. In the case of the hybrid lead halide perovskite, the choice of *solvent 1* is mostly restricted to DMF, DMSO and GBL, due to Pb^{2+} solubility. In inverse temperature crystallization, GBL is the solvent

used for solubilizing the lead halide perovskite precursors. However, thin film fabrication is usually carried out using DMF, DMSO or DMF/DMSO mixtures- solvents that do not allow for ITC. Provided that one finds the right *solvent 2*, liquid-liquid diffusion principally allows the use of the DMF/DMSO mixtures typically used for high-efficiency solar cell fabrication. In chapter 4 and chapter 5, it is shown that alcohols are good solvents to be used as *solvent 2* in combination with DMF/DMSO. Especially Isopropanol is identified as the key *solvent 2* to be used for growing hybrid perovskite crystals using liquid-liquid diffusion. In the case of lead halide perovskite growth, it is found that heat is required for initiating and sustaining single crystal growth when using DMF/DMSO as *solvent 1* and Isopropanol as *solvent 2*. As methylammonium is soluble in Isopropanol, this growth method is not applicable to all of the perovskite compositions. Additional details regarding single crystal growth of hybrid perovskites using liquid-liquid diffusion can be found in Chapter 4.

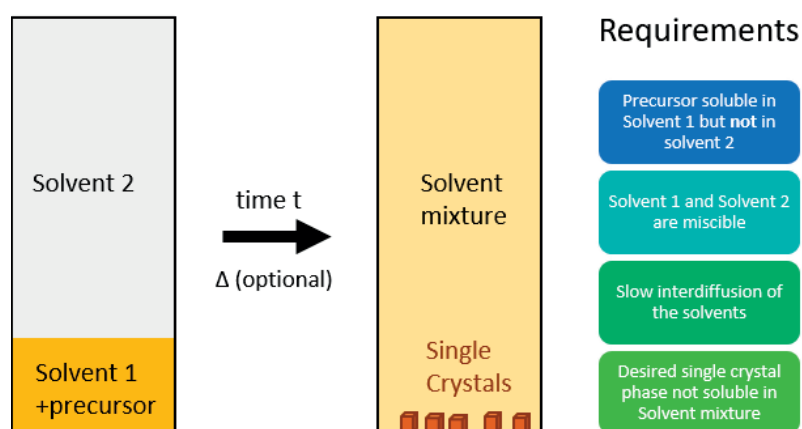


Figure 1.10 Single crystal growth via the “liquid-liquid diffusion” growth method. Slow interdiffusion of two miscible solvents (*solvent 1 and solvent 2*) results in the crystallization of the crystallization material, previously solubilized in solvent 1.

1.4 Perovskite crystal structure: from oxide perovskites to hybrid lead halide perovskites

A helpful guide for writing this section was reference [60]

Considered to be ionic ABX_3 compounds, perovskites have to abide by the charge neutrality equation:

$$q_A + q_B = -3q_X$$

Some of the possible combinations include:

- $q_X = -1$, $q_A = +1$ and $q_B = +2$. This is the case for halide perovskites such as the hybrid halide perovskites described in this work or for example the inorganic fluoride perovskite KNiF_3 .
- $q_X = -2$, $q_A = +1$ and $q_B = +5$: e.g. NaNbO_3
- $q_X = -2$, $q_A = +2$ and $q_B = +4$: e.g. CaTiO_3
- $q_X = -2$, $q_A = +3$ and $q_B = +3$: e.g. LaAlO_3

The ideal perovskite structure (=“aristotype”) has cubic symmetry. Because the original perovskite CaTiO_3 was actually shown to be orthorhombic, the ideal perovskite structure is usually referred to as the room-temperature SrTiO_3 structure. Two representations, differing by whether the A cation lies at the corner positions or at the central position of the unit cell are generally used to depict the structure. In representation 1, the unit cell is described by the A cations at the corner positions, B cations at the body center and the X anions are face-centered. In representation 2, the A cation lies at the center of a simple cubic cell in a cuboctahedral cage (12-fold coordination) formed by its 12 nearest neighbours. The atomic positions are described in **Table 1.1** and the structures can be seen from **Figure 1.11**.

It is convenient to consider the perovskite structure as a supramolecular assembly of two building blocs consisting of AX_{12} and BX_6 polyhedra. The AX_{12} building bloc forms a cuboctahedral cage, whereas the AX_6 building bloc forms an octahedra. The tetrad axes of the BX_6 octahedra overlap with the cubic crystal axes, which is an advantage of representation 2. In the cubic structure, the octahedra are all corner-connected. The reason for considering these two building blocks is that the optoelectronic properties of the perovskite are largely determined by the connectivity and the tilt of these octahedra, as well as the cuboctahedral cage volume, as will be discussed in the next sections. **Table 1.1** Description of the atomic positions in the two representations used to describe the perovskite crystal structure

Table 1.1 Description of the atomic positions in the two representations used to describe the perovskite crystal structure

Representation 1	Atomic Positions	
A	(0, 0, 0)	corner positions
B	(1/2, 1/2, 1/2)	body-centered
X	(1/2, 1/2, 0); (1/2, 0, 1/2); (0, 1/2, 1/2)	face-centered
Representation 2	Atomic Positions	
A	(0, 0, 0)	body-centered
B	(1/2, 1/2, 1/2)	corner positions
X	(1/2, 0, 0); (0, 1/2, 0); (0, 0, 1/2)	face-centered

In hybrid halide perovskites, the organic cation has a strong impact on the symmetry considerations and properties. Indeed, when using an organic cation, one potentially changes the spherical symmetry of the A site to a reduced symmetry. Moreover, by introducing a polar molecule in the center of the perovskite cage, orientational disorder and polarization effects are expected.

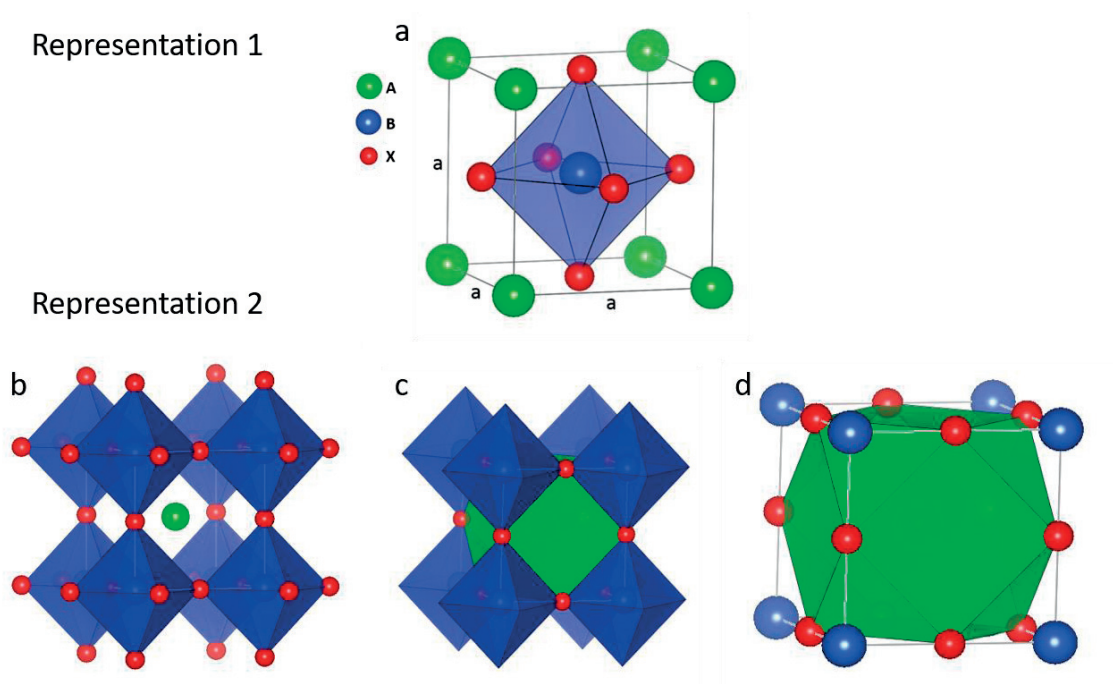


Figure 1.11 a. Representation 1 with A cations at the corner positions; b, c, d. Representation 2 with the A cation at the center depicts the cuboctahedral void, the size of which determines which A cations can be accommodated. (The ionic radii of the above structures are arbitrarily chosen.)

1.4.1 Goldschmidt tolerance factor

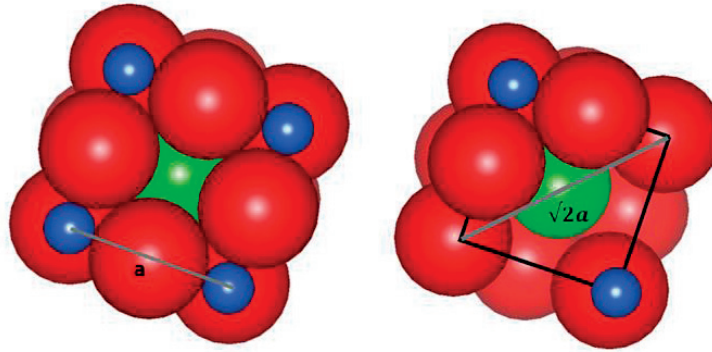


Figure 1.12 Illustration of the Goldschmidt tolerance factor concept: close-packed ABX_3 perovskite structure (hard sphere model).

The Goldschmidt tolerance factor concept was developed by Victor G. Goldschmidt in 1928 as a simple tool to predict the crystal structure as well as the geometric stability and distortions of oxide perovskites. It is based on a close-packed hard-sphere model in which, in the end, only ionic radii need to be known in order to make the predictions. The tolerance factor is a dimensionless number because it consists in the ratio of the ionic radii of the A cation, B cation and X anion. Since ionic radii are known very precisely in the case of oxide perovskites, the predictions are very accurate. Although the ionic radii of hybrid perovskites are much more difficult to determine due to the presence of the organic cation, the concept has been shown to be fairly accurate also in the case of halide perovskites, which is why I will emphasize the concept in the present section.

Figure 1.12 illustrates the derivation of the tolerance factor formula, which is straightforward. The cubic unit cell edge is equal to two times the B-X bond length $d_{(B-X)}$ and the cuboctahedral cage site width equals twice the A-X bond length, i.e. $d_{(A-X)}$.

$$a = 2d_{(B-X)}$$

$$\sqrt{2}a = 2d_{(A-X)}$$

Thus, the ideal structure forms if:

$$\frac{d_{(A-X)}}{d_{(B-X)}} = \sqrt{2} \rightarrow \frac{d_{(A-X)}}{\sqrt{2} \cdot d_{(B-X)}} = 1$$

In the 1920s, Goldschmidt proposed this relation in order to predict how likely it is that ions would form a stable perovskite phase. Since at that time not many crystal structures had been solved, the bond distances were not easily determined, thus resulting in the proposition of using ionic radii instead (Goldschmidt's rule). Making the approximation that the cations are in contact with the anions, the ideal perovskite structure is formed if the ratio of the ionic radii is equal to 1:

$$t = \frac{r_A + r_x}{\sqrt{2}(r_B + r_x)} \stackrel{ideal}{\cong} 1$$

This simple formula allows to test the compatibility of a set of 3 ions to form a perovskite structure. In the case of oxide perovskites, where ionic radii are known to great precisions, tolerance factors ranging from 0.9-1.0 (instead of exactly 1.0) have shown to yield cubic perovskite structures. In general, tolerance factors between 0.71-1.0 lead to a perovskite structure. However, for tolerance factor values between 0.71-0.9, the octahedral framework starts to distort, resulting in symmetry lower than the ideal cubic symmetry (**Table 1.2**). Tolerance factor values larger than unity are also observed. This leads to the formation of hexagonal perovskites, which are described in the following section.

Table 1.2 Predicted perovskite structures based on tolerance factor values.

Tolerance factor	Structure	Explanation
>1.0	hexagonal polytypes	A cation too big (or B cation too small)
0.9-1.0	cubic	optimal conditions
0.71-0.9	rhombohedral orthorombic	A cation too small (distorted perovskites)

1.4.2 Hexagonal perovskites

In principle, any A cation of charge +1 is a potential candidate as long as it fits within the (approximately cuboctahedral) cage. However, if the cation is too large, the three dimensional perovskite structure is partially or totally broken, as predicted by tolerance factors larger than 1. Whereas “normal” perovskites ($t \leq 1$) are identified by cubic close-packed AX₃ layers, the term “hexagonal perovskites” denominates any perovskite containing at least one repeatedly occurring hexagonal close-packed layer, thus referring to either mixed hexagonal-cubic AX₃ stacking pat-

terns or to a pure hexagonal AX_3 stacking sequence. In theory, any linear combination of hexagonal and cubic stacking sequences is possible. Hexagonal perovskites differ from their cubic analogues only by looking perpendicular to the c -axis and are therefore forming a family of “perovskite polytypes”. $BaNiO_3$ is considered to be the ideal hexagonal analogue of the ideal $CaTiO_3$ cubic perovskite. It is referred to as a 2H perovskite because it consists of only hexagonally stacked AX_3 layers. The polytype nomenclature will be explained in the following paragraphs.

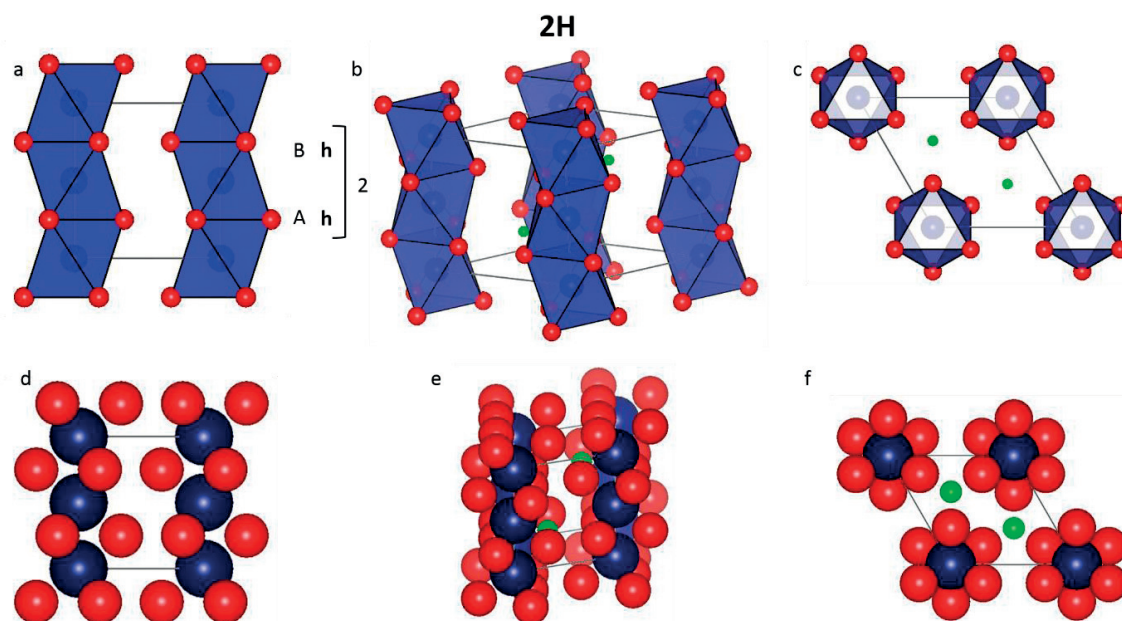


Figure 1.13 Structure of the 2H polytype. The 2H hexagonal polytype consists of 1D columns of face-sharing BX_6 octahedra: structure type $BaNiO_3$; analogous to the δ -phase of $FAPbI_3$ perovskite. The AX_3 stacking sequence nomenclature is AB (ABC notation), h (hc notation) or 2H (Ramsdell notation); pure hexagonal stacking.

In order to accommodate the larger A cation, the octahedral connectivity needs to change. In the extreme case (pure hexagonal 2H), the octahedra are 1D columns that are not connected between each other. Mixed cubic-hexagonal stacking results in a mixture of corner- and facesharing octahedral. This octahedral connectivity has influence on the bandgap of the material as will be discussed in Chapter 4 and Chapter 5. Most importantly, mixed face- and corner-sharing positions create two different octahedral positions which are energetically different. Thus, it can be predicted that only two different types of halides enable the formation of stable 4H and 6H perovskite polytypes (more details in Chapter 4 and 5).

The 2H polytype is a one-dimensional polytype containing columns (arrays) of purely face-sharing octahedral, as can be seen from **Figure 1.13**. There are different nomenclatures used to describe hexagonal perovskites, e.g. ABC sequence, h-c notation, Ramsdell notation. The nomenclature is developed according to the concept of close-packing of spheres. Changing from one notation to another is straightforward when starting from the ABC sequence. In the h-c notation, one then assigns the letter “h” for any hexagonal close-packed AX_3 layer, which means one has to look in the ABC sequence for a letter that is surrounded by the *same* two letters. If the letters before and after a given letter differ, one assigns the letter “c” to that layer. The Ramsdell notation then corresponds to the sum of the “h” and “c” within one unit cell followed by the letter describing the symmetry of the unit cell, e.g. R for rhombohedral, H for hexagonal or C for cubic.

The ABC sequence of the purely hexagonal close-packed polytype is ABABAB... Therefore, this corresponds to “hh” in the h-c notation and 2H in the Ramsdell notation (**Figure 1.13a**). The ABC notation of the 50%/50% mixed cubic-hexagonal polytype is ABCB... This corresponds to “hc” and 4H (**Figure 1.14**). Another possible polytype has the ABC sequence ABCACB..., which is equivalent to “hcc” or 6H (**Figure 1.15**). These mixed hexagonal perovskites thus present corner- as well as face-sharing octahedra.

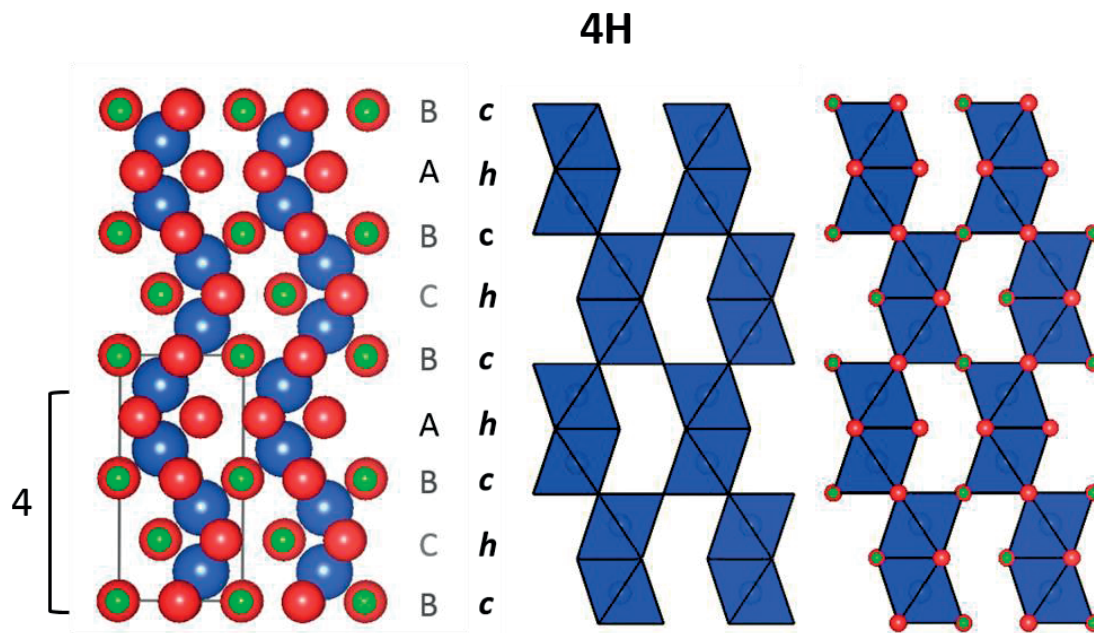


Figure 1.14 Structure of the 4H polytype. The 4H hexagonal polytype consists of 3D network of face-sharing as well as corner-sharing BX_6 octahedra. The AX_3 stacking sequence nomenclature is ABCB (ABC notation), hc (hc notation), 4H (Ramsdell notation). Cubic over hexagonal stacking ratio: 1:1

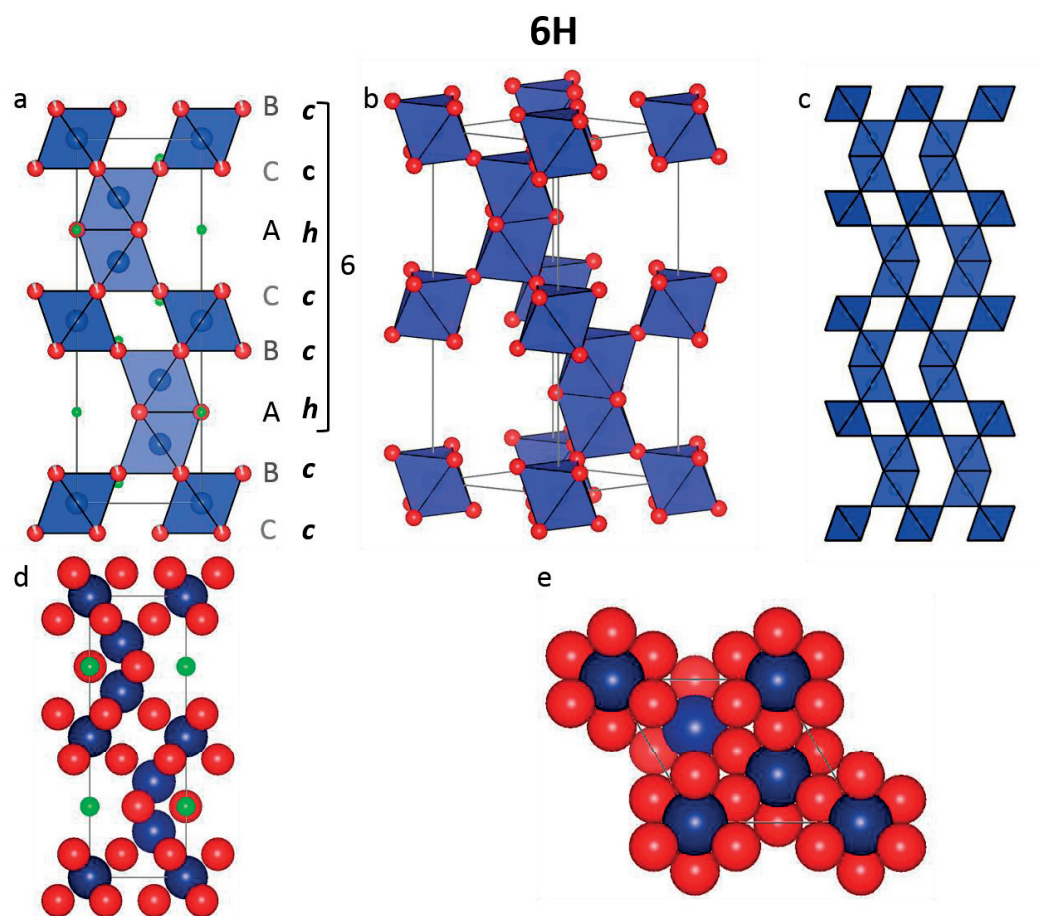


Figure 1.15 Structure of the 6H polytype. The 6H hexagonal polytype consists of a 3D network of face-sharing as well as corner-sharing BX₆ octahedra. The AX₃ stacking sequence nomenclature is ABCACB (ABC notation), hcc (hc notation), 6H (Ramsdell notation). Cubic over hexagonal stacking ratio: 2:1

Apart from the 2H, 4H and 6H polytypes, many other hexagonal oxide polytypes such as 8H, 10H, 12H, 9R etc.. are known to date. In this work, the concept of 3D hexagonal perovskites is extended for the first time to lead halide perovskites (Chapter 4). B-cation-deficient hexagonal oxide perovskites have important applications as dielectric materials⁶¹. It would be interesting to verify whether hexagonal halide perovskites can also be tuned for B-cation deficiency.

1.4.3 Octahedral connectivity and octahedral tilting

The AX_6 octahedral connectivity and octahedral tilting (**Figure 1.16**) are key concepts of perovskites. In the hexagonal perovskites, I showed that part or all of the corner-sharing connectivity is replaced by face-sharing connectivity. This has implications for the stability of the structure. Indeed, B-cation/B-cation electrostatic repulsive forces are stronger in shared faces than in corner-sharing octahedra. This repulsive effect is particularly strong in B^{4+} perovskites; in halide perovskites it could be rather small due to the weaker coulombic interaction between the adjacent Pb^{2+} . Thus, although face-sharing connectivity allows to accommodate larger A cations, it comes also at the expense of Madelung energy, basically a large electrostatic force between B cations in face-shared octahedral. Madelung energy is part of the cohesive energy of ionic crystals. In oxide perovskites, this loss can be partially compensated via B-B bonding, B-O covalency or B-site vacancy because these are all factors favouring hexagonal stacking over cubic stacking. Moreover, for oxide perovskites having tolerance factor >1 , stretching of the B-O bond is known to occur. This stretching enhances any tendency for ferroelectric distortions. Whether some or all of these considerations can also be applied to hexagonal lead halide perovskites, remains to be investigated.

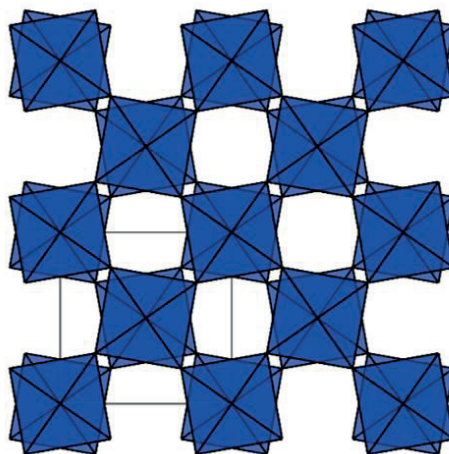


Figure 1.16 Octahedral tilting displayed in $MAPbI_3$.

Tilting of the octahedral typically occurs when tolerance factors are below 1 (smaller A cation for example). Such tilting leads to more flexibility in the A cation coordination whereas the B cation

environment remains mainly the same. Many oxide perovskites can be specifically tuned for octahedral tilting in order to obtain the desired properties. But a typical example for tilted perovskite is also the MAPbI_3 perovskite.

1.5 Characterization techniques

1.5.1 Current-Voltage (J-V) and External Quantum Efficiency (EQE) measurements

Current-Voltage (J-V) characterization is by far the most important measurement for the assessment of the quality and power conversion efficiency of a solar cell. Although the exact working principle and equivalent circuit of the different types of solar cells differ from each other, key parameters such as the “squareness” of the J-V curve (=fill factor), J_{sc} and V_{oc} remain the first choice for describing their performance. Using a sourcemeter, the output current is recorded upon swiping the voltage either from reverse bias to forward bias (forward scan) or from forward bias to reverse bias (backward scan). Generally, a dark scan precedes the actual efficiency measurement under full AM1.5⁴ illumination. So-called “solar simulators” that are either constituted of a Xenon arc lamp or, more recently, an array of LEDs, artificially imitate this AM 1.5 sun irradiation.

The difference between the forward scan curve and the backward scan curve is denominated as hysteresis. Especially for perovskite solar cells, hysteresis constitutes one of the main challenges that remains not entirely understood⁶². The voltage scan speed greatly affects the intensity of the hysteresis. It has been shown that hysteresis is lowest in intermediate scan speeds⁶³, which is why I selected this range of scan speeds for the J-V characterization of perovskite solar cells in this thesis. Moreover, there is a procedure called “light soaking”, which means that one exposes the solar cell to be measured to light for a certain time (generally seconds). This can be done either at no applied bias or at a voltage slightly higher than V_{oc} . In some cases, this dramatically increases solar cell performance. Although the improvement has been attributed to trap filling and related capacitive effects⁶⁴, this procedure is generally considered as not very reproducible and mostly inexplicable, which is why one should mostly refrain from it. Due to large performance differences

⁴ AM stands for relative “Air-Mass”. It denotes the most common correction coefficient applied to sun irradiation for taking into account the optical path through the terrestrial atmosphere (incident angle). AM1.5 is universally used for evaluating solar cells under standardized conditions at temperate latitudes. In equatorial and tropical regions, AM1 to AM1.1 can be used because the sun’s angle to the Earth’s surface is small (between 0° and 25°)

observed upon various measurement protocols, perovskite solar cell characterization now (towards the end of my PhD studies) mainly relies on maximum power point tracking (MPPT) algorithms and stability tests carried out at the maximum power point.

The external quantum efficiency (EQE) of a solar cell is measured by scanning the wavelength of incoming light λ over a certain range while measuring at the same time the current produced by the solar cell at short-circuit for each wavelength. It is thus a measure of the extracted current divided by the number of incoming photons. By summation over the solar spectrum, the maximum current (J_{sc}) that the solar cell can produce under 1 sun illumination is obtained. The higher the absorption of light and the higher the charge collection (less recombination), the higher the EQE value.

The mathematical derivation of the quantum yield (external quantum efficiency-EQE or Incident Photon to Charge Carrier Efficiency-IPCE) of a solar cell goes as follows:

$$\text{Quantum Yield (QY)} = \frac{n}{N}$$

where n equals the number of carriers and N equals the number of photons.

$$QY = \frac{\frac{en}{s \text{ cm}^2}}{\frac{eN}{s \text{ cm}^2}} = \frac{\frac{I[A]}{\text{cm}^2}}{\frac{eN}{s \text{ cm}^2}} \quad (1)$$

$$P\left(\frac{J}{s \text{ cm}^2}\right) = N \frac{hc}{\lambda} = \left(\frac{N}{s \text{ cm}^2}\right) \frac{6.6 \cdot 10^{-34} \text{ Js} \cdot 3 \cdot 10^8 \text{ m/s}}{\lambda(nm) \cdot 10^{-9} \text{ m}} \rightarrow \left(\frac{N}{s \text{ cm}^2}\right) = \frac{P\left(\frac{W}{\text{cm}^2}\right) \cdot \lambda(nm) \cdot 10^{17}}{19.9}$$

By substitution into (1):

$$QY(\%) = EQE(\%) = IPCE(\%) = \frac{I_{sc}\left(\frac{A}{\text{cm}^2}\right)}{P\left(\frac{W}{\text{cm}^2}\right)} \cdot \frac{1240}{\lambda(nm)} \cdot 100$$

From this, I_{sc} can be easily calculated by summation over all of the measured wavelengths and taking reference values for sun irradiation power at each wavelength. The obtained current value is then compared to the I_{sc} value obtained from the J-V scan.

1.5.2 Conductivity and hole mobility using Organic-Field-Effect-Transistors (OFET)

Thin-film conductivity of organic semiconductors was measured by solution processing the chemically oxidized (doped) hole transport material onto commercially available OFET transistor substrates (Fraunhofer IPMS, **Figure 1.17**). The same substrates were also used for hole mobility measurements, with the difference that in this case the pristine HTM and not the doped HTM has to be used in order to obtain the desired field effect. These measurements required the development of a microprobe station- details can be found in Chapter 6.

Conductivity values were extracted by fitting the linear (Ohmic) current-voltage curves typically obtained after sweeping the voltage from -10V to 10V and back (channel length 2.5 μ m). Starting from the general expression of Ohm's law:

$$J = \sigma E \rightarrow \frac{I}{a} = \sigma \frac{U}{l}$$

Where l is the channel length, a is the area, σ the conductivity and U the potential. Resistance and resistivity are linked via the expression below and conductivity is the inverse of the conductivity:

$$R = \rho \frac{l}{a} \text{ and } \rho = \frac{1}{\sigma} \rightarrow \sigma = \frac{l}{a \cdot R}$$

$$\rightarrow \frac{I}{a} = \frac{l}{a \cdot R} \frac{U}{l}$$

Thus, one finds Ohm's law under the well-known form $U=RI$. After fitting, the conductivity is simply calculated as below:

$$I = \underbrace{\frac{1}{R}}_{\text{to be fitted from } I-V \text{ scan}} \cdot U \rightarrow \sigma = \frac{l}{a \cdot R}$$

Conductivity of organic materials is often measured using a 4-point probe configuration in order to remove any potential contact resistivity between the metal electrode and the organic film. In this work, 2-point probe measurements, although not removing contact resistance, were considered accurate because Ohmic contacts were always achieved for well-performing HTMs. Contact resistance could thus be neglected.

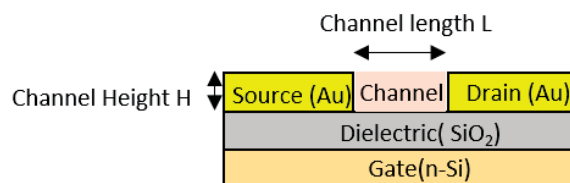


Figure 1.17 Top-contact OFET transistor configuration used for 2-point conductivity measurements and hole mobility measurements

Hole mobility determination via field effect requires a 3-electrode device such as an Organic-Field-Effect-Transistor (OFET). This device consists in a SiO_2 layer acting as a dielectric, which is grown on top of a conductive n-Si silicon wafer substrate (gate). Then, gold electrodes are deposited in special arrangement so that one OFET chip contains 4×4 transistors, 4 of each channel length $2.5 \mu\text{m}$, $5 \mu\text{m}$, $10 \mu\text{m}$ and $20 \mu\text{m}$.

A voltage applied at the third electrode (gate) controls the current flow between source and drain gold contacts. Since the analysed organic semiconductor materials are exclusively p-type, the source-drain voltage and the source-gate voltage are negative. Increase in voltage now refers to an increase in the absolute value. When no gate voltage is applied, no current flows because the material is not conductive. This is called the OFF state. Applying a gate voltage leads to accumulation of holes which are uniformly distributed across the channel length. Thus, the channel becomes conductive, which is referred to as the ON state. The minimum voltage required to turn it on is called the threshold voltage V_T .

When a gate voltage is applied, three regimes, namely linear regime, pinch-off point and saturation regime (beyond pinch-off) determine the shape of the current-voltage curve. At small source-drain voltages ($V_{DS} \ll V_G$) I_{DS} varies linearly with increasing V_{SD} . Increasing V_{DS} results in the formation of a depletion region near the drain that is due to the difference between the local potential $V(x)$ and the gate voltage. It gets larger until it reaches a point where the channel is pinched off ($V_{DS} = V_G - V_T$). Further increasing V_{DS} results in space-charge-limited saturation current flowing across the depletion region. Now the carriers are swept from the pinch-off point to the drain by the electric field that determines the depletion region (saturation regime). The equation governing the saturation regime drain-source current is:

$$I_{DS,sat} = \frac{W}{2L} \mu_{sat} C_i (V_{GS} - V_T)^2$$

By plotting the square root of I_{DS} vs. V_{GS} , the mobility can be calculated from the slope of a linear fit. Two different measurements called *output characteristics (OC)* and *transfer characteristics (TC)* are

typically performed for assessing the properties of an OFET. An OC measurement consists in sweeping V_{DS} while keeping V_{SG} constant. A set of 4-5 different V_{SG} values are typically scanned. This allows to assess the quality of the OFET by analyzing if the channel shows a clear linear behaviour as well as a saturation regime. In a TC measurement, V_{DS} is kept constant while the V_{SG} is swept. This allows to determine the saturation mobility according to the equation above and also the I_{ON}/I_{OFF} ratio as well as the V_T can be extracted.

Measuring the hole mobility in an organic field effect-transistor can be quite challenging in terms of achieving high absolute mobility values. Indeed, defects in the SiO_2 act as trap states which need to be filled before the channel becomes conductive. Passivation strategies such as functionalizing the SiOH bonds with silanes exist, however they have not yielded better mobility values than the bare substrates in my case, which is why I refrained from using this strategy

Mobility and conductivity are dependent on each other via the following equation:

$$\sigma = q(n\mu_n + p\mu_p)$$

It shows that increasing the free carrier concentration n or p results in an increase of the conductivity, which is the basis of doping in semiconductors. Unfortunately, the mobility itself is often a function of n (resp. p), resulting in a much more complicated relation between conductivity and mobility in practice.

1.5.3 Secondary Electron Microscopy (SEM) – Energy Dispersive X-ray analysis (EDX)

High-energy electron bombardment (typically 0.5-30 keV) of a sample surface results in a particle collision cascade producing low energy secondary electrons (from the sample), back-scattered electrons (from the primary beam), absorbed electrons, Auger electrons as well as characteristic x-rays. The electrons and the x-rays can be detected by detectors placed within an electron microscope at an angle and position where the intensity of the signal will be highest. The intensity of the secondary electrons is mainly determined by the surface topography of the sample. Consequently, raster-scanning a primary electron beam across a sample allows for spatially resolved secondary electron detection, from which an image of the topography can be constructed. By focusing the primary beam to a small spot, high spatial resolution of 10 nm and below can be achieved. Thus, secondary electrons can be used for nanoscale imaging and the highest sensitivity for the surface is obtained by lowering the primary electron beam energies to 1 keV and below.

For imaging of lead halide perovskite samples, low beam energies are preferred due to their instabilities under high energy bombardment. Typically, I used an acceleration voltage of 1-2 keV for high-resolution imaging of perovskite surface grains as well as for cross-sectional analysis.

The emitted x-rays can be characterized with an energy-dispersive x-ray (EDX) detector which in principle allows for quantitative elemental analysis. However, in general the analysis is more qualitative than quantitative because of the lack of suitable reference samples, especially in the case of the sensitive halide perovskite samples. Depending on the elements to be analyzed, bombardment at relatively elevated energies between 5-10 keV are required in order to produce characteristic x-rays. For lead halide perovskites, one wants to induce characteristic x-rays from Pb ($M=2.34$ keV), I ($L_{\alpha}=3.94$ keV), Br ($L_{\alpha}=1.48$ keV) and N ($K_{\alpha}=0.39$ keV). This is the reason why I used energies around 8 keV. These high acceleration energies are mostly detrimental to lead halide perovskite thin films, which is why EDX mapping, which typically takes around 30 min depending on the size of the map, could not be carried out. Charging effects also increase the difficulty of using EDX in combination with halide perovskites. But most importantly, the spatial resolution of EDX mapping is limited to about $1 \mu\text{m}$ (not less than 500nm), which is why I relied on secondary ion mass spectrometry imaging for studying the elemental distribution in halide perovskites at the nanoscale.

1.5.4 Secondary Ion Mass Spectrometry (SIMS): correlative imaging and depth profiling

When a high-energy *ion beam* instead of an electron beam is used to irradiate the sample, sputtering takes place. The secondary particles that are emitted from the sample include in this case atoms, molecules and secondary ions. The latter ones can be extracted and collected by means of an electric field and accelerated into a mass spectrometer, where they are filtered according to their mass to charge ratio and counted by detectors. Depending on the primary ion species, impact energies and dose (ions/cm²), molecular information (limited fragmentation) or elemental information (complete fragmentation) is obtained. In the present work, SIMS has been exclusively used for obtaining elemental information, either by using dynamic depth-profiling or by using the recently in-house developed Helium Ion Microscope-SIMS (HIM-SIMS)⁶⁵.

An impacting primary ion beam yields a collision cascade in which only atoms close to the sample surface obtain enough energy to be sputtered. Thus, most of the sputtered atoms originate from the top three monolayers of the sample, resulting in a confined information depth. In order to maximise the probability of ionization (resulting in a higher secondary ion signal), reactive primary

ion species are usually used. Cesium (a very electropositive element) primary ions typically increase the negative secondary ion intensity whereas oxygen (a very electronegative element) results in an enhancement of the positive secondary ion signal.

By raster-scanning a focused ion beam over the analyzed surface, one can perform SIMS imaging. Using a secondary electron detector at the same time, correlative imaging (morphology+chemical information) can be obtained. Currently, the highest lateral resolution for 2D elemental mapping is achieved by the CAMECA NanoSIMS and is about 50 nm. But this lateral resolution of 50 nm is well above the ultimate physical limitation of the lateral resolution. Indeed the lateral dimension of the collision cascade triggered upon primary ion impact can be as low as 6-10nm (impact energies in the 10keV range)⁶⁶, depending on the sample material and the primary ion species. In order to reach the ultimate physical limitation, Wirtz et al. introduced in 2015 SIMS relying on a gas field ion source producing He⁺ and Ne⁺ ions^{67,68}. The sputter yield and the ionization efficiency obtained by He⁺ and Ne⁺ bombardment is lower because these ions are lighter than Cs⁺ and O⁻ as well as non-reactive. However, this can be compensated by the higher bombardment density, allowing for high-sensitivity imaging and a surface resolution down to 10nm. There are several advantages over other analytical microscopy techniques. TEM for instance requires complicated sample preparation which is tedious, time-consuming and possibly already affecting the analyzed material. SEM/EDX is limited to lateral resolutions in the order of about 0.5 μm. Optical analytical tools are diffraction-limited and therefore also unable to compete. HIM-SIMS thus provides unprecedented insights into the chemical composition of thin films for example.

A typical drawback in SIMS is the lack of being directly quantitative. Indeed, as the ionisation probability of secondary ions depends heavily on the element of interest and the local sample composition, the secondary ion intensities generally do not reflect the local sample composition but rather mostly reflect the ionisation processes. For example, detecting bromide sputtered from a KBr or a LiBr matrix would not give the same yields. This problem is commonly called 'matrix effect'. For quantification, a reference sample is required.

Perovskite thin films, which are hybrid materials, can be relatively easily sputtered even with Ne⁺ bombardment. Another advantage of perovskite samples is that they contain very electronegative species such as iodide and bromide which are easily detected in SIMS.

The most common analytical mode in SIMS is actually depth profiling rather than imaging. Sputtering layer-by-layer, one is able to detect profile variations in elemental composition as a function of depth. Using low impact energies (down to 100-150eV), one is able to study for instance interfaces with sub-nm depth resolution. This mode of operation has been used extensively during decades by the semiconductor industry⁶⁹ in order to quantify dopants (using standard reference

samples). In this work, I applied depth profiling to perovskite solar cells by studying possible elemental gradients in the capping layer. However, I obtained only preliminary results, as many parameters such as sample preparation, reference sample analysis and beam energy still need to be optimized in a lengthy process which was beyond the scope of the thesis.

Concerning the secondary electron image resolution, the helium ion microscope (HIM) is typically superior to a conventional SEM. As the interaction volume in the near surface region (i.e. in the volume relevant for SE emission) between the He^+ beam and the sample is much smaller than in the electron/sample case, the HIM exhibits substantially higher resolution (0.3 nm) than that of a modern SEM. Using a low-energy electron flood gun for charge compensation, insulating samples can be imaged without prior coating, so that surface details that would be typically masked by such a coating can be revealed. Furthermore, the GFIS column allows to obtain images that have 5 to 10 times greater depth of field when compared to images acquired with Field Emission SEM.

1.5.5 Atomic Force Microscopy (AFM)/Kelvin Probe Force Microscopy (KPFM)

While standard AFM provides nanoscale imaging and information about surface topography (including roughness), many more informations can be obtained by using different kinds of tips. Among the most commonly used techniques is Kelvin Probe Force Microscopy (KPFM), which is a very valuable tool because it can provide information about the surface potential / work function in addition to the topographical image. KPFM relies on a contact potential difference (CPD) between the tip and the sample (**Figure 1.18**). One of the drawbacks is the surface sensitivity of many samples, especially since an AFM placed inside a protected atmosphere is not commonly found in research laboratories. Absolute surface potential values have been interpreted with great care and knowledge that the results are potentially skewed. This is why reference samples have been used and the measurements on perovskites were mostly “simple” measurements, analyzing surface potential heterogeneities rather than absolute values.

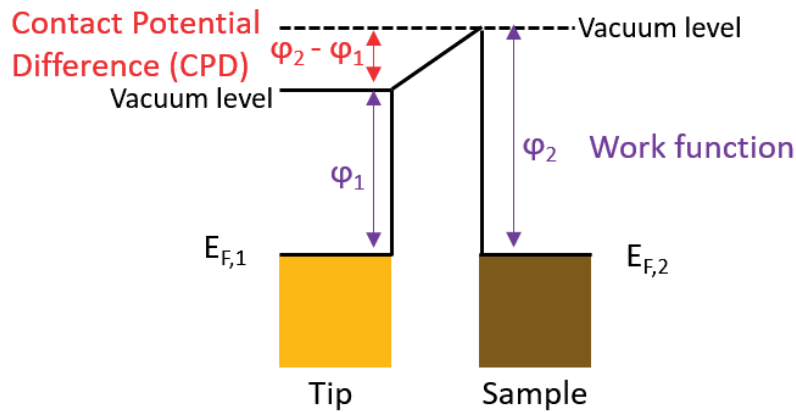


Figure 1.18 Band diagram of the KPFM tip and the sample.

1.5.6 Raman and Photoluminescence spectroscopy of thin films

Raman spectroscopy is widely used for obtaining structural and chemical information of semiconductors. It is based on the comparison of the frequency difference between the incoming photons and the scattered photons. So, contrary to Rayleigh scattering, Raman scattering is an inelastic scattering process, which means that the kinetic energy of the incoming photons is not conserved (**Figure 1.19**). At room temperature, the Stokes process largely prevails because the electrons are mostly in their vibrational ground state. The Raman frequency shift provides valuable information about the vibrational modes. In solids, these can be very difficult to understand and predict so that quantum chemical calculations are necessary to understand Raman spectra of perovskite films.

Contrary to Raman spectroscopy, which is based on scattering, Photoluminescence spectroscopy is based on excitation of an electronic state upon light absorption and the subsequent radiative relaxation (emission). This requires that the excitation wavelength must be at least equal to the energy difference between the valence and conduction band (resonant conditions). Photoluminescence is governed by the selection rules of electronic dipole transitions.

Both PL and Raman can be obtained from the same laser setup. For this thesis, I used a combined Raman-PL setup which also contains microscope objectives, thus allowing for PL and Raman mapping at sub-micron spatial resolution. The biggest difference between the PL and Raman signal is that the Raman signal is very weak. Approximately only $1 \cdot 10^{-7}$ of the scattered photons

are frequency-shifted (Raman), so that relatively strong excitation densities are required. The reason is that Raman scattering is a two-photon process, which is an event less likely to occur than the one-photon photoluminescence process. Consequently, any fluorescent trace impurity, even with low quantum efficiency, can easily overwhelm the Raman scattering signal.

The required strong excitation densities can lead to perovskite degradation, which is why, for the sake of scientific accuracy, devices have been encapsulated with a glass substrate under inert atmosphere. Moreover, first the PL maps were gathered at very low excitation densities before the Raman maps were acquired at higher excitation densities.

Steady-state PL experiments provide no information about the timescale at which deactivation of the excited state occurs. But transient PL experiments can be carried out to study the characteristic lifetime (transition probability) associated with fluorescence. The lifetime is strongly affected by any competing nonradiative processes (quenching). This can be used to study the dynamics of the electron or hole transfer to the ETM or HTM layer respectively. Simple indications for injection of part of the photogenerated carriers into the ETM or HTM layers can also be observed by a decrease of steady-state PL intensity.

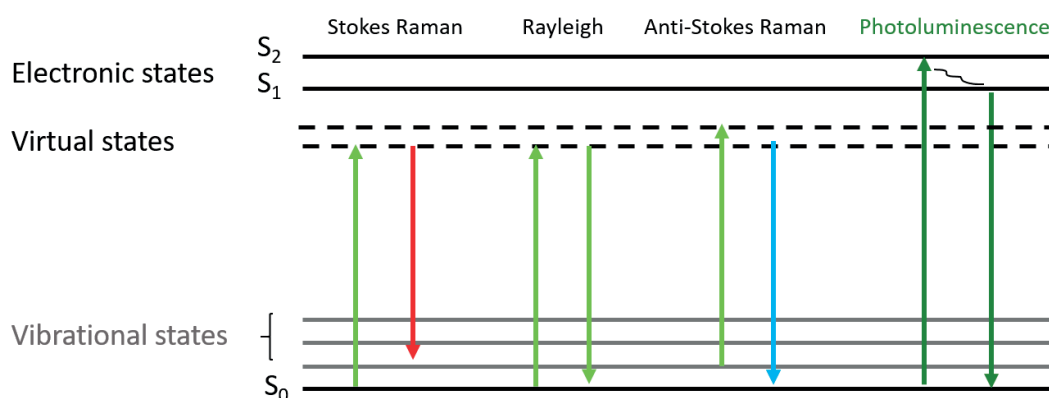


Figure 1.19 Illustration of three different light scattering mechanisms and photoluminescence

1.5.7 X-ray diffraction of single crystals and polycrystalline thin films

The wavelength of X-rays is similar to the distance between atoms. Upon X-ray irradiation, the incoming electromagnetic waves are elastically scattered and they interfere either constructively or destructively, yielding a characteristic diffraction pattern on a detector. In a crystal, parallel planes of atoms spaced by distance d apart (identified by hkl Miller indices) determine directions

and distances. Constructive interference takes place if the path difference for reflected rays from 2 adjacent planes, which is $2d\sin\Theta$ as can be seen from **Figure 1.20**, is equal to an integer number (set to 1) of wavelengths λ :

$$\lambda = 2d_{hkl}\sin\Theta \text{ (Bragg equation)}$$

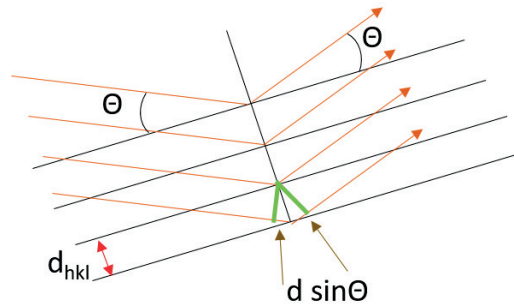


Figure 1.20 Illustration of the Bragg equation. The path difference of two x-rays scattered between two adjacent planes is depicted by the green lines.

Re-arranging the Bragg equation yields:

$$\sin\Theta = \left[\frac{\lambda}{2} \right] \left[\frac{1}{d_{hkl}} \right]$$

The distance of a diffraction spot from the center of the whole pattern is proportional to $\sin\Theta$ and therefore also to $1/d_{hkl}$. This allows to understand the reciprocal (inverse) nature of the geometrical relationship between a crystal lattice and its diffraction pattern.

Scattered X-rays coming from a single crystal form a distinct pattern of spots having a characteristic geometry, symmetry and intensity. These three properties correspond to the properties of the crystal structure that one wants to determine. Indeed, the geometry and symmetry of the spots allow to obtain information about the unit cell geometry and symmetry. The determination of the entire structure requires also the measurement of the intensities, which is a much longer task. The complete theory behind X-ray diffraction is beyond the scope of this short introduction section, which is why I will only describe the practical aspects behind solving a single crystal structure.

1. The first and most important task consists in selecting a suitable crystal of best possible quality under an optical microscope before mounting it on a pin (with the help of a drop of oil). The ideal crystal size depends on the size of the primary beam, the absorption coefficient of the analyzed materials as well as on how well the material diffracts. Perovskites containing heavy elements such as Pb diffract very well. Generally, the crystals

should have the size of a few hundred micrometers. The pin is then mounted on the goniometer head and the crystal is beam-centered manually.

2. Secondly, one measures several diffraction patterns allowing to obtain the unit cell geometry and preliminary symmetry information such as the crystal system or space group. This measurement takes only a few minutes, which is why I usually mounted and measured several different crystals in order to select the one with the most beautiful diffraction patterns. The obtained diffraction patterns are actually a preliminary subset of the complete diffraction pattern. By assigning hkl Miller indices to each of the reflections and by measuring Bragg angle for a few reflections, the unit cell parameters a , b , c , α , β and γ are determined via the Bragg equation.
3. Subsequently, one measures the intensity data, which typically takes a few hours, depending on how well the crystal diffracts and on the degree of symmetry. Obviously the highest symmetry requires the least number of diffraction patterns that need to be collected. The procedure yields a list of thousands of reflections, each one having hkl indices as well as intensities assigned. Standard uncertainty is also calculated for each intensity, providing information about how reliable the measurement was.
4. Then, data reduction is performed. This consists in corrections related to the geometry of the equipment, polarized radiation, absorption effects, ...
5. After successful measurement and data correction, one can proceed to solving the structure, which will yield the atomic positions in the asymmetric unit cell. The atoms in the unit cell are then created by symmetry. This requires to recombine the individual diffracted beams into a picture of the electron density distribution in the unit cell. However, this can not be achieved directly because the phase of the reflections is not known (the well-known phase problem), making a direct calculation of the electron density impossible. Different methods have been developed to estimate an initial structure model.
6. Once a basic structure is obtained, one has to complete the structure, which means one needs to find all the atoms. This is generally achieved by having a look at the difference electron density map. This can be quite tedious, especially if the data quality is poor.
7. The last step consists in refining the structure model, which means one refines atom positions and displacement parameters. Solving and refining is here carried out using SHELX implemented in the Olex2 software.

Analyzing diffraction from a polycrystalline thin film is considered as a powder diffraction experiment. In such a case, crystal orientation is ideally completely random, thus every orientation should be equally represented. When measuring a thin film, the projected 3D reciprocal space

encountered in single crystal diffraction is projected onto a single dimension. Peak position typically depends on d spacing, characteristic for the investigated phase and is varying through parameters affecting the crystal lattice, such as atomic substitution or temperature. Integrating the peaks potentially yields the degree of crystallinity (% crystallinity) and allows for quantitative analysis. Peak width gives information about crystallite size and crystal perfection.

Most of the XRD experiments were carried out using Bragg-Brentano geometry. This allows for high beam intensity and high-resolution, however precise alignments are needed and effects such as preferred orientation possibly make analysis of peak intensity difficult. Samples to be sent for synchrotron experiments were prepared in capillaries, allowing to get rid of preferred orientation. Details about the in-situ chamber specially designed for the present work can be found in Chapter 4.

1.6 Motivation and Strategies

When the photovoltaic properties of halide perovskites were discovered, concepts and the architecture from solid-state DSSC could be readily applied to perovskite. This allowed achieving very rapid progress in terms of device efficiencies. However, many important questions regarding stability, phase purity, general device operation remained unanswered. In this thesis, I decided to address the many aspects and implications related to the **perovskite composition**. For this, I decided to fabricate high efficient devices through optimization before analyzing the phase composition in detail. The idea was that the crystallization process is at the center of the studies.

Since the perovskite layer is composed of grains at the nanoscale, the size and composition of which potentially play a critical role in the efficiency of the device, I decided to adopt the following strategies:

- First, I studied the influence of non-stoichiometric precursors (PbI_2 excess) on device efficiency. This led to the development of record-breaking MAPbI_3 device efficiencies and resulted in understanding the importance of the grain size on solar cell performance as well as the TiO_2 perovskite interface in general.
- After realizing the importance of the grain size, questions regarding the nano- and microscale properties of these crystalline grains remained. This is why I decided to study composition of high-efficiency mixed anion mixed cation perovskites. After being able to

fabricate high efficient devices based on this composition, I studied the grain composition by means of SIMS imaging, KPFM as well as spatially resolved combined Photoluminescence/Raman spectroscopy. Contrary to common beliefs, I found that high efficient mixed I/Br perovskite grains contain nano-domains that do not contain Iodide. In general, a rather heterogenous phase composition was found at micro- and nanoscale. These nano-domains seem not to hamper device efficiencies, suggesting that they are actually beneficial.

- Studying the composition of mixed cation/mixed anion perovskites then resulted in the discovery of 3D hexagonal lead halide polytypes. Studying the in-situ crystallization process, I find that these phases are involved by taking the role of stable intermediates. The sequence is found to be $2H \rightarrow 4H \rightarrow 6H \rightarrow 3C/3R$, here reported the first time to take place in halide perovskites. Incorporation of cesium ions prevents the formation of these defect-prone hexagonal phases, thus bypassing this complicated crystallization sequence. This study involved the development of a holder allowing for temperature-dependent and controlled-atmosphere XRD measurements.
- Moreover, I prove that the hexagonal phases are also stable when replacing bromide by the smaller chloride ions. For the first time, I show a lead halide perovskite structure (hexagonal) that contains both I and Cl atoms at the same time. I am also able to suggest a generalization of the crystallization process of mixed anion/mixed cation perovskites.

Lastly, I was also able to reduce the cost of perovskite solar cell fabrication by successfully employing a new small molecule HTM that is cheap and efficient in the same time. In order to characterize HTM's, I decided to develop a probe station which can be used for temperature-dependent hole mobility and conductivity measurements of organic as well as perovskite thin films.

Chapter 2 Relevance of the stoichiometry of precursors in MAPbI₃ perovskite solar cells

*This chapter is based on work published in Energy and Environmental Science (EES)⁷⁰. The chapter is a **completely re-written and modified** version of the original publication. I had the original idea for this publication, carried out a great part of the experiments and fabricated the champion device (19.1%), which was, at the time of publication, the champion MAPbI₃ perovskite solar cell of the laboratory (LPI/GMF, EPFL) and the second highest reported in the world.*

2.1 Introduction

Perovskite Photovoltaics have evolved rapidly over the last years, with standard Power Conversion Efficiency (PCE) values for MAPbI₃ reaching over 17%^{71–74} (2015). Improvements are generally made by either tuning the ABX₃ perovskite structure itself (A) or by optimizing the crystallization process by modifying the way of perovskite processing (B):

- A) Anion tuning has been achieved by partially or totally replacing iodide by bromide, yielding CH₃NH₃PbI_xBr_{1-x} perovskites⁷⁵. However, inherent stability and efficiency problems have been discovered for the mixed phase, which easily segregates into pure iodide and bromide perovskite³⁹. Incorporation of Chloride has also been studied, resulting in improved charge transport⁵⁵ and reduced charge recombination^{76,77}. However, intense debates have started whether the small Cl atoms can fit into a perovskite structure together with the larger I atoms. It is now mostly believed that Cl solely enhances the crystallization of the thin film, but evaporates during the process, leaving behind a pure CH₃NH₃PbI₃ perovskite phase⁷⁸.

Cation replacement, namely Methylammonium (MA) by Formamidinium (FA) has been shown to be an efficient strategy for lowering the band-gap, thus collecting more photons from the red part of the solar spectrum, which leads to an increase of the short-circuit current (J_{sc})³¹. Based on this result, Seok et al. published a breakthrough study showing both anion (mixed I and Br) and cation tuning (mixed FA and MA) in

the same time, resulting in the record-breaking mixed cation/mixed anion perovskite formulation (FAPbI₃)_{0.85}(MAPbBr₃)_{0.15}.⁴⁰

- B) Improving the thin film quality via crystallization enhancement is a common strategy that is adopted by researchers in the halide perovskite community. Especially nucleation and uniform film growth have been identified as the key parameters one should rigorously control. Solvent engineering and antisolvent vapour-assisted approach have been for example extensively explored to control the crystallization^{41,72}. Both the sequential deposition, developed by Burschka et al. in 2014¹³, and the single-step approach, yield perovskite thin films with characteristic nano-sized grain structure. The size of these grains and their roughness can be controlled using different approaches.

Using a two-step approach (sequential deposition), the grain size can be controlled by varying the concentration of the solution in which the PbI₂ film is to be dipped (MAI in Isopropanol). By changing the optimized standard conditions (8mg/ml), one can either increase the grain size (e.g. 6mg/ml) or decrease the grain size (e.g. 10mg/ml). This shows the complexity and difficulty to obtain good reproducibility using the sequential deposition method (time in IPA bath, MAI concentration change between dipping the first substrate and the last substrate into the solution, etc).

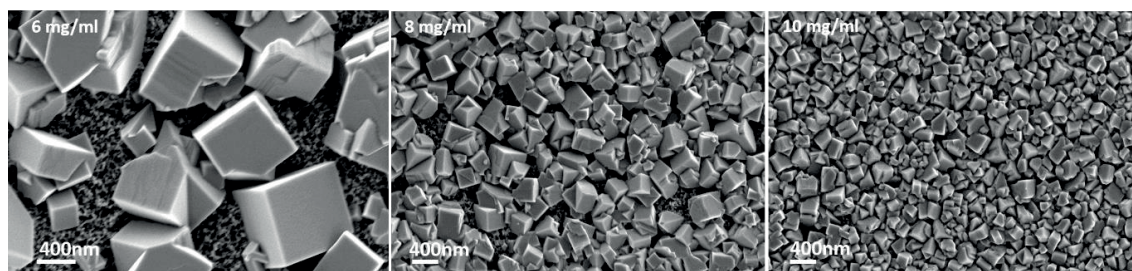


Figure 2.1 MAPbI₃ perovskite films on mesoporous TiO₂ converted from PbI₂ films dipped into Methylammonium iodide solutions of different concentration (in Isopropanol): 6mg/ml 8mg/ml and 10mg/ml. The good coverage of the TiO₂ (necessary to reduce electron-hole recombination) strongly varies due to the difference in grain size.

In the case of sequential deposition, increased grain size (6mg/ml) is accompanied by increased roughness and decreased TiO₂ coverage. In contrast, conversion of PbI₂ films from 10mg/ml solutions yields smaller grains, decreased roughness but very good surface coverage. Thus, solar cells made from films with larger grains show increased current but decreased V_{oc} due to recombination of electrons in bare TiO₂ partially in contact with the hole transporting material due to the less good surface coverage. The message from these simple experiments is clear: The capping layer, i.e. the nano-sized perovskite grains on top of the TiO₂, play a crucial role in enhancing the

solar cell performance. The challenge is set: How to make large capping layer grains with good coverage, thus obtaining good V_{oc} and J_{sc} values in the same time? In this respect, two-step conversion is more challenging than single-step conversion, which is why I decided to choose the latter one as the method of choice during my whole PhD thesis. It turns out that the single-step approach, allowing to control the capping layer crystal size, will be one of the crucial steps towards highest efficiencies.

Another strategy for improving film quality would be to optimize the stoichiometry of the precursor materials (MAI : PbI₂). The presence of PbI₂ in MAPbI₃, evidenced by an XRD reflection at 12.8° (Cu K α), is generally considered harmful for device performance as the degradation process of MAPbI₃ is accompanied by an increase of the amount of the PbI₂ phase within the film. For example, excessive annealing time or high temperatures result into gradual film decomposition and appearance of PbI₂. However, in this work it is shown that solar cells fabricated using intentional excess of PbI₂ (originating from the non-stoichiometric precursor solution) outperform conventional MAI:PbI₂ (1:1) solar cells. Incorporation of unconverted PbI₂ into the perovskite grains, playing the role of an additive, influences the crystallization process in such a way that power conversion efficiencies are substantially boosted. By improving the fill factor and the V_{oc} , average PCE values increase from 16.2% to 18%, including several devices above 18% and a champion device of over 19%. These results show that, although somewhat counter-intuitively, the performance of the hybrid semiconductor MAPbI₃ is enhanced when solution-processed with additional PbI₂.

2.2 Results and Discussion

All of the solar cells described below are based on the single-step perovskite deposition process. The detailed solar cell fabrication procedure can be found in the Appendix (Chapter 8). Several series of devices were fabricated using precursor solutions containing a different MAI:PbI₂ ratio: 1:1 (no excess PbI₂), 1:1.05 (5% excess PbI₂), 1:1.10 (10% excess PbI₂), 1:1.15 (15% excess PbI₂) and 1:1.20 (20% excess PbI₂).

Average device efficiencies and the corresponding current-voltage (J-V) characteristics are shown in **Figure 2.2**. Each of the curve represents a solar cell that approaches a value closest to the average values reported in **Table 2.1**. Remarkably, all of the precursor solutions allow to fabricate

solar cells of high performance, even in the case of as much as 20% excess PbI₂. The highest average performance is achieved for perovskite films containing 10% PbI₂ excess, namely 18.4% PCE. Less PbI₂ excess or even more (up to 20%) only slightly decreases the performance. The data show that remaining PbI₂ in the perovskite film does not cause the solar cell to underperform compared to the stoichiometric case, rather it increases the performance. J_{sc} , V_{oc} as well as the fill factor (FF) all improve upon excess PbI₂ addition. Whereas 10% PbI₂ excess results in an increase of the V_{oc} by 30 mV from an average 1.05 V to an average of 1.08 V, the J_{sc} only slightly improves. However, one would not expect any variation in J_{sc} at all because the high band-gap semiconductor PbI₂ is not expected to be relevant in photocurrent generation. Constantly showing values above 0.76, the parameter that improves the most upon addition of $\geq 10\%$ PbI₂ excess is the fill factor.

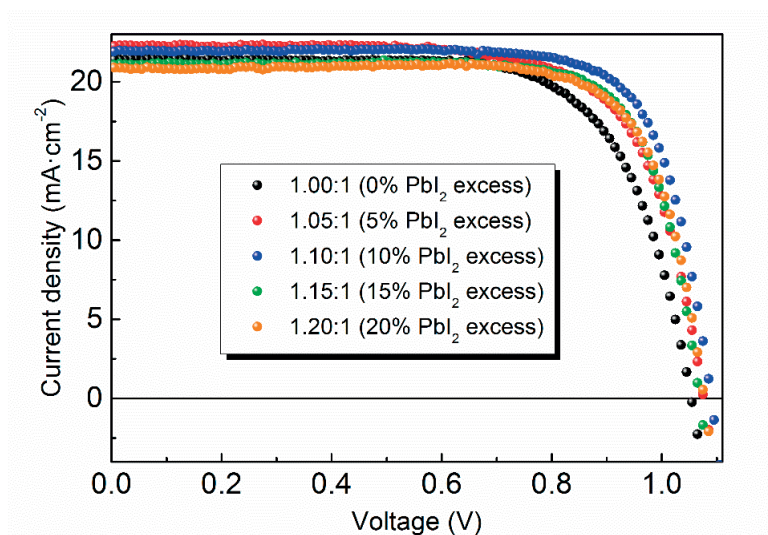


Figure 2.2 Current-Voltage characteristics of selected solar cells closest to the average value. The data show that lead iodide excess is beneficial for device performance.

Table 2.1 Parameters describing the performance of the solar cells made from different precursor solutions (average values).

PbI ₂ :MAI	J_{sc} (mA cm ²)	V_{oc} (V)	FF (%)	PCE (%)
1 : 1 (0%)	21.45	1.054	70.3	15.95
1.05 : 1 (5%)	22.28	1.076	71.3	16.97
1.10 : 1 (10%)	22.15	1.081	76.2	18.42
1.15 : 1 (15%)	21.21	1.075	76.3	17.37
1.20 : 1 (20%)	20.87	1.077	76.0	17.17

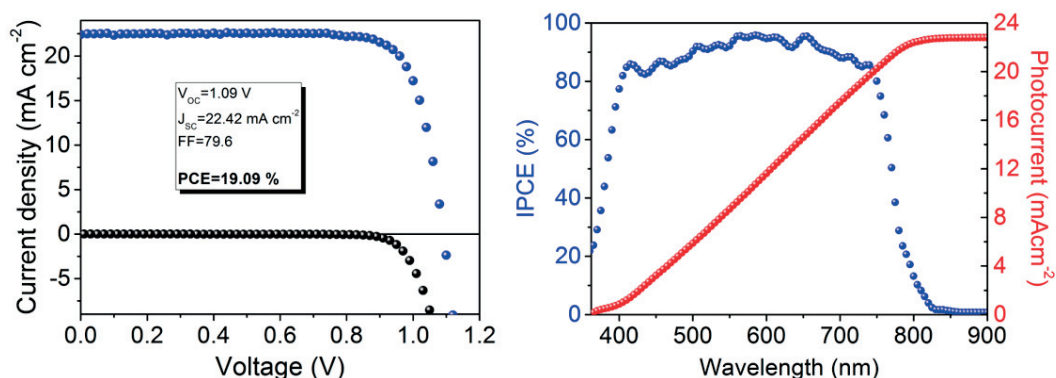


Figure 2.3 Dark current and current-voltage characteristics of the champion MAPbI₃ solar cell (10% PbI₂ excess). The device shows an impressive **19.1%** Power Conversion Efficiency (PCE) under 1 sun illumination.

The champion device, depicted in **Figure 2.3**, shows a PCE of 19.1%, one of the highest reported values for pure MAPbI₃ solar cells. Especially the fill factor, approaching 0.80, and the impressive 1.09V open-circuit voltage make this device so efficient. The incident photon-to-current efficiency (IPCE), also called external quantum efficiency (EQE) shows a photocurrent generation onset at about 820 nm. The obtained integrated photocurrent value is close to the J_{sc} value determined from the current-voltage scan. The J-V scan of the solar cell showing the highest obtained fill factor value in this study, namely 0.807 (forward scan), and corresponding to a precursor solution containing 10% PbI₂ excess, is presented in **Figure 2.4a**. This value is among the highest reported among n-i-p perovskite solar cells, approaching the theoretical thermodynamic limit of ~0.86. **Figure 2.4b** shows that hysteresis between the forward and backward scan direction is negligible at scan speeds of 10 mV/s. The shelf-life stability (dark and dry air conditions) was tested and it was found that the solar shows almost no signs of degradation (efficiency drop from 18.8% to 18.4%), even after a period of over 3 months.

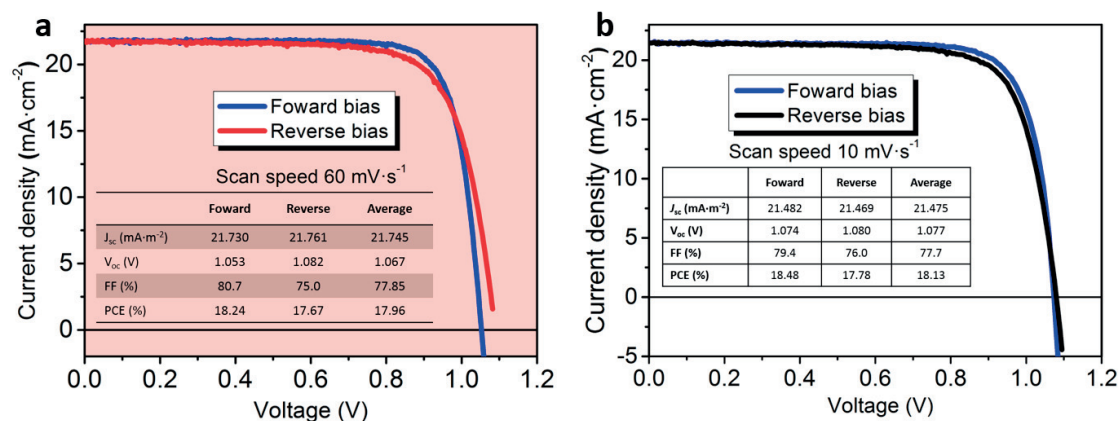


Figure 2.4 **a.** Solar cell showing a remarkably high fill factor (80.7%) in the forward scan direction. **b.** no significant hysteresis between the forward and the reverse scan of a typical high-efficiency solar cell at 10 mV/s scan speed.

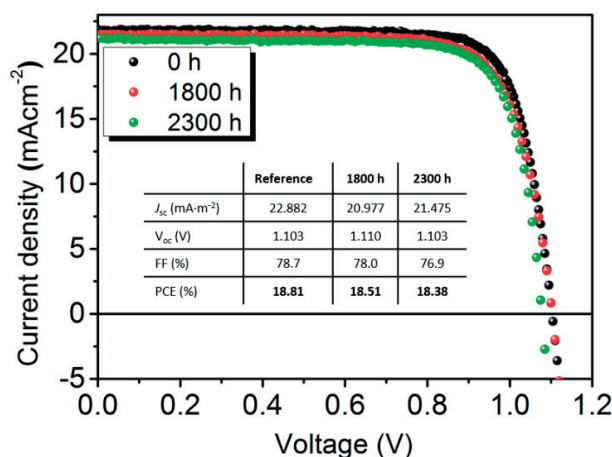


Figure 2.5 Shelf-life stability of a high-efficient solar cell kept in dark and dry conditions between the IV scans (reference=0h; after 1800h; 2300h). No significant signs of degradation appear after more than 3 months.

Surface and cross-sectional Scanning Electron Microscopy (SEM) analysis of perovskite thin films provides the first good understanding of the improved efficiencies due to PbI₂ excess. Although the surface morphology of the bare perovskite layer (no cathode) is similar in all of the cases

(nano-sized grains featuring distinct grain boundaries), the grain size distribution is affected by PbI₂ excess (**Figure 2.6**).

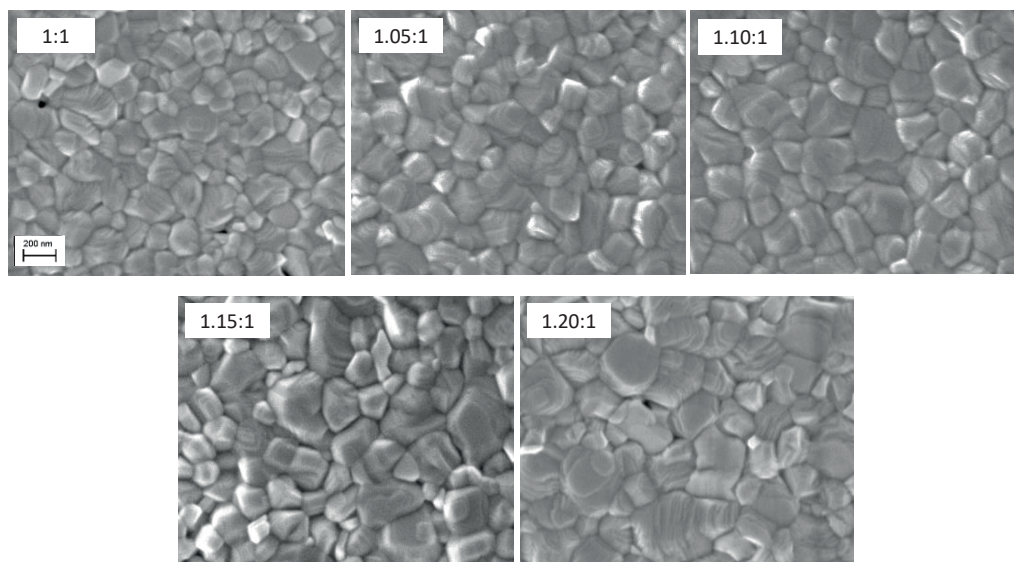


Figure 2.6 SEM pictures (top view) of the perovskite capping layer. The grain size distribution depends on the precursor stoichiometry.

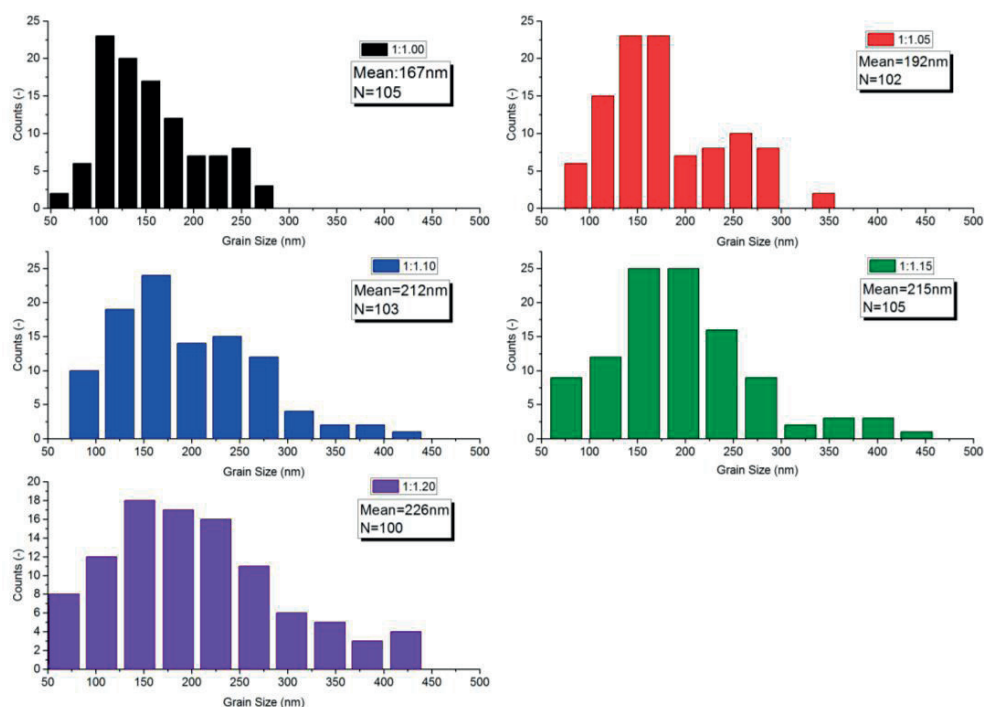


Figure 2.7 Distribution of the crystallite size of ~ 100 grains as determined from SEM images of the corresponding solar cells without cathode (no HTM, no gold electrode).

The larger the amount of PbI₂ excess, the bigger the grains. Indeed, grain size analysis over approximately 100 grains of each composition (**Figure 2.7**) reveals that the average grain size increases from 167 nm (no excess) to 226 nm (20% excess). The number of grains close to or bigger than 300 nm dramatically increases with the addition of excess PbI₂. Cross-section images of the corresponding full solar cells (**Figure 2.8**) provide further insights into the benefits of PbI₂ excess over the stoichiometric composition. In all of the cases, one part of the perovskite infiltrates the mesoporous TiO₂ scaffold and another part forms a capping layer. Whereas the thickness of the capping layer does not vary much from one composition to another, there is a difference in the grain morphology. Indeed, the grains are more “granular” in the stoichiometric case. 5% and 10% PbI₂ excess results in distinctive, well-defined grains showing clear grain boundaries whereas 15% and 20% PbI₂ excess lacks this distinctive feature.

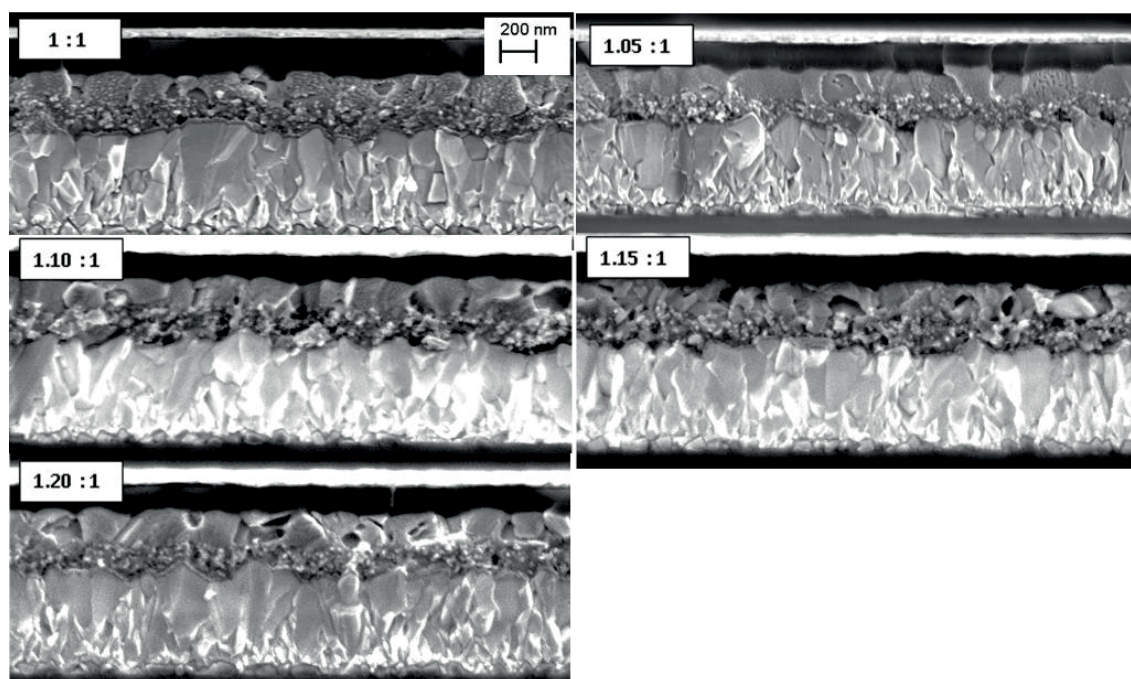


Figure 2.8 Cross-Section Secondary Electron images of solar cells fabricated from precursor solutions containing no excess (1:1), 5% excess PbI₂ (1:1.05), 10% excess PbI₂ (1:1.10), 15% excess PbI₂ (1:1.15) and 20% excess PbI₂ (1:1.20).

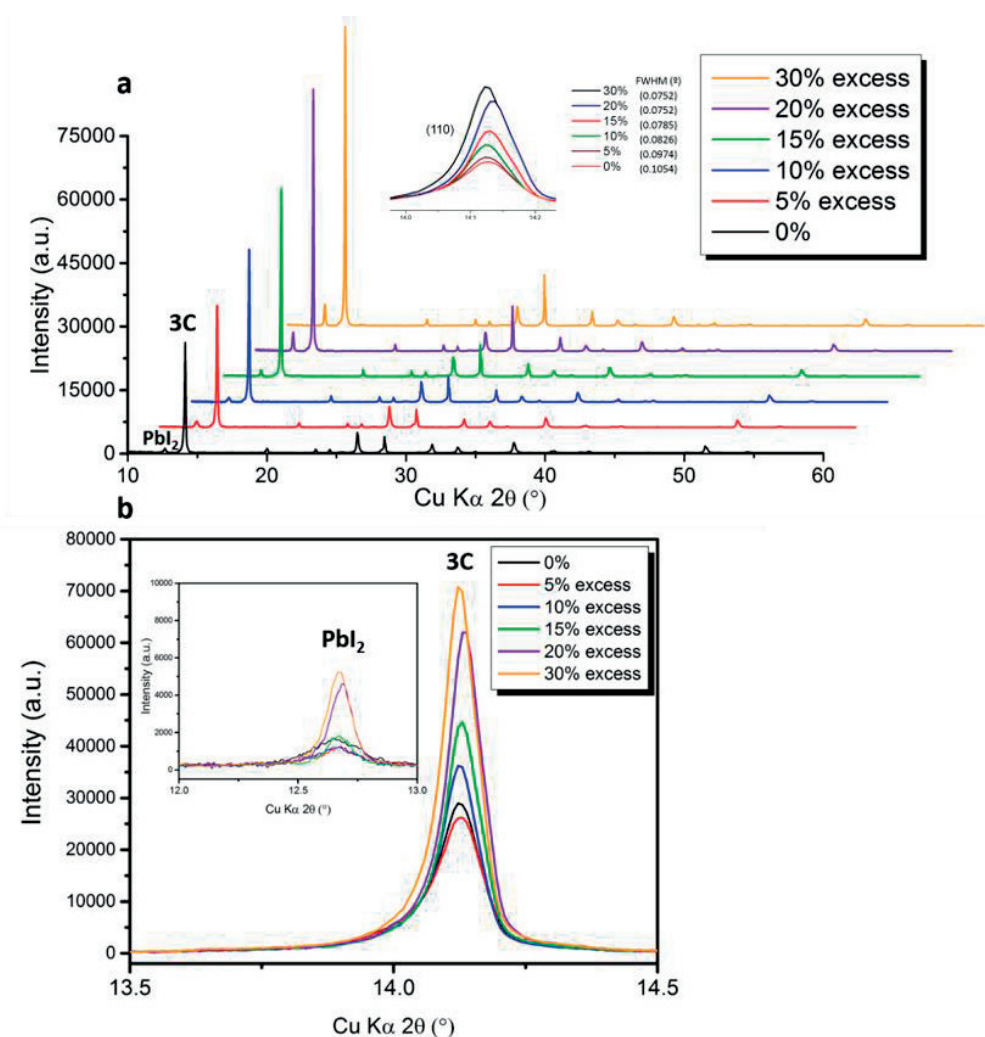


Figure 2.9 XRD diffractograms corresponding to solar cells (without cathode) made from precursor solutions containing different amounts of excess PbI₂. **a.** Increased intensity of the characteristic 3C perovskite peak (14.1°) with increasing amount of PbI₂ excess. **b.** Analysis of the perovskite peak shape and intensity. Inset: Weak reflection characteristic of PbI₂ phase. More PbI₂ excess results in a slight increase of the peak intensity. The film without PbI₂ also shows a tiny PbI₂ reflection, probably due to first signs of film degradation.

In order to understand the influence of PbI₂ incorporation on crystallinity and crystal quality, XRD measurements of thin films with different perovskite compositions were performed: stoichiometric precursors, 5%, 10%, 15%, 20% and 30% PbI₂ excess. **Figure 2.9** shows the obtained diffractograms using Bragg-Brentano geometry and Cu K_α X-ray source. The tetragonal perovskite phase is readily identified by a strong reflection at 14.1°. A tiny crystalline PbI₂ phase can be detected around 12.7° in all of the films, too (inset). Interestingly, a more intense PbI₂ peak also results in a more intense perovskite peak. Excess PbI₂ in the precursor solution yields films with

more intense (110) perovskite reflections. This can be either attributed to a slightly increased film thickness, a denser packing of the perovskite grains or an increased crystallinity within the thin film. Since cross-section SEM images did not show any difference in the film thickness, the data strongly suggest that the perovskite film quality is enhanced when co-crystallizing with excess PbI₂. A decrease in peak broadening (the values of the full-width-at-half-maximum are provided in **Figure 2.9a**) also accompanies this co-crystallization, possibly indicating the presence of larger perovskite grains in the capping layer. This confirms the surface SEM image analysis, which also revealed larger grains when co-crystallizing the perovskite from excess PbI₂ precursor solutions. In the case of the stoichiometric film, there is an unexpected tiny PbI₂ reflection at 12.7°. This can be readily attributed to first signs of film degradation.

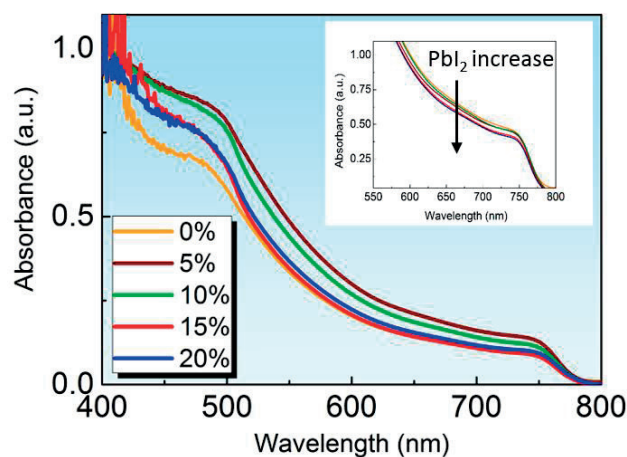


Figure 2.10 UV-Vis absorption spectra (normalized at 400nm). Inset = non-normalized data.

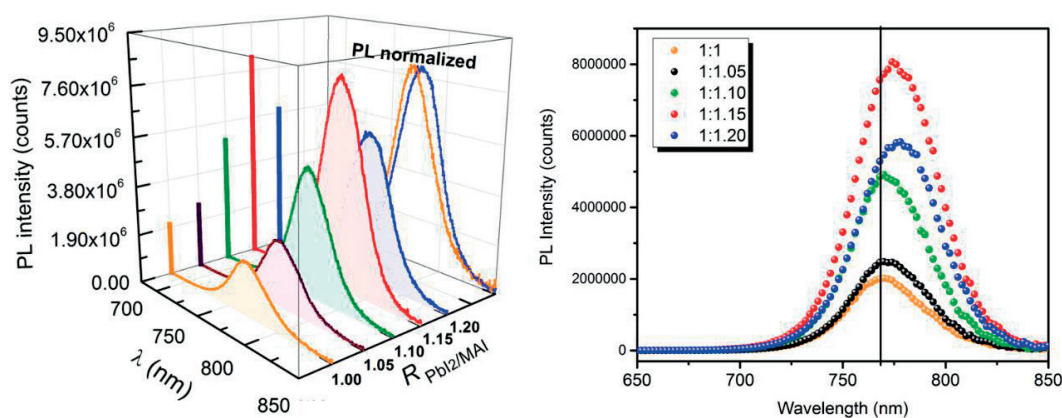


Figure 2.11 Stady-State PL measurements represented in a 3D plot and a standard 2D plot. PbI₂ excess results in a PL red-shift attributed to larger grain size/improved crystallization.

Optical characterization by means of UV-Vis, steady-state PL and transient PL was carried out on the different films in order to observe which properties are affected by the PbI₂ excess (0-20% excess). UV-Vis reveals an absorption onset at ~770 nm for all of the films, showing that the band-gap is not significantly affected by the PbI₂ excess (**Figure 2.10**). This is expected because the presence of the non-converted PbI₂ precursor phase should a priori not affect the band-gap of the perovskite phase. It is important to notice however that the UV-Vis measurements are carried out in transmission, which implies that the optical properties of both the perovskite infiltrated in the TiO₂ and the the perovskite capping layer are probed, resulting in some sort of average. As will be shown later, steady-state PL measurements carried out from the capping layer do show a peak shift that can be attributed to a change in the band-gap. In terms of absorption intensity, only slight variations between the different films can be observed. The non-normalized data (inset of **Figure 2.10**) suggest that PbI₂ excess results in a decrease of the the absorption intensity, which could be related to an overall slightly reduced amount of the MAPbI₃ phase (increased relative amount of PbI₂). The influence on optical properties due to increased grain size upon PbI₂ excess is more readily probed by means of photoluminescence spectroscopy. Indeed, **Figure 2.11** reveals a trend when upon increased PbI₂ excess: first an increase in PL intensity is observed (maximum for 15% excess); second, there is a slightly red-shifted emission for the films containing a certain amount of unreacted PbI₂ phase (up to 10 nm). This red-shift could be indicative of a reduced band gap associated with improved crystallization. This further supports the interpretation of the XRD data as well as the SEM image analysis. Indeed, it has been shown in literature that the formation of larger crystals is related to a more relaxed lattice structure due to the presence of excess PbI₂ during crystallization^{79,80}. Moreover, it has been speculated that the interplay between organic and inorganic interactions affects the lattice strain, thus influencing the band gap of semiconductors. Organic cations that freeze in a preferential head-to-tail-like configuration reduce the lattice strain, resulting in the crystallization of MAPbI₃ into larger grains. The reduced strain automatically leads to a lattice expansion, which in turn causes the reduction of the band gap, observed as a red-shift in the photoluminescence emission^{79,80}.

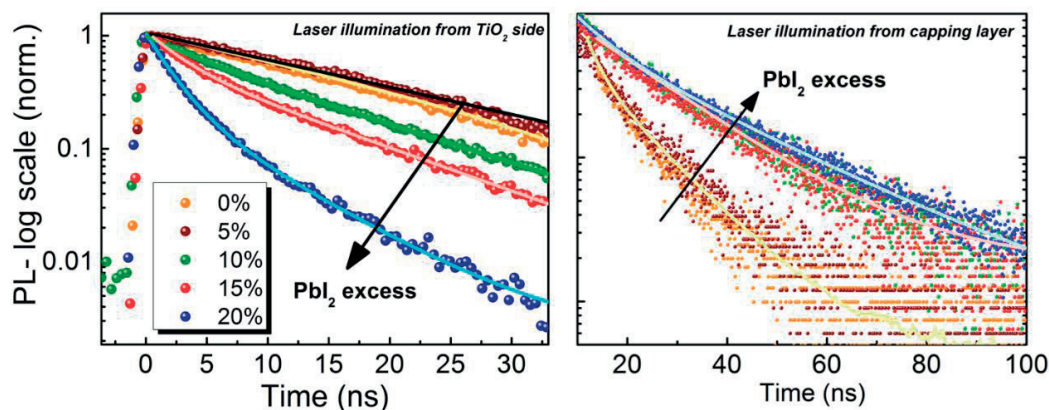


Figure 2.12 Transient PL measurements carried out from TiO₂ side (through glass) and directly through the capping layer.

The data presented in this Section strongly suggest that the improved solar cell efficiencies are closely linked to an improved film quality, i.e. higher crystal quality, a direct consequence of the formation of bigger grains. In order to gain more insight into the photophysical properties that might change upon addition of PbI₂ excess, transient PL measurements were performed. Previous studies have shown that improved film quality results in longer carrier recombination lifetimes, indirectly indicating longer charge diffusion length and superior performance^{81,82}. Given the high absorption coefficient of MAPbI₃ perovskite, the penetration depth of the 460 nm laser can be estimated in the range of 100 nm⁷⁹. Since the perovskite film thickness is about 150-200 nm in the mesoporous TiO₂ and 200-300 nm in the capping layer, it is possible to make these measurements in two possible ways: the first possibility consists in illuminating the sample through the glass side, probing the properties of the perovskite infiltrated within the mesoporous TiO₂ scaffold (perovskite/TiO₂ interface); the second possibility consists in illuminating the sample directly from the perovskite capping layer side, thus probing mostly the influence of the perovskite grain size. Illumination from the capping layer side (**Figure 2.12**) shows that PbI₂ excess in the capping layer (increased grain size) increases PL lifetime so that it exceeds the temporal window of 100 ns. The longer-living PL component, the higher PL intensity and the red-shifted band gap suggest that the crystallization dynamics have a tremendous impact on the photophysical properties of perovskite. Similar observations have been made by other groups^{80,83}, who reported that morphological changes (i.e. the crystal grain dimension) affect the optical properties of the perovskite thin films. Tuning the average crystallite dimension results in a change of the optical band gap and longer photoluminescence lifetime. In correlation with the above results, larger crystallites have

been found to have a smaller band gap and longer lifetime, corresponding to a smaller radiative bimolecular recombination coefficient⁷⁹. It has also been reported that the presence of defect states or shallow trapping levels in the grain boundaries (which can act as non-radiative recombination centres) causes PL quenching. PbI₂ excess, resulting in larger grains, possibly prevents PL quenching because the total number of grains and total number of grain boundaries is lower than in the stoichiometric case (smaller grains means more grain boundaries). XRD analysis (more intense perovskite reflection), steady state PL (red-shifted band gap) as well as TRPL (enhanced PL lifetime) all support the fact that larger grains are formed upon PbI₂ excess.

In order to obtain a more complete picture of the influence of PbI₂ excess, TRPL measurements were also performed by using illumination from the TiO₂ side (**Figure 2.12**). Due to quenching of the PL by TiO₂, the PL decay times are lower than in the previous case, namely illumination from the capping layer side. One could also claim that the confined space that the mesoporous TiO₂ scaffold offers (pores of ~30 nm) automatically restricts the perovskite crystallite size to 30 nm, resulting in the observed faster PL decay. Indeed, small crystals confined in an insulating scaffold have previously been found to exhibit faster PL dynamics due to an intrinsically lower charge recombination lifetime⁸³. In MAPbI₃ perovskite, this usually takes place in the range of hundreds of nanoseconds. However, in the present case, conductive TiO₂ is used as a mesoporous scaffold and the observed decay times are much faster. The original role of this scaffold, namely allowing electron injection to occur, strongly suggests that the reduced PL lifetime of the perovskite studied here is mainly a result of quenching due to efficient charge injection (the effect of reduced crystal size could be neglected). When comparing the perovskite thin films containing different amounts of PbI₂ excess, a very clear trend can immediately be observed. Increasing the PbI₂ excess results in a faster PL decay, possibly indicating improved charge injection. Indeed, the time constant of the decay component can be as low as 2 ns in the case of 20% PbI₂ excess (**Table 8.1**). Since all the perovskite films containing PbI₂ excess (up to at least 20%) have shorter decay times than the stoichiometric reference, it is reasonable to state that PbI₂ favors electron transfer from perovskite to TiO₂. The reason for the improved perovskite/TiO₂ interface could be a better energy level alignment and a stronger interfacial coupling at the interface, as theoretically predicted for mixed-halide perovskite⁸⁴. Improved electron transfer from perovskite to TiO₂ implies enhanced charge extraction in the solar cell, explaining the improved power conversion efficiencies. Another possibility for the improved perovskite/TiO₂ interface upon PbI₂ excess would be the passivation effect of the iodine atoms at the interface. However, the most likely explanation is the improved electronic coupling between perovskite and TiO₂ (more favourable electronic energy

levels at the interface). Indeed, in another work by Mosconi et al.⁸⁵, it was speculated that PbI₂ excess is predominantly located at the TiO₂ interface. A PbI₂ pre-treatment of the mesoporous TiO₂ layer followed by perovskite solar cell fabrication from a stoichiometric 1:1 precursor solution also resulted in faster PL decay times, comparable to solar cells directly fabricated using non-stoichiometric precursor solutions. These results suggest that the grain size is not the only parameter behind improved efficiencies upon PbI₂ excess.

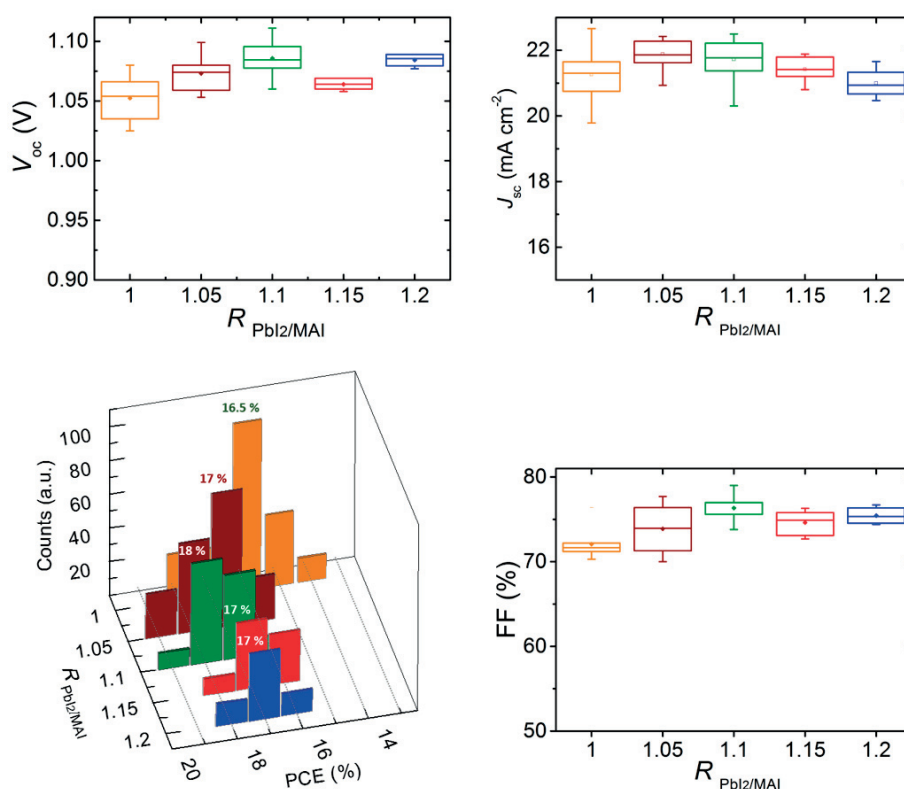


Figure 2.13 Device statistics based on ~50 solar cells. Compared to the stoichiometric reference, all of the PbI₂ excess compositions show an improved fill factor. The J_{sc} improves slightly for 5-10% PbI₂ excess and the V_{oc} is highest for 10% PbI₂ excess. Overall, 10% PbI₂ excess yields highest power conversion efficiencies.

Figure 2.13 shows the device statistics of about 50 solar cells. It is shown that 10% PbI₂ excess in the precursor solution yields the highest average efficiencies, mainly due to an improvement of fill factor and V_{oc} . The fill factor is the only parameter that is consistently higher for all of the perovskite compositions. Whereas the V_{oc} is improved upon 10% PbI₂ excess, this seems to be the parameter that shows a not so clear correlation for PbI₂ excess. This is possibly due to the fact that V_{oc} is highly affected by the electron transporting layer (TiO₂) conductivity, which is

difficult to control from one solar cell to another. Also the coverage of the hole-transporting layer strongly influences the V_{OC} . Pinholes due to solution-processing are quite common and will introduce partial contact between the subsequent gold layer and the perovskite layer. This results in enhanced charge carrier recombination and thus a decrease in V_{OC} . The J_{SC} is highest for 5-10% PbI₂ excess.

The results demonstrate that the quality of MAPbI₃ polycrystalline films can be easily enhanced by simply using a perovskite composition containing excess PbI₂. The device architecture (ETM and HTM) can remain exactly the same.

2.3 Conclusion and Perspective

In this Chapter, the successful preparation of highly efficient MAPbI₃ solar cells is reported. It is shown that a simple variation in the solution precursor ratio leads to improved power conversion efficiencies. A ratio of PbI₂: MAI (1.10:1.00) is found to yield the best solar cells. This shows, somewhat unexpectedly, that it is unnecessary to try to fabricate MAPbI₃ solar cells of perfect 1:1 stoichiometry. Even up to 20 mol% PbI₂ excess allows to fabricate devices that show impressive performance. The performance enhancement upon incorporation of PbI₂ excess is attributed to a larger capping layer grain size, improved perovskite crystallinity as well as improved charge injection at the perovskite/TiO₂ interface. These results provide a clear guide towards boosting the efficiencies of MAPbI₃ solar cells closer to the theoretical value.

The improvements due to PbI₂ excess suggest that PbBr₂ excess in mixed cation/mixed anion perovskites or pure bromide perovskites would also be beneficial. However, this has up to date not been shown to be a promising strategy. It is probably due to the fact that PbI₂ has a different crystal structure from PbBr₂. Whereas PbI₂ adopts a 2-dimensional layered structure of edge-sharing PbI₆ octahedra, PbBr₂ has characteristic edge- and corner-sharing octahedra. Moreover, it has been suggested that PbI₂ excess is only beneficial when the perovskite solar cells are fabricated inside an inert-atmosphere glovebox. Devices fabricated under ambient conditions would actually benefit from MAI excess⁸⁶. The message is however clear in both cases: larger grains are beneficial. It has also been shown from surface potential plots of MAPbI₃ perovskite films in the dark that the potential barrier between the grains is about ~ 45 meV⁸⁷, indicating that charge trapping at

grain boundaries is less problematic than in CdTe or CIGS. However, the empirical observation of enhanced device performance and charge carrier diffusion length with increasing grain size presented here and subsequently supported by other reports strongly suggests that the grain boundaries are not benign.

Chapter 3 Nano- and microscale properties of high-efficiency mixed cation/mixed anion perovskite thin films

This chapter is based on work published in JACS (Gratia et al.⁸⁸). I had the original idea for this publication and I performed or assisted all of the experimental measurements, wrote the manuscript and plotted as well as analyzed the data. Theoretical modelling was performed by the group of Prof. de Angelis (Perugia, Italy). The SIMS measurements were carried out, in my presence and assistance, by Dr. Jean-Nicolas Audinot at the Luxembourg Institute of Science and Technology (LIST) under the supervision of Dr. Tom Wirtz. The champion solar cell efficiency was achieved by Dr. Yonghui Lee, my personal best being 19.8%. I had the idea to collaborate with AINA (LIST) as well as with Prof. Sivula's laboratory (EPFL) in order to gain deep insights into nano- and microscale properties of the mixed perovskite thin films. The work having been published as a JACS communication, here I write an extended version including revised and more extensive discussion of all the data leading to this publication, including supporting information as well as unpublished data.

In the previous Chapter, I showed that MAPbI₃ perovskite, in strong contrast to other high-performance semi-conductor materials, does not need to be phase-pure. Rather, there are substantial benefits of off-stoichiometry in these thin films. Indeed, excess (5-10 mol%) of one of the precursor materials, namely PbI₂, is shown to yield better solar cell performance than the fabrication of solar cells based on a stoichiometric ratio (PbI₂ / MAI 1:1) of precursor materials. However, at least one important open question remains: What is the local distribution of the excess PbI₂ phase within the perovskite thin film? Does it go to the grain boundaries?

Parallel to my work proving the beneficial device performance of excess PbI₂ in MAPbI₃, a breakthrough publication by the group of Prof. Seok introducing the mixed anion/mixed cation (FAPbI₃)_{0.85}(MAPbBr₃)_{0.15} perovskite concept⁴⁰ represented a significant step toward halide perovskite optimization. Subsequently, work by the group of Prof. Grätzel⁸⁹ showed also improved performance of PbI₂ excess for mixed cation/mixed anion (FAPbI₃)_{0.85}(MAPbBr₃)_{0.15} perovskites. Again, the question of the distribution of the chemical elements arose. This motivated me to carry out an in-depth investigation of these complex yet highly efficient (FAPbI₃)_{0.85}(MAPbBr₃)_{0.15} perovskites. In theory, this complex perovskite composition would allow for complete phase segregation into iodide and bromide perovskite. Indeed, phase segregation has been shown to take place in MAPbI_xBr_{1-x} perovskites³⁹. However, in the case of formamidinium containing

(FAPbI₃)_x(MAPbBr₃)_{1-x} perovskite, this has not been observed by XRD (only one perovskite diffraction peak instead of two) or PL (only one emission peak instead of two). Nonetheless, I remained convinced that, due to the low energetical barrier between I/Br⁹⁰ exchange, the nano- and microscale scale analysis will reveal **a non-phase pure material**. Indeed, although compositional engineering of mixed cation/mixed halide perovskite in the form of (FAPbI₃)_{0.85}(MAPbBr₃)_{0.15} is one of the most effective strategies to obtain record-efficiency perovskite solar cells, the perovskite self-organization upon crystallization and the final elemental distribution, paramount for device optimization, are still poorly understood. In this Chapter, the nanoscale charge carrier and elemental distribution of mixed perovskite films yielding 20% efficient devices is mapped. Combining a novel in-house-developed high-resolution Helium Ion Microscope coupled with a Secondary Ion Mass Spectrometer (HIM-SIMS) with Kelvin Probe Force Microscopy (KPFM), it is shown that part of the mixed perovskite film intrinsically (= no halide migration upon electrical bias or photonic pressure) segregates into **iodide-rich perovskite nano-domains** on a length scale **up to a few hundred nanometers**. Thus, the homogeneity of the film is disrupted leading to a variation in the optical properties at the micron-scale. These results provide unprecedented understanding of the nanoscale perovskite composition.

3.1 Introduction

Among the large variety of perovskite compositions, the mixed cation/mixed halide (FAPbI₃)_{0.85}(MAPbBr₃)_{0.15} perovskites currently hold the lead since they have repeatedly proven to yield high power conversion efficiencies (PCE) beyond 20%^{40,42}, competing with established thin film PV technologies. This has been achieved by the exceptional ease of tuning of the material's optoelectronic properties and processing upon simple chemical substitution^{31,41,91}. Efforts in the optimization of pure methylammonium lead iodide (MAPbI₃)¹³, by compositional engineering of cations (e.g. the substitution of the methyl ammonium (MA) cation by formamidinium (FA)), and anions (e.g. introducing a small amount of Br), along with the addition of excess lead iodide have indeed induced a breakthrough in device efficiency and reproducibility^{31,70}. Recent developments even include triple cation structures containing cesium, MA and FA⁴³. The higher efficiency compared to single MAPbI₃ perovskite structures has been generically attributed to the improved crystal quality of the film⁴⁰, however, the exact reasons remain under intense debate. Currently, the perovskite community has identified two main problems of perovskite solar cells: stability and

reproducibility. Numerous reports have published detailed procedures for the reproducible fabrication of highly-efficient perovskite solar cells, however it seems that fellow researchers cannot exactly reproduce the results. This is most likely due to this non-homogenous composition of perovskites, which is very much dependent on the exact environment during solution processing. In order to move away from the lengthy optimization via trial and error, there is currently an urgent need in understanding the perovskite composition at the nanoscale.

Previous reports have found that light-induced halide segregation in $\text{MAPbBr}_x\text{I}_{3-x}$ (no FA cation)^{39,92}, iodine migration in MAPbI_3 perovskites⁹³ as well as electric field-induced halide migration⁹⁴ have enormous impact on the device behavior. Nevertheless, a rational investigation of the intrinsic mixed cation/mixed halide $(\text{FAPbI}_3)_{0.85}(\text{MAPbBr}_3)_{0.15}$ perovskite composition is still missing. Important properties such as valence and conduction band positions or the Raman spectrum are missing and the crystal structure is also debated. I believe that part of the disagreement arises from the fact that most reports address bulk properties of the samples, providing average film properties whilst ignoring local information which is of crucial importance in films processed from complicated solution mixtures.

Here, I aim to provide in-depth insight into the local chemical composition and basic spectroscopic properties of high-efficiency mixed perovskite devices by using advanced nanoscale mapping techniques. In particular, I monitor the nanoscale elemental distribution using a novel in-house developed technique called Helium Ion Microscopy-Secondary Ion Mass Spectrometry (HIM-SIMS) and combine the findings with micro-photoluminescence (PL) and micro-Raman mapping in order to link the observed chemical composition, structural and optical properties. Do highly efficient devices processed from mixed perovskite solutions form homogeneously mixed perovskite layers or is there any evidence for a mixture of different perovskite phases?

3.2 Results and Discussion

High-efficient $(\text{FAPbI}_3)_{0.85}(\text{MAPbBr}_3)_{0.15}$ solar cells have been fabricated using a one-step antisolvent approach previously described by Jeon et al.⁴¹ Device current-voltage (I-V) characteristics showing a champion device efficiency of 20.4% and device statistics are plotted in **Figure 3.1**

The current-voltage curves were recorded scanning at 20 mV s^{-1} with 3 seconds light soaking before the scan. The devices show negligible hysteresis upon this medium scan speed Full solar

cells were fabricated alongside the half-devices analyzed in the following sections in order to perform the fundamental characterization on high efficient devices. This guarantees that the measurements were carried out on efficient perovskite layers, thus validating the following results. Batch #1 corresponds to a batch of solar cells fabricated one day before batch #2. Note that the samples used for HIM-SIMS and for the optical measurements deliver as control up to 19.8% PCE. Devices for KPFM measurements have been fabricated following the very exact sample preparation conditions with a controlled solar cell delivering nearly 19% PCE.

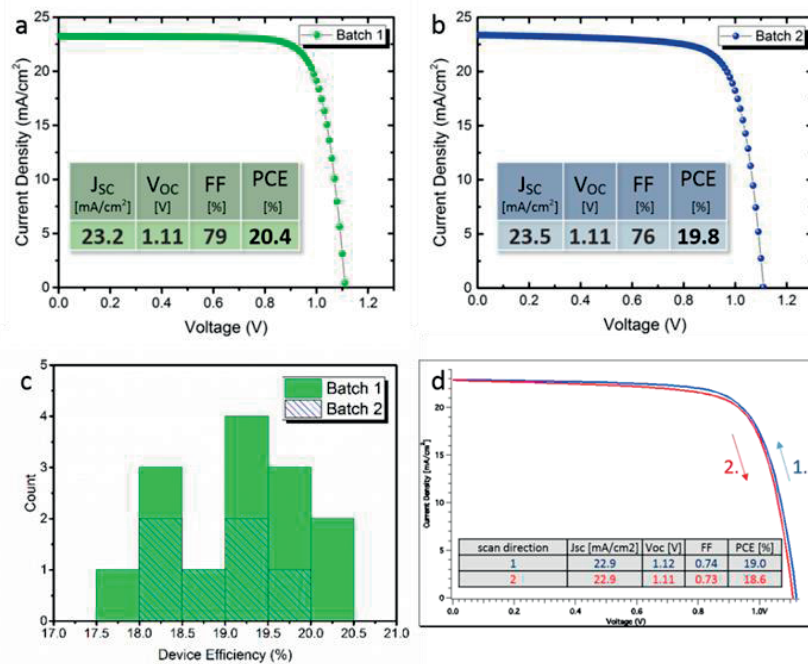


Figure 3.1 Device characteristics. **a.** record solar cell with 20.4% PCE for batch 1 and **b.** 19.8% for batch 2. High device reproducibility is shown in **c.** **d.** Device from **b.** (initially 19.8%) after storage of 2 months (dark and dry air)

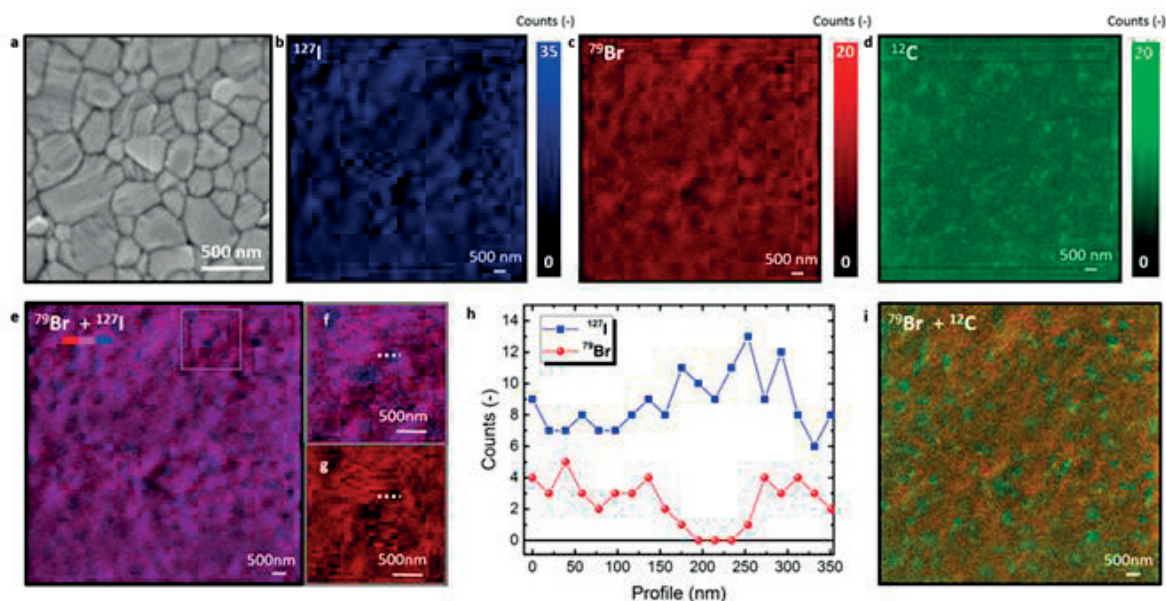


Figure 3.2 Elemental nanoscale HIM-SIMS mapping. **a.** SEM surface image of $(\text{FAPbI}_3)_{0.85}(\text{MAPbBr}_3)_{0.15}$ perovskite deposited on mesoporous TiO_2 scaffold; **b-d.** HIM-SIMS elemental mapping of ^{127}I (blue), ^{79}Br (red) and ^{12}C (green) across a $10 \times 10 \mu\text{m}^2$ area; **e.** Overlap of ^{79}Br (red) and ^{127}I (blue) signals. The “blue” spots have low ^{79}Br signal but high ^{127}I intensities; **f., g.** Zoom into combined ^{79}Br and ^{127}I as well as ^{79}Br alone, respectively; **h.** Profile of the ^{79}Br and ^{127}I signal across the dashed line in panels **f., g.**; **i.** Overlap of ^{79}Br and ^{12}C signals revealing that the carbon hotspots in **d.** correspond to ^{79}Br signal minima.

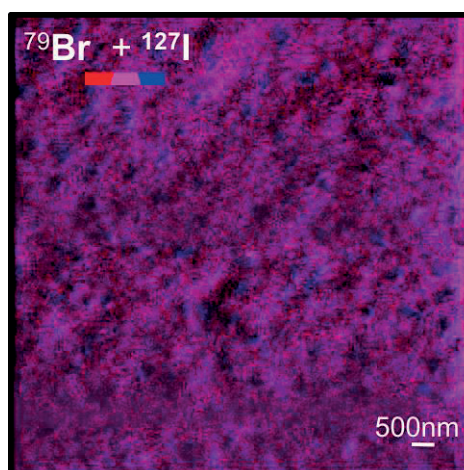
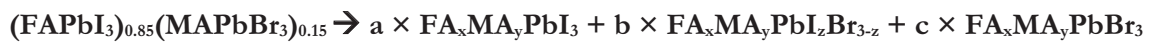


Figure 3.3 Large view of Figure 3.2 e, allowing to clearly identify Iodide-rich nano-domains (blue spots) The measurements presented in this work have been carried out on twin samples fabricated within the same batches as the high efficient devices. **Figure 3.2 a** shows the scanning electron microscope (SEM) image of the top surface of the mixed $(\text{FAPbI}_3)_{0.85}(\text{MAPbBr}_3)_{0.15}$ device consisting

of crystal grains ranging from 100 nm to 500 nm in size. **Figure 3.2 b-d** show the elemental distribution of the ^{127}I , ^{79}Br and ^{12}C isotopes across a $10 \times 10 \mu\text{m}^2$ area of the perovskite surface obtained by the unique HIM-SIMS setup developed in 2015 by Wirtz et al. from the Luxembourg Institute of Science and Technology^{65,68}. Note that the instrument allows for high-sensitivity imaging of surfaces (surface sensitivity is 10-20 nm) with lateral resolution down to 10 nm, a factor 5 enhancement with respect to the best commercially available SIMS instrument (Cameca NanoSIMS 50). Details can be found in a recent book⁶⁷ and in the Introduction Chapter.

By mapping three isotopes, namely ^{127}I , ^{79}Br and ^{12}C , we observe that the ^{79}Br content varies from null/very low to high intensity, indicating compositional non-homogeneity at the nanoscale. In the case of ^{79}Br , several local minima extend to regions up to 300 nm (**Figure 3.2 c**). Local carbon hotspots are clearly revealed (**Figure 3.2 d**), although a background ^{12}C signal is also present due to vacuum contamination. Combining the elemental maps of ^{79}Br and ^{127}I in **Figure 3.2 e** and **Figure 3.3**, a clearer correlation is visible. Most of the regions with null/very low ^{79}Br content correspond to regions with a high amount of ^{127}I (“blue spots”). A zoom into a region containing such a “blue spot” as well as the profile of the ^{79}Br and ^{127}I signals along the dashed white line are shown in **Figure 3.2 f-h**. Although the SIMS technique is not quantitative, it clearly illustrates that ^{127}I counts totally prevail over ^{79}Br counts for at least 100 nm. We exclude that such regions consist of pure PbI_2 , because they mostly correspond to the ^{12}C hotspots. This strongly underlines the presence of FA/MA cations, ruling out the presence of PbI_2 . Since both MA and FA contain one C atom, the variation of the ^{12}C signal can be assigned to the difference of the corresponding SIMS signal obtained from $\text{FA}_x\text{MA}_y\text{PbI}_3$ phase as compared to the one that also contain ^{79}Br . We suggest that the segregation of the $(\text{FAPbI}_3)_{0.85}(\text{MAPbBr}_3)_{0.15}$ results in:



where a, b, and c represent the relative weight of each phases. While b dominates, HIM-SIMS shows that $a \neq 0$. $\text{FA}_x\text{MA}_y\text{PbBr}_3$ is not revealed either because $c \approx 0$ or because those phases segregate below the resolution limit of our measurements. In the first case, for mass conservation, the excess of Br can be contained in the $\text{FA}_x\text{MA}_y\text{PbI}_z\text{Br}_{3-z}$ where z is slightly less than 0.85. Overall the analysis proves the non-homogeneity in the elemental composition of the mixed perovskite surface and indicates that multiple interconnected perovskite phases with different halide content are formed at nanometer scale. In order to determine whether the ^{79}Br and ^{127}I amount varies through the depth of the capping layer, we also performed conventional SIMS depth profiling (without lateral resolution as in HIM-SIMS) of the capping layer. **Figure 3.4** shows the cross-section SEM image of a mixed perovskite device without cathode (turned 90° anti-clockwise) on

top of which the SIMS signals of Pb, Br and I are overlaid. Conventional SIMS with impact energies of the primary ions ranging from a few hundred eV to a few keV provides depth-profile resolution in the range of only a few nanometers, but averaged over the analyzed area, which ranges typically from several hundred μm^2 up to a few mm^2 . The experiments reported here were performed using a Cs^+ primary ion source with a primary current of 10nA and an impact energy of 3 keV while the analyzed area had a diameter of 60 μm . In the perovskite capping layer, all of the three signals are stable. Once the mesoporous/perovskite interface is reached the signals drop significantly. Roughness of the FTO glass makes the data from this layer less meaningful. However, although a slight decrease of the slope for both I and Br signal can be observed, the ratio I/Br or the Pb remains similar across the 550 nm capping layer, showing that crystallization upon a heating step at 100°C for 50 min does not result in a significant halide gradient. Lower impact energies (hundreds of eV) might show slight differences in halide ratio and should therefore be considered for future experiments. This will require the fabrication perovskite films that show very little roughness, which is a challenging task.

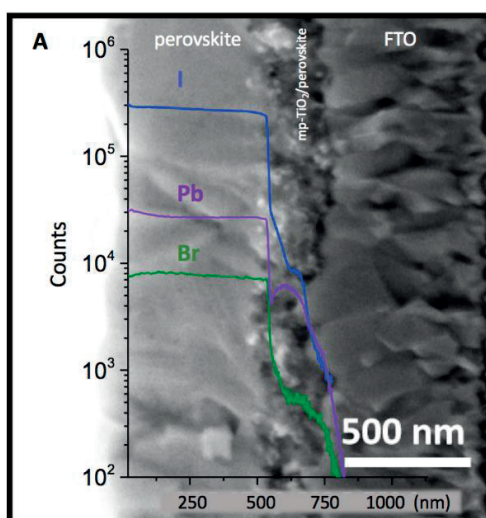


Figure 3.4 SIMS depth-profiling. Superposition of the SIMS depth-profile of a solar cell (without Au electrode) and a cross-sectional SEM image (rotated by 90° anticlockwise). No significant halide gradient (depth) is observed across the capping layer. Note: resolution is in z (depth). The xy signal corresponds to average over a 60 μm spot.

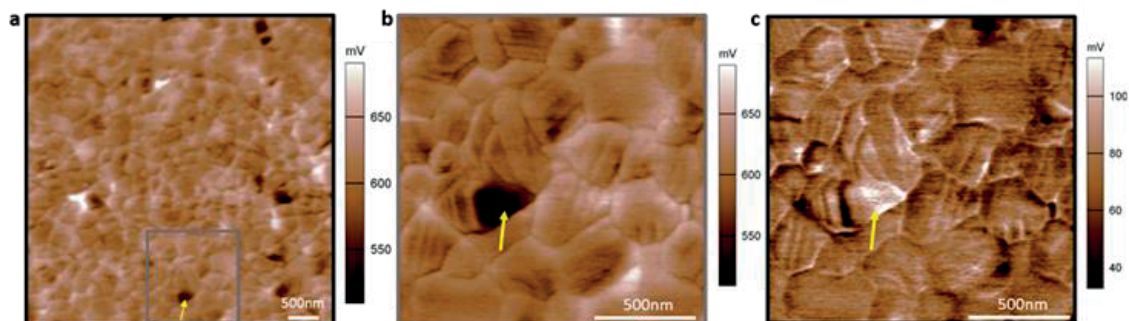


Figure 3.5 KPFM measurements in the dark and under illumination. **a.** $5 \times 5 \mu\text{m}^2$ surface potential map of the capping layer of a mixed perovskite solar cell (no cathode) in the dark; **b.** $1.5 \times 1.5 \mu\text{m}^2$ map of a selected area in Figure 2a (grey box); **c.** Corresponding photo-voltage built-up which links bright regions to dark regions in Fig. 2b, indicating possible hole accumulation.

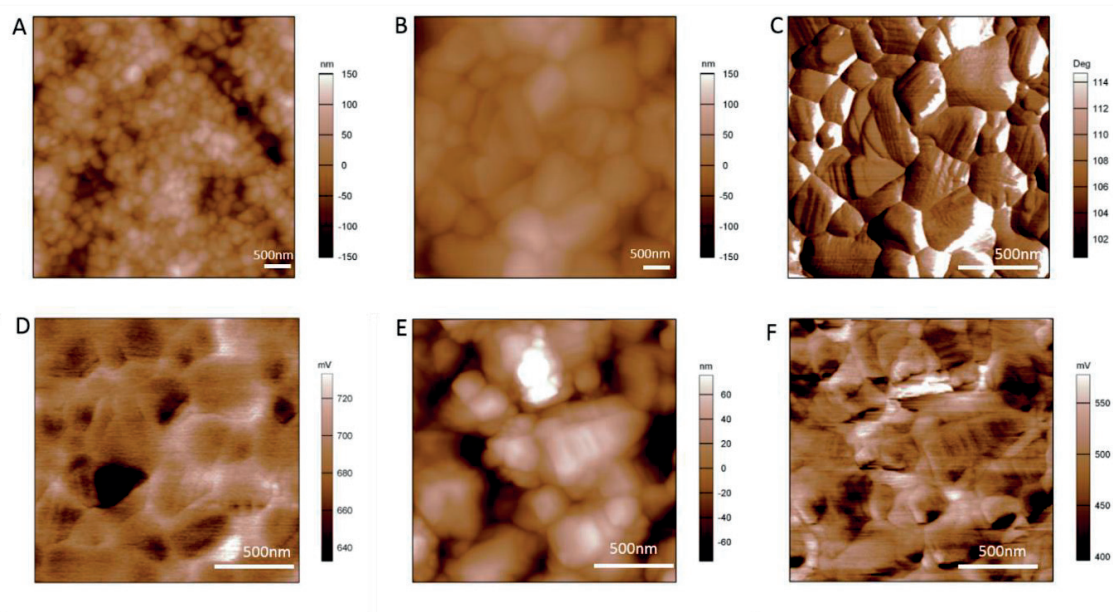


Figure 3.6 AFM and KPFM of mixed perovskite and MAPbI_3 . **a.** AFM height trace of mixed perovskite ($5 \times 5 \mu\text{m}^2$), **b.** AFM height trace of a $1.5 \times 1.5 \mu\text{m}^2$ map (mixed perovskite); **c.** phase of the same $1.5 \times 1.5 \mu\text{m}^2$ map (mixed perovskite); **d.** Surface potential of $1.5 \times 1.5 \mu\text{m}^2$ map (mixed perovskite) under white LED illumination; **e.** height trace ($1.5 \times 1.5 \mu\text{m}^2$ map) of pure MAPbI_3 perovskite; **f.** Surface potential of pure perovskite in the dark.

To confirm the surface non-homogeneity and to investigate the influence of the composition on the charge carrier distribution, we carried out KPFM measurements. **Figure 3.5** shows the results

from the mixed cation/mixed halide perovskite surface (capping layer). A $5 \times 5 \mu\text{m}^2$ KPFM surface potential map of the perovskite capping layer in the dark shows characteristics that can be immediately linked to the grain morphology, see **Figure 3.6 a** and **Figure 3.2 a**. The map shows an average contact potential difference (CPD) of around 600 mV. Interestingly, the map is not homogeneous but we observe the presence of several darker spots, with lower CPD (as the one indicated by the arrow in Fig. **Figure 3.5 a**). Note that a lower CPD value is related to a higher work function and therefore a deeper Fermi level. A $1.5 \times 1.5 \mu\text{m}^2$ map in **Figure 3.5 b** reveals that these lower CPD regions overlap with well-defined crystal grains. In addition, darker stripes on the crystal grain facets also exhibit lower CPD values. In **Figure 3.5 c**, corresponding to the difference of the map under illumination and in the dark, a clear trend is observed: high CPD regions in the dark lead to lower photo-voltage, whereas low CPD areas (such as the dark grain indicated by the arrow) are connected to higher photo-voltage. These findings can be rationalized in the following way: the average CPD value of the mixed perovskite (600 mV) is about 120 mV higher than in the darker spots, where the CPD equals 480 mV. This value exactly matches with the results on the pure MAPbI_3 perovskite surface (see **Figure 3.6 f** for comparison) and indicates the presence of nano-domains constituted of $\text{FA}_x\text{MA}_y\text{PbI}_3$ perovskite phases on the surface of the mixed-anion/mixed-cation perovskite. In agreement, the higher photo-voltage is caused by a slight down-shift in the Fermi level under illumination which could be due to hole accumulation within the I-rich perovskite grain. This correlates with the HIM-SIMS measurements and demonstrates that the segregation of $\text{FA}_x\text{MA}_y\text{PbI}_3$, extending up to about 300 nm, is a fundamental property of the $(\text{FAPbI}_3)_{0.85}(\text{MAPbBr}_3)_{0.15}$ films (excluding the possibility of ion beam induced segregation). It is also worth noting that the chemical composition of the grain might vary with the crystal facet present at the surface, responsible for the local change in CPD. However, this seems unlikely, given that several flat crystals do not exhibit low CPD. Moreover, the possibility that the low CPD grain (higher photo-voltage) is composed of a precursor crystal (e.g. PbI_2) is excluded due to unfavorable band alignment for hole accumulation. Overall, the measurements suggest compositional non-homogeneities across the film at nanometer scale due to *intrinsic* halide segregation. These local non-homogeneities are not usually revealed by standard characterization tools, such as X-Ray Diffraction measurements (XRD), Raman and optical analysis, since they usually interrogate microscopic volumes of the sample⁹⁵. Indeed, from XRD **Figure 3.7**, no clear evidence for any phase segregation in the mixed perovskite layer could be observed. The relatively broad diffraction peaks could however indicate the presence of domains in the perovskite having different phase compositions as the change in the lattice parameters upon small amount of Br substitution is expected to be small.

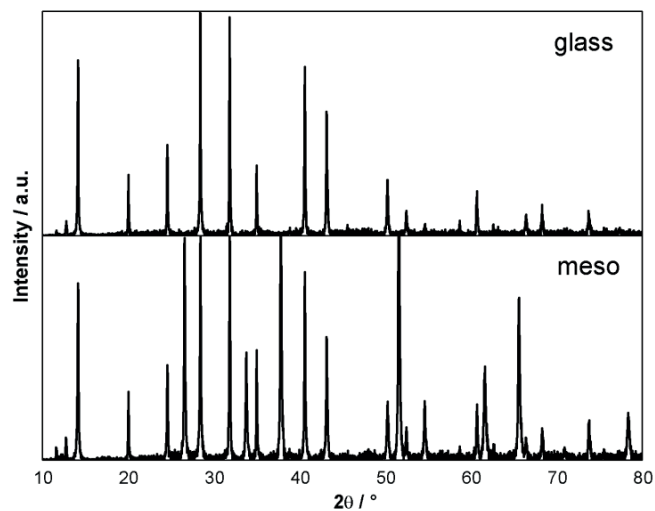


Figure 3.7 XRD pattern of $(\text{FAPbI}_3)_{0.85}(\text{MAPbBr}_3)_{0.15}$

On the other side, combined micro-Raman and micro-Photoluminescence (PL) spectroscopy, although averaged over a diffraction-limited spot size of 300 nm, can provide further information about local heterogeneities⁹⁵. **Figure 3.8 a**, showing the PL peak position map across the film over a $90 \mu\text{m}^2$ area, reveals an optical inhomogeneity. Representative peak position wavelengths at points 1, 2, 3 are plotted in **Figure 3.8 b** along with the pristine MAPbI_3 and FAPbI_3 films.

Within the mixed cation/mixed halide $(\text{FAPbI}_3)_{0.85}(\text{MAPbBr}_3)_{0.15}$ perovskite film, the peak position of points 1-3 shifts from 766 to 775 nm. Although these measurements are averaging over a ~ 300 nm spot, the shift can be related to a variation of the Br content with respect to I ⁹⁶.

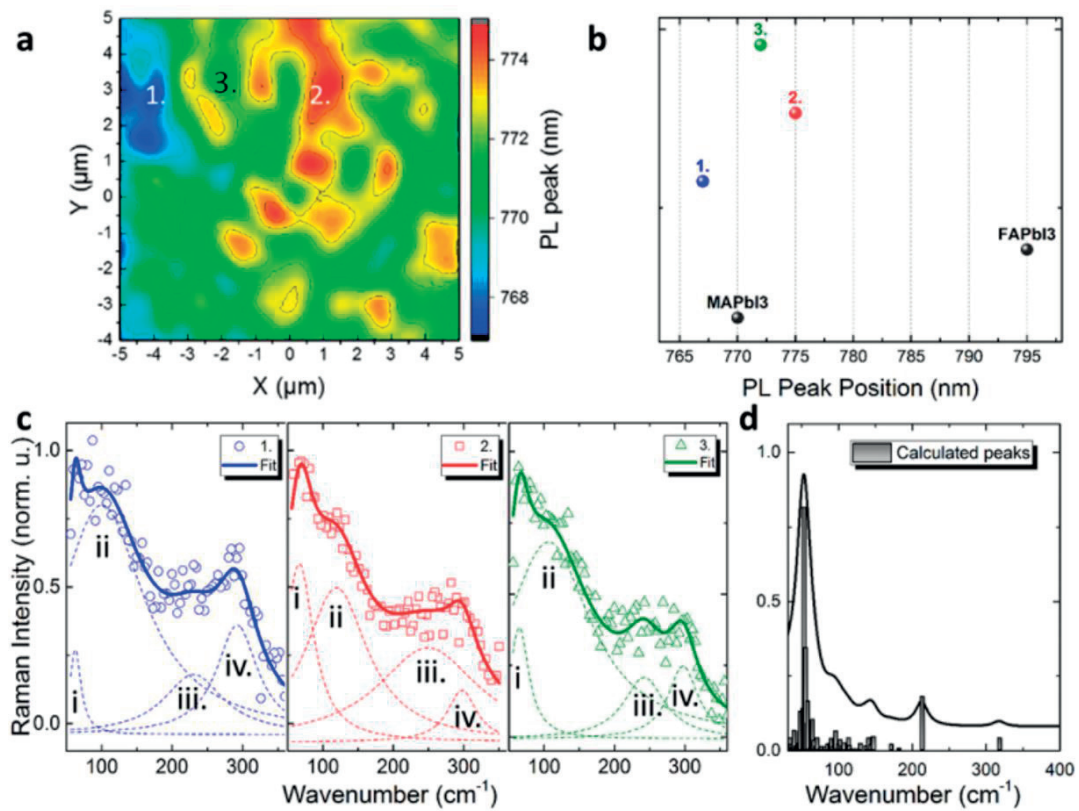


Figure 3.8 Optical and vibrational characterization. **a.** Micro-PL peak shift map of the perovskite surface. Note that re-absorption effects are negligible due to the homogeneity in thickness of the film; **b.** PL peak position of pure MAPbI₃, pure FAPbI₃ compared to selected points referred to as 1, 2 and 3 as indicated in panel a; **c.** micro-Raman spectra at points 1, 2 and 3. Solid line: fitting of the experimental data. The samples are encapsulated to prevent any air/moisture effects; **d** DFT-simulated Raman spectrum of the mixed perovskite.

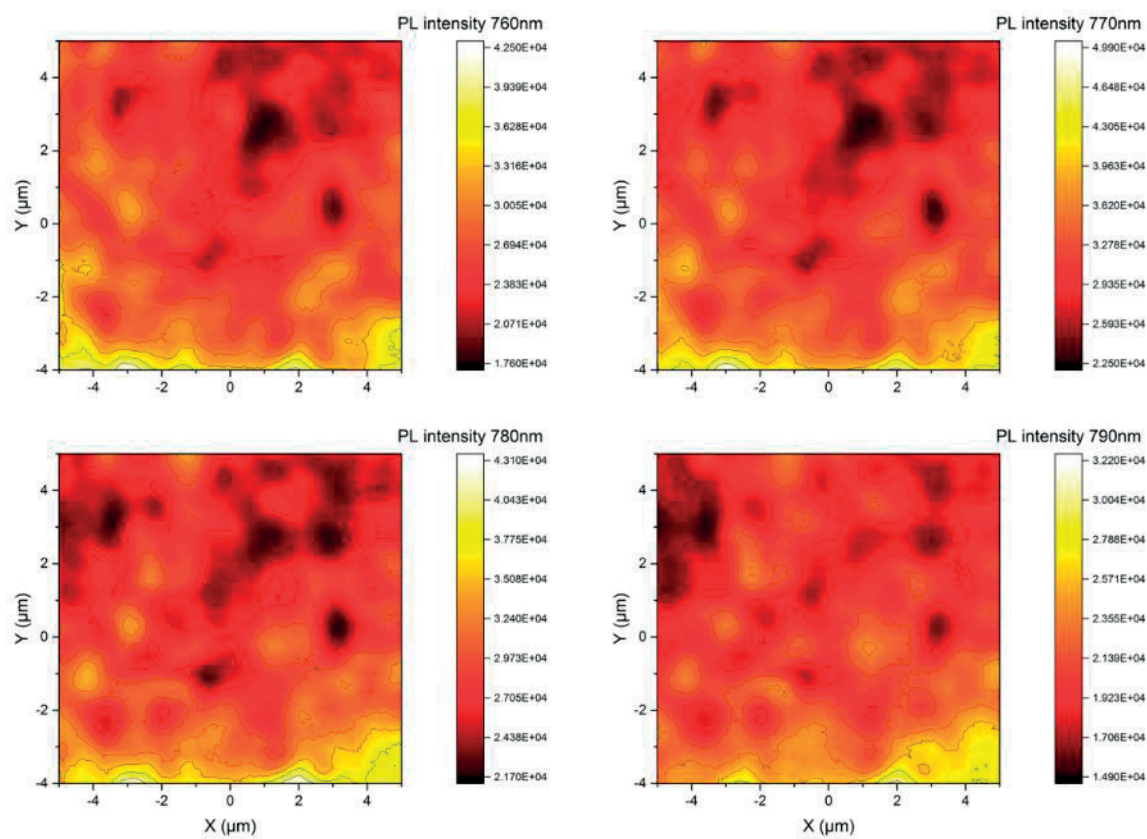


Figure 3.9 PL intensity maps (760nm, 770nm, 780nm, 790nm) corresponding to the PL peak shift map from Figure 3.8a. PL intensity varies by a factor of ~ 2 across the $(\text{FAPbI}_3)_{0.85}(\text{MAPbBr}_3)_{0.15}$ perovskite thin film.

In particular, point 2. (**Figure 3.8a** and **Figure 3.10b**) exhibits a red-shifted emission similar to what is reported for $\text{FA}_y\text{MA}_x\text{PbI}_x\text{Br}_{3-x}$ with a minimal Br content. This further indicates the presence of halide redistribution within the film. As for the PL intensity maps (**Figure 3.9**), plotted at 760 nm, 770 nm, 780 nm and 790 nm, there seems to be no direct correlation between PL peak shift and intensity. However, there are variations in the total PL counts, varying with a factor 2-3. This could be partly explained by local crystallinity variations across the thin film, partly by compositional variations. In any case, it further supports the concept of a non phase pure $(\text{FAPbI}_3)_{0.85}(\text{MAPbBr}_3)_{0.15}$ perovskite film. Since a wide compositional range of halide perovskite phases show strong PL, it is not possible to further discuss phase composition based solely on local PL intensity variations.

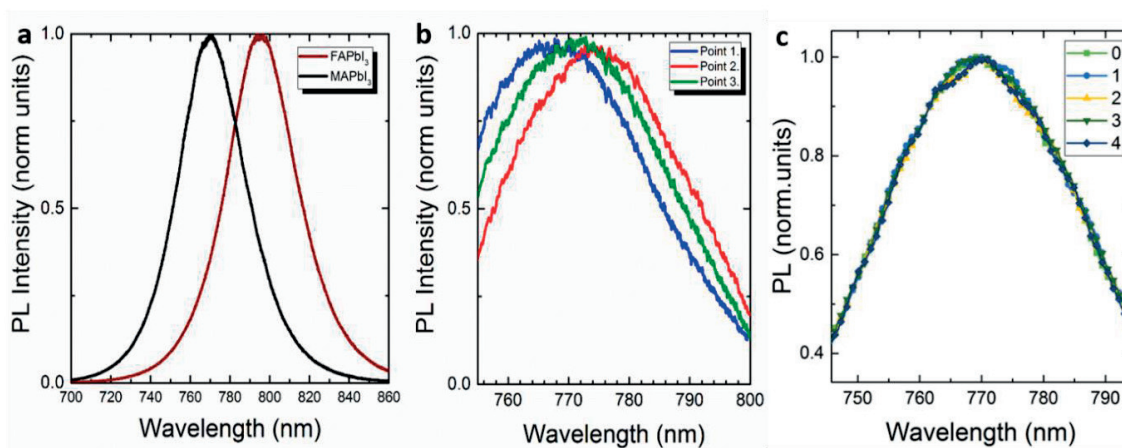


Figure 3.10 **a.** PL spectra of MAPbI₃, FAPbI₃ ; **b.** micro-PL spectra of three relevant spots (Point 1, Point 2, Point 3) from a (FAPbI₃)_{0.85}(MAPbBr₃)_{0.15} perovskite film, corresponding to the PL map from Figure 3.8. **c.** Five (0 to 4) repeated PL spectra of (FAPbI₃)_{0.85}(MAPbBr₃)_{0.15} carried out on the same spot indicating that light-induced halide segregation did not skew the results of the PL map from Figure 3.8

In order to gain more insight into compositional changes across the films, a structural investigation by means of micro-Raman spectroscopy on exactly the same area than the PL map has been carried out. The signal from points 1, 2, 3. (**Figure 3.8 c**) have been collected and, in parallel, we theoretical analysis has been performed to support the modes assignment (**Figure 3.8 d**).

Note that the Raman spectrum of the mixed (FAPbI₃)_{0.85}(MAPbBr₃)_{0.15} perovskite film is here reported and simulated for the first time. The measured and DFT-calculated vibrational modes are listed in **Table 3.1**. Further information regarding the computational setup and geometries are presented in the Annex and in **Figure 3.12**. The Raman spectra of the three points consist of four main peaks (see **Table 3.1**). Similarly to the pristine MAPbI₃ perovskite^{97,80}, peak **i** and **ii** represent a combination of the inorganic stretching and bending along with a minor contribution of the organic cations, while peaks **iii**. and **iv**, a double feature not present in the MAPbI₃ perovskite^{97,80} (see **Figure 3.11**), are related to a combination of FA and MA torsional modes linked together.

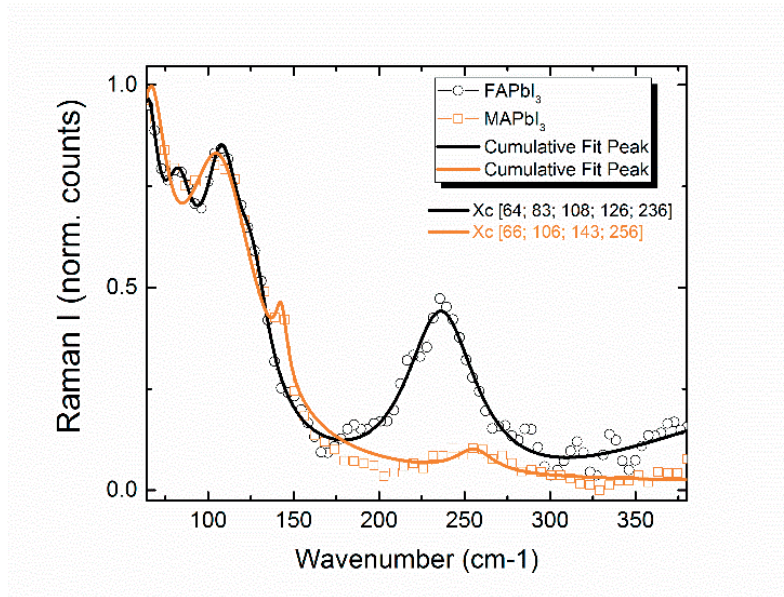


Figure 3.11 Raman spectrum of FAPbI₃ and MAPbI₃.

We thus believe that this characteristic is unique to the mixed structure. The retrieved peak positions closely resemble the calculated Raman spectrum (**Figure 3.8 d**). Comparing the three different points, we first observe that the relative amplitude of peaks **i** and **ii** changes. Peak **ii** dominates in Point 1 and it is broader, while its intensity and broadening are reduced in Point 2. An opposite trend is observed for peaks **iii** and **iv** which are related to FA and MA vibrational modes, respectively. This variation can be induced by the structural inhomogeneity throughout the film. Note also that the slight shift in the mode frequencies can be due to the presence of different halides in the inorganic cage which influence the organic motion through hydrogen bonds^{80,98}. Point 3 features intermediate characteristics between Points 1 and 2. Although this measurement does not aim to be exhaustive, it further supports the structural and compositional inhomogeneity across the film. Such inhomogeneity is responsible for the local PL variation, possibly induced by a locally different perovskite structure or a modified band-gap due to the different halide composition.

Peaks	1.	2.	3.	Calculated	Mode Assignment
i. (cm^{-1})	62	66	65	50	Pb-I / Pb-Br bending and FA/MA libration
ii. (cm^{-1})	100	119	105	100	Pb-I / Pb-Br stretching and FA/MA libration
				150	FA/MA libration
iii. (cm^{-1})	231	249	240	212	FA torsion
iv. (cm^{-1})	292	297	297	317	MA torsion

Table 3.1 Fitted and DFT-calculated peaks (cm^{-1}) associated to the Raman spectra in **Figure 3.8c**.

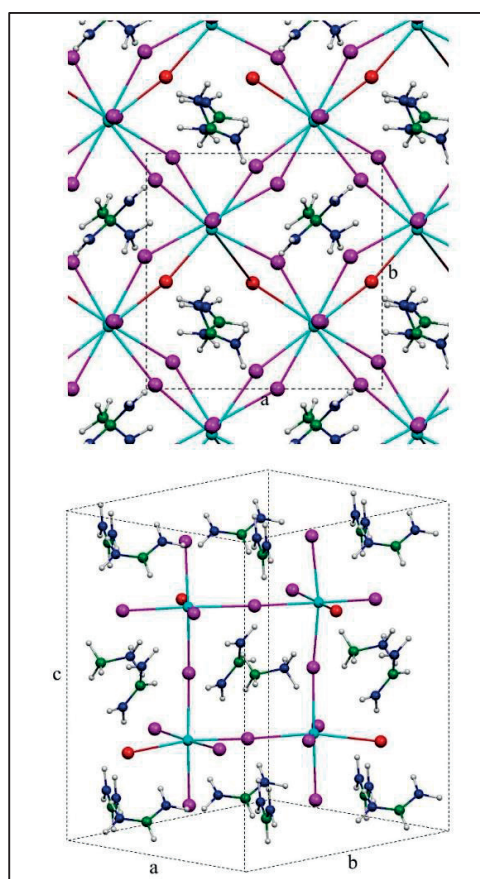


Figure 3.12 Optimized geometry of structure 1 (C in green, N in blue, H in grey, I in purple, Pb in cyan and Br in red). The optimized cell parameters are $a = b = 8.82$ and $c = 12.90$ Å and the calculated band gap is 1.63 eV.

3.3 Conclusion and Perspective

Combining HIM-SIMS, KPFM and micro-PL/Raman measurements, this study provides unprecedented insights into nanoscale properties of high-efficiency mixed cation/mixed halide perovskite solar cells. It is demonstrated that highly efficient perovskite devices are not constituted of a perfectly homogeneous crystalline structure, as a conventional thin film solar cell would require, but, contrary to expectations, a partial nanoscale segregation of multiple perovskite compositions occurs. In particular, $\text{FA}_x\text{MA}_y\text{PbI}_3$ -rich domains within the mixed cation/mixed halide perovskite films extending up to hundreds of nanometers have been identified. It can be envisaged that exploiting the concept of nanometer phase segregation, ultimately leading to a “bulk-heterojunction” perovskite solar cell, will be a potentially successful strategy for a significant advance in perovskite solar cell technology.

These results are highly interesting because it once more underlines the tolerance of perovskite thin films towards non-pure perovskite phases. This is possible because each of the perovskites formed upon halide or cation exchange are photoactive by themselves and possess good solar cell characteristics. A kind of Gaussian distribution of perovskite phases, namely $a \times \text{FA}_x\text{MA}_y\text{PbI}_3 + b \times \text{FA}_x\text{MA}_y\text{PbI}_z\text{Br}_{3-z} + c \times \text{FA}_x\text{MA}_y\text{PbBr}_3$ can be even beneficial since it could allow for fast carrier separation and carrier transport in a similar fashion than what is targeted in organic bulk heterojunction solar cells (provided that coefficients a and c are low compared to b). The previous results could suggest that the appearance of different phases is solely a surface phenomenon. Even if this would be the case, the results are still interesting because the interface between the perovskite layer and the hole extracting material is known to be crucial in order to fabricate solar cell of the highest efficiencies. A third possibility would be that apart from the high point defect tolerance of perovskite films, there is also a large “phase defect” tolerance. However, given the fact that the solar cells reported above approached or even surpassed 20% PCE (champion device), it is more likely that the multiple compositional variations are beneficial for device performance.

The reason for the compositional variation is likely due to the spin coating process itself or due to the temperature gradient and non-homogenous solvent evaporation process upon crystallization of a glass substrate at 100°C. Having nano-phases of slightly different composition within the same film could also be linked to the fact that photogenerated carriers dissociate immediately into free carriers.

Chapter 4 The crystallization process of mixed cation-mixed anion perovskite: discovery and role of 3D hexagonal lead halide perovskites

This chapter is based on work published in ACS Energy Letters⁹⁹. The chapter is an extended version of the submitted publication. The original idea for this publication resulted from discussions between Dr. Zimmermann and myself. I performed most of the experimental work and wrote the manuscript. Rietveld Analysis was carried out by Dr. Schouwink. Single crystal growth and analysis was made by both Dr. Zimmermann and me.

In Chapter 3, I showed that high-performing mixed cation-mixed anion perovskite thin films crystallized from solutions of the record-breaking composition $(\text{FAPbI}_3)_{0.85}(\text{MAPbBr}_3)_{0.15}$ are not phase-pure. Local non-homogeneities in the chemical composition ranging up to hundreds of nanometer as well as optical and structural variations point toward the fact that the exact composition of these complex perovskite thin films is governed by thermodynamics and local instabilities. Indeed, these films are solution-processed and spin-coated, making perfect crystallization highly unlikely. I suggested that the $(\text{FAPbI}_3)_{0.85}(\text{MAPbBr}_3)_{0.15}$ films are actually a distribution of mixed perovskite phases, especially at the capping layer surface, centering on the desired $x = 0.85$ composition. The main phase (for example $> 90\%$ of the total volume of the thin films) would still correspond to exactly $x = 0.85$. In order to gain a deeper understanding of the composition of the final perovskite film, it is of paramount importance to understand the solution-based crystallization process. This understanding has immediate repercussions on fabrication of reproducible and efficient perovskite solar cells.

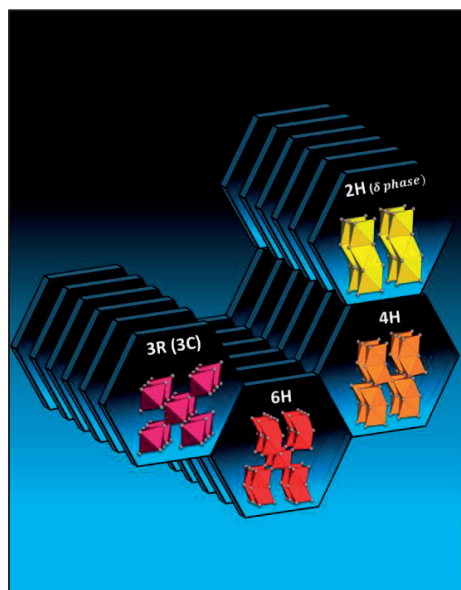


Figure 4.1 Artistic impression of the 2H-4H-6H-3R(3C) crystallization sequence

In Chapter 4, I study the in-situ crystallization process of a variety of perovskite compositions relevant for perovskite solar cells, leading to the discovery of a new class of perovskite polytypes, namely the **first ever reported 3D hexagonal lead-halide polytypes**. These polytypes are found to be ubiquitous in mixed halide perovskites and orchestrate the perovskite crystallization process, which is found to be **2H-4H-6H-3R(3C)**. This sequence is well-known among oxide perovskites. However, as opposed to the oxide perovskite case which requires extreme pressure and temperature conditions, the halide perovskite conversion even partially starts at room temperature and ambient pressure. A full conversion can be achieved within 30 seconds by heating the film at 80-100°C.

This crystallization sequence is greatly influenced by the composition of the perovskite starting solution and can be predicted by mere tolerance factor considerations. Importantly, the discovery of this sequence allows to **understand the role of Cs⁺ cation addition** to (FAPbI₃)_{0.85}(MAPbBr₃)_{0.15} perovskites. In particular, I find that the incorporation of > 3% Cs⁺ into the lattice successfully inhibits the formation of these environmental sensitive polytypes, elucidating the origin of the widely reported improved device stability and reproducibility of Cs⁺ containing mixed ion perovskites.

This study required the design of a controlled atmosphere XRD temperature holder (**Figure 4.2**). Based on an initial holder by Prof. Züttel (EPFL), not suitable for thin films, I designed a holder that can fit up to 2.5 cm x 2.5 cm substrates. The requirement for in-situ experiments on solution-

processed perovskite films is an extremely simple and fast but reliable procedure for the sample enclosure. I came up with a two-piece holder:

- 1) Piece 1: A metal base piece (**Figure 4.2b**) allowing different gas (N_2 , dry air ...) to enter. It fits the motor-controlled stage. The central part consists in a copper plate fixed into a polymer disk (preventing the sample to move and assuring that all the sample are put on exactly the same position)
- 2) Piece 2: A cover ring (**Figure 4.2b**) made from metal and covered with cellophane. This allows the X-rays to go through while making sure that the atmosphere is protected. This ring has a diameter slightly larger than Piece 1 so that one can easily put the sample on the hotplate and place the metal ring within ~ 2 seconds.

The perovskite thin films were spin-coated inside the same Nitrogen glovebox than the one used for making high-efficiency perovskite solar cells. Immediately after spin-coating the film, it was transferred into a small airtight container and transferred within about 30 seconds to the XRD equipment in the basement. This procedure allowed me to make sure that the total time between the films leaving the spin-coater and the start of the measurement never exceeded 50 seconds, thus reliably studying perovskite thin film crystallization (controlled atmosphere + temperature).

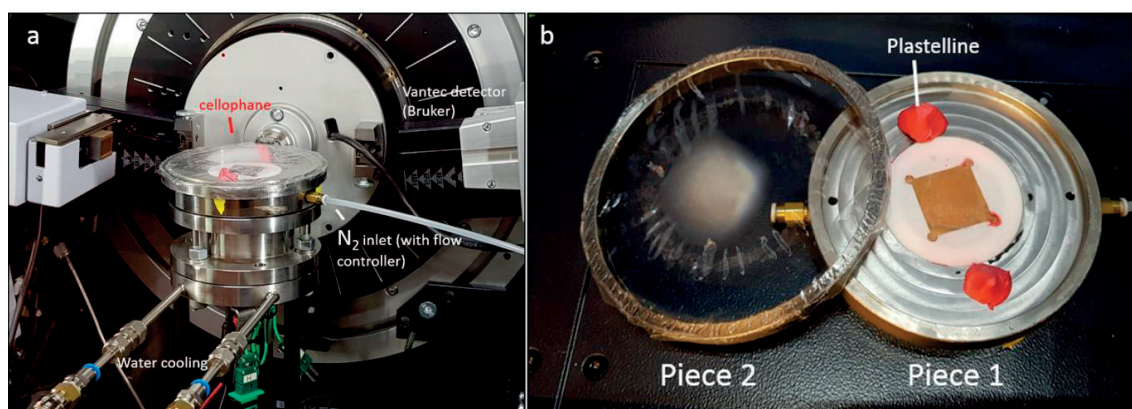


Figure 4.2 a. controlled atmosphere and temperature XRD holder on a motorized one-axis stage (height); b. base piece (Piece 1) + metal ring (Piece 2). Plastelline as well as slight overpressure prevents the cellophane to touch the wet perovskite film.

4.1 Introduction

Compositional engineering by cation and anion substitution has been identified as one of the key aspects in optimizing the optoelectronic properties. Accordingly, some of the best performing devices reported in the literature are based on the solid solution $(\text{FAPbI}_3)_x(\text{MAPbBr}_3)_{1-x}$ or even more complex substitution schemes such as the partial replacement of organic cations by inorganic Cs and Rb cations^{40,45,89}. The understanding and control of the crystallization process of such composite structures from blends of various starting materials are therefore of paramount importance for the fabrication of efficient and reproducible PSCs.

A central issue missing in our knowledge of perovskite films remains the in-depth understanding of the actual phase composition (reaction intermediates) that is involved in the formation of the final perovskite. Competing phase stabilities and shallow minima in the free energy give rise to highly complicated phase equilibria that have not been rigorously investigated. Our limited understanding of these phase stabilities contributes to frequent reproducibility problems regarding device efficiency. Perovskite thin films are spin-coated from a precursor solution prior to various kinds of heating steps. Whereas a growing body of literature has studied the fully crystallized perovskite thin film, previous work has failed to correctly address the nature of the reaction intermediates.

In this work, we report for the first time on the existence of 3D hexagonal polytypes in lead halide perovskites and unravel their role as intermediates during the crystallization process. Single crystal structures obtained from crystals grown by liquid-liquid diffusion of the mixed ion perovskite precursor solution revealed the formation of the as-yet unknown polytypic structures 4H and 6H, which were found to dominate the phase composition in the unannealed perovskite films. The obtained crystal structures allowed a full quantitative characterization of all major phases of the films. Furthermore, in-situ X-ray diffraction experiments carried out to monitor the perovskite crystallization process upon heating revealed that these polytypes play a crucial role as intermediates between the precursor film and the final black perovskite phase. In particular, a specific crystallization pathway, namely 2H-4H-6H-3C is unveiled. So far, such a complex sequence has only been described in transition metal oxide perovskites, at elevated pressures and/or temperatures. We show that the stability of these phases is strongly composition-dependent and that low substitution of Cs^+ cations (3%) successfully inhibits the formation of the hexagonal phases, thus rationalizing the widely reported superior device reproducibility and stability in Cs-containing mixed perovskite solar cells^{43,100,101}

4.2 Results and Discussion

Hexagonal lead halide perovskite polytypes

Polytypism denotes a subset of polymorphism in which the crystalline structure is identical along two dimensions but varies in the third. Accordingly, polytypes of the classical ABX_3 perovskite structure differ in the stacking sequence of the close-packed AX_3 layers. Well known among oxide perovskites, hexagonal polytypes commonly occur in the case of a tolerance factor $t > 1$ (1), which arises due to an increase of the radius of the A cation (r_A) or a decrease of the radius of the B cation (r_B), respectively, X anion (r_X).

$$t = \frac{r_A + r_X}{\sqrt{2}(r_B + r_X)} \quad (1)$$

Whereas perovskites derived from the cubic aristotype Pm-3m adopt a cubic close-packed (c) AX_3 stacking sequence (3C polytype) resulting in BX_6 corner-sharing octahedra (CSO), the hexagonal polytypes are typically composed of a combination of both hexagonal close-packed (h) and c stacking sequences, giving rise to face-sharing BX_6 octahedra. From a fundamental point of view, the vast number of stacking possibilities leads to a plethora of potential new structures with different physical properties related to the octahedral connectivity, notably the band structure. Amongst the lead halide perovskites, only the pure hexagonal close-packed 1D phase (infinite chains of face-sharing PbI_6 octahedra) has been reported up to date and almost exclusively referred to as “delta phase”¹⁰². Here, we report on the discovery and on the seminal role of two 3D polytypes, i.e. 4H and 6H (structure types HT-BaMnO₃ and h-BaTiO₃), which can structurally be derived from the 1D delta phase, but are more complex due to their higher dimensionality (**Figure 4.3**). We also show that $(FAPbI_3)_x(MAPbBr_3)_{1-x}$ does not exclusively crystallize in cubic symmetry (3C)¹⁰³ but also in rhombohedral symmetry, i.e. 3R, when grown under conditions resembling those of film-processing. The terms 4H, 6H, 3R and 3C refer to the well-established Ramsdell notation¹⁰⁴ widely used for describing oxide perovskite polytypes. Consequently, we propose to use the term 2H to refer to the “delta phase” in lead halide perovskites. **Table 4.1** compares the different notations, including the useful h-c notation¹⁰⁵, and the symmetry characterizing these phases, as obtained from single crystal growth.

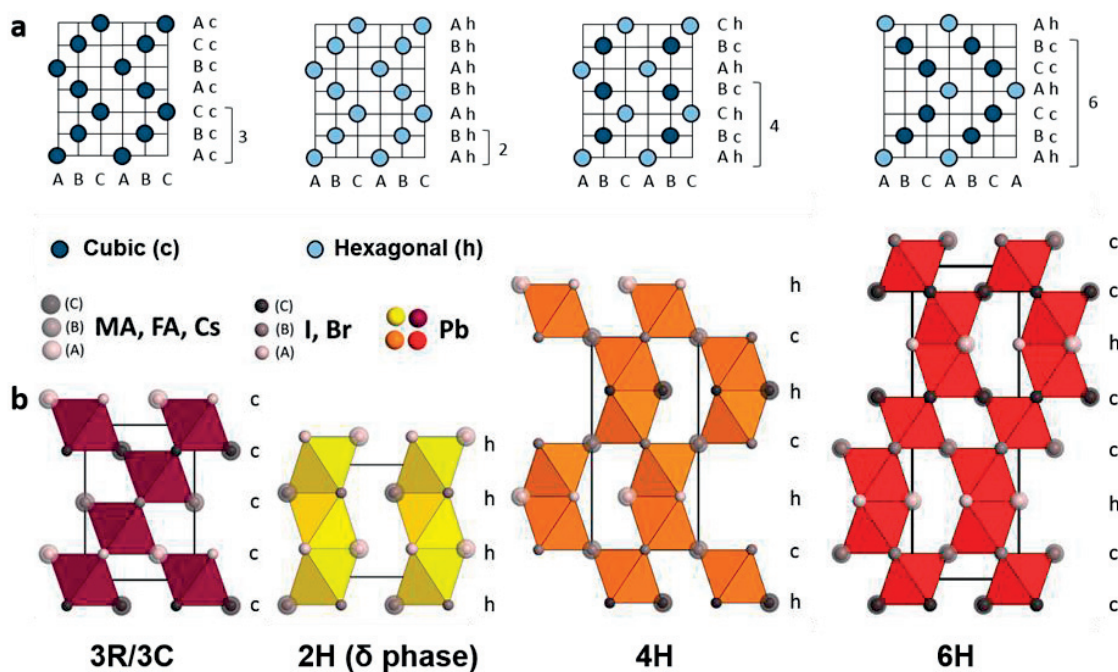


Figure 4.3 Comparison of the AX_3 stacking sequence (h: hexagonal close-packed: light blue circles, c: cubic close-packed: dark blue circles) between three different hexagonal lead halide perovskite polytypes i.e. 2H ('delta phase'), 4H, 6H and the cubic resp. rhombohedral perovskite phases 3C, 3R. **b**, Corresponding representation of the refined single crystal structure viewed along a, showing the different possible arrangements and the connectivity of the PbI_6 octahedra. Face-sharing leads to a 1D array (2H) whereas corner-sharing (3C/3R) or a linear combination of corner- and face-sharing octahedra favors a 3D framework (4H, 6H).

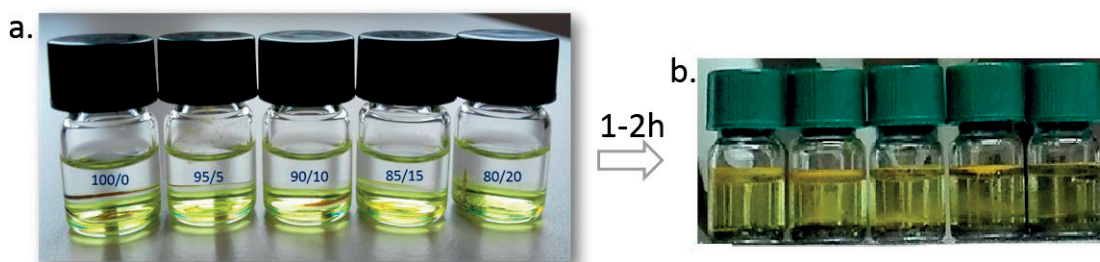
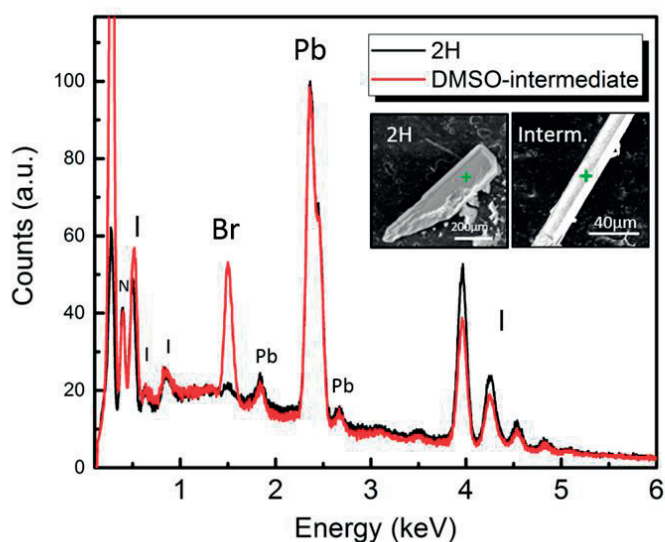


Figure 4.4 a. Single crystal growth by liquid-liquid diffusion. The top phase is Isopropanol; the lower phase consists in exactly the same perovskite precursor solution than the one used for solar cell fabrication. This allows for almost direct comparison between single crystals and thin films; **b.** black single crystal formation in a glovebox for all of the compositions. Waiting several more hours, the black crystals gradually transform into hexagonal crystals in the case of composition $x = 90, 85, 80$.

Single crystals of two novel perovskite polytypes 4H and 6H were obtained by liquid-liquid diffusion (**Figure 4.4**~~Error! Reference source not found.~~~~Error! Reference source not found.~~), a growth method that has not previously been applied to lead halide perovskite, from their corresponding precursor solutions. Different compositions of $(\text{FAPbI}_3)_x(\text{MAPbBr}_3)_{1-x}$, where $0.8 < x < 1$, were used to grow the single crystals. In so doing, black rhombohedral perovskite crystals (3R) were obtained after allowing the solvents to slowly mix for a few hours. Surprisingly, in the case of $(\text{FAPbI}_3)_{90}(\text{MAPbBr}_3)_{10}$, $(\text{FAPbI}_3)_{85}(\text{MAPbBr}_3)_{15}$ and $(\text{FAPbI}_3)_{80}(\text{MAPbBr}_3)_{20}$, continuous heating of the same solution resulted in a gradual transformation of the black crystals into dark red and orange crystals, precisely the 6H and 4H polytypes, along with a small number of 2H crystals. One possible explanation would be that MA cations, which are more soluble in Isopropanol than FA cations, get gradually washed out, thus increasing the tolerance factor which leads to the appearance of hexagonal phases. As opposed to previous crystal growth approaches, to the best of our knowledge, the herein reported method for the first time allows growing single crystals from the exact same precursor solution used for solar cell preparation. We, therefore, expect to find the same structural phases involved in the crystallization process. Despite reproduction of device fabrication conditions, liquid-liquid diffusion yields 3R perovskite crystals of lesser quality compared to other methods. Black crystals grown this way crystallize in a 3-fold supercell of space group symmetry R-3 to the basic Pm-3m unit and are twinned by reticular merohedry. Upon cooling this cell transforms into a larger cell, maintaining its uniaxial symmetry in R-3, this phase transformation can be compared to the Pm-3m – Im-3 transition in the cubic $\text{FA}_{0.85}\text{MA}_{0.15}\text{PbI}_3$ (**Appendix**). We additionally grew crystals by gel diffusion, a method that yields cubic symmetry and no signs of hexagonal polytypes in the solution, in agreement with Xie et al.,¹⁰³ who used inverse temperature crystallization. Since the liquid-liquid diffusion technique is based on the precursor solution, we strongly believe that mixed ion perovskite crystallizes in rhombohedral symmetry in perovskite thin films. This was tested by means of Rietveld refinement on processed films, which remained inconclusive, since the scattering pattern is dominated by the octahedral PbX_3^- a framework which is identical in both space groups. For this reason, we will always use the notation 3C/3R to refer to the black perovskite phase in this paper.

Table 4.1 Comparison of the stacking sequences, different notations and unit cell parameters between the different hexagonal polytypes (2H, 4H, 6H) and the rhombohedral/cubic perovskite (3R, 3C) phases.

<i>Ramsdell notation</i>	<i>ABC sequence</i>	<i>h-c notation</i>	<i>a [Å]</i>	<i>c [Å]</i>	<i>Volume [Å³]</i>	<i>crystal system</i>	<i>space group</i>
2H	AB	h	8.66	7.9	513	hexagonal	P63/mmc
3R	ABC	c	8.85	11.23	761	rhombohedral	R-3
3C	ABC	c	6.31	6.31	251	cubic	Pm-3m
4H	ABCB	hc	8.81	15.2	1023	hexagonal	P63/mmc
6H	ABCACB	hcc	8.84	22.45	1520	hexagonal	P63/mmc

**Figure 4.5** EDX analysis of a 2H single crystal and a DMSO-intermediate single crystal. As opposed to the DMSO-intermediate crystal, the 2H crystal does not contain bromide (the tiny potential peak is assigned to surface contamination of the crystal, which was grown from a solution containing bromide as described above).

Crystal spot #	C	N	Br	I	Pb
1	8.93	2.67	0.55	3.35	1
2	6.33	1.92	0.45	3.41	1
3	6.86	1.64	0.51	2.99	1
4	6.57	2.14	0.46	3.10	1
5	6.50	2.34	0.55	3.50	1
6	5.50	2.03	0.61	2.91	1
Average	6.78	2.12	0.52	3.21	1

Ratio Br/I **0.16**

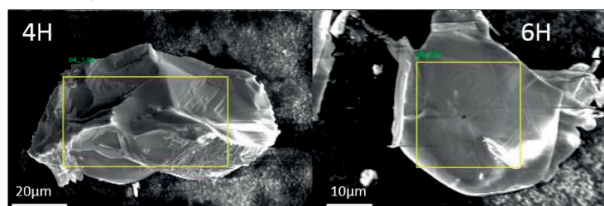


Figure 4.6 EDX analysis of a 6H crystal. 6 different points spots within the yellow rectangle were measured. The average ratio Br/I is about 0.16, in good agreement with the precursor solution where Br/I is 0.15.

Importantly, EDX analysis (**Figure 4.5** and **Figure 4.6**) and single crystal structure refinements reveal the uptake of both I and Br in the 4H and 6H polytypes as well as the DMSO-intermediate. The 2H phase, on the other hand, does not take up any Br, even when it is grown from bromide containing precursor solutions. The ratio of Br/I (**Figure 4.6**) in the 3D hexagonal phases is found to be in good agreement with the Br/I ratio present in the precursor solution, showing that all of the bromide rapidly exchanges with Iodide, favouring cubic stacking over hexagonal stacking. It also suggests that the 6H to 3C/3R conversion probably does not involve any bromide-Iodide exchange reaction. FA-MA exchange possibly explains the 6H to 3C/3R conversion.

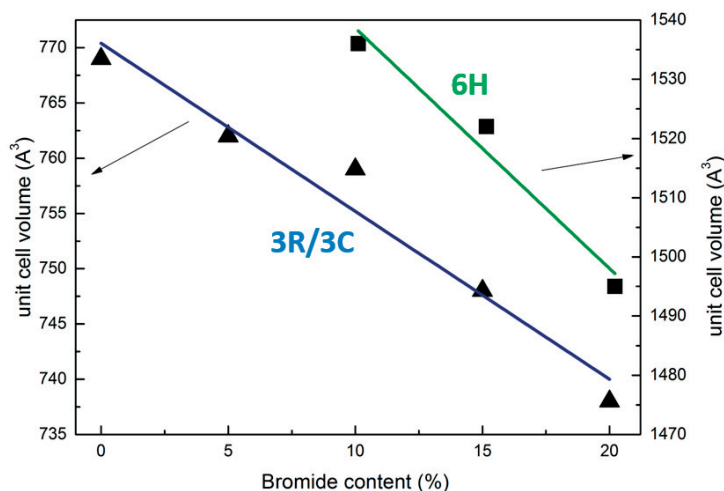


Figure 4.7 Compositional dependency of unit cell volume of crystals grown from precursor solutions in Figure 4.4

The compositional dependency of unit cell volume (**Figure 4.7**) shows that the 6H and 3C structure are mixed ion compositions, confirming the EDX data, as opposed to 2H, which is a pure Iodide phase. This is corroborated by structural data collected on 2H, 4H, 6H and 3C single crystals. In both the 4H and 6H polytypes, the space group symmetry generates 2 crystallographically distinct anion positions related to face- and corner-sharing of octahedra. We note that, in the hexagonal perovskite polytypes 4H and 6H, the heavier iodide anion preferentially occupies the face-sharing position (*see CIF files; this concept will be elaborated in Chapter 5*) The unraveled crystallization sequence must thus be triggered by Br- \leftrightarrow I- exchange in the 2H-phase, which breaks up the face-sharing connectivity of the 2H phase. This initial anion exchange drives the polytypic transformations.

Phase competition in dried out intermediate perovskite films

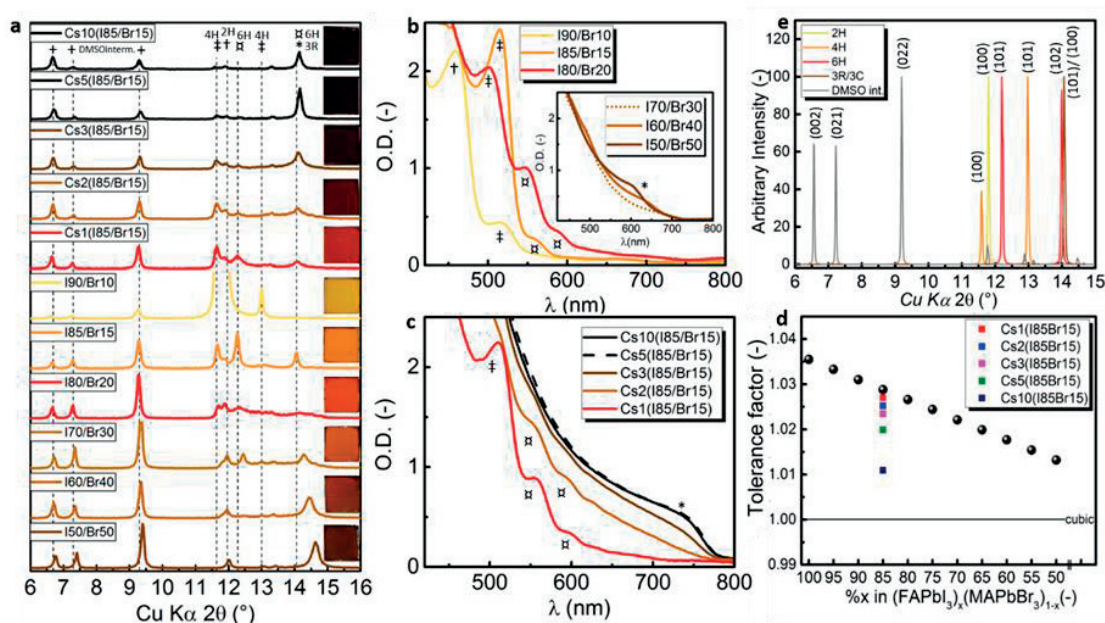


Figure 4.8 a. X-ray diffraction pattern of room-temperature vacuum-dried thin films prepared from perovskite precursor solutions with varying compositions: $(\text{FAPbI}_3)_x(\text{MAPbBr}_3)_{1-x}$ where $0.9 > x > 0.5$ and 1%, 2%, 3%, 5%, 10% CsPbI₃ into $(\text{FAPbI}_3)_{0.85}(\text{MAPbBr}_3)_{0.15}$ (inset = optical photograph of film on 2x2cm FTO substrate) b,c. Corresponding UV-Visible spectra. d. Calculated tolerance factor e. Calculated XRD patterns from single crystal data.

A remarkable feature of halide perovskites lies in the ease of tuning the band gap upon compositional change. However, to date, the phase composition of the as-prepared film before annealing and conversion to perovskite has not been rigorously investigated. **Figure 4.8** shows ex-situ XRD and UV-vis data collected at room-temperature on vacuum-dried thin films (on FTO) cast from different perovskite precursor solutions of nominal composition $(\text{FAPbI}_3)_x(\text{MAPbBr}_3)_{1-x}$, where $0.9 > x > 0.5$ and 1%, 2%, 3%, 5%, 10% CsPbI₃ into $(\text{FAPbI}_3)_{0.85}(\text{MAPbBr}_3)_{0.15}$. In the following, these perovskite compositions are denoted as I85/Br15, I90/Br10, Cs1(I85/Br15), Cs2(I85/Br15) etc.

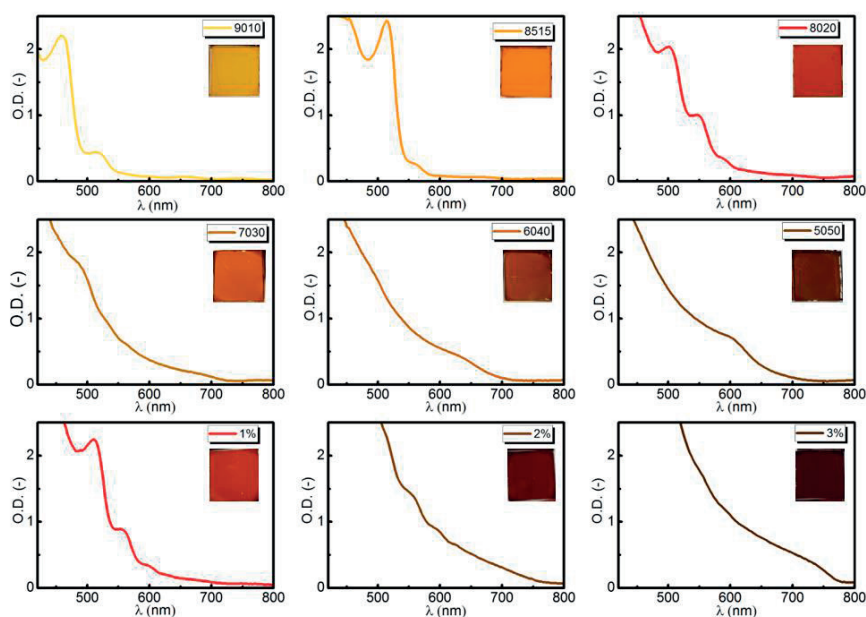


Figure 4.9 Uv-Vis spectra and photograph of corresponding film (inset) of perovskite thin films of different compositions, dried out in vacuum at room temperature. Corresponds to *Figure 4.8b and c*. Tolerance factor variations due to replacement of the I atom by the smaller Br atom or FA by MA or Cs explain the observed changes in color: the lower the tolerance factor, the more cubic stacking is favoured. Pure cubic stacking yields a black perovskite phase, whereas hexagonal stacking yields different phases with different bandgap.

Comparing the calculated XRD peaks of the solved and refined single crystal hexagonal phases reported in the previous section with the experimental powder XRD pattern from the dried out films allows us to identify various hexagonal phases in these intermediate films. Up to date, only the crystal structures of the 2H (δ phase) and the DMSO intermediate have been reported, other Bragg peaks have either been erroneously assigned to PbI_2 (Matsui et al.,⁴⁴) or not assigned at all. Indeed, the polytypic relationship between phases complicates peak assignment due to strong signals either overlapping or coming to lie at very similar scattering angles, rendering it impossible without the knowledge of the actual crystal structures. The characteristic strong Bragg peaks used in the following to monitor phase composition are depicted in **Figure 4.8a**. **Figure 4.8e** shows that the 2H phase can be identified by a peak at 11.8° , whereas strong signals of the 4H are found at 11.6° and 13.0° , the latter being the more intense. Two reflections at 12.2° and 14.0° fingerprint

the 6H phase. Importantly, the peak at 14.0° strongly overlaps with the well-known 3C/3R perovskite peak at 14.1° , and the peak at 12.2° can be readily mistaken for lead iodide (12.8°). As can be seen from **Figure 4.10**, many main peaks but the one at 12.2° overlap with perovskite peaks, making this peak the most suitable peak for identifying the co-existence of 6H and 3R/3C perovskite.

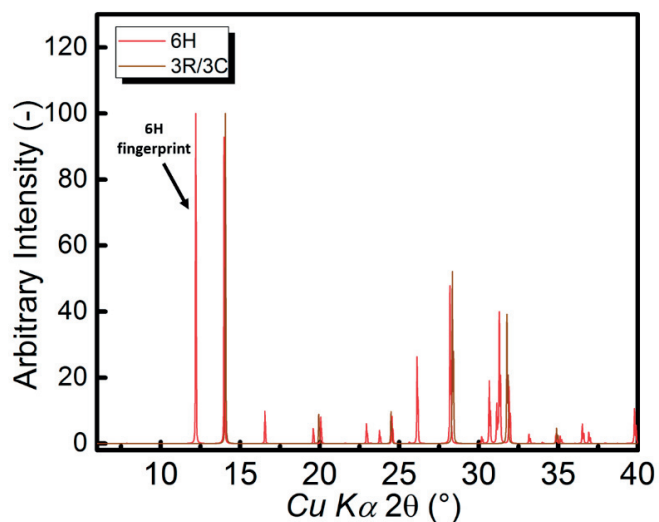


Figure 4.10 Calculated XRD pattern from single crystal of 6H and 3R/3C. The main perovskite peak overlaps with one of the 6H peaks. The peak at 12.2° can be seen as a fingerprint peak of the 6H phase.

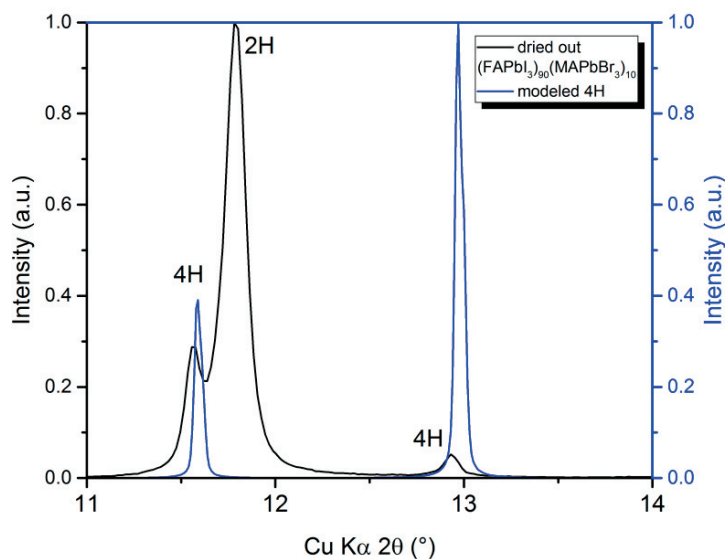


Figure 4.11 Comparison of modelled and measured main 4H XRD peaks. The relative intensity between the characteristic 4H peaks at 11.6° and 13° is inverted for the model $((\text{FAPbI}_3)_{0.85}(\text{MAPbBr}_3)_{0.15})$ and the measured $((\text{FAPbI}_3)_{0.90}(\text{MAPbBr}_3)_{0.10})$ thin film, indicating preferred orientation.

Our experiments reveal that the color of these films (inset of **Figure 4.8a** and **Figure 4.9**), ranging from yellow to black, depends largely on the composition of the precursor solution. Increasing the amount of MAPbBr_3 gradually changes the color of the film from yellow to orange, red and brown. Likewise, adding an increasing percentage of CsPbI_3 to an I85/Br15 solution has a similar effect on the color (ranging from red to black). Interestingly, both the room-temperature dried-out Cs1(I80/Br20) and the I80/Br20 film appear red, indicating similarities in phase composition supported by the very similar UV-Vis spectra (**Figure 4.8b** and **Figure 4.8c** as well as **Figure 4.9**). Whereas I90/Br10, I85/Br15 and I20/Br20 show multiple peaks between 450 nm and 600 nm that can be attributed to the non-perovskite hexagonal phases, I70/Br30, I60/Br40, I50/Br50 (**Figure 4.8** and **Figure 4.9**) show perovskite-like absorption spectra with varying onsets, in agreement with the $\text{FAPbI}_3/\text{MAPbBr}_3$ ratio (blue-shift with increasing percentage of MAPbBr_3). Incorporating 5% cesium into the lattice, i.e. Cs5(I85/Br15) generates the black perovskite phase, in agreement with the results from Matsui et al⁴⁴. We find that lower amounts of cesium, i.e. Cs1(I85/Br15) and Cs2(I85/Br15) still show non-perovskite absorption bands and determine the single-phase formation threshold to be the composition Cs3(I85/Br15).

While all compositions contain both the DMSO intermediate (reflections at 6.6° , 7.2° and 9.2°) and the 2H phase (11.8°), there are large discrepancies in the relative phase yields of the 3D hexagonal phases 4H and 6H. While the composition (I₉₅/Br₀₅) contains mainly the 2H phase (**Figure 4.12**), upon adding 10% MAPbBr₃ (I₉₀/Br₁₀), the hexagonal 4H polytype (11.6° and 13.0°) appears, again suggesting that bromide is a stabilizing ingredient to generate polytypism. Discrepancies between the calculated and experimental peak intensities (within thin films, the 4H peak at 13° is much less intense than the one at 11.6° , see **Figure 4.11**) may be attributed to preferred orientation, known to occur in perovskite films. This explains why the 4H peak at 13° only occurs in I₉₀/Br₁₀. The 6H phase (12.2°) dominates over the 4H phase in both the I₈₅/Br₁₅ and I₈₀/Br₂₀ films, as supported by UV-vis. It is noted that for the composition I₈₀/Br₂₀ the hexagonal phases are much less crystalline which can be seen from the low peak intensity and broad peak shape in the region of 11.5° - 12.5° . Increasing the bromide perovskite content further to I₇₀/Br₃₀ or higher results in the decrease of hexagonal phases and appearance of perovskite. Remarkably, we found that the addition of Cs to the precursor solution showed a similar effect. Doping the precursor solution with 3% Cs was sufficient to completely suppress the formation of any hexagonal phases. Furthermore, based on the 2θ dependence of Bragg signals, we can exclude Br-uptake by the 2H phase, whose characteristic Bragg peak does not shift upon varying bromide content, indicating a pure FAPbI₃ phase. At the same time, the peak used to monitor the intermediate phase does shift with composition changes, suggesting that Br (and MA) can be incorporated into the crystal structure. This supports the findings from EDX analysis on 2H and DMSO-intermediate single crystal in the previous section.

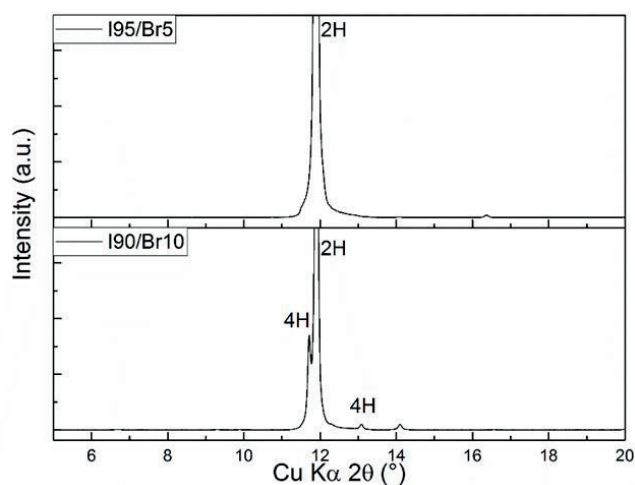


Figure 4.12 Comparison between dried out (FAPbI₃)_{0.95}(MAPbBr₃)_{0.05} and (FAPbI₃)_{0.90}(MAPbBr₃)_{0.10} perovskite thin films. No 3D hexagonal phases form upon drying out (FAPbI₃)_{0.95}(MAPbBr₃)_{0.05}. The

threshold for 3D hexagonal lead halide perovskite phases of mixed anion/mixed cation phases thus lies between $(\text{FAPbI}_3)_{0.90}(\text{MAPbBr}_3)_{0.10}$ and $(\text{FAPbI}_3)_{0.95}(\text{MAPbBr}_3)_{0.05}$, corroborating with the previous results that single crystals grown from $(\text{FAPbI}_3)_{0.95}(\text{MAPbBr}_3)_{0.05}$ do not transform into hexagonal red/orange 6H/4H crystals.

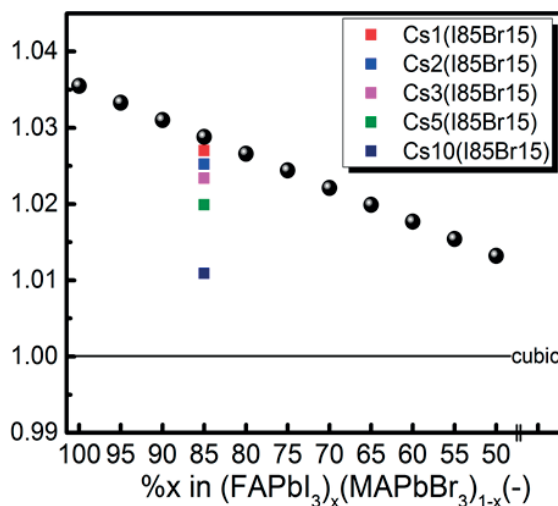


Figure 4.13 tolerance factor calculation of the analysed perovskite compositions. The ionic radii are taken from updated values and calculated according to the formula explained below. Relative values are important here: Both the relative increase of MAPbBr_3 or Cs^+ lowers the tolerance factor, favouring cubic over hexagonal stacking.

Our findings can be rationalized on the basis of tolerance factor considerations. **Figure 4.8d** and **Figure 4.13** show the behavior of the tolerance factor, calculated using re-visited values from Travis et al.,¹⁰⁶ and following a simple approximation described in the Methods section, as a function of composition. Tolerance factors close to 1 are approached upon increasing the amount of MAPbBr_3 , thus stabilizing the black 3R/3C perovskite phase. $\text{I}_{60}/\text{Br}_{40}$ and $\text{I}_{50}/\text{Br}_{50}$ completely suppress the formation of the 6H phase.

Similarly, the addition of CsPbI_3 into $\text{I}_{85}/\text{Br}_{15}$ reduces the tolerance factor, thus also allowing the stabilization of the black 3R/3C perovskite phase. It is noted that cesium incorporation seems to be more effective in stabilizing the perovskite phase than predicted by mere geometrical tolerance factor calculations.

The color of the hexagonal phases can be explained by band gap variations depending on the connectivity of the PbI_6 octahedra. This is in analogy with a recent report by Kamminga et al.¹⁰⁷ who showed that increasing the connectivity from corner-, via edge-, to face-sharing results in an increase in the band gap (based on DFT calculations on bybenzylammonium lead iodide).

In-situ X-ray diffraction of solution-processed perovskite films

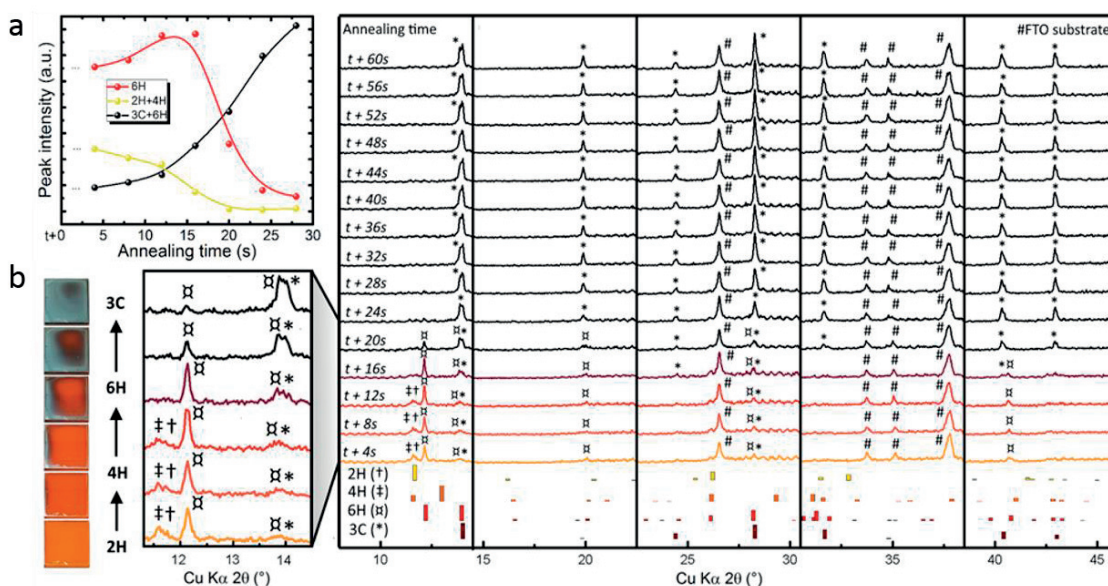


Figure 4.14 In-situ X-ray diffraction experiment monitoring the perovskite film formation on FTO substrates during the annealing process at 100° . The scans were recorded with an interval of 4s and a detector opening of 8 degrees. Scans from several individual experiments were combined to obtain an extended 2θ range, separated by vertical lines. **a** evolution of the different perovskite polytypes during the crystallization process from the peak intensities. **b** Photographs showing the color change during the heating process (left). Close up on the 2θ range in between 13.5° and 14.5° (right). The consecutive sequence of 2H transferring into 6H and finally into 3R can be observed from the peak evolution. **c** X-ray diffraction patterns of the in-situ experiment over an extended range of 6.5° to 46° . Diffraction lines calculated from the single crystal data are shown in the bottom.

To investigate the role of the discovered hexagonal perovskites during the crystallization process at 100°C , in-situ XRD diffraction experiments were carried out on the freshly spin-coated films. **Figure 4.14** illustrates the in-situ perovskite conversion of a thin film having a composition of $\text{I}_{85}/\text{Br}_{15}$ at 100°C under a nitrogen atmosphere, recorded using a pseudo-2D detector (Vantec-1) with an opening of 8° and the necessary time resolution of several seconds. Measurements on several individual samples were combined to obtain the 2θ range from 8° to 46° separated vertically by black lines. Time t , typically about 10 seconds, corresponds to the time between placing the sample on the hotplate, closing the enclosure of the diffractometer and the actual start of the measurement. The exact procedure can be found in the beginning of the chapter and in the annexe section.

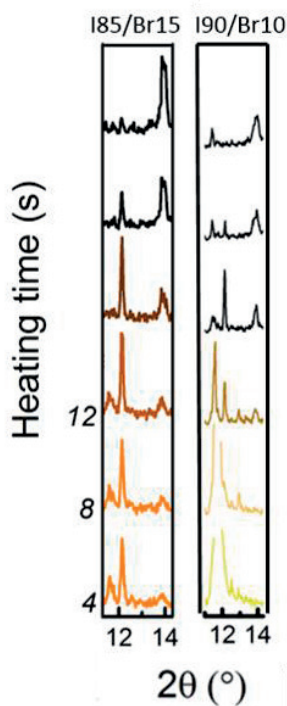


Figure 4.15 Comparison of the crystallization sequence between $(\text{FAPbI}_3)_{0.85}(\text{MAPbBr}_3)_{0.15}$ and $(\text{FAPbI}_3)_{0.90}(\text{MAPbBr}_3)_{0.10}$ perovskite thin films. Both cases show a $2\text{H} \rightarrow 4\text{H} \rightarrow 6\text{H} \rightarrow 3\text{C}$ crystallization sequence. $(\text{FAPbI}_3)_{0.85}(\text{MAPbBr}_3)_{0.15}$ favours a ratio of cubic/hexagonal stacking that is greater than in the case of $(\text{FAPbI}_3)_{0.90}(\text{MAPbBr}_3)_{0.10}$, therefore not clearly showing the 2H phase. $(\text{FAPbI}_3)_{0.90}(\text{MAPbBr}_3)_{0.10}$ has all the phases (11.8° : 2H; 13° :4H; 12.2° :6H; 14° : 3C/3R), providing **hard proof** for the $2\text{H} \rightarrow 4\text{H} \rightarrow 6\text{H} \rightarrow 3\text{C}/3\text{R}$ crystallization sequence

Characteristic strong Bragg peaks of each phase were determined to monitor the phase composition. Calculated diffraction patterns from the single crystal structure determination reveal that the most intense peaks of the different perovskite structures are found in the region between 8° and 14.5° . Peaks at 11.6° (4H), 11.8° (2H), $12.2^\circ/14.0^\circ$ (6H) and 14.1° (3R/3C) fingerprint the hexagonal phases as well as the black photoactive perovskite during the annealing procedure. Intensities of these signals are displayed as a function of annealing time in **Figure 4.14a**. Photographs of the perovskite films during the annealing process as well as a close up on the diffraction pattern from 8° to 14.5° are shown in **Figure 4.14b** and **Figure 4.15**. The evolution of the peak intensities allows for qualitative phase analysis (**Figure 4.14a**). The amount of the 2H and 4H phase (peaks 11.8° and 11.6° overlapping) rapidly decreases upon heating, while the 6H perovskite first increases before transforming to the 3C/3R, manifested as opposite trends in signal intensity. From these observations we suggest that the crystallization sequence most likely follows $2\text{H} \rightarrow 4\text{H} \rightarrow 6\text{H} \rightarrow 3\text{R}/3\text{C}$, in agreement with the sequence found at elevated pressures and/or temperatures in inorganic transition metal oxide perovskites. We hypothesize that heating a thin lead halide perovskite film leads to internal pressure variations due to bromide (smaller ionic radius)-Iodide (larger ionic radius) exchange.

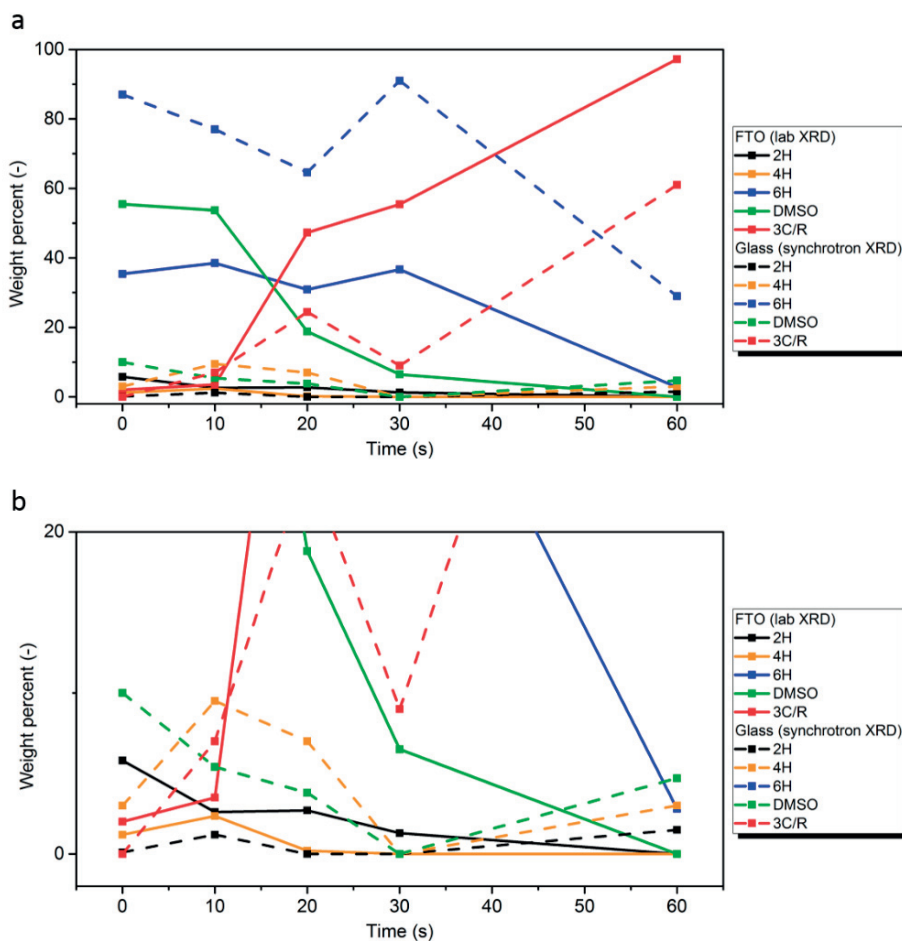


Figure 4.16 Quantitative phase analysis of $(\text{FAPbI}_3)_{0.85}(\text{MAPbBr}_3)_{0.15}$ perovskite crystallization in good agreement with qualitative phase analysis from the above in-situ XRD experiments. **a.** good agreement between synchrotron transmission experiments (perovskite scrapped from several glass substrates heated during time t .) and thin film XRD experiments (on FTO glass) carried out in Bragg-Brentano geometry. **b.** zoom into 0-20 wt% region.

To support our qualitative phase analysis carried out in-situ, we performed quantitative analysis ex-situ. In a first step, films of different composition, dried out at different heating times and scrapped off a certain number of glass substrates, were measured in Deybe-Scherrer geometry using synchrotron radiation, as transmission measurements were not possible in our labs due to the significant X-ray absorption by the material. The transmission data allowed us to quantify phase yields with Rietveld refinement using our single crystal structural models as input, since texture effects and preferred orientation, ubiquitous in deposited thin films, are minimized in transmission. The refinements on synchrotron data were then used as input models to quantify films of

the same composition in Bragg Brentano standard measurements, carried out on our lab diffractometers. Given the accurate input models obtained in transmission, it was then possible to apply intensity corrections due to preferred orientation, where necessary. Rietveld plots and phase composition for times 0 sec, 10 sec, 20 sec, 30 sec and 60 sec are shown in (**Appendix and Figure 4.16**) for a film composition of I₈₅/Br₁₅. To our knowledge, this is the first time that these films, complex both in terms of composition as well as microstructure, have successfully been refined with the Rietveld method. The quantitative phase analysis is in good agreement with the qualitative in-situ XRD data described in the previous section. The main difference is the presence of the DMSO-intermediate phase, as already discussed above, which only forms when drying out the film (incomplete crystallization). This is clearly proven by the decrease of the weight % of this phase with prolonged heating times. As soon as the 2H→4H→6H→3C/3R sequence is overcome after about 30seconds at 100°C, no DMSO-intermediate phase can be observed in the dried out films. This phase does not play an active role in the real in-situ crystallization of perovskite thin films, as will be explained below.

In order to understand the role of the DMSO-intermediate phase, which is only showing up in vacuum-dried films but not during the in-situ experiments, we vacuum-dried two perovskite films (I₈₅/Br₁₅) to allow for DMSO-intermediate crystallization. Subsequently, the two films were heated at 100°C resp. 150°C during 30min. Heating up to 100°C results in the disappearance of the DMSO-intermediate phase (no reflections at 6.6°, 7.2° and 9.2°) but the 6H phase largely remains within the film (the color of the film is dark-red). This is in contrast with heating up to 150°C, which results in the disappearance of the 6H phase diffraction peak, forming black perovskite (3C/3R) as well a large amount of PbI₂, characterized by the strong reflection at 12.8° (**Figure 4.17**) These data suggest that solid-state conversion takes place at temperatures >150°C, but at the expense of film degradation.

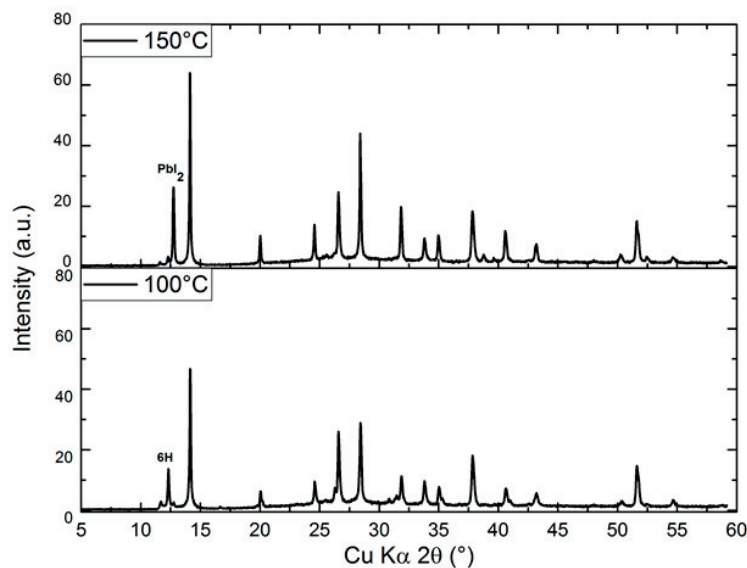


Figure 4.17 XRD pattern of two substrates of room temperature vacuum-dried $(\text{FAPbI}_3)_{0.85}(\text{MAPbBr}_3)_{0.15}$ perovskite thin films subsequently (after drying out) heated at 100°C resp. 150°C . The 6H phase remains at 100°C while at 150°C the 6H phase disappeared to partially form 3C/3R perovskite, however at the expense of clear film degradation revealed by the strong PbI_2 reflection (12.8°). The DMSO-intermediate phase (no reflections at 6.6° , 7.2° and 9.2°) disappears in both cases.

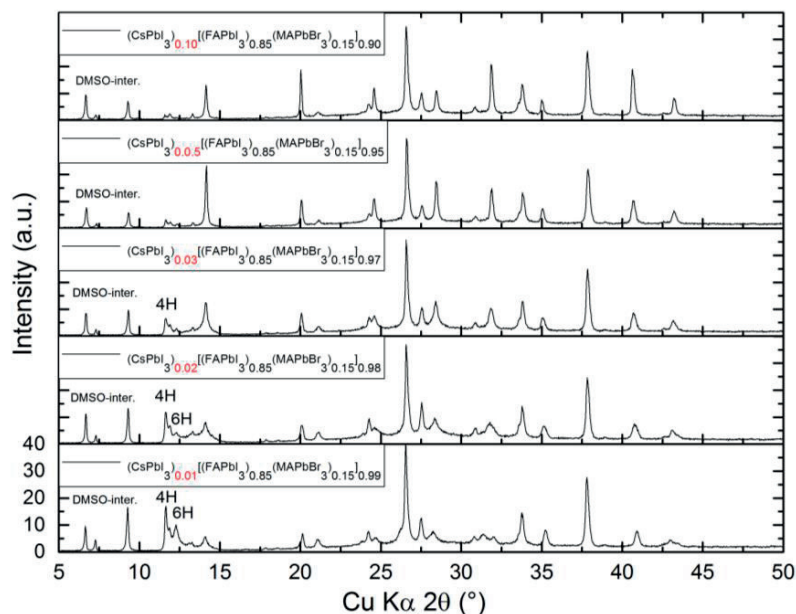


Figure 4.18 Powder XRD diffraction pattern of cesium containing triple cation perovskite thin films that were dried out at room-temperature. The data confirm that the threshold amount of Cs% necessary to induce 3D hexagonal perovskite formation is about ~ 3 mol%. The DMSO-intermediate phase forms independently of the composition.

The compositional influence on the in-situ phase competition was explored by repeating analogous experiments with different perovskite compositions (

Figure 4.19a). As shown for the dried-out films (**Figure 4.14**), the composition is crucial in stabilizing the different perovskite polytypes. Interestingly, for composition I_{90}/Br_{10} and I_{80}/Br_{20} , the hexagonal perovskite polytypes do not completely disintegrate after the heating process at $100^{\circ}C$, as opposed to I_{85}/Br_{15} (**Figure 4.14**). It is known that the tolerance factor can be controlled by substituting Cs^{+} for the organic cation^{43,108}. In-situ crystallization experiments were thus carried out and the diffraction data show Bragg peaks corresponding to the 6H and the 2H/4H phases upon doping of Cs1% (

Figure 4.19a). Increasing the amount of Cs^{+} to 2% reduces the yields of 2H/4H and 6H to minor impurities. Finally, the absence of peaks at 11.8° and 12.2° upon 3% cesium incorporation into I_{85}/Br_{15} (=Cs3%) is indicative of any hexagonal phase formation, thus corroborating the conclusions drawn above, namely that Cs3% represents a threshold composition. Interestingly, Cs3% also shows the most intense perovskite peak at 14° among the different cesium compositions. The crystallization scheme of mixed ion perovskite can be rationalized as follows (**Figure 4.19b**). At $100^{\circ}C$, a Br^{-} containing precursor matrix diffuses, in the presence of DMF/DMSO, into the 2H phase (pure Iodide phase), leading to a Br-I exchange reaction producing the 3D hexagonal iodide/bromide containing polytype 4H. Subsequently, 4H gradually transforms into 6H and 3R/3C via continuous exchange reactions. Whether the MA/FA exchange already takes place between 2H and 4H (unlikely since it requires *concerted* I/Br and MA/FA), 4H and 6H or only later between 6H and 3C/3R remains an open question at this stage. It is conceivable that *continuous* MA/FA exchange reactions drive the crystallization sequence. Both bromide for iodide replacement and MA for FA replacement will lower the tolerance factor, thus stabilizing cubic AX_3 stacking over hexagonal stacking. These questions will be further addressed in the next Chapter. At room temperature, competition between DMSO-intermediate crystallization (“bromide-capturing sink”) and bromide uptake from 2H takes place. Upon crystallization of the DMSO-intermediate, elevated temperatures ($T > 150^{\circ}C$) are required to proceed to solid-state exchange reactions that convert the hexagonal phases further to 3C/3R. These temperatures are close to the thermal stability of black perovskite in the film, which results in film degradation, manifested by the appearance and increasing phase fraction of PbI_2 (**Figure 4.17**).

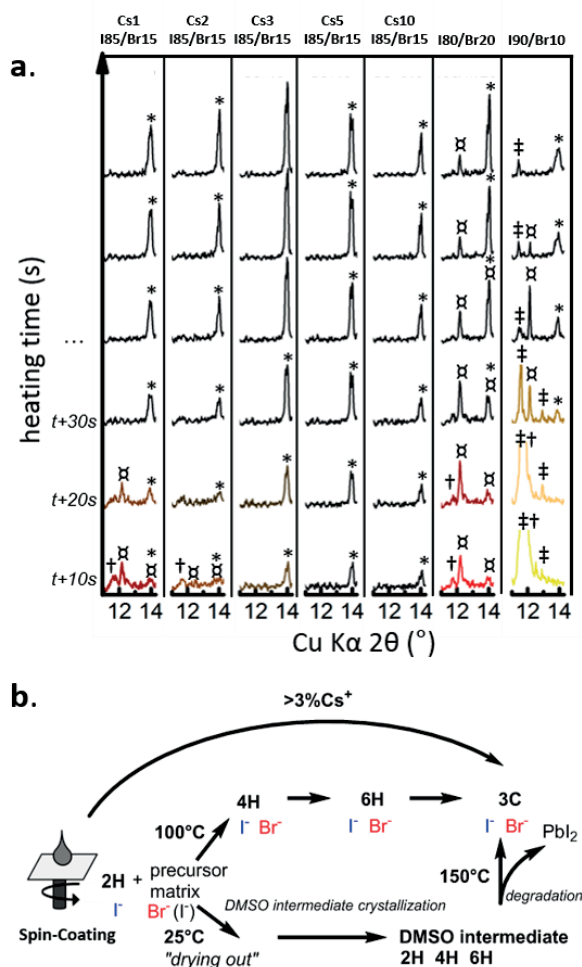


Figure 4.19 **a** in-situ XRD pattern (11.5 $^{\circ}$ -14.5 $^{\circ}$) representing the crystallization of different perovskite compositions: Cs1(I85/Br15), Cs2(I85/Br15), Cs3(I85/Br15), Cs5(I85/Br15), Cs10(I85/Br15), I80/Br20 and I90/Br10. The time resolution is 10sec and the symbols used for peak assignment are the same than specified above. In I90/Br10, the peak at 11.8 $^{\circ}$ is cut for the sake of clarity. **b.** suggested crystallization sequence. Cs⁺ incorporation (>3%) bypasses the crystallization via hexagonal perovskite phases, possibly explaining enhanced reproducibility and stability of cesium containing mixed cation-mixed anion perovskites.

We hypothesize that the driving force for the 2H \rightarrow 4H \rightarrow 6H \rightarrow 3R/3C crystallization sequence is an increase of Madelung energy as the stacking of AX₃ layers goes from pure hexagonal (2H) to a cubic/hexagonal ratio of 1:1 (4H), 2:1 (6H) and eventually pure cubic (3C). Indeed, B cation repulsion between face-sharing octahedra results in a loss of Madelung energy. B-B bonding, B-

X covalency, and B-site vacancies can compensate for this loss and stabilize hexagonal over cubic stacking.

Crystallization studied by Kelvin Probe Force Microscopy (KPFM) and Helium Ion Microscopy-Secondary Ion Mass Spectrometry (HIM-SIMS)

The motivation for studying the crystallization process using KPFM and HIM-SIMS lies in the discovery of the 3D hexagonal perovskite phases described above. The different phases (4H, 6H, 3C/3R, DMSO-intermediate) could possibly be distinguished from variations of surface potential and morphology.

The crystallization process of the two most relevant perovskite compositions for device fabrication, i.e. I85/Br15 and Cs10(I85/Br15), was followed by using KPFM, to determine changes in the morphology or surface potential at the nanoscale. Four perovskite films of each of the two compositions were heated at 100°C during respectively 0sec, 10sec, 30sec and 50min (**Figure 4.20** and **Figure 4.21**)

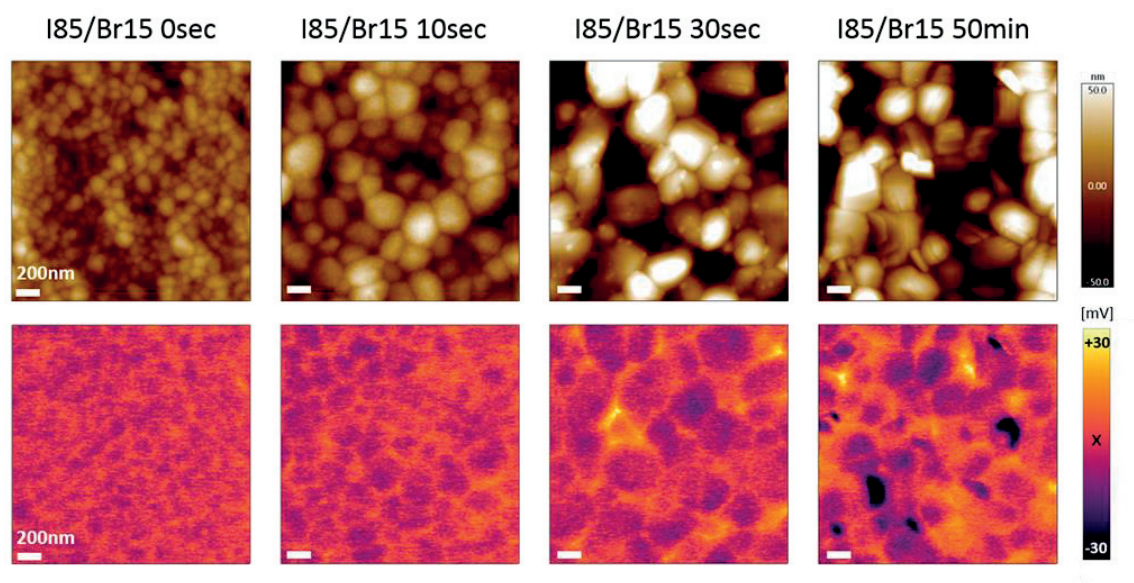


Figure 4.20 Crystallization of $(\text{FAPbI}_3)_{0.85}(\text{MAPbBr}_3)_{0.15}$ perovskite solar cell (without cathode- no HTM, no metal electrode).

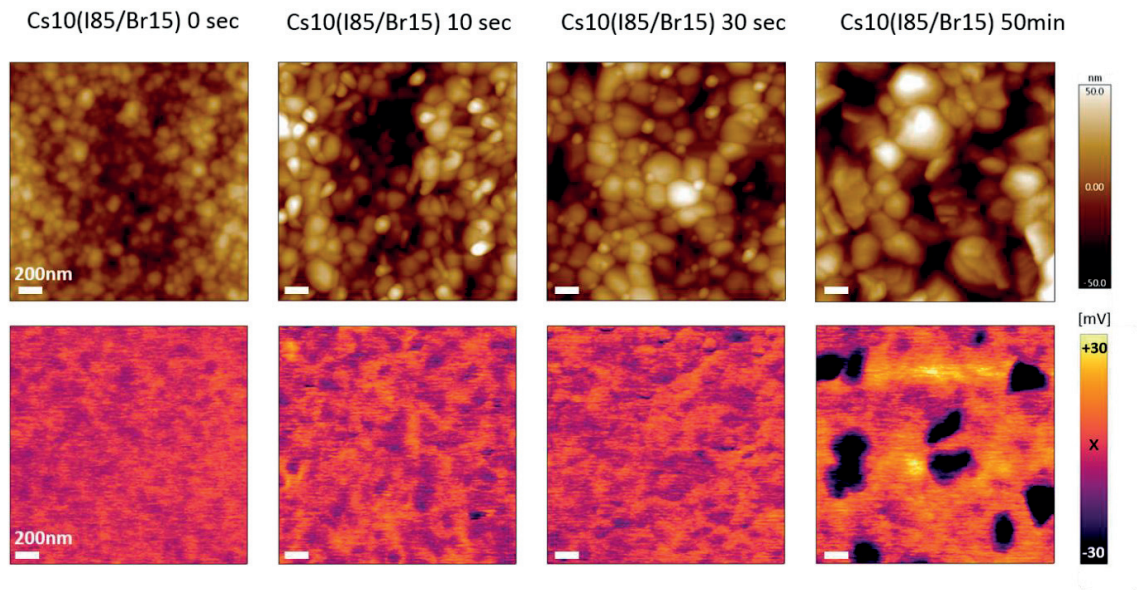


Figure 4.21 Crystallization of $(\text{CsPbI}_3)_{0.10}[(\text{FAPbI}_3)_{0.85}(\text{MAPbBr}_3)_{0.15}]_{0.90}$ perovskite solar cell (without cathode- no HTM, no metal electrode).

In both I85/Br15 and Cs10(I85/Br15), heating resulted in a rapid increase of the grain size from $\sim 50\text{nm}$ to $\sim 300\text{nm}$ within the first 30 seconds, subsequently slowing down to attain just slightly larger sizes within the following 50 min (**Figure 4.20** and **Figure 4.21**). Interestingly, though multiple phases co-exist in I85/Br15, the distribution of the surface potential was rather homogenous throughout the first 30 seconds, suggesting homogenous mixing of these phases within the perovskite grains. With increased heating time, we observe an increasingly heterogeneous distribution of the surface potential of the film, the 50 min sample showing strong surface potential deviations among some grains, previously already attributed to bromide absences by Gratia et al⁸⁸.

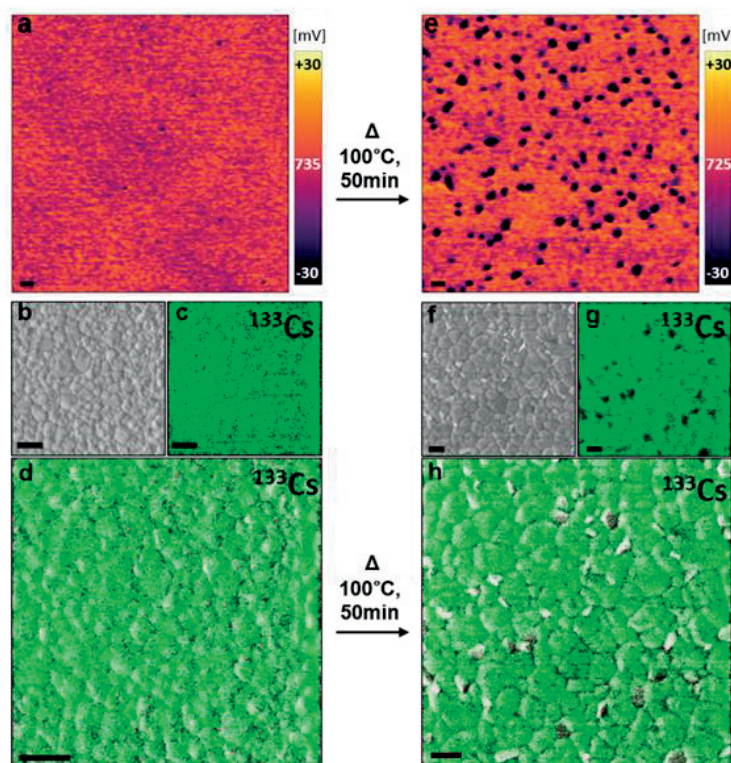


Figure 4.22 Comparison of a $\text{Cs}_{10}(\text{I}_{85}/\text{Br}_{15})$ perovskite film before (vacuum dried at room temperature) and after annealing for 50min at 100°C . **a,e.** Kelvin Probe Force Microscopy (KPFM) under dark conditions **b,f.** Secondary electron (SE) images from Helium Ion Microscopy (HIM) before and after heating at 100°C . **c,g.** Secondary-Ion-Mass-Spectrometry (SIMS) imaging of ^{133}Cs before and after heating at 100°C . **d,h** Combined SIMS and HIM imaging correlating local variations in ^{133}Cs with grain morphology. The scale bar corresponds to 500nm in all of the images.

In the case of $\text{Cs}_{10}(\text{I}_{85}/\text{Br}_{15})$, the surface potential is homogeneous prior to heating (**Figure 4.22**), which is expected due to the film mainly consisting of the black perovskite phase, as described in the previous sections. Similar to $\text{I}/_{85}\text{Br}_{15}$, the surface potential distribution more heterogeneous with longer annealing times. After 50min, the surface potential of multiple grains is $>30\text{mV}$ lower than the average grain value (**Figure 4.22b**). Using HIM-SIMS, a correlative microscopy-based technique recently developed by Wirtz et al.⁶⁵ which allows correlation of secondary electron images with mass-filtered secondary ion images, we were able to track the ^{133}Cs distribution in the $\text{Cs}_{10}(\text{I}_{85}/\text{Br}_{15})$ film before heating and after heating for 50min at 100°C . We find that the cesium distribution is homogeneous before heating (**Figure 4.22c**), at a smaller grain size. After 50min, accompanied by grain growth, the cesium distribution becomes heterogeneous (**Figure 4.22g**). Indeed, **Figure 4.22h**, which consists in the superposition of **Figure 4.22f** and **Figure 4.22g**

reveals that several entire grains do not contain any cesium at all, suggesting that the grains identified to have surface potential $> 30\text{mV}$ lower than average (**Figure 4.22e**), are cesium-free. Whether this partial deprivation of cesium within the surface upon prolonged heating is a sign of completeness of crystallization, hence beneficial for device efficiencies, will be the subject of future investigations. It is highly possible that heating is responsible for diffusion of cations and possibly the halide atoms, especially at the surface. Indeed, the temperature gradient could be responsible for these effects.

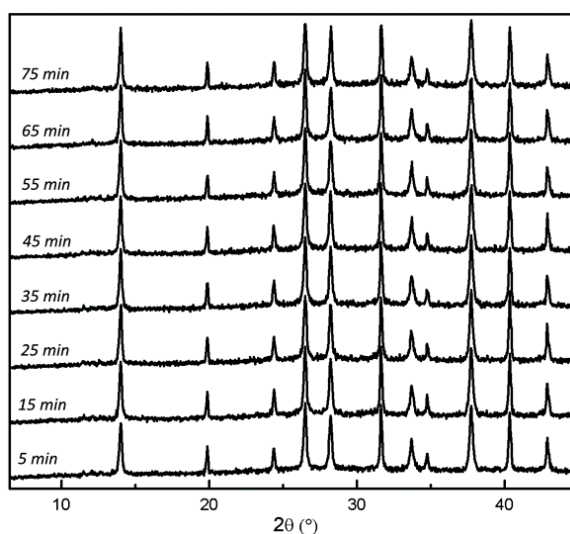


Figure 4.23 crystallization process of $(\text{FAPbI}_3)_{0.85}(\text{MAPbBr}_3)_{0.15}$ during 75min. No clear difference between 5min or 75min heating. This shows that macroscale techniques like XRD are insufficient to understand the crystallization.

Considering macroscopic phase composition, the crystallization process is more or less complete after about 30sec at 100°C when followed by XRD (see previous section) and extended heating time (**Figure 4.23**) does not produce any significant change in the XRD pattern. The combination of KPFM and SIMS is thus a valuable tool to investigate separate nano-domains, not easily detectable by means of XRD, that form upon increase of the crystal size during longer crystallization times. Since our data do not show any correlation between height trace and surface potential, we exclude increased grain roughness as the main reason behind the increased surface potential heterogeneity. Overall, the measurements suggest that increased surface potential heterogeneity during the crystallization process is more strongly correlated to grain growth than to macroscopic phase composition.

4.3 Conclusion and Perspective

In this work, the crystallization process of organic-inorganic mixed ion perovskites is unveiled. The polytypic sequence $2H \rightarrow 4H \rightarrow 6H \rightarrow 3C/3R$, known to exist amongst inorganic transition metal oxide perovskite upon elevated pressures and/or temperatures, points towards a rich phase diagram with small differences in the free energy of discrete and solid solution phases. For the first time, we are able to perform quantitative phase analysis using Rietveld refinement thanks to the correct modeling of all the possible phases based on crystal structures obtained on single crystals grown from similar conditions occurring during film processing. The herein reported experimental phase stabilities and underlying crystal structures are of huge impact for the perovskite solar cell community, in that they allow to understand the origins of possible efficiency losses and to rationalize the role of cesium incorporation into the perovskite lattice. Structural strain due to bromide-iodide (+MA/FA) exchange or cesium incorporation lies at the origin of the composition-dependent crystallization sequence. The investigated polytypism and crystal structures of these phases lay a basis for future theoretical understanding of the thermodynamics and kinetics of crystallization, and provide a rich playground for spectroscopists dealing with annealed mixed ion perovskites, who are now aware of the existence of two new phases that can remain in the final film, potentially skewing investigations on black perovskite phase. Based on this fundamental understanding, we expect future studies targeting the systematic control of this polytypism to enhance reproducibility and device efficiency. At the same time, the discovery of room-temperature/ambient pressure accessible 3D hexagonal perovskites with potentially interesting physical properties hitherto not described, will be of great interest for the general perovskite and material science community. Moreover, we present two simple single crystal growth methods (liquid-liquid diffusion and gel-growth) that have not yet been successfully applied to inorganic-organic perovskites. The existence of different crystallization pathways depending on composition rationalizes reproducibility and stability problems widely encountered in mixed ion perovskite fabrication. In particular, cesium incorporation allows to bypass crystallization via environment sensitive, defect-prone 3D hexagonal phases (due to low Madelung energy), thus facilitating device fabrication under various external conditions.

In order to push perovskite photovoltaics towards commercialization, it is in the interest of the scientists to simplify the crystallization process of this material as much as possible. Although mixed cation/mixed anion structures are interesting for tuning optical and electrical properties,

one should be aware of the highly complex crystallization process that accompanies halide and cation mixing. Cesium incorporation is easy and straight-forward, lowers the tolerance factor and thus results in the simplification of the crystallization process. As the crystallization process is immediately linked to reproducibility problems across research laboratories working on perovskite solar cells, I strongly believe that these results represent a large step in controlling perovskite solar cell fabrication, leading to a huge enhancement in reproducibility.

The results from this chapter open up a wide range of research areas in perovskite solar cells. Indeed, the results presented in this Chapter predict that the tolerance factor is one of the main tools for creating or avoiding 3D hexagonal perovskite structures. Any perovskite structure characterized by a tolerance factor slightly larger than 1 is predicted to yield 3D hexagonal perovskites, thus opening up a large class of new materials to be investigated for their optoelectronic properties! As perovskite materials are not only used in solar cells, these new 3D hexagonal phases are potentially interesting candidates for any applications related to halide perovskites.

Cesium incorporation not only changes the crystallization process but also the fabrication process. Indeed, when adding cesium, the perovskite film is already black (3R/3C phase) before putting on hotplate. Without cesium, the films are orange (2H, 4H and 6H phase). One expects a crystallization to be rather homogenous when happening during the spin coating process at room temperature. Without cesium, the 2H phase needs to react with bromide and methylammonium containing phases at 100°C. At this temperature, defect-prone hexagonal phases are exposed to the surrounding atmosphere which either contains harmful solvents if fabricated inside a glovebox or oxygen if fabricated outside. I believe that this is the reason behind much higher device reproducibility observed for cesium-containing mixed cation/mixed anion perovskite formulations.

Chapter 5 The relevance of lead-halide hexagonal perovskites

*This short chapter is based on a **manuscript in preparation**. The results are a continuation of the results discussed in the previous Chapter. Here I try to extend, improve and rationalize the understanding of the 3D lead halide hexagonal perovskites. This Chapter is not intended to provide a final story as still many open questions surrounding the hexagonal perovskite phases remain and are under investigation at the time of writing of this PhD thesis. It rather underlines the importance of the results from the previous Chapter, which is paving the way for a new class of perovskite materials with potentially very interesting electronic and optical properties. Many data sets were not ready at the time of writing this thesis, which is why part of the discussion in this chapter might seem too speculative considering the limited number of data shown here. I do have preliminary data supporting the statements in the results and discussion part.*

In the previous chapter, I showed that hexagonal lead halide perovskites are omnipresent intermediates of FA/MA-iodide/bromide mixed perovskites. Not only restricted to their role as intermediates, these phases are thermodynamically stable so that involuntary incomplete crystallization results in the presence of hexagonal phases in the final perovskite film, potentially skewing the results of optoelectronic measurements carried out on these films. Indeed, as opposed to the high-band gap pale yellow 2H phase (delta phase), the 4H and 6H phases are intensely orange and red, showing interesting photoactive properties yet to be unraveled. Intensive studies on optical and structural properties of these phases have not been the subject of the previous chapter, mainly because of the difficulty to produce films constituted of single phases of 4H or 6H. Due to the complex thermodynamic interplay between the 2H, 4H, 6H and 3R (3C) phase, it has been extremely challenging to selectively synthesize and characterize a single phase. What happens if one tunes the cations and anions beyond the simultaneous FA/MA and I/Br exchange investigated in the previous chapter? Is it possible to make a phase pure 4H or 6H film? How to understand the hexagonal single crystal formation? What happens when replacing Br atoms by Cl atoms? What is the role of the MA and FA cations?

5.1 Introduction

Anion and cation tuning has revealed to be a very successful strategy for improving the stability of perovskite as well as to tune physical properties in the desired way. When perovskite research grew rapidly in 2012, chloride as well as bromide were investigated as partial replacement for iodide anions. Whereas the beneficial role of bromide has been rapidly elucidated and accepted among the community, the role of chloride addition to MAPbI₃ solutions has been intensively debated. Although improved charge transport properties and decreased charge recombination were advanced as the reasons behind improved efficiencies, there was no proof of Cl incorporation into the perovskite crystal structure. In general, although these complex solid solutions have proven to be beneficial, the crystallization process leading to the final black perovskite phase was not understood until the discovery of 3D hexagonal lead halide perovskites, which have been identified as key intermediates in the (FAPbI₃)_x(MAPbBr₃)_{1-x} crystallization. Questions regarding the exact position and role of bromide in these hexagonal perovskites are still open. Optoelectronic properties of the single 3D hexagonal phases have not yet been reported. Can the even smaller Chloride atom also form stable 3D hexagonal mixed halide perovskite phases? Here I show that 3D hexagonal perovskite polytypes are also intermediates of the mixed iodide/chloride perovskites. These hexagonal perovskites require the use of a certain amount of the large FA cation instead of the smaller MA cation.

5.2 Results and Discussion

Using the liquid-diffusion growth method described in Chapter 1 and in Chapter 4, single crystals have been grown from perovskite precursor solutions containing (FAPbI₃)_{0.85}(MAPbCl₃)_{0.15}, (FAPbI₃)_{0.85}(FAPbCl₃)_{0.15} and (FAPbI₃)_{0.85}(FAPbBr₃)_{0.15} as well as from a 3-month old (FAPbI₃)_{0.85}(MAPbBr₃)_{0.15} precursor solution. It is found that all of the solutions yield a decent amount of 3D hexagonal perovskite polytype structures.

- (FAPbI₃)_{0.85}(FAPbBr₃)_{0.15} yields 3D hexagonal perovskite single crystals, proving that MA is not required to form hexagonal 3D polytypes
- Old (FAPbI₃)_{0.85}(MAPbBr₃)_{0.15} solutions result immediately in 3D hexagonal perovskite single crystals. In the previous chapter (fresh solutions), it was observed that first black crystals formed. After some time, these crystals would transform into orange and red hexagonal crystals. This experiment can be explained by degradation of MA cations, most

likely by DMSO. Indeed, it is found that aged $(\text{FAPbI}_3)_{0.85}(\text{MAPbBr}_3)_{0.15}$ perovskite precursor solutions (month scale) do not allow to fabricate 3C/3R perovskite thin films. The color of the film remains orange-red on a hotplate kept at 100°C . This result is independent of whether the precursor solution was stored for months in a glovebox or in a drawer. The crystallization process always stops at the 4H or the 6H phase. In the previous chapter I showed that the 2H phase consists in FAPbI_3 , and 4H and 6H perovskites only form upon uptake of bromide. This strongly suggests that FA, I and Br ions are still active in the aged solutions. This is why 4H and 6H single crystals could also be grown from aged solutions, but there are no signs of 3R/3C. This observation explains the single crystal growth mechanism from the previous chapter: First black crystals are formed because MA is not yet decomposed by the solvent. After a while, MA decomposes, preventing the crystallization process to continue to 3C/3R. It follows that the $2\text{H} \rightarrow 4\text{H} \rightarrow 6\text{H} \rightarrow 3\text{R}(3\text{C})$ crystallization process of mixed anion/mixed cation perovskites is actually a sequential process, as will be discussed below.

- $(\text{FAPbI}_3)_{0.85}(\text{FAPbCl}_3)_{0.15}$ as well as $(\text{FAPbI}_3)_{0.85}(\text{MAPbCl}_3)_{0.15}$ precursor solutions yield exclusively hexagonal perovskites. The 6H structure is shown below.

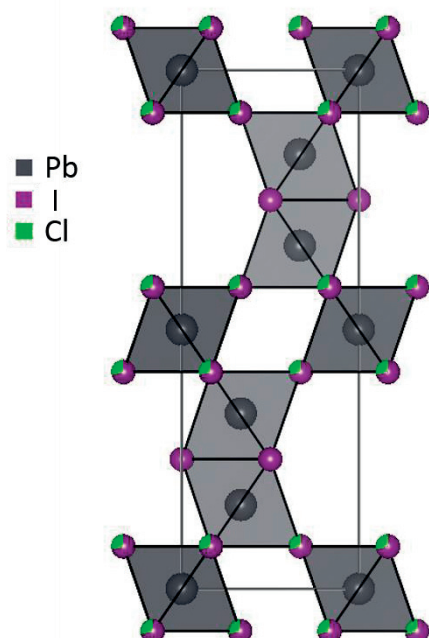


Figure 5.1 6H crystal structure grown from $(\text{FAPbI}_3)_{0.85}(\text{FAPbCl}_3)_{0.15}$. Face-sharing atomic positions are occupied only by the larger iodide anions.

Figure 5.1 shows the single crystal structure of a 6H perovskite polytype containing FA, Pb, I and Cl ions. This proves for the first time the existence of a perovskite structure containing both the large iodide anion as well as the small chloride anion. In the case of $\text{MAPbI}_3\text{Cl}_{1-x}$, such structures do not form, rather the pure MAPbI_3 phase forms. By replacing most or all of the MA cations with FA cations, the tolerance factor is above 1, enabling the existence of hexagonal perovskites. As discussed in the previous chapter and in the introduction, these polytypes are composed of face-sharing as well as corner-sharing octahedra. This results in different halide positions. The face-sharing octahedra are exclusively occupied by the larger iodide anions, whereas the corner-sharing positions are occupied by both the iodide and chloride atoms.

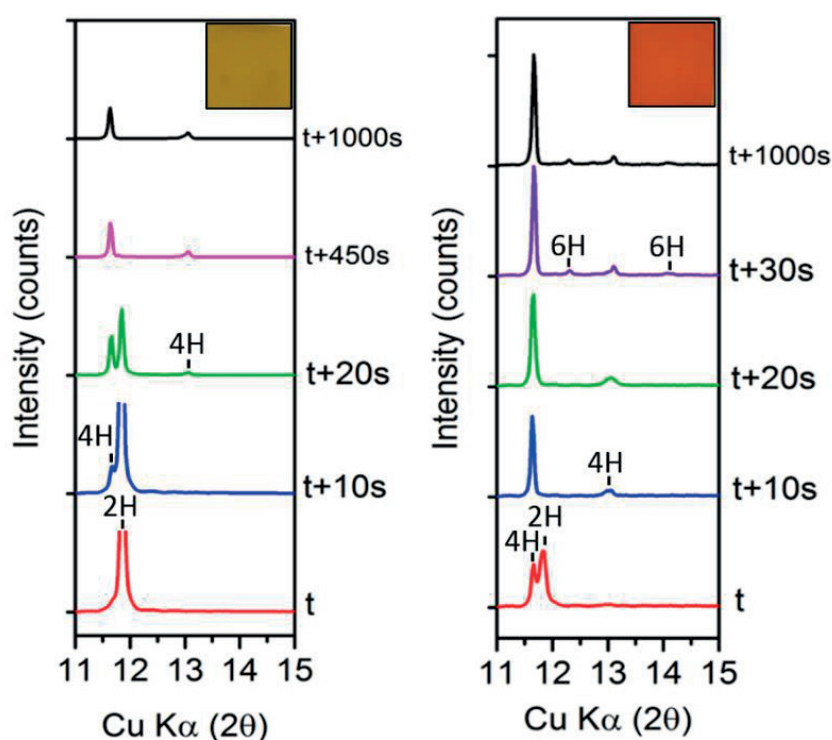


Figure 5.2 In-situ XRD measurements at 100°C . **left:** $(\text{FAPbI}_3)_{0.85}(\text{FAPbCl}_3)_{0.15}$ **right:** $(\text{FAPbI}_3)_{0.85}(\text{MAPbCl}_3)_{0.15}$ (inset=photograph of perovskite thin film deposited on 2×2 cm FTO substrate). t corresponds to time needed before the XRD measurement starts (see Appendix and previous chapter).



Figure 5.3 Photograph of three different compositions showing the effect of MA/FA ratio (from left to right): $\text{FA}_{0.5}\text{MA}_{0.5}\text{PbI}_{2.47}\text{Cl}_{0.53}$; $(\text{FAPbI}_3)_{0.85}(\text{MAPbCl}_3)_{0.15}$; $(\text{FAPbI}_3)_{0.85}(\text{FAPbCl}_3)_{0.15}$.

Figure 5.2 depicts the in-situ crystallization process of $(\text{FAPbI}_3)_{0.85}(\text{FAPbCl}_3)_{0.15}$ and $(\text{FAPbI}_3)_{0.85}(\text{MAPbCl}_3)_{0.15}$. For information about the experimental procedure, please refer to the previous chapter. One can immediately see the better quality of the diffraction pattern compared to the bromide case from the previous chapter. Chloride does improve crystallinity of perovskite thin films, as has already been shown several times in the literature⁷⁸.

During the first 20 seconds, 2H partially transforms into 4H. After 60 seconds, a phase pure 4H perovskite film is achieved. This is of particular interest because it allows to gain insight into this phase by means of spectroscopy and other thin film characterization techniques. When replacing 15% of the FA cations by MA cations, the crystallization process is accelerated, leading to faster transformation 2H-4H. As opposed to the pure FA case, 4H partially converts into 6H, showing that the MA cation might play a role in the hexagonal perovskites, at least for the conversion 4H to 6H. It could however also be possible that 15% MA helps the crystallization process to proceed faster, thus reaching the 6H step, without actually getting itself incorporated at this stage.

Here, using the $\text{FAPbI}_{0.85}\text{Cl}_{0.15}$ formulation, I was able to obtain a phase pure 3D hexagonal polytype phase (4H) for the first time. In the bromide case, a mixture of 4H, 6H and 3R(3C) phases seemed unavoidable. The same experiment carried out using the $\text{FA}_{0.85}\text{MA}_{0.15}\text{PbI}_{0.85}\text{Cl}_{0.15}$ formulation yields a mixture of 4H and 6H phases but no 3R(3C) phase. Even by heating during more than an hour or at temperatures above 100°C, it is not possible to obtain a black perovskite phase. These data show that, contrary to the iodide-bromide case, iodide and chloride cannot randomly occupy corner-sharing positions due to the large size difference between chloride and iodide. The data suggest that previous reports claiming that iodide and chloride cannot occupy the same perovskite structure are partially correct, however only for the pure cubic-stacked AX_3 perovskite. Mixed cubic-hexagonal AX_3 stacking (4H and 6H) allows iodide and chloride to occupy a 3D perovskite structure.

When increasing the amount of MA/FA ratio (**Figure 5.3**), a black perovskite films is obtained. This is the same situation as reported in literature: pure MAPbI_3 has formed (XRD data not shown here). Iodide and chloride do not fit into the same pure cubic perovskite structure.

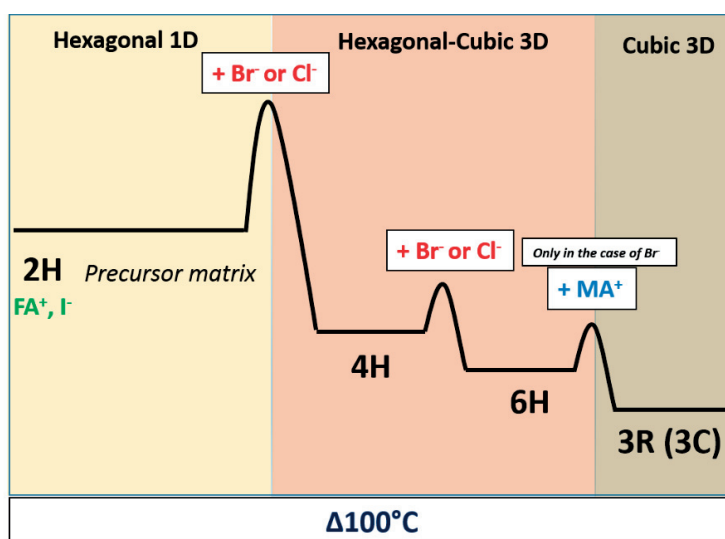


Figure 5.4 Illustration of the mixed anion-mixed cation perovskite crystallization mechanism.

Figure 5.4 depicts the summary of the crystallization mechanism of (mixed FA/MA)–(mixed I/Cl or I/Br) perovskite formulations as a sequential two-step crystallization process:

1. At 100°C (activation energy), starting from a 2H FAPbI_3 yellow non-perovskite phase (1D), chloride or bromide exchange with iodide resulting in the formation of a 4H 3D hexagonal perovskite phase (h/c stacking ratio=1:1).
2. More I-Br respectively I-Cl exchange reactions take place, stabilizing cubic stacking over hexagonal stacking even more (because bromide and chloride lower the tolerance factor). 4H transforms into 6H, resulting in a h/c stacking ratio of 1:2.
3. In the case of the mixed iodide/bromide formulation, the 6H phase further transform into the pure cubic-stacked perovskite phase 3R (rhombohedral). In the case of the mixed iodide/chloride formulation, the 6H phase cannot transform into a pure cubic-stacked structure due to the size difference between iodide and chloride anions. In the case of the mixed chloride/bromide formulation (not shown here), no hexagonal phases form, due to the similar size of chloride and bromide anions.

In this process, the solvents DMF and DMSO play an active role. So far, any attempts in converting any 2H films into 4H by dipping into bromide solutions (in isopropanol) has failed.

5.3 Conclusion and Perspective

Mixed iodide/bromide as well as mixed iodide/chloride 3D hexagonal perovskite polytypes exist. Mixed bromide/chloride hexagonal polytypes do not exist. I believe that the driving force for creating stable hexagonal polytypes is in the same time linked to the size of the FA cation and to the size difference between iodide and chloride respectively bromide. Hexagonal polytypes afford two different halide positions, the existence of which is linked to the fact that one used two different halide anions. The use of the large FA cation (larger than MA) is required in order to obtain a tolerance factor larger than 1, which is necessary for obtaining the hexagonal perovskite structure.

One of the main questions that needs to be answered as soon as possible is related to whether MA cations go into these 3D hexagonal structures or not. Single crystal experiments do not provide a direct answer to this. Carefully designed and accurate powder XRD experiments will need to be performed. Rietveld refinement will then be able to tell whether MA goes into the hexagonal structures or whether it is only responsible for the 6H-3R(3C) phase transition. What is clear is that, contrary to the FA, MA is not required to form 4H or 6H phases. Pure MA precursor solutions have been found to never result in any hexagonal perovskite phase.

Chapter 6 Carbazole-based Small Molecule Hole-transporting Materials for Perovskite Solar Cells

This Chapter is based on work carried out during the first year of my PhD thesis. It is mostly based on a scientific publication in Angewandte Chemie¹⁰⁹. Back in 2015, the development and perovskite research was still at its earliest stage, explaining the lack of data such as device stability for example, generally required for a more mature research field (as of 2017). The hole-transporting materials were synthesized by Artiom Magomedov from the group of Prof. Vytautas Getautis (Kaunas University, Lithuania). Ionization potential, DSC/TGA and TOF measurements were also measured in Lithuania. I carried out the device fabrication and characterization as well as part of the basic characterization of the molecules. The solar cells based on carbazole derivatives apart from molecules V886, V885 and V911 were first screened and selected by myself but further optimized for obtaining high efficiencies by Dr. Sangyuhun Paek (EPFL).

Understanding the properties of the perovskite semiconductor material is crucial but the choice of the adjacent layers, too. In order to fabricate efficient solar cells, the hole transporting layer is of paramount importance. The efficient blocking of the photogenerated electrons within the perovskite active layer, resulting in a large increase of the shunt resistance and open-circuit voltage of the device, is one important aspect. This is achieved by carefully designing the energy level (HOMO) of the hole-transporting material in such a way that hole injection can occur but electron injection is blocked by an energy barrier. The other key parameters are related to the material's abilities to efficiently transport the injected holes without large loss. Bad performance can be due to low hole mobility or low electrical conductivity, reflected by a higher series resistance and resulting in energy loss into heat.

The characterization of electronic properties such as hole mobility and conductivity of hole transporting materials can be reliably carried out using the organic field-effect transistor (OFET) configuration. The theory behind these methods can be found in the introduction chapter. Instead of fabricating the transistor from scratch each time, it is most convenient to use pre-fabricated OFET substrates (Fraunhofer IPMS), containing pre-patterned gold electrodes of different channel length (**Figure 6.1**). As solution-processed organic semiconductors typically used in solar cells have low hole mobilities (typically 10^{-6} - 10^{-4} $\text{cm}^2 \text{V}^{-1} \text{s}^{-1}$) and electrical conductivity (typically 10^{-6} - 10^{-3} S cm^{-1}) compared to inorganic semiconductors, the dimension of these transistors needs to be

in the micrometer-scale in order to allow for reliable measurements with voltages below 100V. This requires the use of a microprobe station in order to connect the micrometer-sized contact pads to the sourcemeter (here: Keithley 2400A). During this PhD thesis, I developed and designed a suitable probe station (**Figure 6.2**) based on an initial design by Prof. Sivula (EPFL).

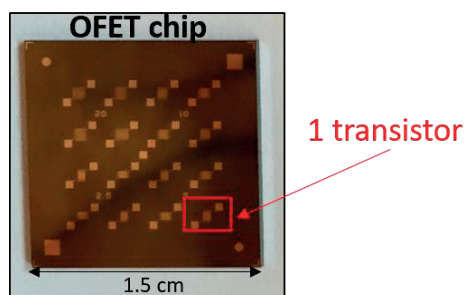


Figure 6.1 Picture of a typical pre-fabricated OFET chip (Fraunhofer IPMS) used for 2-point probe conductivity measurements as well as hole mobility determination. 4 x 4 transistors of channel lengths 2.5 μm , 5 μm , 10 μm and 20 μm . Conductivity measurements were usually carried out on the 2.5 μm channel whereas the hole mobility measurements were based on the 20 μm channel.

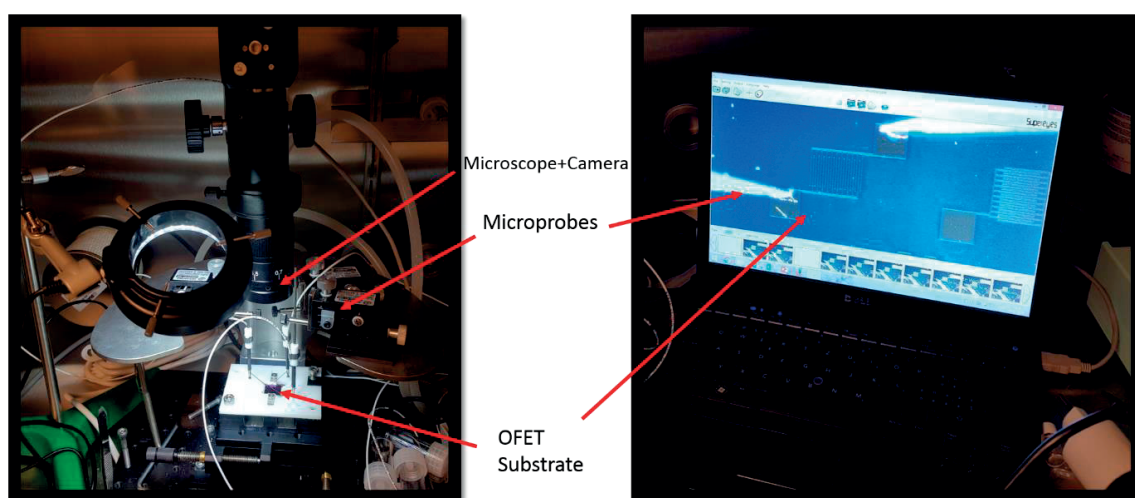


Figure 6.2 Picture of the microprobe-station installed inside a solvent-free Argon glovebox allowing for reliable (and temperature-dependent) conductivity and hole mobility measurements. A microscope+camera system is connected to a laptop placed inside the same glovebox.

The OFET substrates need to be rinsed with acetone to remove the protection layer. Then, after rinsing in absolute ethanol followed by an oxygen plasma cleaning step of 20min, the substrates were immediately transferred to an inert atmosphere glovebox where the HTM was deposited from chlorobenzene solution. The OFET hole mobility values of the carbazole HTMs I was

working with was very low and not consistent. This is why conductivity upon molecular doping with CoTFSI was a preferred property to assess the performance of the HTM because it reflects the real device parameter (molecular doping usually necessary). Without doping, most of the small molecule HTMs exhibit very low conductivity and thus do not work well in a solar cell. Spiro-OMeTAD and PTAA mobility has been measured as a reference and mobility measurements were carried out on molecules specially designed to be used without molecular dopants. These molecules are however not part of this PhD thesis. Most of the results from this probe station include hole mobility measurements and conductivity measurements that I carried out for projects which are not part of this work¹¹⁰⁻¹¹³.

I designed the probe station in such a way that temperature-dependent measurements are possible. A heat exchange element connected to a circulator provides a temperature range from -20°C to + 100°C. For lower temperatures, I adapted a Peltier element to be installed on top of the heat exchanger, allowing for measurements down to -60°C. For even lower temperature the use of liquid nitrogen is unavoidable.

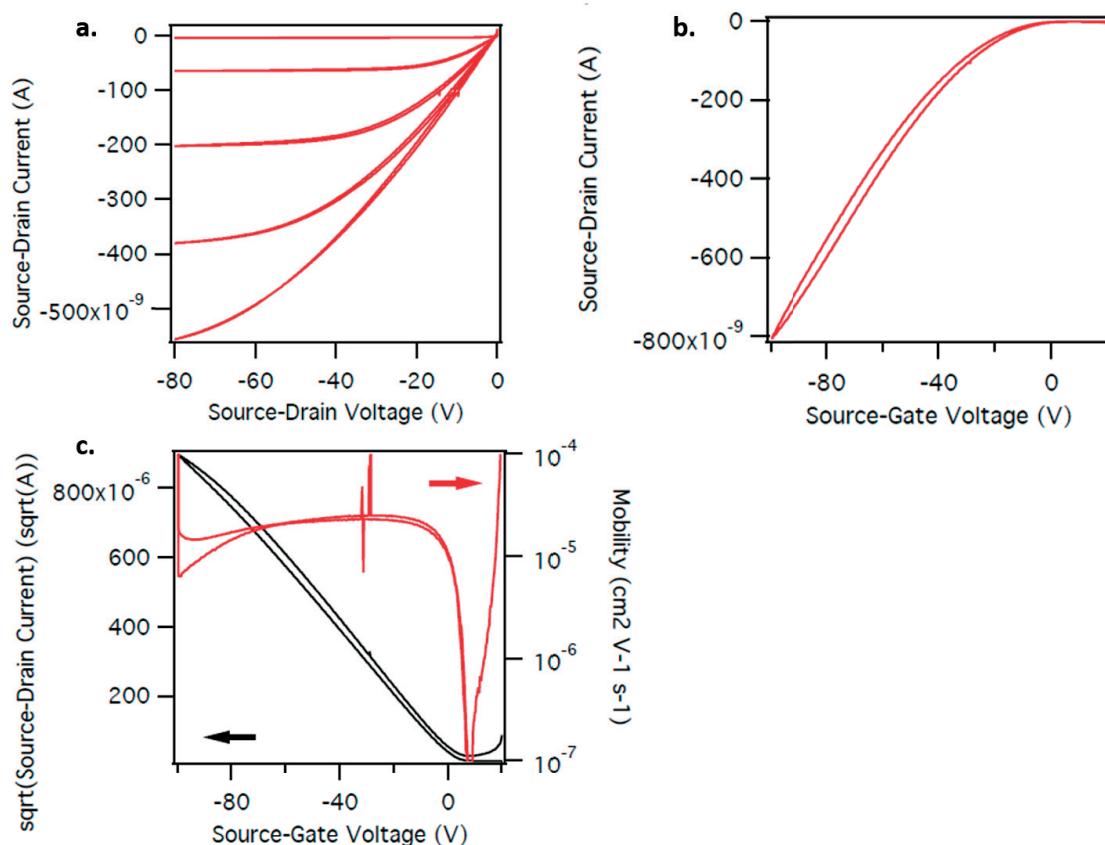


Figure 6.3 Organic Field-Effect Transistor (OFET) –based hole mobility determination of solution-processed Spiro-OMeTAD. **a.** Output Characteristics (OC); **b.** Transfer characteristics (TC); **c.** hole mobility plot. The hole mobility value of spiro-OMeTAD lies between $10^{-5} - 10^{-4} \text{ cm}^2 \text{ V}^{-1} \text{ s}^{-1}$.

6.1 Introduction

The properties of the ideal hole transporting material to be used in perovskite solar cells can be listed as follows:

- Charge carrier selectivity: electrons should be efficiently blocked while holes are selectively extracted
- Energy level matching between perovskite valence band and HOMO of HTM.
- Favourable chemical interaction between perovskite and HTM
- Solution processability: vacuum-free deposition allows for cheap solar cell production
- High conductivity and/or high hole mobility
- No parasitic light absorption
- Stability under continuous heat and light exposure

Hybrid organic–inorganic methylammonium lead iodide perovskites have been intensively investigated by Mitzi et al. for semiconductor and opto-electronic applications²⁵. Due to the excellent absorption properties and very high molar extinction coefficient of methylammonium lead iodide perovskite, Miysaka et al. have used it as a sensitizer in dye-sensitized solar cells in combination with iodine/iodide as liquid electrolyte¹⁰. The perovskite materials are soluble in most polar and protonated solvents, which is why the fabricated perovskite-sensitized solar cells exhibited very low efficiency and instability. To overcome the disadvantage of the solubility of the perovskite absorber layer, a solid-state dye-sensitized solar cell was constructed using spiro-OMeTAD as a hole conductor¹⁴ along with the perovskite^{13,114}. However, spiro-OMeTAD is one of the major drawbacks for successful perovskite solar cell commercialization. It is undesirable because the synthesis of spiro-OMeTAD is prohibitively expensive since it includes reaction steps that require low temperature (-78°C) as well as sensitive (n-butyllithium or Grignard reagents) and aggressive (Br₂) reagents. In addition, high-purity sublimation-grade spiro-OMeTAD is required to obtain high-performance devices. Tremendous efforts have been made to develop alternative molecules with similar performance. However, most of these molecules fail to show performance similar to that of spiro-OMeTAD^{115–121}. The only hole-transporting material (HTM) without the spiro motif known to date that demonstrated device efficiencies close to 15% requires custom-made boronic acids as precursors for the final synthesis¹²².

6.2 Results and Discussion

Here we report a new hole-transporting twin molecule (V886), based on methoxydiphenylamine-substituted carbazole, with performance very similar to that of spiro-OMeTAD. Moreover, it does not require an extensive and expensive synthetic procedure. The high solubility of V886 in organic solvents (e.g. > 1000 mg/mL in chlorobenzene) makes this molecule very appealing for solution processing applications. Perovskite solar cells employing V886 as a HTM show power conversion efficiency up to 16.91 %, which is to the best of our knowledge, one of the highest reported values for a small-molecule-based HTM. Furthermore, its simple two-step synthesis as well as the ready availability of the starting materials makes this HTM very appealing for commercial prospects of perovskite solar cells. The synthesis of V886 (1345.61 g/mol) involves the click reaction of 1,2-bis(bromomethyl)benzene with 3,6-dibromo-carbazole, followed by a palladium-catalyzed C–N cross-coupling reaction with 4,4'-dimethoxydiphenylamine (**Figure 6.4**).

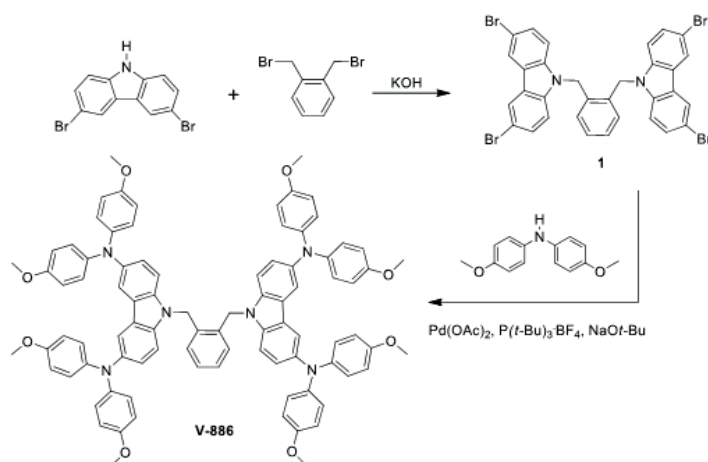


Figure 6.4 Synthesis scheme towards the carbazole-based V886 molecule. It involves a simple and cost-inexpensive 2-step reaction procedure.

More detailed information about the synthesis can be found in reference¹⁰⁹. The performance of V886 was tested in $\text{CH}_3\text{NH}_3\text{PbI}_3$ -based solar cells using a mesoporous TiO_2 photoanode and an Au cathode (**Figure 6.5**) following a procedure based on antisolvent engineering developed by Seok et al.⁴¹

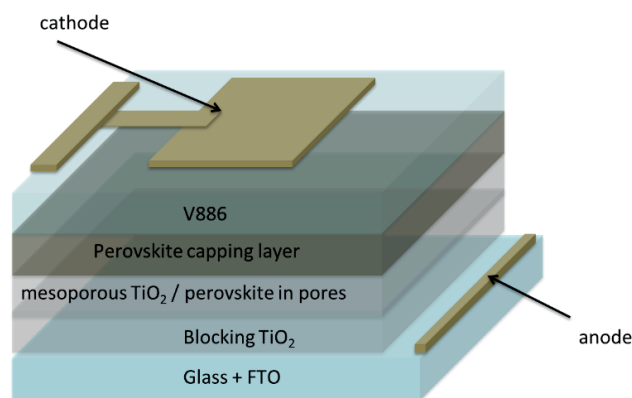


Figure 6.5 Solar cell architecture used for this study.

The perovskite device with V886 shows a maximum power conversion efficiency (PCE) of 16.91% under AM 1.5 G illumination, while PCE values exceeding 14% are routinely observed. The measured fill factor was 0.73, the current density (J_{sc}) 21.38 mA/cm^2 , and the open-circuit voltage close to 1.09 V (**Figure 6.6**). The best device from the same batch of solar cells, prepared following the same device fabrication procedure but using Spiro-OMeTAD as hole-extracting layer,

displayed a PCE of 18.36% as displayed in the same figure. The cross-section scanning electron micrograph of the best V886 device is shown in **Figure 6.7**.

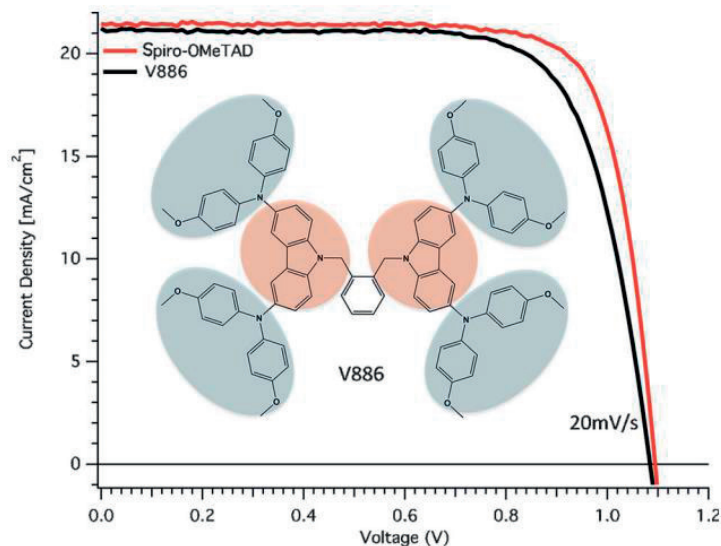


Figure 6.6 Current-Voltage (I-V) characteristics of champion perovskite solar cell containing V886 and the Spiro-OMeTAD reference as the hole transporting material.

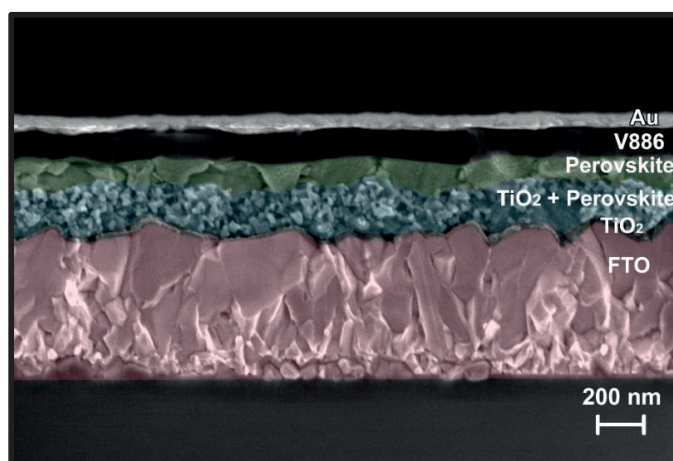


Figure 6.7 SEM cross-section image of an efficient perovskite solar cell employing V886 as the HTM instead of the commercial spiro-OMeTAD. The optimized V886 layer thickness (less than 200nm) is obtained for a V886 concentration of 30mM, less than the \sim 60mM optimized concentration for spiro-OMeTAD (\sim 300nm).

These perovskite solar cells typically exhibit hysteresis in the current–voltage curve, but according to recent work by Unger et al, very slow scans lead to hysteresis-free current-voltage curves⁶³. In the same way, the hysteresis of the V886-containing perovskite solar cell decreases with decreasing

scan rate as shown in **Figure 6.8**. Fast scan rates ($> 20 \text{ mV s}^{-1}$) lead to significant hysteresis, while scans recorded at 20 mV s^{-1} and 10 mV s^{-1} show only little hysteresis.

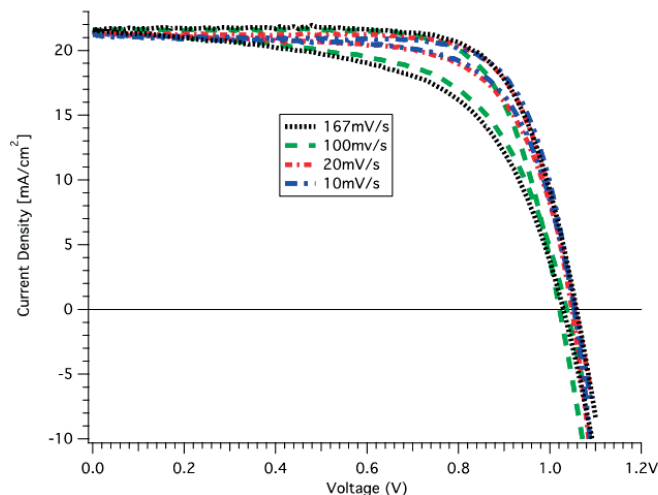


Figure 6.8 Hysteresis behaviour versus different scan speeds. The lower the scan speed, the smaller the hysteresis between the forward and the backward scan.

Figure 6.9 shows the difference in absorbance upon chemical oxidation of V886 by the cobalt(III) complex FK209¹²³. In its pristine form, V886 absorbs only in the UV region below 450 nm, while the chemically oxidized V886 exhibits visible absorption bands at 628 nm and 814 nm, showing the formation of the oxidized species. Since the $\text{CH}_3\text{NH}_3\text{PbI}_3$ perovskite absorption cuts off at 780 nm, the absorption of the oxidized V886 at 823 nm does not contribute to parasitic absorption in MAPbI_3 perovskite. Additionally, the oxidized V886 does not absorb in the infrared part of the spectrum (**Figure 6.9**), making this hole conductor an interesting option for the semi-transparent devices that are part of a hybrid tandem architecture¹²⁴.

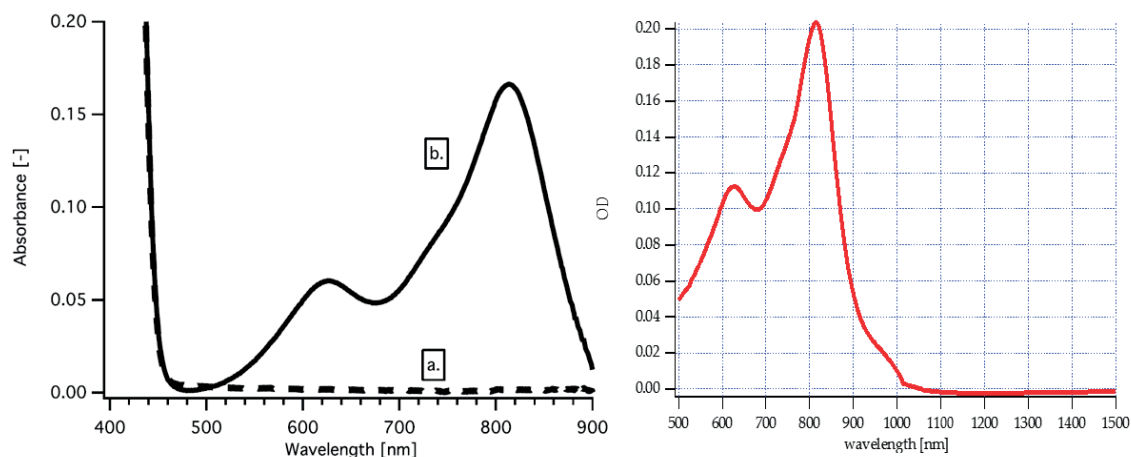


Figure 6.9 Absorption spectrum of pristine (a.) and oxidized (b.)V886 (using CoTFSI). No parasitic absorption observed above ~ 900 nm, making this molecule an interesting candidate for tandem applications.

Moreover, solubility tests show the very high solubility of V886 in some organic solvents like THF and chlorobenzene (> 1000 mg/ml). Lateral thin-film conductivity of V886 and Spiro-OMeTAD layers was measured on aspin-coated thin film (chlorobenzene) on OFET substrates (**Table 6.1**). In the absence of FK209, no Ohmic contact could be obtained and the measured current was very small compared to the current measured upon addition of FK209. In the case of oxidized V886, Ohmic contacts are formed with gold and the conductivity upon addition of 10 mol % of FK209 is extracted using a linear fit and Ohm's law. The conductivity of oxidized V886 was determined to be $4.2 \times 10^{-5} \text{ S cm}^{-1}$, indicating that the chemical oxidation of V886 actually results in doping, that is, an increase of carrier concentration and hence conductivity (**Figure 6.10**). It is about one order of magnitude lower than the conductivity measured in the doped Spiro-OMeTAD ($4.7 \times 10^{-4} \text{ S cm}^{-1}$). However, this is sufficient for good performance in devices with about 100nm thick HTM films.

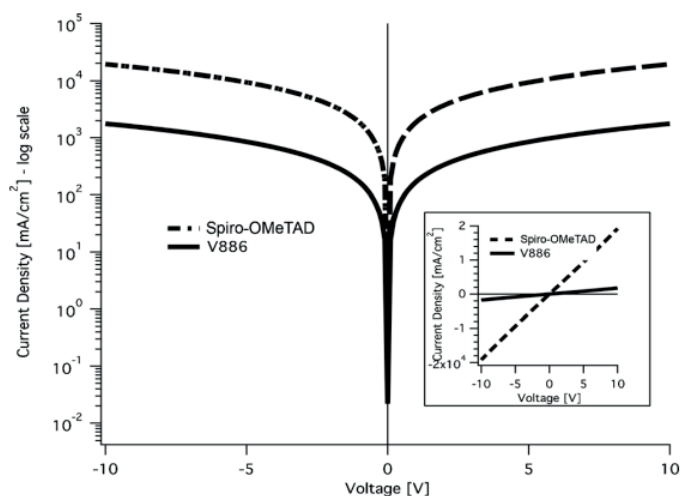


Figure 6.10 Conductivity plot of a doped V886 and spiro-OMeTAD thin film (log scale and linear scale). Ohmic contacts between doped V886/spiroOMETAD and the gold contacts are formed. Conductivity was extracted from a linear fit in the -5V to 5V region.

Table 6.1 Comparison of key properties of Spiro-OMeTAD and V886. Spiro-OMeTAD performs slightly better in terms of hole mobility and electrical conductivity. [a] Ionization potential was measured from films by the photoemission in air method. [b] Mobility value at zero field strength. [c] Mobility value at $6.4 \times 10^5 \text{ V cm}^{-1}$ field strength.

Compound	Spiro OMeTAD	V886
I_p , [eV] [a]	5.00	5.04
I_p^{CV} [eV vs. vacuum]	5.12	5.27
TOF mobility μ_0 , [cm ² V ⁻¹ s ⁻¹] [b]	$4 \cdot 10^{-5}$	$2 \cdot 10^{-5}$
TOF mobility μ , [cm ² V ⁻¹ s ⁻¹] [c]	$6 \cdot 10^{-5}$	$5 \cdot 10^{-5}$
Lateral Conductivity (10mol% FK209) [S/cm]	$4.7 \cdot 10^{-4}$	$4.2 \cdot 10^{-5}$

The hole mobility of V886 films (**Table 6.1**) was measured by the xerographic time-of-flight method (XTOF). XTOF measurements indicate that the hole-drift mobility of V886 is $2 \times 10^{-5} \text{ cm}^2 \text{ V}^{-1} \text{ s}^{-1}$ at weak electric fields and $6.4 \times 10^{-4} \text{ cm}^2 \text{ V}^{-1} \text{ s}^{-1}$ at a field strength of $6.4 \times 10^5 \text{ V cm}^{-1}$. The mobility values are of the same order of magnitude as the ones for Spiro-OMeTAD measured in

this work and reported elsewhere¹²⁵. When one considers the use of an organic material for optoelectronic applications, it is important to know its solid-state ionization potential (I_p). The solid-state ionization potential of undoped V886 was measured by photoelectrospectroscopy in air (PESA) and compared to the I_p of V886 in solution, determined by cyclic voltammetry (CV). The difference between the energies measured in the film (5.04 eV) and in the solution (5.27 eV) could be attributed to the different measurement techniques and conditions (solution in CV and solid film in the photoemission method). The CV measurement also reveals that the HTM undergoes a reversible one-electron oxidation and the second oxidation peak is at 5.43 eV (**Figure 6.11**).

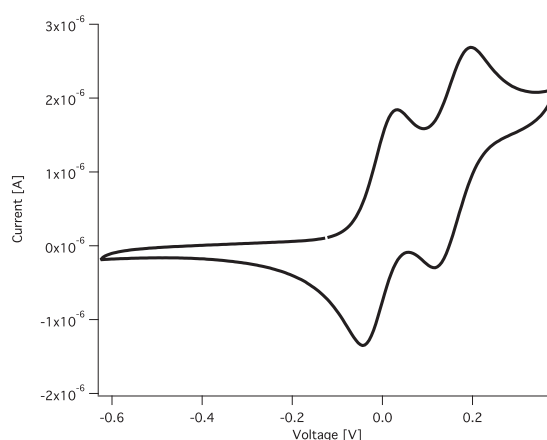


Figure 6.11 Cyclic voltammetry curve of V886.

Differential scanning calorimetry (DSC) and thermogravimetric analysis (TG) measurements reveal that V886 films are amorphous and show good thermal stability; the material starts to decompose at temperatures around 390°C (**Figure 6.12a**). DSC scans demonstrated that V886 is fully amorphous and shows a glass transition temperature of $T_g=141^\circ\text{C}$ (**Figure 6.12b**). This value is higher than that of Spiro-OMeTAD (125°C)¹²⁵, indicating a more stable amorphous state. Since V886 is fully amorphous, it is legitimate to link the lateral conductivity to the vertical conductivity, which is a more realistic parameter for characterization of a solar cell based on the architecture described here.

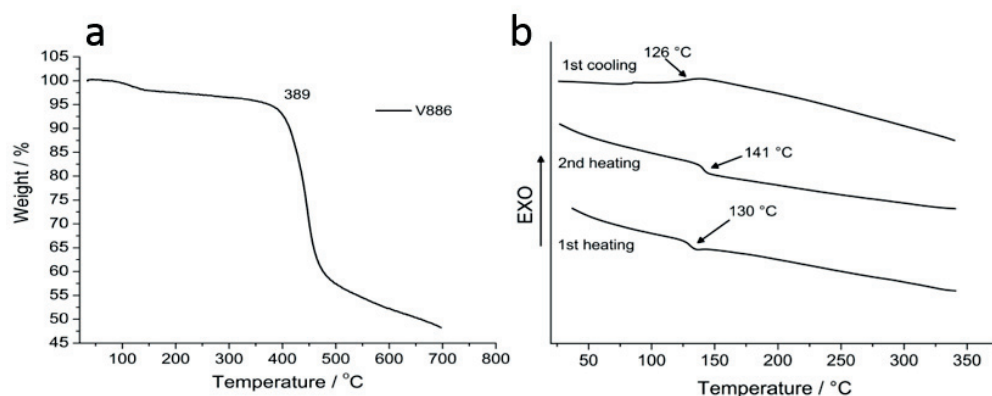


Figure 6.12 Thermo gravimetric heating curve of V-886 (heating rate $10\text{ }^{\circ}\text{C min}^{-1}$), and differential scanning calorimetry first and second heating curves of V-886 (heating rate $10\text{ }^{\circ}\text{C min}^{-1}$).

Carbazole derivatives other than V886 have also been synthesized by Artiom Magomedov (group of Prof. Getautis, Kaunas University). The structures and device performance data can be found in the Appendix. I characterized the electrical conductivity (**Figure 6.13**) by means of lateral 2-point probe measurements and the perovskite/HTM interface by means of photoluminescence spectroscopy (**Figure 6.14**). The HTM solutions were doped with 6 mol% CoTFSI for the conductivity measurements. For PL, full devices without Au electrode were used. Ideally, in order to only study the perovskite/HTM interface, a non-quenching ETM (not TiO_2) should be used. However, this will not reflect the real device structure. It can be assumed that the capping layer on top of the TiO_2 scaffold is thick enough so that most of the detected photoluminescence differences between the HTMs originate from the perovskite/HTM interface. I found that the micro PL setup (5x objective, green laser) was accurate for comparison between the different carbazole derivatives, namely: V886 isomers (V885, V911); methyl-(instead of methoxy functional group) analogues (V908, V928, V931); 3-branched analogue (V1039); substitution isomer V946. The electrical thin-film conductivity results (**Figure 6.13**) show that spiro-OMeTAD still yields conductivity almost one order of magnitude higher than the best carbazole derivatives, which are group formed by the three isomers ortho-V886, para-V911 and meta-V885 ($\sim 10^{-5}\text{ S/cm}$). These also yield devices with the highest average power conversion efficiencies (cf. Appendix). Steady-state PL reveals (**Figure 6.14**) that the PL intensity of these derivatives is greatly quenched compared to the reference device without any HTM, unravelling efficient hole transfer from perovskite to the HTM. In terms of PL quenching, spiro-OMeTAD again performs the best. V1039 shows poor conductivity and no strong PL quenching, thus also relatively low device efficiencies

(Appendix). V946 is interesting because it shows very good conductivity, close to the value obtained for spiro-OMeTAD. However, the PL is not correctly quenched, suggesting poor hole transfer to this HTM. Despite the good transport properties, the interface perovskite/V946 is poor and consequently also lower device efficiencies are obtained. Given the good transport properties, I suggest that this molecule should be tested in combination with a different perovskite composition. The methyl analogues V908, V928 and V931 show lowest conductivity, relatively poor device efficiencies (Appendix) as well as no signs of efficient quenching. The reason why the PL is even higher than the reference device can be that the devices were not encapsulated. The reference was thus not protected by any HTM layer against moisture, possibly explaining a PL intensity lower than expected. Overall, the data suggest that methoxy functional groups are absolutely crucial for performance and that the original V886 derivative, extensively described in this Chapter, so far remains one of the best carbazole derivatives.

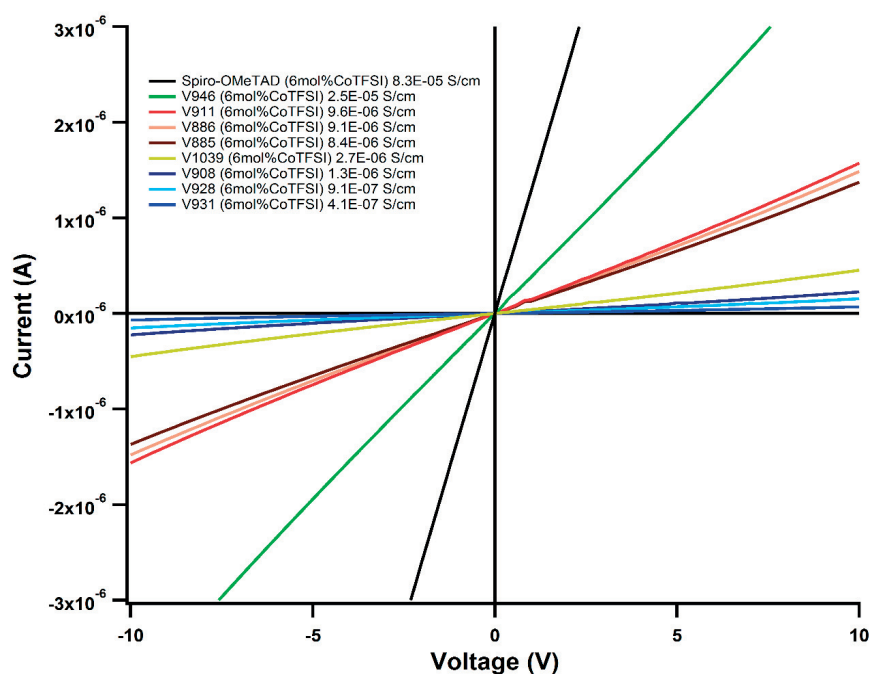


Figure 6.13 Thin-film conductivity measurements of carbazole based hole transporting materials. The methoxy analogues yield higher conductivity than the methyl analogues.

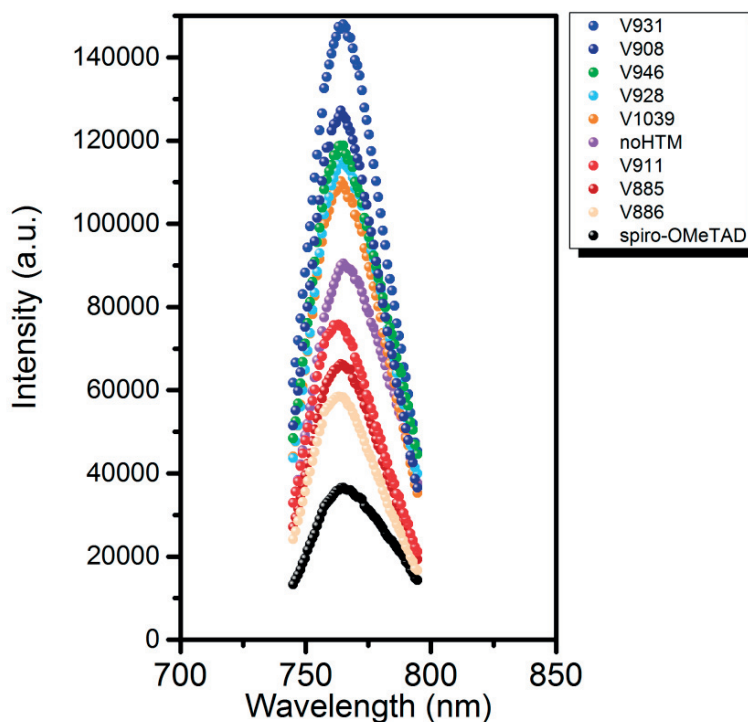


Figure 6.14 Steady-state Photoluminescence (PL) quenching of various carbazole derivatives of V886.

6.3 Conclusion and Perspective

In conclusion, a small-molecule hole conductor (V886) that yields high current density ($> 21 \text{ mA cm}^{-2}$) and overall efficiency close to 17% in $\text{CH}_3\text{CH}_2\text{NH}_3\text{PbI}_3$ -based solar cells is demonstrated. V886 is less expensive than the spiro hole conductors: it can be synthesized in two steps from commercially available materials, and is thus useful for large-scale production of perovskite solar cells. The good solubility ($>1000 \text{ mg/ml}$ in Chlorobenzene) and film-forming properties allows the formation of thicker films of high quality. Moreover, sublimation grade purity is not required, dramatically decreasing the cost of this material. I strongly believe that V886 can be also an ideal candidate for other optoelectronic applications such as OLEDs and solid-state dye-sensitized solar cells.

Although the conductivity of the carbazole-based molecules is slightly lower than spiro-OMeTAD, this can be easily compensated by decreasing the concentration to 30 mmol (instead of 60 mmol for spiro-OMeTAD), which results in thinner but equally efficient HTM layers. The

thinner film (shorter distance for the hole to be transported to the electrode) allows to compensate the increased resistance due to the lower conductivity. This explains why good fill factors could be easily obtained with the carbazole molecules.

In combination with the state-of-the-art perovskite formulation $[\text{CsPbI}_3]_{0.10}[(\text{FAPbI}_3)_{0.85}(\text{MAPbBr}_3)_{0.15}]_{0.90}$, efficiencies up to 19% could be achieved with V886 and its isomers. The V886 isomer derivatives are shown to be the most efficient among other carbazole-based derivatives.

The only drawback is that additives such as LiTFSI, ter-butylpyridine and CoTFSI are necessary, potentially hampering device stability. This is why the future HTMs might be of inorganic nature such as CuSCN, which has been shown to be suitable for fabricating efficient, stable and additive-free perovskite solar cells¹²⁶. Organic HTMs will however be still interesting for other optoelectronic applications.

Chapter 7 General Conclusion

7.1 Achieved results

During my PhD thesis, I contributed to the rapid progress that was made related to the understanding, characterization and controlling of the lead halide perovskite composition upon crystallization. I studied the effect of secondary phases introduced either voluntarily (PbI_2) or involuntarily (remaining hexagonal polytype phases, nano-phases exempt of bromide) during crystallization. These phases can be either beneficial or detrimental for the device performance. Most importantly, my results allow for the understanding of the crystallization process of one of the most efficient perovskite formulations, namely $(\text{FAPbI}_3)_x(\text{MAPbBr}_3)_{1-x}$. The discovery of hexagonal lead halide phases during crystallization also results for the first time in the rationalization of the role of the widely employed Cs^+ incorporation into the perovskite lattice.

Starting from the original MAPbI_3 hybrid perovskite, researchers used more and more complex perovskite formulations and stoichiometries in order to improve the solar cell performance and tune the optoelectronic properties. I identified that PbI_2 excess is a good strategy for the fabrication of record-breaking MAPbI_3 solar cells due to the reduction of the number of grain boundaries, enhancement of film crystallinity and generally improved perovskite/ TiO_2 interface (improved carrier injection into TiO_2).

After the mixed anion-mixed cation perovskite formulation $(\text{FAPbI}_3)_{0.85}(\text{MAPbBr}_3)_{0.15}$ was introduced, questions related to the possibility of partial segregation of iodide and bromide arose. Although macroscale investigations did not reveal the presence of more than one phase, I was able to show partial phase segregation at the micro-scale and nanoscale. The very efficient $(\text{FAPbI}_3)_{0.85}(\text{MAPbBr}_3)_{0.15}$ formulation results in a thin film composition that contains a distribution of phases of similar but different stoichiometry, centering on the desired $(\text{FAPbI}_3)_{0.85}(\text{MAPbBr}_3)_{0.15}$ stoichiometry. Importantly, bromide absences within a certain fraction of the total number of grains (at least at the surface) as well as general elemental and optical inhomogeneities supported this interpretation.

Later, the incorporation of Cs^+ into the $(\text{FAPbI}_3)_x(\text{MAPbBr}_3)_{1-x}$ formulation resulted in world-record solar cell efficiencies, improved device reproducibility and stability but the reason behind this was mostly unknown. The study of the $(\text{FAPbI}_3)_x(\text{MAPbBr}_3)_{1-x}$ thin film crystallization process allowed me to identify hitherto unknown hexagonal lead halide polytypes, which are acting as intermediate phases during the mixed perovskite crystallization. I found that the commonly utilized strategy of Cs^+ incorporation into $(\text{FAPbI}_3)_x(\text{MAPbBr}_3)_{1-x}$ stabilizes the desired final cubic/rhombohedral perovskite phase, thus by-passing the crystallization pathway via defect-prone 3D hexagonal polytypes. I find that the crystallization pathway without Cs^+ incorporation is following a well-defined sequence, namely 2H-4H-6H-3R(3C), known to take place at the solid-state in oxide perovskites under high temperatures and pressures. Apart from the interesting consequences of such a complex crystallization scheme, this is, to the best of my knowledge, the first time that such phase transitions take partially place even at room temperature (complete process at 100°C). The reason for this is that the lead halide perovskite films can be solution processed so that the solvent actually plays an active role in these phase transitions under mild conditions.

I was able to show that the concept of the 3D hexagonal perovskites is not limited to iodide bromide perovskites as iodide/chloride perovskites also form stable hexagonal perovskite phases. This unravels one of the mysteries around the question whether or whether not chloride goes into a perovskite structure together with iodide.

Another important discovery resulting from the study of hexagonal perovskite consists in the development of liquid-liquid perovskite single crystal growth. Not only is this method straightforward and easy to reproduce, it also allows for the first time to use exactly the same precursor solution for perovskite single crystal growth than the one used for thin film fabrication. This allows to associate crystal symmetries formed during thin film crystallization to the single crystal symmetry.

The discovery of hexagonal polytypes also allows to rationalize the general concept of compositional mixing. First, the formamidinium cation was found to be more stable than the methylammonium cation and also allowed to tune the optical properties. Then, mixed FA/MA-mixed iodide-bromide perovskite formulations further enhanced optoelectronic properties. This composition was however found to be not very reproducible because upon publication of the Cs^+ incorporation into the mixed perovskite, most researchers switched to this new cesium-containing formulation. Cesium is mainly necessary to prevent the 3D hexagonal perovskite formation, as reported in the present thesis. The subsequent quadruple cation formulation containing also the

rubidium cation further increased the yield of radiative recombination and thus also the device performance because a good solar cell needs to be a good LED.

Lastly, I successfully introduced a small-molecule based hole transporting materials to be used in cheap but highly efficient perovskite solar cells. This molecule has been patented and is now commercially available

7.2 Future development

Given the rapid progress of perovskite photovoltaics, commercialization of perovskite solar cells can be projected to take place within the next 5-10 years. Whether these solar cells will only be used for niche applications or whether they are able to compete with the conventional mono- and polycrystalline Silicon technology will depend on the power conversion efficiency that can be reached in *large-area* perovskite panels. Indeed, solution processing, although offering the low-cost solution processability characteristic of organic semiconductors while displaying the long carrier lifetime and diffusion lengths characteristic of inorganic semiconductors, has many drawbacks when it comes to reproducibility and upscaling. Moreover, the possible Pb contamination in case of the destruction of the sealing of the solar panel may constitute a key risk that still needs to be thoroughly assessed. Concerning the quest for efficient, cheap and stable HTMs, I believe that in the particular case of the application in perovskite solar cells, the organic HTMs will lose the battle in favour of the inorganic HTMs such as CuSCN, which has recently been demonstrated to be extremely cheap, efficient and stable at the same time¹²⁶

My results allow to better understand the influence of solid solution mixing in halide perovskites. Presumably, many other compositions trigger the formation of hexagonal perovskites, most likely including new polytypes that have not been described yet for halide perovskites. Indeed, many more hexagonal oxide perovskites are known apart from 4H and 6H. Some of these polytypes include 8H, 10H, 12H, 12R etc. The discovery of these phases will probably open up a whole research field on properties related to hexagonal halide perovskites, as it is already the case for oxide perovskites. Moreover, stoichiometry tuning is a common strategy in hexagonal oxide perovskites in order to obtain various optoelectronic properties. As the halide hexagonal perovskites are photoactive, with exact properties still to be determined, I believe that efficient photovoltaics based on 3D hexagonal perovskites will be shown very soon.

Chapter 8 Appendix

8.1 Appendix to Chapter 2

8.1.1 Sample preparation

The solar cells were fabricated on FTO covered glass substrates based on a previously reported architecture, where the active layer is sandwiched between a mesoporous TiO₂ electron transport material and a 2,2',7,7'-tetrakis(*N,N*-di-*p*-methoxyphenylamine)-9,9'-spirobifluorene (spiro-OMeTAD) hole transport layer. After cleaning the substrates by ultrasonication and UV-ozone treatment, a thin TiO₂ compact layer of 25 nm was deposited on FTO *via* spray pyrolysis at 450 °C, followed by a sintering process of the layer at 450 °C during 30 minutes. Then a mesoporous TiO₂ layer was deposited by spin coating a 30 nm particle paste (Dyesol 30 NR-D) diluted in ethanol for 10 s at 4000 rpm, to achieve a 150 nm thick layer. These layers were sintered again at 450 °C for 30 min under dry air flow. The perovskite films were prepared from a precursor solution of 1.25 M of both components PbI₂ and CH₃NH₃I in dimethyl sulfoxide (DMSO) in the case of a 1 : 1 molar ratio. After following a one-step anti-solvent based procedure described previously in this work, the film was annealed at 100 °C for 45 minutes in an inert atmosphere. Finally, a 200-300 nm layer of doped spiro-OMeTAD was deposited as the hole transport material prior to the deposition of 100 nm gold as the electrode.

8.1.2 Grain size analysis

Image J (now Fiji) software was used to manually average the diameter of about 100 grains.

8.1.3 Transient PL measurements

Table 8.1 Time constants of PL decay

Excitation from the perovskite capping layer				
PbI ₂ /MAI ratio	τ_1 (ns)	τ_2 (ns)	A1 (%)	A2 (%)
1 : 1	0.70	10.3	48.36	51.64
1.05 : 1	5.4	19.2	25.6	74.4
1.1 : 1	8.9	41.4	16.6	83.3
1.15 : 1	10.7	39.0	15.9	84.1

1.2 : 1	9.0	31.0	22.1	77.9
Excitation from the meso-TiO₂ layer				
1 : 1	18	-	100	-
1.05 : 1	19	-	100	-
1.1 : 1	13	4,6	77	23
1.15 : 1	11.4	2.7	54	46
1.2 : 1	6.9	2	26	74

8.2 Appendix to Chapter 3

8.2.1 Sample preparation

Mixed perovskite: Conductive FTO glass (NSG10) was sequentially cleaned by sonication in a 2 % Helmanex solution and isopropanol for 15 min respectively. A 30 nm titania blocking layer was applied on the substrates by spraying a solution of titanium diisopropoxide bis(acetylacetonate) in ethanol at 450 °C. In order to obtain a ~200 nm mesoporous TiO₂ layer, 30 NR-D titania paste from Dyesol diluted in ethanol (ratio 1:8 by weight) was spin-coated at 2000 rpm for 10s followed by a sintering step at 500 °C for 20 min. Subsequently, the substrates were Lithium-treated by spin-coating 60 µl of a solution of Tris(bis(trifluoromethylsulfonyl)imide) (Li-TFSI) in acetonitrile (10mg/ml) onto the mesoporous layer, followed by a sintering step at 500 °C for 10 min to decompose the Li-salt as previously described⁴⁷. The perovskite layers were fabricated using a single step spin-coating procedure reported by Seok et al⁴¹. For the perovskite precursor solution 508 mg of PbI₂(TCI), 68 mg PbI₂ (TCI), 180.5 mg formamidinium iodide (Dyesol) and 20.7 mg methylammonium bromide (Dyesol) were dissolved in a 1:4 mixture of DMSO:DMF. The perovskite solution was spun at 5000 rpm for 30s using a ramp of 3000rpms-1. 15s prior to the end of the spin-coating sequence, 100 µl chlorobenzene were poured onto the spinning substrate. Afterwards the substrates were transferred onto a heating plate and annealed at 100 °C for 50 min. Full devices were fabricated using the hole-transporting material polytriarylamine (PTAA). The solution was prepared in toluene (10mg/ml) using the additive Li-bis(trifluoromethanesulfonyl) imide (from a 170 mg/ml Li-TFSI/acetonitrile stock solution) and 4 µl of 4-tert-butylpyridine (TBP). The final HTM solutions were spin-coated on top of the perovskite layers at 3000 rpm for 30 s. The gold electrodes were deposited by thermal evaporation (Kurt Lesker) of 100 nm gold using a shadow mask under high vacuum conditions.

FAPbI₃ perovskite: anode preparation same as for mixed perovskite devices. Precursor solution prepared following recipe described elsewhere⁹⁶. MAPbI₃ perovskite: Anode preparation same as for mixed perovskite devices. The perovskite precursor solution contained PbI₂ (TCI, 507mg) and Methylammonium Iodide (synthesized in-house, 159mg) in 800 microliter DMSO (Acros). The Spin coating procedure was the same as for the mixed perovskite.

8.2.2 HIM-SIMS

HIM-SIMS is a recently developed technique at the Luxembourg Institute of Science and Technology which allows for high-sensitivity imaging down to 10 nm surface resolution as well as surface sensitivity in the order of nm. The measurement parameters of the Helium Ion Microscope were as follows: the source gas injected into the gas field ion source was Neon, the resulting primary ions Ne^+ , the acceleration voltage of the primary ions 25 kV, the column aperture 70 μm and the current was 2.2 pA. The SIMS system parameters were as follows: the sample voltage was -500 V to extract negative secondary ions, the spectrometer acceleration voltage was 3000 V, the analyzed masses were ^{12}C , ^{79}Br and ^{127}I . The images contained 512 x 512 pixels, the raster size was 10 x 10 μm^2 and the counting time 5 ms/pixels.

8.2.3 Micro-PL and Micro-Raman measurements

The measurements were carried out using a Renishaw InVia Raman microscope. PL and Raman mapping was done exclusively on glass-encapsulated devices (encapsulated inside N_2 glovebox using Torr Seal epoxy). The microscope objective was L100x (spot size of about 400 nm). The PL map was recorded before the Raman map (5% laser intensity) using a 532 nm green laser. No visible degradation signs have been observed after PL mapping. We use a relatively low excitation density of around 3mW/cm² (0.005%) and the light exposure time per measurement of 0.15 seconds. Raman data were fitted using multipeak fitting procedure with Origin 8 program.

8.2.4 Computational Details

The simulations of the spectroscopic properties of MAFAPbIBr have been carried out with the PWSCF and PHONON packages of Quantum-Espresso¹²⁷. Following the procedure previously reported by some of us⁹⁷, the Raman spectrum has been calculated using the LDA approach since Raman intensities are only available in Quantum-Espresso within LDA. LDA has been shown to deliver vibrational frequencies of inorganic perovskites of comparable quality to GGA results¹²⁸. Norm conserving, scalar relativistic pseudopotentials have been used with electrons from N, C 2s2p, H 1s, Pb 6s6p5d, Br 4s,4p and I 5s5p explicitly included in the calculations. We have chosen a cut-off of 70 Ry for the plane wave expansion and a 2 x 2 x 2 mesh for the sampling of the first Brillouin zone, as a compromise between accuracy and computational cost. Geometry optimization has been carried out by relaxing both the cell parameters and the atomic positions.

8.2.5 AFM/KPFM measurements

The AFM/KPFM measurements were carried out using a Cypher AFM from Asylum Research. Devices were fabricated as specified above (no cathode). The illumination source was white light LED. The devices were exposed to controlled dark/dry air environment until the beginning of the measurements.

Sample storage conditions: An extreme attention has been kept for sample handling and storage in order to obtain consistent and reproducible data. More in details, the samples for PL/Raman measurements have been prepared and encapsulated in inert atmosphere using a thin glass coverslip to protect the films and enable their storage for weeks. Samples for HIM-SIMS and KPFM were also prepared under inert atmosphere and subsequently stored in permanent dry and dark conditions, together with the solar cells that were fabricated in the same time as control samples.

8.2.6 Dynamic SIMS

A Conventional Dynamic Secondary Ion Mass Spectrometry instrument (Sc-Ultra, Gennevilliers, France) was used to characterize the mixed perovskite based solar cell in depth profile mode. The experiments reported here were performed using a Cs⁺ primary ion source with a primary current of 10nA and an impact energy of 3 keV. The positively charged Cs-metal clusters were detected from a surface size of 60 μm (analyzed area) and the signals were normalized by the Cs⁺ signal intensity to reduce the matrix effect⁶⁸.

8.3 Appendix to Chapter 4

8.3.1 XRD measurements

Perovskite thin films were spin-coated inside a nitrogen-filled glovebox from the different precursors solutions onto plasma-cleaned FTO substrates following a procedure mentioned below. Immediately after the spin-coater stops, the substrates were transferred into a closed plastic vial and transported within <30seconds to the XRD machine. The films were then transferred into a nitrogen-flushed in-house developed XRD temperature cell at 100°C (cf. Supporting Information). The total time t consists in putting the sample into the temperature cell, closing the door of the machine and the start of the measurement did not exceed 5 seconds. XRD diffractograms were recorded using a quasi-2D Vantec 1 detector (opening of 8°), on a Bruker D8 Discover. Thin films were measured using a Bruker D8 Advance in Bragg-Brentano geometry under Cu K α radiation. For transmission measurements minimizing texture effects, thin films of (FAPbI₃)_{0.85}(MAPbBr₃)_{0.15} were prepared on microscope glass using the precursor solution recipe and spin-coating procedure described below. After heating the films for respectively 0sec, 10sec, 20sec, 30sec and

50min at 100°C, the films were scratched using a razor blade and the powder was filled into 0.8mm Borosilicate capillary.

Transmission measurements were performed at the Swiss-Norwegian beamline of ESRF (Grenoble) using a wavelength of 0.7223 Å. Data were collected on a Pilatus 2M area detector and integrated with Bubble. Rietveld refinements were carried out using TOPAS.

Single crystals were measured on a Bruker D8 Venture equipped with a Photon II detector and Mo micro-source. Single crystal data were integrated using APEX III. Structures were solved using ShelXT¹²⁹ and refined with ShelXL¹³⁰ interfaced through Olex2¹³¹

8.3.2 Single Crystal Growth

Liquid-liquid diffusion: Inside an Argon glovebox, 1ml Isopropanol (Sigma) was added into a 2ml vial before slowly introducing 150µl of precursor solution $(\text{FAPbI}_3)_x(\text{MAPbBr}_3)_{1-x}$ at the bottom using a micropipette. Subsequently, the vial was closed and left on a hotplate at 100°C. Several black perovskite crystals are collected and selected after a few hours, while most of the black crystals stay in the vial, transforming into hexagonal crystals after 1-2 days.

Gel growth: Lead iodide and lead bromide were dissolved in a mixture of concentrated HI and HBr (1ml) in a vial. Tetramethyl orthosilicate (0.1ml) was added to allow the formation of a solid gel. Formamidinium iodide and methylammonium bromide were dissolved in isopropanol (800µl) and poured on top of the gel to allow crystal growth by slow diffusion. Stoichiometric amounts of starting materials were used with a final lead concentration of 0.5M. Crystals (3C perovskite and DMSO-intermediate) were obtained within few days and were manually selected under an optical microscope for further analysis.

8.3.3 UV-Visible measurements

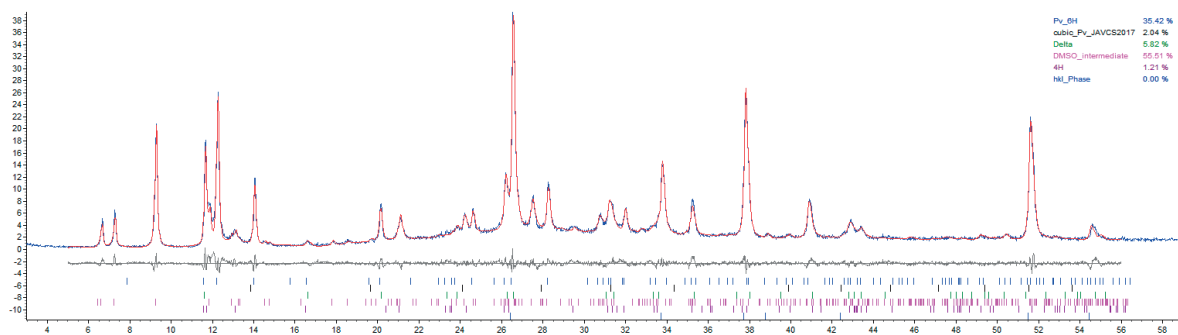
Perovskite films were spin-coated using procedure and compositions described below onto plasma-cleaned 2x2cm FTO-covered glass substrates. Absorption measurements were performed using Perkin Elmer Lambda 950S equipped with an integrating sphere.

8.3.4 SEM-EDX measurements

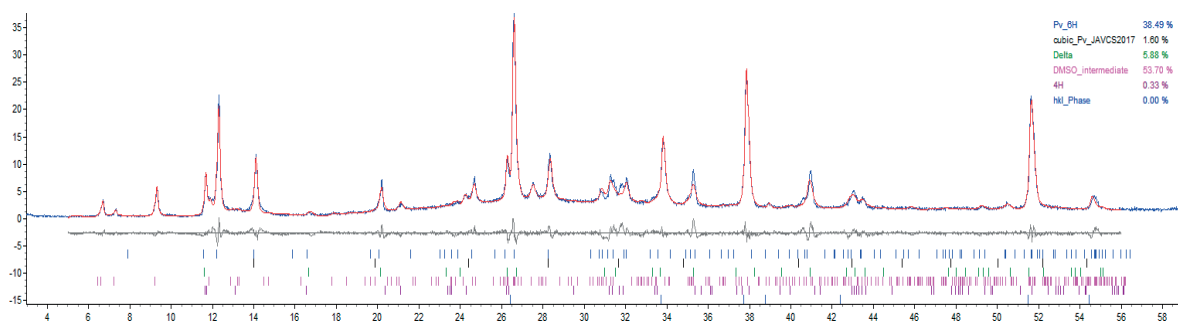
EDX analysis (8kV) was carried out using a FEI Teneo microscope equipped with an EDX detector. The single crystals were placed on SEM pin stubs covered with a conductive carbon film.

8.3.5 Rietveld refinements

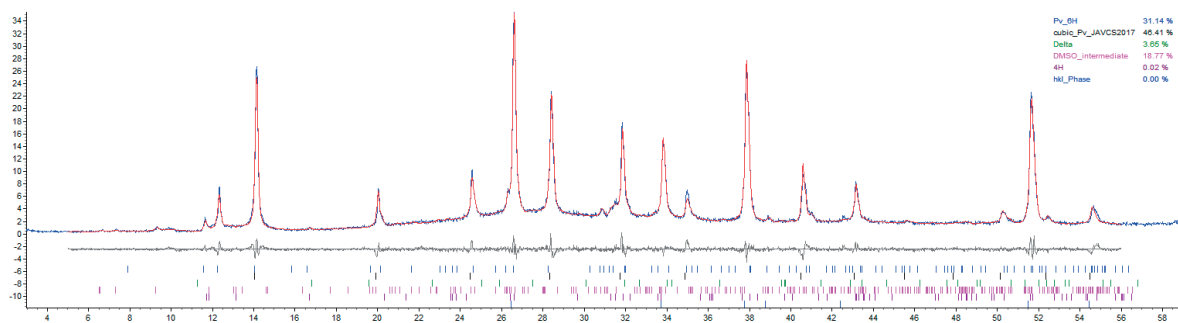
Rietveld plots generated by Topas for I85/Br15 films heated during 0, 10, 20, 30 and 60s, refined on data measured in-house. These refinements were carried out by Dr. Pascal Schouwink (EPFL).



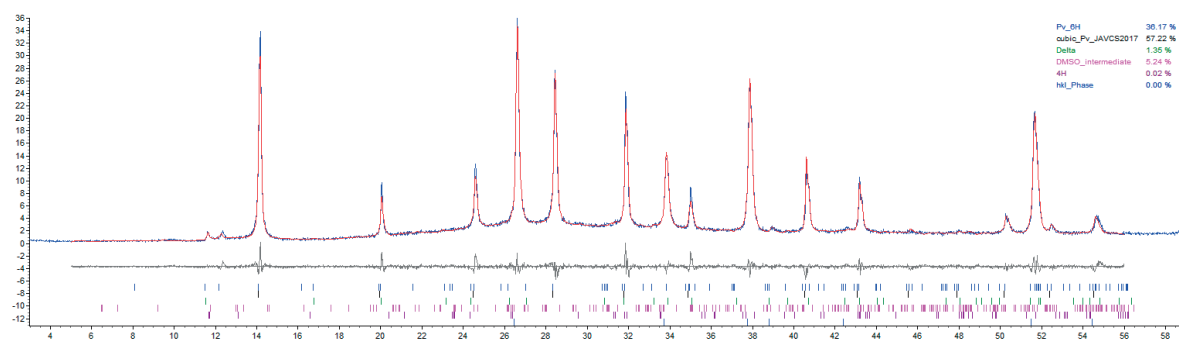
0s



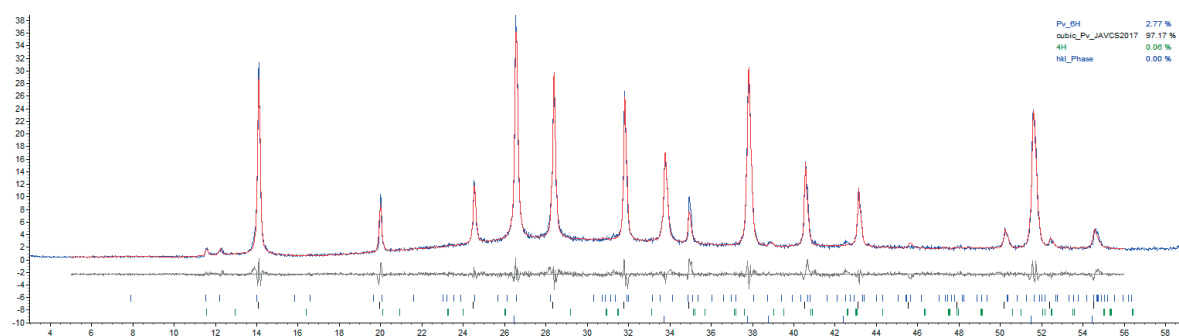
10s



20s



30s



60s

8.3.6 Preparation of perovskite precursor solutions

The perovskite precursor solutions were always prepared by weighing in four powders, i.e. PbI_2 (TCI), PbBr_2 (TCI), MABr (Dyesol), FAI (Dyesol) with the desired proportions, before adding 1ml DMF/DMSO (4:1 v/v) mixture. PbI_2 /FAI ratio is 1.05 and concentration of Pb^{2+} 1.27-1.29M. The solutions were stirred at room temperature overnight. The exact compositions are as follows:

$(\text{FAPbI}_3)_{0.50}(\text{MAPbBr}_3)_{0.50}$: PbI_2 (303.0mg); PbBr_2 (229.0mg); FAI(106.4mg); MABr(68.5mg)

$(\text{FAPbI}_3)_{0.60}(\text{MAPbBr}_3)_{0.40}$: PbI_2 (359.0mg); PbBr_2 (181.5mg); FAI(127.2mg); MABr(55.2mg)

$(\text{FAPbI}_3)_{0.70}(\text{MAPbBr}_3)_{0.30}$: PbI_2 (421.0mg); PbBr_2 (136.2mg); FAI(149.0mg); MABr(41.4mg)

$(\text{FAPbI}_3)_{0.80}(\text{MAPbBr}_3)_{0.20}$: PbI_2 (479.5mg); PbBr_2 (91.0mg); FAI(170.3mg); MABr(27.7mg)

$(\text{FAPbI}_3)_{0.85}(\text{MAPbBr}_3)_{0.15}$: PbI_2 (508.0mg); PbBr_2 (68.0mg); FAI(180.5mg); MABr(20.7mg)

$(\text{FAPbI}_3)_{0.90}(\text{MAPbBr}_3)_{0.10}$: PbI_2 (537.0mg); PbBr_2 (13.9mg); FAI(190.8mg); MABr(45.4mg)

$[\text{CsPbI}_3]_x[(\text{FAPbI}_3)_{0.85}(\text{MAPbBr}_3)_{0.15}]_{1-x}$ was prepared by mixing the desired amount of 1M stock solution of CsPbI_3 in DMF/DMSO (4:1 v/v) with $(\text{FAPbI}_3)_{0.85}(\text{MAPbBr}_3)_{0.15}$

8.3.7 Tolerance factor calculations

The radii are based on the revisited values from reference Travis et al. The tolerance factor of the mixed structures is approximated by: $t(\text{FAPbI}_3)_x(\text{MAPbBr}_3)_{1-x} = x*t(\text{FAPbI}_3) + (1-x)*t(\text{MAPbBr}_3)$ and $t(\text{CsPbI}_3)_y[(\text{FAPbI}_3)_{0.85}(\text{MAPbBr}_3)_{0.15}]_{1-y} = y*t(\text{FAPbI}_3)_x(\text{MAPbBr}_3)_{1-x} + (1-y)*t(\text{CsPbI}_3)$

The radii are as follows: $r(\text{Pb}^{2+}) = 0.98\text{\AA}$ for Bromide perovskite and $r(\text{Pb}^{2+}) = 1.03\text{\AA}$ for Iodide perovskite. $r(\text{Cs}^+) = 1.67\text{\AA}$; $r(\text{MA}^+) = 2.16\text{\AA}$; $r(\text{FA}^+) = 2.53\text{\AA}$; $r(\text{I}^-) = 2.20\text{\AA}$; $r(\text{Br}^-) = 1.96\text{\AA}$

8.3.8 Thin film preparation

Thin perovskite films were prepared following a one-step anti-solvent approach. Inside a Nitrogen-filled glovebox, perovskite precursor solutions were spin-coated on plasma-cleaned FTO glass using a 2-step spin coating procedure (step1: 10sec, 1000rpm 1000rpm/s; step2: 15sec 5000rpm. 3000rpm/s). 110 μl chlorobenzene are poured on the film 5 seconds prior to the end.

8.3.9 HIM-SIMS measurements

Measurements were performed using an in-house developed SIMS detector mounted on a Zeiss Helium Ion Microscope (NanoFab). Cesium secondary ions were collected in positive mode (+500V) upon Ne bombardment (25keV).

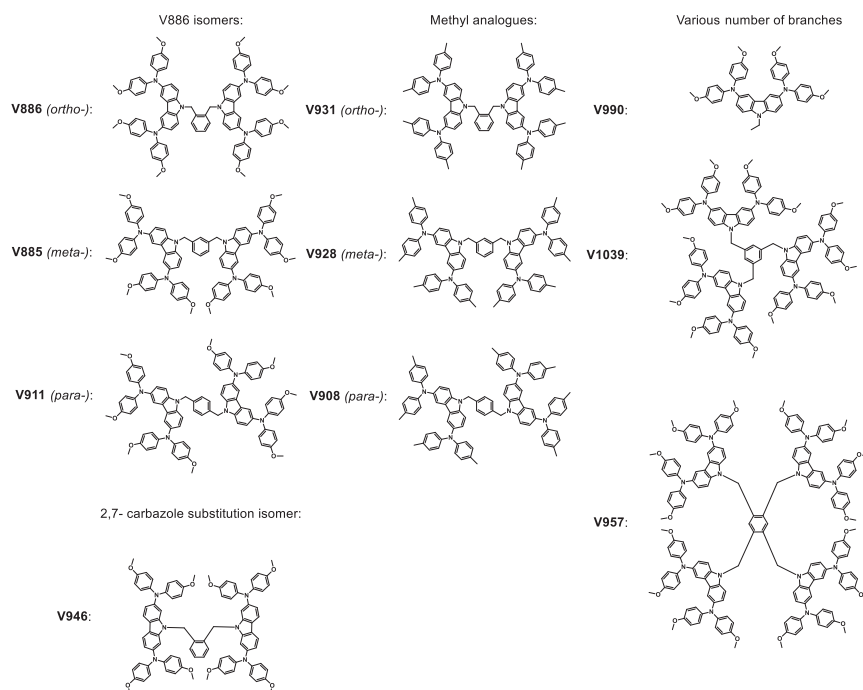
8.3.10 KPFM measurements

Images of height trace and surface potential were obtained using a Cypher atomic force microscope (Asylum Research) under ambient conditions. Image treatment was carried out using Asylum Research software based on Igor Pro.

8.4 Appendix to Chapter 6

8.4.1 Structures of the various carbazole derivatives

These molecules were synthesized by Artiom Magomedov (Kaunas University).



8.4.2 Solar cell performance of carbazole derivatives

These performance data are based on $[\text{CsPbI}_3]_{0.10}[(\text{FAPbI}_3)_{0.85}(\text{MAPbBr}_3)_{0.15}]_{0.90}$ perovskite solar cells fabricated by Dr. Sanghyun Park (EPFL).

Compound	Scan	J_{sc} [mA/cm ²]	V_{oc} [V]	FF	PCE [%]	<i>Average PCE</i> [%]
Spiro-OMeTAD	Reverse	22.25	1.11	0.761	18.79	
V886	Reverse	22.09	1.107	0.757	18.45	<i>18.41</i>
	Forward	22.07	1.092	0.762	18.38	
V885	Reverse	22.43	1.104	0.764	18.92	<i>18.78</i>
	Forward	22.39	1.089	0.765	18.65	
V911	Reverse	22.4	1.103	0.763	18.86	<i>18.72</i>
	Forward	22.38	1.087	0.764	18.59	
V931	Reverse	21.02	1.078	0.719	16.30	<i>16.02</i>
	Forward	20.92	1.071	0.703	15.74	
V928	Reverse	21.83	1.038	0.73	16.54	<i>16.41</i>
	Forward	21.78	1.025	0.73	16.28	
V908	Reverse	21.31	1.044	0.735	16.35	<i>16.41</i>
	Forward	21.28	1.032	0.75	16.47	
V990	Reverse	12.58	0.947	0.421	5.02	
V1039	Reverse	22.10	1.054	0.723	16.84	<i>17.11</i>
	Forward	22.08	1.045	0.754	17.39	

Appendix

V957	Reverse	22.12	1.041	0.729	16.78	<i>16.92</i>
	Forward	22.10	1.025	0.754	17.07	
V946	Reverse	21.86	1.068	0.730	17.02	<i>17.07</i>
	Forward	21.84	1.050	0.747	17.12	

References

- (1) The Paris Agreement - main page http://unfccc.int/paris_agreement/items/9485.php (accessed Dec 4, 2017).
- (2) Jacobson, M. Z.; Delucchi, M. A.; Bauer, Z. A. F.; Goodman, S. C.; Chapman, W. E.; Cameron, M. A.; Bozonnat, C.; Chobadi, L.; Clonts, H. A.; Enevoldsen, P.; Erwin, J. R.; Fobi, S. N.; Goldstrom, O. K.; Hennessy, E. M.; Liu, J.; Lo, J.; Meyer, C. B.; Morris, S. B.; Moy, K. R.; O'Neill, P. L.; Petkov, I.; Redfern, S.; Schucker, R.; Sontag, M. A.; Wang, J.; Weiner, E.; Yachanin, A. S. *Joule*.
- (3) World energy supply. <http://elways.se/world-energy-supply/?lang=en> (accessed Dec 1, 2017)
- (4) Green, M. A.; Emery, K.; Hishikawa, Y.; Warta, W.; Dunlop, E. D. *Prog. Photovolt. Res. Appl.* **2015**, *23* (1), 1.
- (5) Dou, L.; You, J.; Hong, Z.; Xu, Z.; Li, G.; Street, R. A.; Yang, Y. *Adv. Mater.* **2013**, *25* (46), 6642.
- (6) Hagfeldt, A.; Boschloo, G.; Sun, L.; Kloo, L.; Pettersson, H. *Chem. Rev.* **2010**, *110* (11), 6595.
- (7) Chen, C.-C.; Chang, W.-H.; Yoshimura, K.; Ohya, K.; You, J.; Gao, J.; Hong, Z.; Yang, Y. *Adv. Mater.* **2014**, *26* (32), 5670.
- (8) Mathew, S.; Yella, A.; Gao, P.; Humphry-Baker, R.; Curchod, B. F. E.; Ashari-Astani, N.; Tavernelli, I.; Rothlisberger, U.; Nazeeruddin, M. K.; Grätzel, M. *Nat. Chem.* **2014**, *6* (3), 242.
- (9) Kakiage, K.; Aoyama, Y.; Yano, T.; Oya, K.; Fujisawa, J.; Hanaya, M. *Chem. Commun.* **2015**, *51* (88), 15894.
- (10) Kojima, A.; Teshima, K.; Shirai, Y.; Miyasaka, T. *J. Am. Chem. Soc.* **2009**, *131* (17), 6050.
- (11) These are the top 10 emerging technologies of 2016 <https://www.weforum.org/agenda/2016/06/top-10-emerging-technologies-2016/> (accessed Jul 18, 2016).
- (12) Yang, W. S.; Park, B.-W.; Jung, E. H.; Jeon, N. J.; Kim, Y. C.; Lee, D. U.; Shin, S. S.; Seo, J.; Kim, E. K.; Noh, J. H.; Seok, S. I. *Science* **2017**, *356* (6345), 1376.
- (13) Burschka, J.; Pellet, N.; Moon, S.-J.; Humphry-Baker, R.; Gao, P.; Nazeeruddin, M. K.; Grätzel, M. *Nature* **2013**, *499* (7458), 316.
- (14) Lee, M. M.; Teuscher, J.; Miyasaka, T.; Murakami, T. N.; Snaith, H. J. *Science* **2012**, *338* (6107), 643.
- (15) Janani, M.; Srikrishnarka, P.; Nair, S. V.; Nair, A. S. *J. Mater. Chem. A* **2015**, *3* (35), 17914.
- (16) Li, Y.; Meng, L.; Yang, Y. (Michael); Xu, G.; Hong, Z.; Chen, Q.; You, J.; Li, G.; Yang, Y.; Li, Y. *Nat. Commun.* **2016**, *7*, 10214.
- (17) Freitag, M.; Teuscher, J.; Saygili, Y.; Zhang, X.; Giordano, F.; Liska, P.; Hua, J.; Zakeeruddin, S. M.; Moser, J.-E.; Grätzel, M.; Hagfeldt, A. *Nat. Photonics* **2017**, *11* (6), 372.
- (18) Edri, E.; Kirmayer, S.; Cahen, D.; Hodes, G. *J. Phys. Chem. Lett.* **2013**, *4* (6), 897.
- (19) Feng, X.; Shankar, K.; Paulose, M.; Grimes, C. A. *Angew. Chem.* **2009**, *121* (43), 8239.
- (20) Tesla Powerwall <https://www.tesla.com/powerwall> (accessed Dec 4, 2017).
- (21) Møller, C. K. *Nature* **1958**, *182*, 1436.
- (22) Weber, D. Z. *Naturforschung* **1978**, *33b*, 1443.
- (23) Weber, D. Z. *Naturforschung* **1978**, *33b*, 862.
- (24) Mitzi, D. B.; Wang, S.; Feild, C. A.; Chess, C. A.; Guloy, A. M. *Science* **1995**, *267* (5203), 1473.
- (25) Mitzi, D. B. In *Progress in Inorganic Chemistry*; Karlin, K. D., Ed.; John Wiley & Sons, Inc., 1999; pp 1–121.
- (26) Mitzi, D. B.; Chondroudis, K.; Kagan, C. R. *IBM J. Res. Dev.* **2001**, *45* (1), 29.
- (27) Kojima, A.; Teshima, K.; Shirai, Y.; Miyasaka, T. *J. Am. Chem. Soc.* **2009**, *131* (17), 6050.
- (28) O'Regan, B.; Grätzel, M. *Nature* **1991**, *353* (6346), 737.
- (29) Miyata, A.; Mitioglu, A.; Plochocka, P.; Portugall, O.; Wang, J. T.-W.; Stranks, S. D.; Snaith, H. J.; Nicholas, R. J. *Nat. Phys.* **2015**, *11* (7), 582.
- (30) Stranks, S. D.; Snaith, H. J. *Nat. Nanotechnol.* **2015**, *10* (5), 391.

- (31) Pellet, N.; Gao, P.; Gregori, G.; Yang, T.-Y.; Nazeeruddin, M. K.; Maier, J.; Grätzel, M. *Angew. Chem. Int. Ed.* **2014**, *53* (12), 3151.
- (32) Choi, H.; Jeong, J.; Kim, H.-B.; Kim, S.; Walker, B.; Kim, G.-H.; Kim, J. Y. *Nano Energy* **2014**, *7* (Supplement C), 80.
- (33) Yi, C.; Luo, J.; Meloni, S.; Boziki, A.; Ashari-Astani, N.; Grätzel, C.; M. Zakeeruddin, S.; Röthlisberger, U.; Grätzel, M. *Energy Environ. Sci.* **2016**, *9* (2), 656.
- (34) Kaltzoglou, A.; Stoumpos, C. C.; Kontos, A. G.; Manolis, G. K.; Papadopoulos, K.; Papadokostaki, K. G.; Psycharis, V.; Tang, C. C.; Jung, Y.-K.; Walsh, A.; Kanatzidis, M. G.; Falaras, P. *Inorg. Chem.* **2017**, *56* (11), 6302.
- (35) F. Akbulatov, A.; A. Frolova, L.; V. Anokhin, D.; L. Gerasimov, K.; N. Dremova, N.; A. Troshin, P. *J. Mater. Chem. A* **2016**, *4* (47), 18378.
- (36) De Marco, N.; Zhou, H.; Chen, Q.; Sun, P.; Liu, Z.; Meng, L.; Yao, E.-P.; Liu, Y.; Schiffer, A.; Yang, Y. *Nano Lett.* **2016**, *16* (2), 1009.
- (37) Shao, S.; Liu, J.; Portale, G.; Fang, H.-H.; Blake, G. R.; ten Brink, G. H.; Koster, L. J. A.; Loi, M. A. *Adv. Energy Mater.* n/a.
- (38) Zhao, D.; Yu, Y.; Wang, C.; Liao, W.; Shrestha, N.; Grice, C. R.; Cimaroli, A. J.; Guan, L.; Ellingson, R. J.; Zhu, K.; Zhao, X.; Xiong, R.-G.; Yan, Y. *Nat. Energy* **2017**, *2* (4), 17018.
- (39) Hoke, E. T.; Slotcavage, D. J.; Dohner, E. R.; Bowring, A. R.; Karunadasa, H. I.; McGehee, M. D. *Chem. Sci.* **2014**, *6* (1), 613.
- (40) Jeon, N. J.; Noh, J. H.; Yang, W. S.; Kim, Y. C.; Ryu, S.; Seo, J.; Seok, S. I. *Nature* **2015**, *517* (7535), 476.
- (41) Jeon, N. J.; Noh, J. H.; Kim, Y. C.; Yang, W. S.; Ryu, S.; Seok, S. I. *Nat. Mater.* **2014**, *13* (9), 897.
- (42) Li, X.; Bi, D.; Yi, C.; Décoppet, J.-D.; Luo, J.; Zakeeruddin, S. M.; Hagfeldt, A.; Grätzel, M. *Science* **2016**, *353* (6294), 58.
- (43) Saliba, M.; Matsui, T.; Seo, J.-Y.; Domanski, K.; Correa-Baena, J.-P.; Nazeeruddin, M. K.; Zakeeruddin, S. M.; Tress, W.; Abate, A.; Hagfeldt, A.; Grätzel, M. *Energy Environ. Sci.* **2016**, *9* (6), 1989.
- (44) Matsui, T.; Seo, J.-Y.; Saliba, M.; Zakeeruddin, S. M.; Grätzel, M. *Adv. Mater.* **2017**, *29* (15), n/a.
- (45) Saliba, M.; Matsui, T.; Domanski, K.; Seo, J.-Y.; Ummadisingu, A.; Zakeeruddin, S. M.; Correa-Baena, J.-P.; Tress, W. R.; Abate, A.; Hagfeldt, A.; Grätzel, M. *Science* **2016**, *354* (6309), 206.
- (46) Kubicki, D. J.; Prochowicz, D.; Hofstetter, A.; Zakeeruddin, S. M.; Grätzel, M.; Emsley, L. *J. Am. Chem. Soc.* **2017**, *139* (40), 14173.
- (47) Giordano, F.; Abate, A.; Correa Baena, J. P.; Saliba, M.; Matsui, T.; Im, S. H.; Zakeeruddin, S. M.; Nazeeruddin, M. K.; Hagfeldt, A.; Grätzel, M. *Nat. Commun.* **2016**, *7*.
- (48) Ke, W.; Fang, G.; Liu, Q.; Xiong, L.; Qin, P.; Tao, H.; Wang, J.; Lei, H.; Li, B.; Wan, J.; Yang, G.; Yan, Y. *J. Am. Chem. Soc.* **2015**, *137* (21), 6730.
- (49) Malinkiewicz, O.; Yella, A.; Lee, Y. H.; Espallargas, G. M.; Graetzel, M.; Nazeeruddin, M. K.; Bolink, H. J. *Nat. Photonics* **2014**, *8* (2), 128.
- (50) Streetman, B. G.; Banerjee, S. K. Solid state electronic devices <http://cds.cern.ch/record/1280702> (accessed Dec 5, 2017).
- (51) Tanaka, K.; Takahashi, T.; Ban, T.; Kondo, T.; Uchida, K.; Miura, N. *Solid State Commun.* **2003**, *127* (9), 619.
- (52) Even, J.; Pedesseau, L.; Katan, C. *J. Phys. Chem. C* **2014**, *118* (22), 11566.
- (53) Deschler, F.; Price, M.; Pathak, S.; Klintberg, L. E.; Jarausch, D.-D.; Hügler, R.; Hüttner, S.; Leijtens, T.; Stranks, S. D.; Snaith, H. J.; Atatüre, M.; Phillips, R. T.; Friend, R. H. *J. Phys. Chem. Lett.* **2014**, *5* (8), 1421.
- (54) Wehrenfennig, C.; Eperon, G. E.; Johnston, M. B.; Snaith, H. J.; Herz, L. M. *Adv. Mater.* **2014**, *26* (10), 1584.
- (55) Stranks, S. D.; Eperon, G. E.; Grancini, G.; Menelaou, C.; Alcocer, M. J. P.; Leijtens, T.; Herz, L. M.; Petrozza, A.; Snaith, H. J. *Science* **2013**, *342* (6156), 341.
- (56) Stranks, S. D.; Burlakov, V. M.; Leijtens, T.; Ball, J. M.; Goriely, A.; Snaith, H. J. *Phys. Rev. Appl.* **2014**, *2* (3), 034007.
- (57) D'Innocenzo, V.; Grancini, G.; Alcocer, M. J. P.; Kandada, A. R. S.; Stranks, S. D.; Lee, M. M.; Lanzani, G.; Snaith, H. J.; Petrozza, A. *Nat. Commun.* **2014**, *5*, 3586.
- (58) Hutter, E. M.; Gélvez-Rueda, M. C.; Osherov, A.; Bulović, V.; Grozema, F. C.; Stranks, S. D.; Savenije, T. *J. Nat. Mater.* **2017**, *16* (1), 115.
- (59) Kadro, J. M.; Nonomura, K.; Gachet, D.; Grätzel, M.; Hagfeldt, A. *Sci. Reports* **2015**, *5*, 11654.
- (60) Tilley, R. *Perovskites: structure-property relationships*; John Wiley & Sons, 2016.

- (61) Kuang, X.; B. Allix, M. M.; B. Claridge, J.; J. Niu, H.; J. Rosseinsky, M.; M. Ibberson, R.; M. Iddles, D. *J. Mater. Chem.* **2006**, *16* (11), 1038.
- (62) Snaith, H. J.; Abate, A.; Ball, J. M.; Eperon, G. E.; Leijtens, T.; Noel, N. K.; Stranks, S. D.; Wang, J. T.-W.; Wojciechowski, K.; Zhang, W. *J. Phys. Chem. Lett.* **2014**, *5* (9), 1511.
- (63) L. Unger, E.; T. Hoke, E.; D. Bailie, C.; H. Nguyen, W.; R. Bowring, A.; Heumüller, T.; G. Christoforo, M.; D. McGehee, M. *Energy Environ. Sci.* **2014**, *7* (11), 3690.
- (64) Zhao, C.; Chen, B.; Qiao, X.; Luan, L.; Lu, K.; Hu, B. *Adv. Energy Mater.* **2015**, *5* (14), n/a.
- (65) Wirtz, T.; Vanhove, N.; Pillatsch, L.; Dowsett, D.; Sijbrandij, S.; Notte, J. *Appl. Phys. Lett.* **2012**, *101* (4), 041601.
- (66) Orloff, J.; Swanson, L. W.; Utlaut, M. *J. Vac. Sci. Technol. B Microelectron. Nanometer Struct. Process. Meas. Phenom.* **1996**, *14* (6), 3759.
- (67) Wirtz, T.; Dowsett, D.; Philipp, P. In *Helium Ion Microscopy*; G. Hlawacek and A. Götzhäuser.
- (68) Wirtz, T.; Philipp, P.; Audinot, J.-N.; Dowsett, D.; Eswara, S. *Nanotechnology* **2015**, *26* (43), 434001.
- (69) Oechsner, H.; Schoof, H.; Stumpe, E. *Surf. Sci.* **1978**, *76* (2), 343.
- (70) Roldán-Carmona, C.; Gratia, P.; Zimmermann, I.; Grancini, G.; Gao, P.; Graetzel, M.; Nazeeruddin, M. K. *Energy Environ. Sci.* **2015**, *8* (12), 3550.
- (71) Xiao, Z.; Bi, C.; Shao, Y.; Dong, Q.; Wang, Q.; Yuan, Y.; Wang, C.; Gao, Y.; Huang, J. *Energy Environ. Sci.* **2014**, *7* (8), 2619.
- (72) Chen, Q.; Zhou, H.; Hong, Z.; Luo, S.; Duan, H.-S.; Wang, H.-H.; Liu, Y.; Li, G.; Yang, Y. *J. Am. Chem. Soc.* **2014**, *136* (2), 622.
- (73) Ahn, N.; Son, D.-Y.; Jang, I.-H.; Kang, S. M.; Choi, M.; Park, N.-G. *J. Am. Chem. Soc.* **2015**, *137* (27), 8696.
- (74) Im, J.-H.; Jang, I.-H.; Pellet, N.; Grätzel, M.; Park, N.-G. *Nat. Nanotechnol.* **2014**, *9* (11), 927.
- (75) A. Kulkarni, S.; Baikie, T.; P. Boix, P.; Yantara, N.; Mathews, N.; Mhaisalkar, S. *J. Mater. Chem. A* **2014**, *2* (24), 9221.
- (76) Liu, M.; Johnston, M. B.; Snaith, H. J. *Nature* **2013**, *501* (7467), 395.
- (77) Delugas, P.; Filippetti, A.; Mattoni, A. *Phys. Rev. B* **2015**, *92* (4), 045301.
- (78) Unger, E. L.; Bowring, A. R.; Tassone, C. J.; Pool, V. L.; Gold-Parker, A.; Cheacharoen, R.; Stone, K. H.; Hoke, E. T.; Toney, M. F.; McGehee, M. D. *Chem. Mater.* **2014**, *26* (24), 7158.
- (79) D'Innocenzo, V.; Srimath Kandada, A. R.; De Bastiani, M.; Gandini, M.; Petrozza, A. *J. Am. Chem. Soc.* **2014**, *136* (51), 17730.
- (80) Grancini, G.; Marras, S.; Prato, M.; Giannini, C.; Quarti, C.; De Angelis, F.; De Bastiani, M.; Eperon, G. E.; Snaith, H. J.; Manna, L.; Petrozza, A. *J. Phys. Chem. Lett.* **2014**, *5* (21), 3836.
- (81) Stranks, S. D.; Eperon, G. E.; Grancini, G.; Menelaou, C.; Alcocer, M. J. P.; Leijtens, T.; Herz, L. M.; Petrozza, A.; Snaith, H. J. *Science* **2013**, *342* (6156), 341.
- (82) Noel, N. K.; Abate, A.; Stranks, S. D.; Parrott, E. S.; Burlakov, V. M.; Goriely, A.; Snaith, H. J. *ACS Nano* **2014**, *8* (10), 9815.
- (83) De Bastiani, M.; D'Innocenzo, V.; Stranks, S. D.; Snaith, H. J.; Petrozza, A. *APL Mater.* **2014**, *2* (8), 081509.
- (84) Mosconi, E.; Ronca, E.; De Angelis, F. *J. Phys. Chem. Lett.* **2014**, *5* (15), 2619.
- (85) Mosconi, E.; Grancini, G.; Roldán-Carmona, C.; Gratia, P.; Zimmermann, I.; Nazeeruddin, M. K.; De Angelis, F. *Chem. Mater.* **2016**, *28* (11), 3612.
- (86) Son, D.-Y.; Lee, J.-W.; Choi, Y. J.; Jang, I.-H.; Lee, S.; Yoo, P. J.; Shin, H.; Ahn, N.; Choi, M.; Kim, D.; Park, N.-G. *Nat. Energy* **2016**, *1* (7), 16081.
- (87) Edri, E.; Kirmayer, S.; Henning, A.; Mukhopadhyay, S.; Gartsman, K.; Rosenwaks, Y.; Hodes, G.; Cahen, D. *Nano Lett.* **2014**, *14* (2), 1000.
- (88) Gratia, P.; Grancini, G.; Audinot, J.-N.; Jeanbourquin, X.; Mosconi, E.; Zimmermann, I.; Dowsett, D.; Lee, Y.; Grätzel, M.; De Angelis, F.; others. *J. Am. Chem. Soc.* **2016**.
- (89) Bi, D.; Tress, W.; Dar, M. I.; Gao, P.; Luo, J.; Renevier, C.; Schenk, K.; Abate, A.; Giordano, F.; Baena, J.-P. C.; Decoppet, J.-D.; Zakeeruddin, S. M.; Nazeeruddin, M. K.; Grätzel, M.; Hagfeldt, A. *Sci. Adv.* **2016**, *2* (1), e1501170.
- (90) Pellet, N.; Teuscher, J.; Maier, J.; Grätzel, M. *Chem. Mater.* **2015**, *27* (6), 2181.
- (91) Jesper Jacobsson, T.; Correa-Baena, J.-P.; Pazoki, M.; Saliba, M.; Schenk, K.; Grätzel, M.; Hagfeldt, A. *Energy Environ. Sci.* **2016**, *9* (5), 1706.
- (92) Yoon, S. J.; Draguta, S.; Manser, J. S.; Sharia, O.; Schneider, W. F.; Kuno, M.; Kamat, P. V. *ACS Energy Lett.*

- (93) deQuilletes, D. W.; Zhang, W.; Burlakov, V. M.; Graham, D. J.; Leijtens, T.; Oshero, A.; Bulović, V.; Snaith, H. J.; Ginger, D. S.; Stranks, S. D. *Nat. Commun.* **2016**, *7*, 11683.
- (94) Leijtens, T.; Hoke, E. T.; Grancini, G.; Slotcavage, D. J.; Eperon, G. E.; Ball, J. M.; De Bastiani, M.; Bowring, A. R.; Martino, N.; Wojciechowski, K.; McGehee, M. D.; Snaith, H. J.; Petrozza, A. *Adv. Energy Mater.* **2015**, *5* (20), n/a.
- (95) Draguta, S.; Thakur, S.; Morozov, Y. V.; Wang, Y.; Manser, J. S.; Kamat, P. V.; Kuno, M. *J. Phys. Chem. Lett.* **2016**, *7* (4), 715.
- (96) Eperon, G. E.; Stranks, S. D.; Menelaou, C.; Johnston, M. B.; Herz, L. M.; Snaith, H. J. *Energy Environ. Sci.* **2014**, *7* (3), 982.
- (97) Quarti, C.; Grancini, G.; Mosconi, E.; Bruno, P.; Ball, J. M.; Lee, M. M.; Snaith, H. J.; Petrozza, A.; Angelis, F. D. *J. Phys. Chem. Lett.* **2014**, *5* (2), 279.
- (98) Mosconi, E.; Amat, A.; Nazeeruddin, M. K.; Grätzel, M.; De Angelis, F. *J. Phys. Chem. C* **2013**, *117* (27), 13902.
- (99) Gratia, P.; Zimmermann, I.; Schouwink, P.; Yum, J.-H.; Audinot, J.-N.; Sivula, K.; Wirtz, T.; Nazeeruddin, M. K. *ACS Energy Lett.* **2017**, 2686.
- (100) Beal, R. E.; Slotcavage, D. J.; Leijtens, T.; Bowring, A. R.; Belisle, R. A.; Nguyen, W. H.; Burkhard, G. F.; Hoke, E. T.; McGehee, M. D. *J. Phys. Chem. Lett.* **2016**, *7* (5), 746.
- (101) Lee, J.-W.; Kim, D.-H.; Kim, H.-S.; Seo, S.-W.; Cho, S. M.; Park, N.-G. *Adv. Energy Mater.* **2015**, *5* (20), n/a.
- (102) Stoumpos, C. C.; Malliakas, C. D.; Kanatzidis, M. G. *Inorg. Chem.* **2013**, *52* (15), 9019.
- (103) Xie, L.-Q.; Chen, L.; Nan, Z.-A.; Lin, H.-X.; Wang, T.; Zhan, D.-P.; Yan, J.-W.; Mao, B.-W.; Tian, Z.-Q. *J. Am. Chem. Soc.* **2017**, *139* (9), 3320.
- (104) Ramsdell, L. S. *Am. Mineral.* **1947**, *32* (1–2), 64.
- (105) Jagodzinski, H. *Acta Crystallogr.* **1949**, *2* (4), 201.
- (106) Travis, W.; K. Glover, E. N.; Bronstein, H.; O. Scanlon, D.; G. Palgrave, R. *Chem. Sci.* **2016**, *7* (7), 4548.
- (107) Kamminga, M. E.; de Wijs, G. A.; Havenith, R. W. A.; Blake, G. R.; Palstra, T. T. M. *Inorg. Chem.* **2017**, *56* (14), 8408.
- (108) Li, Z.; Yang, M.; Park, J.-S.; Wei, S.-H.; Berry, J. J.; Zhu, K. *Chem. Mater.* **2016**, *28* (1), 284.
- (109) Gratia, P.; Magomedov, A.; Malinauskas, T.; Daskeviciene, M.; Abate, A.; Ahmad, S.; Grätzel, M.; Getautis, V.; Nazeeruddin, M. K. *Angew. Chem. Int. Ed.* **2015**, *54* (39), 11409.
- (110) Rakstys, K.; Saliba, M.; Gao, P.; Gratia, P.; Kamarauskas, E.; Paek, S.; Jankauskas, V.; Nazeeruddin, M. K. *Angew. Chem. Int. Ed.* **2016**, *55* (26), 7464.
- (111) Cho, K. T.; Trukhina, O.; Roldán-Carmona, C.; Ince, M.; Gratia, P.; Grancini, G.; Gao, P.; Marszalek, T.; Pisula, W.; Reddy, P. Y.; others. *Adv. Energy Mater.* **2016**.
- (112) Molina-Ontoria, A.; Zimmermann, I.; Garcia-Benito, I.; Gratia, P.; Roldán-Carmona, C.; Aghazada, S.; Graetzel, M.; Nazeeruddin, M. K.; Martín, N. *Angew. Chem. Int. Ed.* **2016**, *55* (21), 6270.
- (113) Zimmermann, I.; Urieta-Mora, J.; Gratia, P.; Aragón, J.; Grancini, G.; Molina-Ontoria, A.; Ortí, E.; Martín, N.; Nazeeruddin, M. K. *Adv. Energy Mater.* **2016**.
- (114) Bach, U.; Lupo, D.; Comte, P.; Moser, J. E.; al, et. *Nature* **1998**, *395* (6702), 583.
- (115) Liu, J.; Wu, Y.; Qin, C.; Yang, X.; Yasuda, T.; Islam, A.; Zhang, K.; Peng, W.; Chen, W.; Han, L. *Energy Environ. Sci.* **2014**, *7* (9), 2963.
- (116) Jeon, N. J.; Lee, J.; Noh, J. H.; Nazeeruddin, M. K.; Grätzel, M.; Seok, S. I. *J. Am. Chem. Soc.* **2013**, *135* (51), 19087.
- (117) Krishna, A.; Sabba, D.; Li, H.; Yin, J.; P. Boix, P.; Soci, C.; G. Mhaisalkar, S.; C. Grimsdale, A. *Chem. Sci.* **2014**, *5* (7), 2702.
- (118) Choi, H.; Park, S.; Paek, S.; Ekanayake, P.; Khaja Nazeeruddin, M.; Ko, J. *J. Mater. Chem. A* **2014**, *2* (45), 19136.
- (119) Li, H.; Fu, K.; Hagfeldt, A.; Grätzel, M.; Mhaisalkar, S. G.; Grimsdale, A. C. *Angew. Chem. Int. Ed.* **2014**, *53* (16), 4085.
- (120) Xu, B.; Sheibani, E.; Liu, P.; Zhang, J.; Tian, H.; Vlachopoulos, N.; Boschloo, G.; Kloo, L.; Hagfeldt, A.; Sun, L. *Adv. Mater.* **2014**, *26* (38), 6629.
- (121) Qin, P.; Paek, S.; Dar, M. I.; Pellet, N.; Ko, J.; Grätzel, M.; Nazeeruddin, M. K. *J. Am. Chem. Soc.* **2014**, *136* (24), 8516.
- (122) Li, H.; Fu, K.; Boix, P. P.; Wong, L. H.; Hagfeldt, A.; Grätzel, M.; Mhaisalkar, S. G.; Grimsdale, A. C. *ChemSusChem* **2014**, *7* (12), 3420.
- (123) Burschka, J.; Dualeh, A.; Kessler, F.; Baranoff, E.; Cevey-Ha, N.-L.; Yi, C.; Nazeeruddin, M. K.; Grätzel, M. *J. Am. Chem. Soc.* **2011**, *133* (45), 18042.

-
- (124) Bailey, Z. M.; Christoforo, M. G.; Gratia, P.; Bowring, A. R.; Eberspacher, P.; Margulis, G. Y.; Cabanetos, C.; Beaujuge, P. M.; Salleo, A.; McGehee, M. D. *Adv. Mater.* **2013**, *25* (48), 7020.
- (125) Leijts, T.; Ding, I.-K.; Giovenzana, T.; Bloking, J. T.; McGehee, M. D.; Sellinger, A. *ACS Nano* **2012**, *6* (2), 1455.
- (126) Arora, N.; Dar, M. I.; Hinderhofer, A.; Pellet, N.; Schreiber, F.; Zakeeruddin, S. M.; Grätzel, M. *Science* **2017**, eaam5655.
- (127) Giannozzi, P.; Baroni, S.; Bonini, N.; Calandra, M.; Car, R.; Cavazzoni, C.; Davide Ceresoli; Chiarotti, G. L.; Cococcioni, M.; Dabo, I.; Corso, A. D.; Gironcoli, S. de; Fabris, S.; Fratesi, G.; Gebauer, R.; Gerstmann, U.; Gougoussis, C.; Anton Kokalj; Lazzeri, M.; Martin-Samos, L.; Marzari, N.; Mauri, F.; Mazzarello, R.; Stefano Paolini; Pasquarello, A.; Paulatto, L.; Sbraccia, C.; Scandolo, S.; Sclauzero, G.; Seitsonen, A. P.; Smogunov, A.; Umari, P.; Wentzcovitch, R. M. *J. Phys. Condens. Matter* **2009**, *21* (39), 395502.
- (128) Evarestov, R. A. *Phys. Rev. B* **2011**, *83* (1), 014105.
- (129) Sheldrick, G. M. *Acta Crystallogr. Sect. Found. Adv.* **2015**, *71* (1), 3.
- (130) Sheldrick, G. M. *Acta Crystallogr. Sect. C Struct. Chem.* **2015**, *71* (1), 3.
- (131) Dolomanov, O. V.; Bourhis, L. J.; Gildea, R. J.; Howard, J. a. K.; Puschmann, H. *J. Appl. Crystallogr.* **2009**, *42* (2), 339.

Acknowledgements

First, I would like to thank my supervisors Prof. Mohammad Khaja Nazeeruddin and Prof. Michael Grätzel for giving me the possibility to explore my scientific creativity and acquire valuable in-depth research experience. Next, my colleagues at GMF are sincerely acknowledged for making my stay in the research group as enjoyable as possible. In particular, I would like to thank: Iwan Zimmermann for the extensive scientific collaborations, numerous scientific discussions, sharing of ideas and fun outdoor activities; Sadig Aghazada for discussions, scientific support, coffee breaks and many more activities; Giulia Grancini for fruitful scientific collaboration and many laughs; Kasparas Rakstys for the many fun activities.

Moreover, Sanghyun, Kyung-taek, Cristina and Robin are acknowledged for helpful discussions; Pascal Schouwink for assistance and introduction into X-ray diffraction. LPI people, namely Amita, Norman, Ibrahim, Neha, Fabrizio, Wolfgang and many more were making my stay in Lausanne most enjoyable.

I acknowledge Laurent Seydoux, Annabelle Coquoz from the Sion chemical store; Marie Jirousek, Jacky Gremaud from the Lausanne chemical store as well as the team of the EPFL Valais mechanical workshop, namely Robin Délèze and Stéphane Voeffray, the electrical workshop, namely Manuel Tschumi and Patrick Favre, as well as Cédric Passerini for IT related questions. They were of great help for any kind of technical questions and building and design of the setups described in this thesis.

I would also like to acknowledge my parents for their strong support throughout the duration of my PhD studies.

Last but not least I would like to thank Géraldine Gfeller for amazingly helpful administrative assistance and the organization of fun activities; Heidi Francelet, Carmen Biagini and Anne Lene Odegaard for their superb administrative assistance.

Curriculum Vitae

Paul Gratia

Personal Information

Birthdate **16.04.1989.**
Birthplace **Kaiserslautern (Germany).**
Nationality **Luxembourgish.**

Education

- 2013- **PhD Candidate in Chemistry and Chemical Engineering.**
Swiss Federal Institute of Technology (EPFL), Sion (VS), Switzerland
- 2011-2013 **Master of Science MSc in Chemistry.**
Swiss Federal Institute of Technology (EPFL), Lausanne, Switzerland
- 2008-2011 **Bachelor of Science BSc in Chemistry and Chemical Engineering.**
Swiss Federal Institute of Technology (EPFL), Lausanne, Switzerland
- 2001-2008 **Highschool Diploma, graduation in 'Natural sciences and Mathematics' with highest qualification : 'very good'; Lycée Michel Rodange, Luxembourg.**

Research Experience

- 2013- **Doctoral researcher, Subject : Compositional Characterization of Organo-Lead tri-halide Perovskite Solar Cells, Supervisors : Prof. Nazeeruddin and Prof. Grätzel.**
EPFL, Switzerland
- 2012-2013 **Master Thesis, Title : Transparent Composite Electrodes for Hybrid Tandem Solar Cells, Duration : 6 months, Supervisors : Prof. McGehee (Stanford) and Prof. Grätzel (EPFL).**
Stanford University, USA
- 2010 **Internship, Subject : Hybrid Organic Solar Cells, Duration : 6 weeks, Supervisors : Prof. Unger, Prof. Boschloo, Group of Prof. Hagfeldt.**
Uppsala University, Sweden

Teaching Experience

Teaching Assistant of following classes at EPFL (Chemistry department). Includes : exercise session supervision (all) ; exam corrections (all) ; participating in the design of exam and exercise questions (CH-241 and CH-242).

- 2016-2017 **Statistical Thermodynamics (CH-242), Prof. Hagfeldt.**
- 2015-2016 **Statistical Thermodynamics (CH-242), Prof. Hagfeldt.**
- 2014-2015 **Chemical Thermodynamics (CH-241), Prof. Hagfeldt.**
- 2014-2015 **General Chemistry (CH-102), Prof. Corminboeuf.**
- 2014-2015 **Chemical Equilibria and Reactivity (CH-101), Prof. Moser.**
- 2014-2015 **Chemistry Laboratory work (CH-108), Dr. Chauvin.**
- 2013-2014 **General Chemistry, Dr. Chauvin.**
- 2013-2014 **Chemical Thermodynamics I and II (CH-241/242), Prof. Grätzel.**

Conferences, Summer Schools and Awards

- 2017 **EPFL nomination for Global Young Scientist Summit (GYSS@oneNorth), Singapore, 5 selected among all PhDs and Post-docs applicants from EPFL. Selection of 320 worldwide.**
- 2017 **2017 Teaching Excellence Award (for teaching assistants), EPFL.**

108, rue de Lausanne – 1950 Sion (VS) – Switzerland
☎ +41 76 822 13 31 • 📞 +41 21 69 58236 • ✉ paul.gratia@epfl.ch
🌐 <http://gmf.epfl.ch/people>

1/2

- 2017 **2017 Chemistry Travel Award**, *Swiss Academy of Sciences (SCNAT)/Swiss Chemical Society (SCS)*, "contribution of 1000Chf toward active costs of conference participation", 40 awards for selected doctoral students from Swiss Universities ; call : once a year.
- 2016 **2nd International Conference on Perovskite Solar Cells and Optoelectronics (PSCO-2016)**.
Genoa, Italy
Nature Materials Award, *Best Student Poster in Materials Science*, Cash Prize.
- 2016 **10th edition of ISOPHOS International School on Hybrid and Organic Photovoltaics**.
Castiglione della Pescaia, Italy
- 2015 **International Conference on Solution Processed Innovative Solar Cells (SPINS15)**.
Santiago de Compostela, Spain
- 2015 **1st International Conference on Perovskite Solar Cells and Optoelectronics (PSCO-2015)**.
Ecublens, Switzerland
- 2015 **Hybrid and Organic Photovoltaics Conference (HOPV15)**.
Ecublens, Switzerland

Language Skills

English	<i>full professional proficiency</i>
German	<i>native/bilingual proficiency</i>
French	<i>native/bilingual proficiency</i>
Luxembourgish	<i>mother tongue</i>
Latin	<i>basics</i>

Miscellaneous

- 1995-2008 **Extensive Classical Music Education at the 'Luxembourg Music Conservatory'** , <http://www.conservatoire.lu>
- Piano (1995-2008) : Obtention of Diploma "1er prix"/ First prize and "Certificat Supérieur"; Solo Concert Pianist Performance with Orchestra (2006 and 2007)
 - Percussion (2001-2008), Musical Deciphering ("Déchiffrage") (2005-2006), Sollege (1995-2002), Chamber Music (2006-2008), Musical Composition (2006-2008)

108, rue de Lausanne – 1950 Sion (VS) – Switzerland

☎ +41 76 822 13 31 • 📞 +41 21 69 58236 • ✉ paul.gratia@epfl.ch
 🌐 <http://gmf.epfl.ch/people>

2/2

First author

The many faces of mixed ion perovskites: unraveling the crystallization process

Paul Gratia, Iwan Zimmermann, Pascal Schouwink, Jun-Ho Yum, Jean-Nicolas Audinot, Kevin Sivula, Tom Wirtz, Mohammad K. Nazeeruddin
ACS Energy Letters, 2017

Intrinsic Halide Segregation at Nanometer Scale Determines the High Efficiency of Mixed Cation/Mixed Halide Perovskite Solar Cells

Paul Gratia, Giulia Grancini, Jean-Nicolas Audinot, Xavier Jeanbourquin, Edoardo Mosconi, Iwan Zimmermann, David Dowsett, Yonghui Lee, Michael Grätzel, Filippo De Angelis, Kevin Sivula, Tom Wirtz, and Mohammad Khaja Nazeeruddin
JACS, 2016 138, 15821-15824

A Methoxydiphenylamine-Substituted Carbazole Twin Derivative: An Efficient Hole-Transporting Material for Perovskite Solar Cells

Paul Gratia, Artiom Magomedov, Tadas Malinauskas, Maryte Daskeviciene, Antonio Abate, Shahzada Ahmad, Michael Grätzel, Vytautas Getautis, Mohammad Khaja Nazeeruddin
Angewandte Chemie Int. Ed. 2015, 54: 11409–11413

Methoxydiphenylamin-substituiertes Carbazol-Zwillingsderivat: ein effizienter organischer Lochleiter für Perowskit-Solarzellen

Paul Gratia, Artiom Magomedov, Tadas Malinauskas, Maryte Daskeviciene, Antonio Abate, Shahzada Ahmad, Michael Grätzel, Vytautas Getautis, Mohammad Khaja Nazeeruddin
Angewandte Chemie, 2015 12, 11571–11575 (German edition)

High efficiency methylammonium lead triiodide perovskite solar cells: the relevance of non-stoichiometric precursors

C Roldan-Carmona*, P. Gratia*, I Zimmermann*, G Grancini, P Gao, Michael Graetzel, Mohammad Khaja Nazeeruddin
Energy Environ. Science (EES), 2015,8, 3550-3556

*indicates shared equal contribution

Co- author

Dopant-Free Hole-Transporting Materials for Stable and Efficient Perovskite Solar Cells

Sanghyun Paek, Peng Qin, Yonghui Lee, Kyung Taek Cho, Peng Gao, Giulia Grancini, Emad Oveisi, Paul Gratia, Kasparas Rakstys, Shaheen A Al-Muhtaseb, Christian Ludwig, Jaejung Ko, Mohammad Khaja Nazeeruddin
Advanced Materials, 2017, x, xxx

Branched methoxydiphenylamine-substituted fluorene derivatives as hole transporting materials for high-performance perovskite solar cells

Tadas Malinauskas, Michael Saliba, Taisuke Matsui, Maryte Daskeviciene, Simona Urnikaite, Paul Gratia, Robert Send, Henrike Wonneberger, Ingmar Bruder, Michael Graetzel, Vytautas Getautis, Mohammad Khaja Nazeeruddin
Energy Environ. Science (EES), 2016,9, 1681-1686

Highly Efficient Perovskite Solar Cells Employing an Easily Attainable Bifluorenylidene-Based Hole-Transporting Material

Kasparas Rakstys, Michael Saliba, Peng Gao, Paul Gratia, Egidijus Kamarauskas, Sanghyun Paek, Vyintas Jankauskas, Mohammad Khaja Nazeeruddin
Angewandte Chemie Int. Ed., 2016, 55, 7464.

Benzotrithiophene-Based Hole-Transporting Materials for 18.2% Perovskite Solar Cells

Agustín Molina-Ontoria, Iwan Zimmermann, Inés García-Benito, Paul Gratia, Cristina Roldán-Carmona, Sadig Aghazada, Michael Graetzel, Mohammad Khaja Nazeeruddin, Nazario Martín
Angewandte Chemie Int. Ed., 2016, 55, 6270.

Semi-Transparent Polymer Solar Cells with Excellent Sub-Bandgap Transmission for Third Generation Photovoltaics

Zach M Beiley, M Greyson Christoforo, [Paul Gratia](#), Andrea R Bowring, Petra Eberspacher, George Y Margulis, Clément Cabanetos, Pierre M Beaujuge, Alberto Salleo, Michael D McGehee
Advanced Materials, 2013, 25, 7020–7026

Enhanced TiO₂/MAPbI₃ electronic coupling by interface modification with PbI₂

Edoardo Mosconi, Giulia Grancini, Cristina Roldán-Carmona, [Paul Gratia](#), Iwan Zimmermann, Mohammad Khaja Nazeeruddin, Filippo De Angelis
Chemistry of Materials, 2016, 28, 3612–3615

Additive-Free Transparent Triarylamine-Based Polymeric Hole-Transport Materials for Stable Perovskite Solar Cells

Taisuke Matsui, Ieva Petrikyte, Tadas Malinauskas, Konrad Domanski, Maryte Daskeviciene, Matas Steponaitis, [Paul Gratia](#), Wolfgang Tress, Juan-Pablo Correa-Baena, Antonio Abate, Anders Hagfeldt, Michael Grätzel, Mohammad Khaja Nazeeruddin, Vytautas Getautis, Michael Saliba
ChemSusChem, 2016, 9, 2567

Toward higher photovoltage: effect of blocking layer on cobalt bipyridine pyrazole complexes as redox shuttle for dye-sensitized solar cells

Jun-Ho Yum, Thomas Moehl, Junghyun Yoon, Aravind Kumar Chandiran, Florian Kessler, [Paul Gratia](#), Michael Grätzel
J. Phys. Chem. C, 2014, 118, 16799–16805

High open-circuit voltage: fabrication of formamidinium lead bromide perovskite solar cells using fluorene–dithiophene derivatives as hole-transporting materials

Neha Arora, Simonetta Orlandi, M Ibrahim Dar, Sadig Aghazada, Gwénoélé Jacopin, Marco Cavazzini, Edoardo Mosconi, [Paul Gratia](#), Filippo De Angelis, Gianluca Pozzi, Michael Graetzel, Mohammad Khaja Nazeeruddin
ACS Energy Letters, 2016, 1, 107–112

Donor– π –donor type hole transporting materials: marked π -bridge effects on optoelectronic properties, solid-state structure, and perovskite solar cell efficiency

S Paek, I Zimmermann, P Gao, [P Gratia](#), K Rakstys, G Grancini, Mohammad Khaja Nazeeruddin, Malik Abdul Rub, Samia A Kosa, Khalid A Alamry, Abdullah M Asiri
Chemical Science, 2016, 7, 6068–6075

Molecularly Engineered Phthalocyanines as Hole-Transporting Materials in Perovskite Solar Cells Reaching Power Conversion Efficiency of 17.5%

Kyung Taek Cho, Olga Trukhina, Cristina Roldán-Carmona, Mine Ince, [Paul Gratia](#), Giulia Grancini, Peng Gao, Tomasz Marszalek, Wojciech Pisula, Paidi Y Reddy, Tomás Torres, Mohammad Khaja Nazeeruddin
Advanced Energy Materials 2016, 1601733.

A highly hindered bithiophene-functionalized dispiro-oxepine derivative as an efficient hole transporting material for perovskite solar cells

Kasparas Rakstys, Sanghyun Paek, Muhammad Sohail, Peng Gao, Kyung Taek Cho, [Paul Gratia](#), Yonghui Lee, Klaus H Dahmen, Mohammad Khaja Nazeeruddin
J. Mater. Chem. A, 2016, 4, 18259–18264

Molecular Engineering of Face-on Oriented Dopant-free Hole Transporting Material for 19% Perovskite Solar Cells

Kasparas Rakstys, Sanghyun Paek, Peng Gao, Paul Gratia, Tomasz Marszalek, Giulia Grancini, Kyung Taek Cho, Kristijonas Genevicius, Vygtintas Jancauskas, Wojciech Pisula, Mohammad Khaja Nazeeruddin
J. Mater. Chem. A, 2017, 5, 7811–7815

Patent

Small molecule hole transporting material for optoelectronic and photoelectrochemical devices

Paul Gratia, Mohammad Khaja Nazeeruddin, Michael Graetzel, Vytautas Getautis, Artiom Magomedov, Tadas Malinauskas, Maryte Daskeviciene
EPFL-PATENT-221254, Eur. Pat. Appl., 2016

